Université de Montréal

Étude structure-fonction des fructose-1,6-bisphosphate aldolases métallo-dépendantes:

Mécanisme catalytique et développement d'antimicrobiens

par

Mathieu Coinçon

Département de Biochimie

Faculté de Médecine

Thèse présentée à la Faculté de Médecine
en vue de l'obtention du grade de *Philosophiae Doctor* (Ph.D.)
en Biochimie

Septembre, 2010

Université de Montréal
Faculté des études supérieures et postdoctorales

Cette thèse intitulée :

Étude structure-fonction des fructose-1,6-bishosphate aldolases métallo-dépendantes: Mécanisme catalytique et développement d'antimicrobiens

Présentée par :
Mathieu Coinçon

a été évaluée par un jury composé des personnes suivantes :

Dr Christian Baron, président-rapporteur
Dr Jurgen Sygusch, directeur de recherche
Dr Jeffrey Keillor, membre du jury
Dr Peter Pawelek, examinateur externe
Dr Christine Des Rosiers, représentante du doyen de la FES

Résumé

Les fructose-1,6-bisphosphate aldolases (FBPA) sont des enzymes glycolytiques (EC 4.1.2.**13**) qui catalysent la transformation réversible du fructose-1,6-bisphosphate (FBP) en deux trioses-phosphates, le glycéraldéhyde-3-phosphate (G3P) et le dihydroxyacétone phosphate (DHAP). Il existe deux classes de FBPA qui diffèrent au niveau de leur mécanisme catalytique. Les classes I passent par la formation d'un intermédiaire covalent de type iminium alors que les classes II, métallodépendantes, utilisent généralement un zinc catalytique. Contrairement au mécanisme des classes I qui a été très étudié, de nombreuses interrogations subsistent au sujet de celui des classes II. Nous avons donc entrepris une analyse détaillée de leur mécanisme réactionnel en nous basant principalement sur la résolution de structures cristallographiques. De nombreux complexes à haute résolution furent obtenus et ont permis de détailler le rôle de plusieurs résidus du site actif de l'enzyme. Nous avons ainsi corrigé l'identification du résidu responsable de l'abstraction du proton de l'O4 du FBP, une étape cruciale du mécanisme. Ce rôle, faussement attribué à l'Asp82 (chez *Helicobacter pylori*), est en fait rempli par l'His180, un des résidus coordonant le zinc. L'Asp82 n'en demeure pas moins essentiel car il oriente, active et stabilise les substrats. Enfin, notre étude met en évidence le caractère dynamique de notre enzyme dont la catalyse nécessite la relocalisation du zinc et de nombreux résidus.

La dynamique de la protéine ne permet pas d'étudier tous les aspects du mécanisme uniquement par l'approche cristallographique. En particulier, le résidu effectuant le transfert stéréospécifique du proton pro(S) sur le carbone 3 (C3) du DHAP est situé sur une boucle qui n'est visible dans aucune de nos structures. Nous avons donc développé un protocole de dynamique moléculaire afin d'étudier sa dynamique. Validé par l'étude d'inhibiteurs de la classe I, l'application de notre protocole aux FBPA de classe II a confirmé l'identification du résidu responsable de cette abstraction chez *Escherichia coli*

(Glu182) mais pointe vers un résidu diffèrent chez *H. pylori* (Glu149 au lieu de Glu142). Nos validations expérimentales confirment ces observations et seront consolidées dans le futur.

Les FBPA de classe II sont absentes du protéome humain mais sont retrouvées chez de nombreux pathogènes, pouvant même s'y révéler essentielles. Elles apparaissent donc comme étant une cible idéale pour le développement de nouveaux agents anti-microbiens. L'obtention de nouveaux analogues des substrats pour ces enzymes a donc un double intérêt, obtenir de nouveaux outils d'étude du mécanisme mais aussi développer des molécules à visée pharmacologique. En collaboration avec un groupe de chimistes, nous avons optimisé le seul inhibiteur connu des FBPA de classe II. Les composés obtenus, à la fois plus spécifiques et plus puissants, permettent d'envisager une utilisation pharmacologique.

En somme, c'est par l'utilisation de techniques complémentaires que de nouveaux détails moléculaires de la catalyse des FBPA de classe II ont pu être étudiés. Ces techniques permettront d'approfondir la compréhension fine du mécanisme catalytique de l'enzyme et offrent aussi de nouvelles perspectives thérapeutiques.

Mots-clés : aldolase glycolytique, mécanisme catalytique, clivage du substrat, condensation aldolique, transfert de proton stéréospécifique, développement de composés antimicrobiens, radiocristallographie, diffraction macromoléculaire des rayons X, dynamique moléculaire.

Abstract

Fructose-1,6-bisphosphate aldolases (FBPA) are glycolytic enzymes (EC 4.1.2.13) that catalyze the reversible cleavage of fructose-1,6-bisphosphate (FBP) into the triose phosphates, glyceraldehyde-3-phosphate (G3P) and dihydroxyacetone phosphate (DHAP). There are two classes of FBPAs that differ at the level of their mechanism. Class I FBPAs form a covalent iminium intermediate whereas class II FBPAs, being metalloenzymes, generally use a catalytic zinc in their reaction mechanism. In contrast to the mechanism of the class I FBPAs, which has been thoroughly studied, there are several unresolved inquiries as to the mechanism of class II FBPAs. We have therefore pursued a detailed analysis of the reaction mechanism using as a primary tool the elucidation of crystallographic structures. Several high resolution complexes have been resolved and have provided critical evidence to help us suggest the implication and role of several key residues in the active site. Consequently, we have correctly identified the residue which is responsible for the abstraction of the O4 proton from FBP, a vital step in the reaction mechanism. The residue responsible for this abstraction, which had incorrectly been assigned to Asp82 (in *Helicobacter pylori*), has been appropriately consigned to His180, a residue which is involved in coordinating the zinc molecule. Nevertheless, Asp82 remains an important residue as it orients, activates and stabilizes substrates. Finally, our study brings to evidence the dynamic character of our enzyme in which catalysis entails the relocalization of the catalytic zinc and several residues.

The complexity of this reaction, notably one of the proton exchanges in the mechanism, could not be resolved solely by crystallographic means. In fact, the residue responsible for the stereospecific transfer of the pro(S) proton on carbon 3 (C3) of DHAP is situated on a loop that was not resolved in any of our structures. We therefore developed a molecular dynamics approach to study this intricate movement. After preliminary validation by inhibitor studies with class I FBPAs, the protocol was applied to class II FBPAs and several remarkable observations emerged: the residue responsible for this

abstraction in *Escherichia coli* is Glu182 whereas a different residue, Glu149 (instead of Glu142) appears to assume this role in *H. pylori*. Our preliminary validations have confirmed this observation and shall be further consolidated in the future.

Class II FBP aldolases, although absent from the human proteome, are prevalently found in several pathogens, and have further been found to be essential to a number of these organisms. As such, they are ideal targets for the development of novel anti-microbial agents. Developing new analogues of the cognate substrates of these enzymes is therefore not only advantageous for mechanistic studies, but has endless pharmacological potential. In the context of a collaborative effort involving a group of chemists, a compound that initially had an inhibition constant in the millimolar range was optimized and produced a series of compounds that inhibit in the nanomolar range.

This study, which combined several disciplines, including crystallography, enzymology, organic chemistry, and molecular modelization, underscores the interest and significance of a multidisciplinary approach.

Keywords : glycolytic aldolase, catalytic mechanism, substrate cleavage, aldol condensation, stereospecific proton transfer, crystallography, macromolecular X-ray diffraction, molecular dynamics, drug-design.

Table des matières

Liste des tableaux

Liste des schémas

Liste des figures

Liste des abréviations

ADP	Adénosine-5'-diphosphate
Asp	Aspartate
ATP	Adénosine-5'- triphosphate
D	Aspartate
DHAP	Dihydroxyacetone phosphate
E	Glutamate
ecFBPA	Fructose-1,6-bisphosphate aldolase de *Escherichia coli*
FBP	Fructose-1,6-bisphosphate
FBPA	Fructose-1,6-bisphosphate aldolase
FTIR	Spectroscopie InfraRouge par Transformée de Fourier
G3P	Glyceraldehydes-3-phosphate
glFBPA	Fructose-1,6-bisphosphate aldolase de *Giardia lamblia*
Glu	Glutamate
H	Histidine
HBP	Hexitol-1,6-bisphosphate
His	Histidine
hpFBPA	Fructose-1,6-bisphosphate aldolase de *Helicobacter pylori*
kcat	Constante catalytique
Ki	Constante d'inhibition
Km	Constante de Michaelis-Menten
MAD	*Multiple-wavelenght Anomalous Dispersion*
MIR	*Multiple Isomorphous Replacement*
mtFBPA	Fructose-1,6-bisphosphate aldolase de *Mycobacterium tuberculosis*
NADH	Adénosine diphosphate
NOE	*Nuclear Overhauser Effect*
PDB	protein data bank

PGA	Phosphoglycoloamidoxine
PGH	Phosphoglycolohydroxamate
PGHz	Phosphoglycolohydrazide
RMN	Résonance Magnétique Nucléaire
SAD	*Single-wavelenght Anomalous Dispersion*
SCOP	*Structural Classification Of Proteins* (http://scop.mrc-lmb.cam.ac.uk/scop/)
taFBPA	Fructose-1,6-bisphosphate aldolase de *Thermus aquaticus*
TBP	Tagatose-1,6-bisphosphate
tcFBPA	Fructose-1,6-bisphosphate aldolase de *Thermus caldophylus*
TIM	Triose-phosphate isomérase
WT	*Wild-Type*
µM	Micromolaire

À toi qui me rends heureux.

Remerciements

Je voudrais tout d'abord remercier les membres de mon jury pour avoir accepté de corriger cette thèse et de l'avoir fait dans un si court délai.

Je remercie le Professeur Sygusch pour m'avoir accueilli dans son laboratoire et pour m'avoir offert ce sujet après deux départs avortés (les Rab et les protéines de plantes ne mettaient pas destinées). Notre périple ne s'est pas fait dans la tranquillité et nos deux fortes personnalités ont été source de quelques accrochages mais ont ne fait pas de feu sans étincelles. Merci pour la liberté que vous m'avez laissé et qui m'a permis de m'épanouir.

Je suis aussi redevable à tous mes collaborateurs pour avoir étoffer ce doctorat et m'avoir permis d'élargir ma vision scientifique. En particulier les Dr Fonvielle, Therisod *(désolé pour le gant)*, Blonski et Seah.

Merci à mon Directeur de DEA, Philippe Derreumaux pour m'avoir donné le virus et à Sebastien *(Mande et Elliot aussi)* pour avoir accompagné mes premiers pas.

Je remercie tous les membres du synchrotron à BNL pour leur accueil et pour m'avoir permis de joindre le staff de Rapidata. En particulier Annie pour sa gentillesse et son soutient.

Je remercie les membres du laboratoire *(la plupart)* pour avoir supporté mes 'jokes plates' et mes 'chialages'. Guillaume, mon calinours, toujours prêt à me faire rire *('He big mama, t'as mis ton pyjama !!!')*, Paul pour m'avoir tenu compagnie dans ce labo *(pas assez)* désert pendant ma dernière année, Arnold pour ses grands moments de philosophie, Oktavian et Jaan mes deux esclaves adorables, Annie et JF pour leur gentillesse. Miguel pour son énergie et JLV pour ses beaux moments partagés à BNL. Enfin Laurent, mon mentor en biochimie, petit stagiaire qui a formé le jeune doctorant que j'étais au maniement de la pipette et qui m'a toujours tendu une oreille compatissante *(ou peut-être distraite),* ton amitié et ton support m'ont fait beaucoup de bien.

Il m'est difficile de nommer toutes les personnes du département avec qui j'ai partagé quelque chose, que ce soit une discussion de couloir, un café, un fou rire ou une bière. Mais je vous remercie tous pour m'avoir permis de me sentir chez moi dans ces vieux couloirs sombres. En essayant d'écrire ces lignes, je me demande comment avec tous ces moments 'perdus' j'ai pu finir cette thèse *(et je sais que je ne suis pas le seul)*.

Merci à Béatrice, Philippe et Henner pour ces agréables discussions et points de vue. Merci à Jim et Christian pour votre soutient. Merci à toutes les dames du fond du couloir pour l'avoir rempli de votre rire et pour votre gentillesse. En particulier Sylvie.

Merci à tous les membres du CA, pour ces beaux moments et ces réunions qui étaient loin d'être ennuyantes *(Hips!!!)*. Le membres des labs Legaut, Omichinski, Brisson et Baron. En particulier *(nrj)* Etienne *(penses à moi lorsque tu auras monté ton institut….dans 2-3 ans)* et 'blue eyes' JS, mes deux *'Mister Biochimie'* (je pourrais vous dire plein de choses mais je ne vois rien à part merci…….*'What else ?'),*Tom, Mathieu V. *(M&M&Ms powaaaa!!!)*, Nicolas *(c'est pour quand ton opération Géraldine? Bise à Eléonor aussi)* et Benoit *(mon calinours numéro 2)*.

Merci à mes trois drôles de dames, Caro, Chantal et Vanessa. Et aux personnes qui partagent leur vie Adrien, Colin, Stéphane, Angélie et Alizée. Pour tous ces bons moments. votre gentillesse et pour votre amitié.

Mark my Bro from another Mo *(…..)*. Tom, Olivier et Fred *(vous n'étiez jamais loin de moi !!)*.

Ces sept années à Montréal, nous ont offert une deuxième famille qui nous a permis de nous sentir chez nous. Suzanne et Fabrice, Pierrot, Cath et Robert, Suzanne J., Josep, Marionna et Marti, Nancy et Nolive, Matthieu, Geneviève, Antoine et Loic, Carotte, miss V, sa cravache et son Empereur, Nico, Hugo et ma Gregouille. On vous aime tous très fort. Merci, merci, merci!

Merci à nos colocs temporaires Manu et Claire et à Eric et Pascale.

Un gros merci à Samira pour t'être aussi bien occupé de nos trésors.

Merci à mes parents pour leur affection et leur soutient. Et oui Maman, je ne voulais pas faire Médecine car les études sont trop longues *(Arg!!!)*.

Gaël et Pauline, mes deux amours, vous ne pouvez pas savoir le bonheur et la force que vous donnez à votre Papa. Vous voir grandir est un bonheur de tous les instants.

Enfin Sandrine car tu es bien plus que ma moitié.

CHAPITRE I

Introduction

"Le commencement de toutes les sciences,
c'est l'étonnement de ce que les
choses sont ce qu'elles sont."
Aristote, **Métaphysique**

1 Introduction

1.1 Les Fructoses-1,6-bisphosphate aldolases

1.1.1 Historique

Dès les premières heures de l'enzymologie, ce domaine a été étroitement lié au métabolisme et particulièrement à celui des sucres. En 1877, suite aux travaux de Louis Pasteur, Wilhelm Kuhne nomma enzyme (du grec *ενζυμον,* dans le levain) le composant responsable de la fermentation alcoolique des levures. Vingt ans plus tard, Buchner montra que ce composant, qu'il nomma alors zymase, pouvait être extrait des cellules. C'est Emil Fischer qui évoqua pour la première fois le caractère spécifique de l'activité enzymatique en étudiant la catalyse de divers pentoses, hexoses ou heptoses, créant au passage le concept de « clef-serrure ». L'identification de la nature chimique des enzymes, à savoir protéique[1], ne fut démontrée qu'en 1926 par James B. Sumner qui, après avoir purifié par cristallisation l'uréase, la caractérisa chimiquement. John H. Northop et Wendell M. Stanley corroborèrent cette identification et ils se partagèrent tous trois le prix Nobel de Chimie en 1946.

C'est en 1934 qu'Otto Meyerhoff décrivit l'activité de ce qu'il appela alors zymohexase, catalyseur de la transformation d'hexoses bisphosphorylés en triose-phosphates. Deux ans plus tard, il isola les deux composantes de cette zymohexase : l'isomérase et l'aldolase. Notre sujet d'étude venait d'être identifié.

1.1.2 Qu'est-ce qu'une aldolase?

Une aldolase est une enzyme de type lyase (Enzyme Commission number : EC **4**). C'est à dire capable de cliver un lien chimique par des mécanismes autres que l'hydrolyse ou l'oxydation. Dans le cas de la fructose1,6-bisphosphate aldolase (FBPA), c'est le lien

[1] On sait, suite aux travaux de Sydney Altam et Thomas Cech, que des ARN, précisément les ribozymes, sont aussi capables d'avoir une activité catalytique.

carbone-carbone (EC 4.**1**) d'un aldéhyde (EC 4.1.**2**) en l'occurrence celui reliant les carbones C_3 et C_4 du D-fructose1,6-bisphosphate (FBP) (EC 4.1.2.**13**). Ce clivage produit deux triose-phosphates, le dihydroxyacétone-phosphate (DHAP) et le D-glycéraldéhyde-3-phosphate (G3P). La FBPA catalyse aussi la réaction inverse c'est-à-dire la condensation des deux trioses.

Cette réaction de condensation est une aldolisation, réaction durant laquelle un énolate ou un éther d'énol (nucléophile), ici le DHAP après activation, s'additionne à un aldéhyde (électrophile), le G3P.

La condensation aldolique du D-G3P et du DHAP peut donner deux produits stéréoisomères (figure 1-1). Ils diffèrent au niveau de la stéréochimie du lien C3-C4. Dans le cas de la FBPA, le lien est de type 3S-4R. Le produit 3S-4S est le tagatose-1,6-bisphosphate.

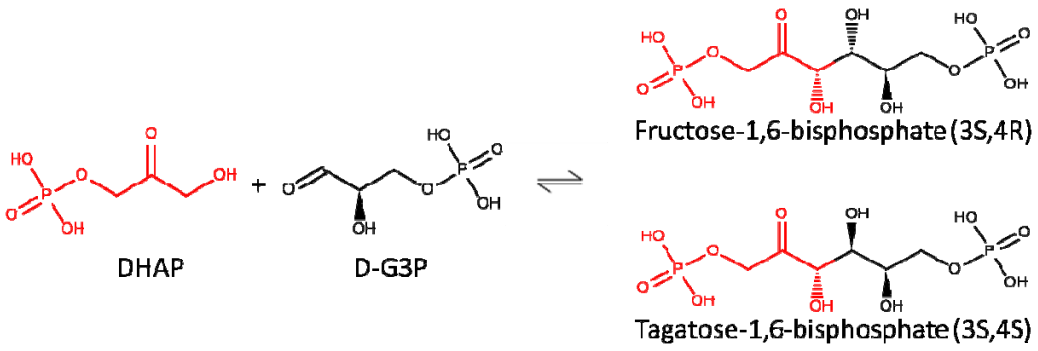

Figure 1-1. Condensation aldolique entre le DHAP et le D-G3P

On classe les aldolases en fonction de la molécule qui s'additionne lors de la condensation. Les types les plus courants sont à DHAP, à pyruvate, à phosphoénolpyruvate et à acétaldéhyde.

D’autres aldolases à DHAP présentent une stéréospécificité de type 3R-4R (Fuculose-1-phosphate aldolase) ou 3R-4S (Rhamnulose-1-phosphate aldolase) mais l’accepteur est le L-lactaldehyde (Takayama, McGarvey, and Wong, 1997).

Une autre classification des FBPA repose sur le type de mécanisme utilisé par l’enzyme, plus précisément sur la manière dont le DHAP est activé, soit par sa transformation en énolate soit en un éther d’énol (énamine).

(page suivante)

Tableau 1-1. Exemples de familles d'aldolase et des réactions qu’elles catalysent.

(modifiée de Whitesides *et al.* (Whitesides and Wong, 1985))

Références: *1*- (Ghalambor and Heath, 1962), *2*- (Ghalambor and Heath, 1966), *3*- (Meloche and Glusker, 1973) , *4*- (Pouyssegur and Stoeber, 1974) , *5*- (Weissbach and Hurwitz, 1959), *6* - (Ray and Benedict, 1980), *7*- (Pricer and Horecker, 1960)

Donneur	Accepteur	Produit	Enzyme
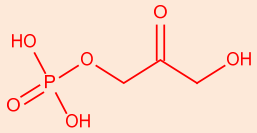 DHAP	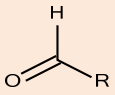	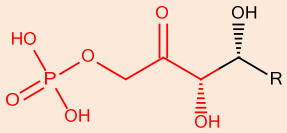	D-Fructose-1,6-bisphosphate aldolase
	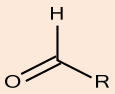	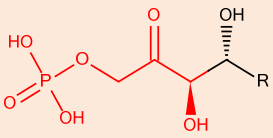	L-fuculose-1-phosphate aldolase[1]
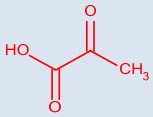 Pyruvate	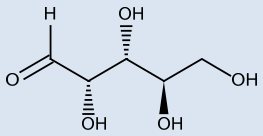	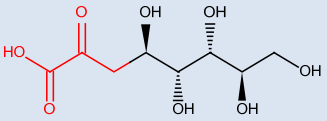	3-deoxy-D-mannooctulosonate Aldolase[2]
	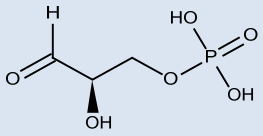	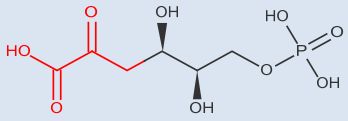	2-keto-3-deoxy-6-phosphogluconate Aldolase[3]
	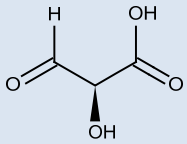	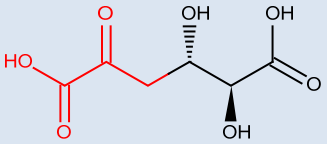	2-keto-3-deoxy-D-glucarate Aldolase[4]
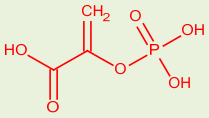 Phosphoénolpyruvate	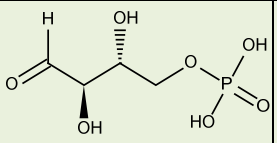	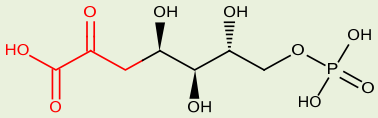	2-keto-3-deoxyheptonate Aldolase[5]
	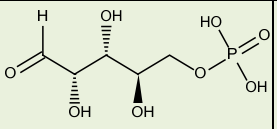	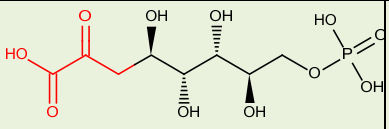	3-deoxy-D-manno-octulosonate-8-phosphate synthase[6]
 Acétaldéhyde		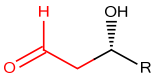	Desoxyribose-phosphate Aldolase[7]

1.1.3 Deux mécanismes - deux classes

C'est William Rutter (Rutter, 1964) qui proposa de diviser les FBPA en deux classes. Les classes I activent le DHAP en formant un intermédiaire covalent iminium, appelé aussi base de Schiff, puis énamine (un éther d'énol). Les classes II utilisent un cation métallique divalent (principalement du zinc) qui va stabiliser un intermédiaire énolate, l'énediolate. Caractériser chimiquement à quelle classe appartient une FBPA est aisé. Les classes I seront inhibées par l'utilisation de sodium borohydride (NaBH4) qui va réduire la base de Schiff. Alors que les classes II seront inactivées par l'utilisation de chélateur puissant tel que l'acide éthylène-diamine-tétraacétique (EDTA).

Dans les deux cas, l'enzyme rend le carbone C2 du FBP plus électrophile afin de faciliter l'abstraction du proton de l'hydroxyle en O4 et la formation de la double liaison C2=C3 des intermédiaires réactionnels (l'énamine pour la classe I, l'énediolate pour la II).

Le mécanisme des classes II sera exposé au chapitre 2.2. Celui des classes I est détaillé dans la thèse de Miguel St-Jean (St-Jean, 2007). La comparaison entre ces deux mécanismes est présentée à la figure 1-2.

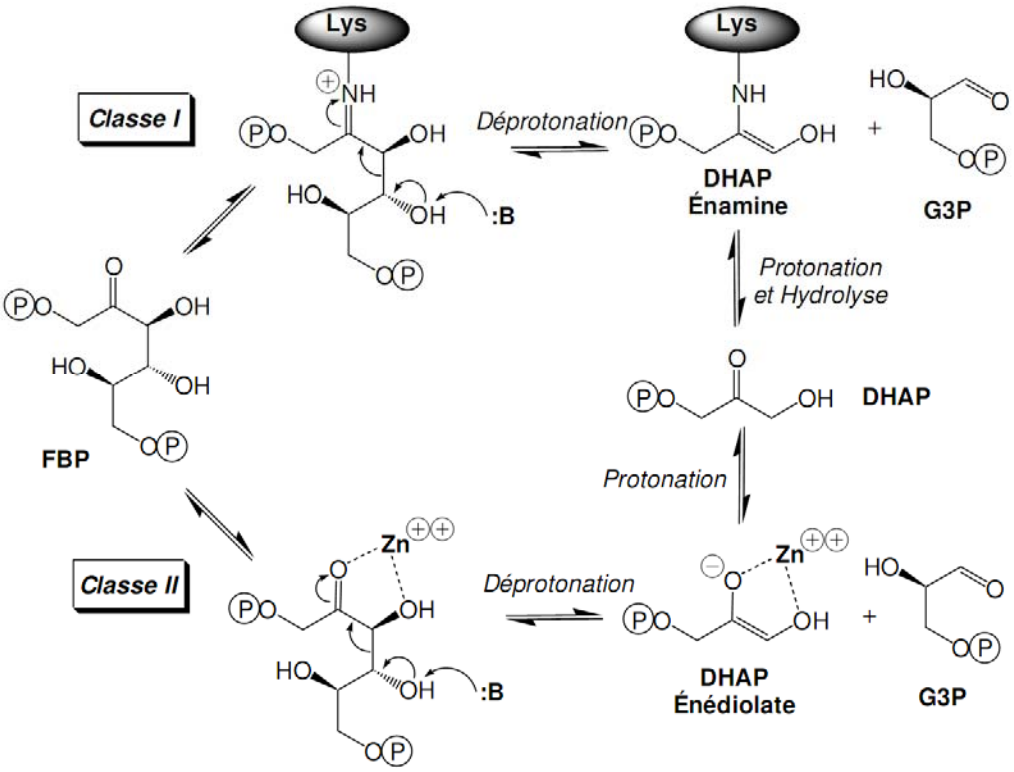

Figure 1-2. Mécanisme du clivage du FBP chez les FBPA de classe I et II

(d'après St-Jean (St-Jean, 2007))

1.1.4 Caractéristiques

1.1.4.1 Un repliement, plusieurs enzymes

Toutes les FBPA présentent un repliement de type $(\alpha/\beta)_8$ (figure 1-3). Ce repliement est aussi appelé « TIM-barrel » puisqu'il a était observé pour la première fois après la résolution de la structure de la triose-phosphate isomérase (Banner et al., 1976; Banner et al., 1975). Cette structure (PDB : 1TIM), qui est d'ailleurs devenue un des exemples classiques de la cristallographie, au même titre que celles du lysosyme (PDB : 2lyz) ou de la myoglobine (PDB : 1mbn), offre l'archétype de ce repliement qui est le plus répandu parmi les structures connues. Il est constitué d'un enchaînement de huit paires hélice-α/brin-β reliées entre elles par des boucles de longueur variable (figure 1-3). Les brins-β constituent un tonneau hydrophobe protégé par les hélices-α qui présentent des résidus hydrophiles au solvant. Ce repliement globulaire est très stable, ce qui peut en partie expliquer que l'on ait obtenu autant de structures cristallines de ce type (la compacité et la stabilité d'une protéine facilitant généralement sa cristallisation).

Dans la classification SCOP (Murzin et al., 1995), les deux classes de FBPA forment deux familles distinctes de la superfamille « aldolase » (qui en compte huit). Cette superfamille faisant partie des trente-trois que comptent les protéines à « TIM barrel ».

Alors que la taille des sous-unités retrouvées chez les deux classes est relativement constante, environ 40kDa, les classes I tendent à former des homotétramères et les classes II des homodimères. Néanmoins la structure quaternaire des classes I peut aller du monomère au décamère chez certains procaryotes (Thomson et al., 1998) et certaines classes II peuvent aussi former des tétramères (Lee et al., 2006).

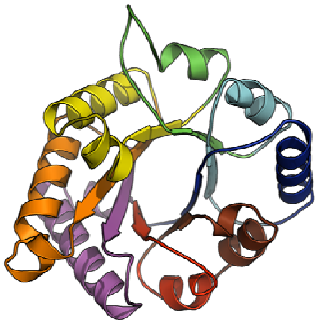

Triose-phosphate isomerase (TIM) de *Gallus gallus* (PDB : 1TIM)

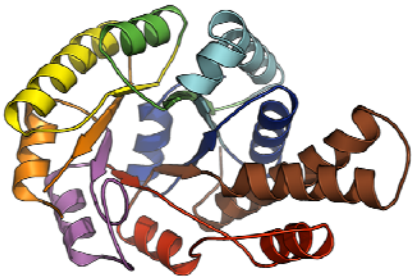

Fructose-1,6-bisphosphate aldolase d'*Helicobacter pylori* (PDB : 3C4U) - Classe II B

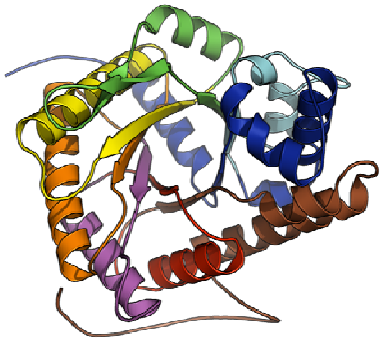

Fructose-1,6-bisphosphate aldolase d' *Oryctolagus cuniculus* (PDB : 1ZAH) - Classe I

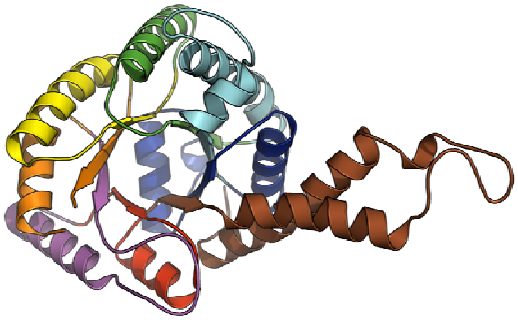

Fructose-1,6-bisphosphate aldolase d'*Escherichia coli* (PDB : 1DOS)- Classe II A

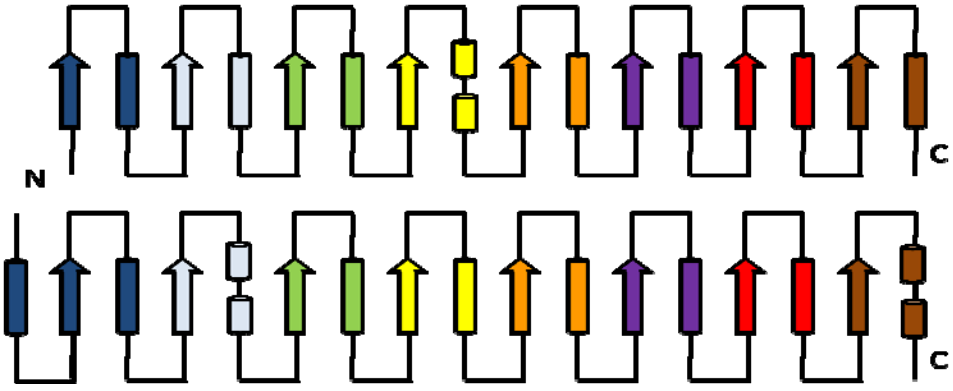

Schéma des structures secondaires de la TIM (haut) et de la hpFBPA (bas).

Figure 1-3. Comparaison des structures secondaires et tertiaires de diverses FBPA avec celle de la TIM

Une étude bioinformatique portant sur les protéines possédant ce repliement (Nagano, Orengo, and Thornton, 2002) a mis à jour plusieurs caractéristiques intéressantes :

1. Ce sont souvent des enzymes et elles représentent cinq des six classes existantes.
2. Le site actif est généralement situé à l'extrémité C-terminale des brins β.
3. Deux tiers de ces protéines lie un métal.
4. On trouve souvent des boucles ayant un rôle catalytique.
5. La moitié possède un site de liaison au phosphate.

Ce sont des caractéristiques qui s'appliquent parfaitement aux FBPA de classe II.

1.1.4.2 Les prémices d'une phylogénie

Un test biochimique facile à réaliser, la disponibilité d'un nombre de séquences d'ADN génomique croissant et la résolution de plusieurs structures tridimensionnelles auraient dû permettre d'obtenir une phylogénie claire des FBPA.

Hélas, leur répartition qui s'annonçait relativement clair, la classe I dans les règnes[2] Animalia, Protista et Plantae, la classe II dans les Bacteria, Fungi et Archaea, n'est qu'apparente.

Certes on pourrait la considérer comme une règle générale mais il existe un grand nombre d'exceptions. Ainsi certaines Archées (*Halobacterium saccharovorum, Thermoproteus tenax, Pyrococcus furiosus*) (Siebers et al., 2001) et Eubactéries (*Micrococcus aerogenes, Staphylococcus aureus, Staphylococcus carnosus*) possèdent une classe I alors que *Giardia lamblia,* un Protiste, possède une classe II. On retrouve même les

[2] Bien qu'obsolète cette classification sera utilisée par soucis de simplicité d'autant qu'aucun consensus ne semble exister actuellement parmi les phyllogénéticiens.

deux classes chez *Escherischia coli, Mycobacterium tuberculosis, Lactobacillus casei, Saccahromyces cerevisae* (Fungi) et *Euglena gracilis* (Protista)

Il est ainsi très difficile de donner une vue complète et une interprétation correcte de la phylogénie et de l'histoire évolutive des FBPA.

Des alignements de multiples de séquencesou des analyses structurales ont néanmoins permis de délimiter des sous-classes. On peut ainsi considérer qu'il existe au moins trois sous-classes chez les classe I (type eucaryote, type *Staphilococcus (Gotz, Fischer, and Schleifer, 1980; Witke and Gotz, 1993)* et type *E. coli (Thomson et al., 1998)*). De plus, la distinction entre les sous-classes IIA et IIB, qui est pourtant basée sur des différences marquées au niveau des séquences des boucles tertiaires, ne permet pas de rassembler ne serait-ce que les protéines provenant d'un même règne. Même ainsi, on ne peut trouver de corrélation avec aucune classification phylogénétique.

Ainsi l'histoire évolutive de ces protéines est confuse et cela malgré le caractère ubiquitaire de leur répartition.

1.1.5 Importance biologique

1.1.5.1 Glycolyse et néoglucogenèse

La glycolyse est considérée comme une des plus anciennes voies de production énergétique (Romano and Conway, 1996). Comme son nom l'indique, c'est une voie métabolique qui dégrade le glucose. Il en existe plusieurs mais Otto Meyerhof, parallèlement à ses recherches sur plusieurs enzymes métaboliques (dont l'aldolase), élucida la voie la plus répandue. Cette voie aussi connue sous le nom de voie « Embden-Meyerhof-Parnas » est une cascade enzymatique de dix réactions qui, à partir de chaque molécule de glucose, aboutit à la formation de deux molécules d'pyruvates tout en générant deux molécules d'ATP et en libérant deux protons et deux NADH :

$$\text{glucose} + 2\ \text{ADP} + 2\ \text{Pi} + 2\ H^+ + 2\ NAD^+ \rightarrow 2\ \text{pyruvates} + 2\ \text{ATP} + 2\ (NADH,H^+) + 2\ H2O$$

La voie est scindée en deux parties (figure 1-4). Une phase de préparation, dites d'investissement énergétique, qui utilise deux molécules d'ATP et produit deux G3P. Puis une phase de récupération/création d'énergie où les G3P sont oxydés en pyruvate. Ils génèrent alors deux ATP et un NADH chacun. Le bilan de la glycolyse est donc assez faible (2 ATP et 2 NADH) mais l'utilisation ultérieure des pyruvates par la respiration cellulaire (cycle de Krebs) ou la fermentation permettra de transformer l'énergie intrinsèque contenue dans ces molécules en énergie utilisable par la cellule, de l'ATP.

Bien qu'étant à la jonction des deux phases, la FBPA n'est pas considérée comme centrale car elle ne semble pas jouer de rôle au niveau de la régulation de la glycolyse, principalement opérée au niveau de l'hexokinase, de la phosphofructokinase et de la pyruvate kinase.

La néoglucogenèse est considérée à tort comme la voie inverse de la glycolyse. En fait, cette voie de synthèse du glucose peut se faire à partir de divers précurseurs non glucidiques (pyruvate, lactate, acides aminés et glycérol). Dans le cas du pyruvate, elle utilise les mêmes enzymes que la glycolyse sauf pour trois étapes non réversibles. Il existe alors des détournements (« shunt » en vert dans la figure 1-4) où des enzymes spécifiques permettent de générer le phosphoénolpyruvate à partir du pyruvate, le fructose-6-phosphate à partir du FBP et enfin le glucose à partir du glucose-6-phosphate.

Enfin, il est à noter que l'aldolase fait aussi partie du cycle de Calvin des végétaux puisque celui-ci utilise une partie des enzymes glycolytiques pour générer le fructose-6-phosphate à partir du 3-phosphoglycérate.

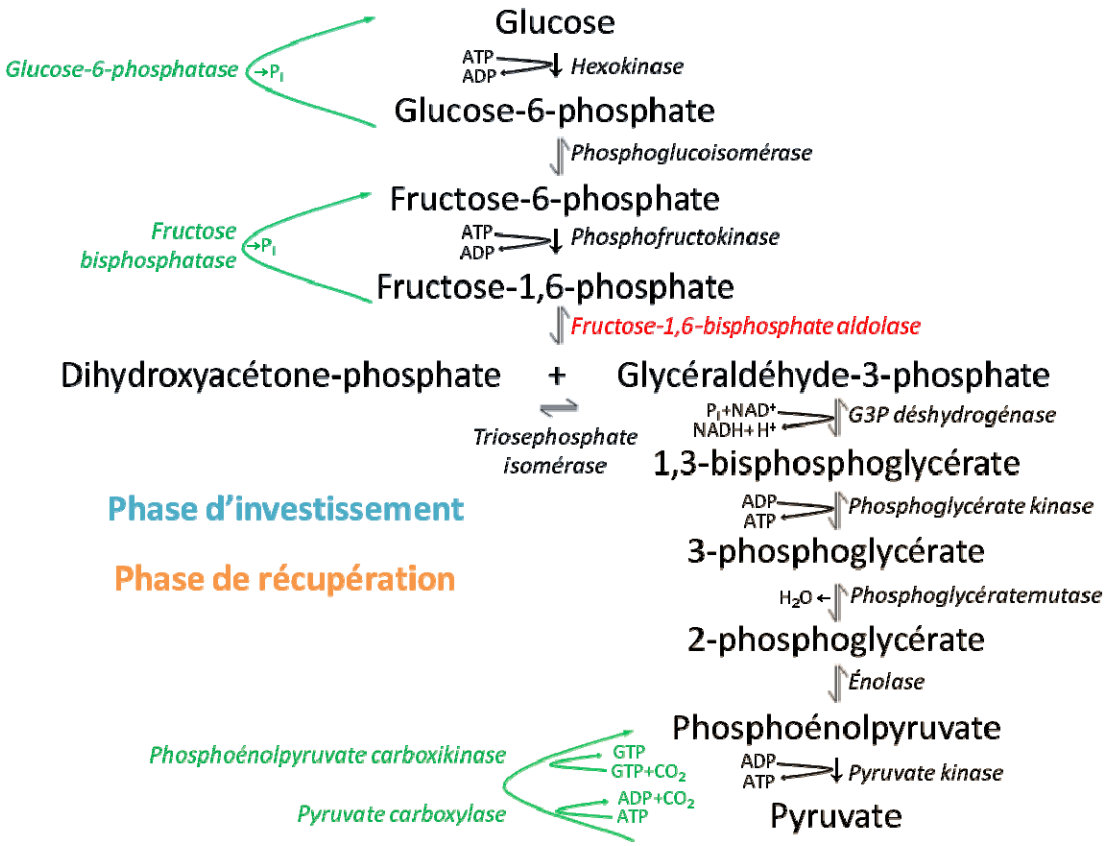

Figure 1-4. Schéma de la glycolyse et de la néoglucogenèse.

1.1.5.2 Fonctions secondaires, les aldolases et le « moonlighting »

Le terme « moonlighting » peut sembler poétique mais doit être traduit par « travail au noir ». Pour une protéine, cela consiste à remplir une ou plusieurs autres fonctions supplémentaires. En ce qui concerne la FBPA, il s'agit d'un rôle différentde son activité catalytique

1.1.5.2.1 Les classes I et leurs interactions

Les classes I sont extrêmement abondantes dans les cellules, pouvant même représenter jusqu'à 5% des protéines solubles des muscles (Maughan, Henkin, and Vigoreaux, 2005). Il semble alors naturel que plusieurs interactions avec d'autres composants cellulaires aient été rapporté.

La FBPA interagit principalement avec le cytosquelette. Sa liaison à l'actine et sa concentration ont un effet sur l'état filamenteux de cette dernière (important pour réguler la gélification du cytoplasme) (O'Reilly and Clarke, 1993; Wang et al., 1996). Elle interagit aussi avec les microtubules (Walsh, Keith, and Knull, 1989) et la tubuline (Karkhoff-Schweizer and Knull, 1987; Volker and Knull, 1997; Volker and Knull, 1993; Volker, Reinitz, and Knull, 1995).

Son état oligomèrique pourrait ainsi lui permettre de lier plusieurs protéines et de jouer un rôle dans leur localisation par son interaction avec le cytosquelette comme cela a été démontré dans le cas de l'exocytose des vésicules contenant le transporteur de glucose GLUT4 (Kao et al., 1999). Sa liaison à des nexines et à des dynamines (SNX9/Dyn2), molécules centrales de l'endocytose des vésicules à clathrine (Lundmark and Carlsson, 2004) renforce cette hypothèse.

Elle interagit aussi avec des molécules jouant des rôles importants dans la signalisation cellulaire comme les inositols-phosphates (Baron, Greeley, and Coburn, 1998; Baron et al., 1995; Baron et al., 1999), les acides-nucléiques (Ronai, 1993) ou les protéines S100 (Zimmer, Wright Sadosky, and Weber, 2003).

La FBPA semble également être impliquée dans l'infection par les parasites *Plasmodium falciparum* (Heiss et al., 2008), vecteur du paludisme, et *Toxoplasma gondi* (Sibley, 2003; Starnes et al., 2009) en interagissant avec l'extrémité C-terminale des adhésines de l'hôte. Ce mode de liaison est identique à celui de l'aldolase avec la protéine du syndrome Wiscott-Aldrich (WASP) (Buscaglia et al., 2007; Buscaglia et al., 2006; St-Jean, Izard, and Sygusch, 2007) comme cela a été mis en évidence par la structure obtenu au laboratoire en 2007.

D'autres types d'interactions s'ajoutent régulièrement à cette liste non exhaustive avec le développement des méthodes à haut débit utilisées en protéomique. Et l'implication de cette enzyme dans un plus grand nombre de fonctions cellulaires ne serait pas étonnante.

D'une manière générale ont peut penser que c'est son rôle de molécule-pont entre diverses protéines et le cytosquelette qui est le principal dénominateur commun entre toutes ces fonctions. Quand on sait que le cytosquelette est un des consommateurs principaux de l'énergie cellulaire, l'utilisation d'une molécule liée au métabolisme semble pouvoir être favorisée. Mais qu'en est-il des classes II que l'on retrouve principalement chez des procaryotes, qui sont eux dépourvu de cytosquelette?

1.1.5.2.2 Les classes II et l'adhésion aux cellules hôtes lors de l'infection

Tout comme les classes I, les FBPA métallo-dépendantes sont très bien exprimées dans les cellules. Elles représentent 2% des protéines acides (c'est-à-dire possédant un point isoélectrique inférieur à 7) solubles chez *Candida albicans* (Yin et al., 2004) et on en retrouve plus de 47000 copies par cellule chez *Escherichia coli* (Ishihama et al., 2008). Cette abondance peut permettre à ces protéines de remplir d'autres fonctions en plus de leur activité catalytique (Schwelberger, Kohlwein, and Paltauf, 1989).

Par contre, les classes II ne semblent pas être des composantes de complexes essentiels à la vie des cellules les exprimant. Ainsi le remplacement de la FBPA de classe II chez *Saccharomyces cerevisiae* par celle de *Drosophila melanogaster*, une classe I, ne

semble avoir aucun effet sur la croissance de ces levures (Boles and Zimmermann, 1993). Mais ce pourrait ne pas être le cas pour tous les organismes.

Malgré cela, leurs interactions pourraient être très intéressantes. On sait qu'elles ont un potentiel antigénique non négligeable comme cela a démontré chez les bactéries *Streptococcus pneumoniae* (Ling et al., 2004) et *agalactiae* (Fluegge et al., 2004), *Clostridium perfrigens* (Kulkarni et al., 2007), les mycètes pathogènes *Paracoccidioides brasiliensis* (da Fonseca et al., 2001) ou *Candida albicans* (Fernandez-Arenas et al., 2004a; Fernandez-Arenas et al., 2004b) et enfin le protiste *Giardia lamblia* (Palm et al., 2003). Dernièrement, la FBPA de *Neisseria meningitidis* (Tunio et al., 2010) a spécifiquement été caractérisée comme nécessaire à une bonne adhésion cellulaire de cette bactérie aux cellules humaines et joue donc un rôle au cours de l'infection. Le fait de les retrouver à la surface de certains de ces pathogènes est un indice supplémentaire sur l'existence probable d'interactions additionnelles de ces enzymes.

1.1.6 Application en synthèse chimique

Contrôler la stéréosélectivité lors de la condensation aldolique est très intéressant en synthèse organique.

D'autant plus lorsqu'on sait que les aldolases à DHAP peuvent accepter un grand nombre de substrats différents comme aldéhyde accepteur (Fessner et al., 1996) et ainsi produire une grande variété de produits. Chez les classes II, le chloroacétalehyde et le methylglyoxal ont ainsi déjà été identifiés (Henderson et al., 1994).

En utilisant une enzyme, on peut ainsi réduire le nombre de stéréoisomères possibles tout en catalysant la réaction. Les aldolases à DHAP sont surtout utilisées pour la synthèse de monosaccarides modifiés (marqués au ^{13}C, hétérosubstitués, fluorés…..) (Gijsen et al., 1996; Schumperli, Pellaux, and Panke, 2007).

Certains de ces monosaccharides sont utilisés comme précurseurs pour la synthèse de produits plus complexes comme des composés cycliques. Les FBPA ont aussi été utilisées pour la synthèse d'aza-sucres, des inhibiteurs de glycosidases (Wong, 1996).

Une meilleure compréhension du mécanisme pourra permettre de modifier l'enzyme afin de développer de nouvelles synthèses. La détermination du rôle spécifique des différents acides aminés du site actif sera alors un atout formidable pour la conduite de cette ingénierie.

1.2 Mécanisme catalytique des FBPA de classe II

Encore aujourd'hui les phénomènes fins qui contrôlent le mécanisme des FBPA de classes II ne sont pas clairement définis. Chez les classes I, les travaux réalisés par Miguel St-Jean dans le cadre de son doctorat (St-Jean, Blonski, and Sygusch, 2009; St-Jean et al., 2005; St-Jean and Sygusch, 2007) ont permis de détailler les événements moléculaires et le rôle précis de plusieurs résidus impliqués dans la catalyse de l'aldolase de muscle de lapin. Ne se contentant pas d'interpréter les données cinétiques des mutants, il les a cristallisés en présence des trois ligands naturels ou d'inhibiteurs. Ainsi il a pu par exemple rectifier l'identification du résidu responsable du transfert stéréospécifique du proton sur la base de Schiff, Tyr363, rôle faussement attribué à Asp33 par des études antérieures.

La partie suivante présente les recherches menées sur le mécanisme des classes II. Ces études ayant été menées principalement chez la FBPA de *E. coli* (ecFBPA), la figure 1-5 présente les résidus du site actif de cette enzyme. Ces études, très complètes au niveau des données cinétiques et biochimiques, s'appuient aussi sur plusieurs structures. Malgré tout, certaines questions restent en suspens.

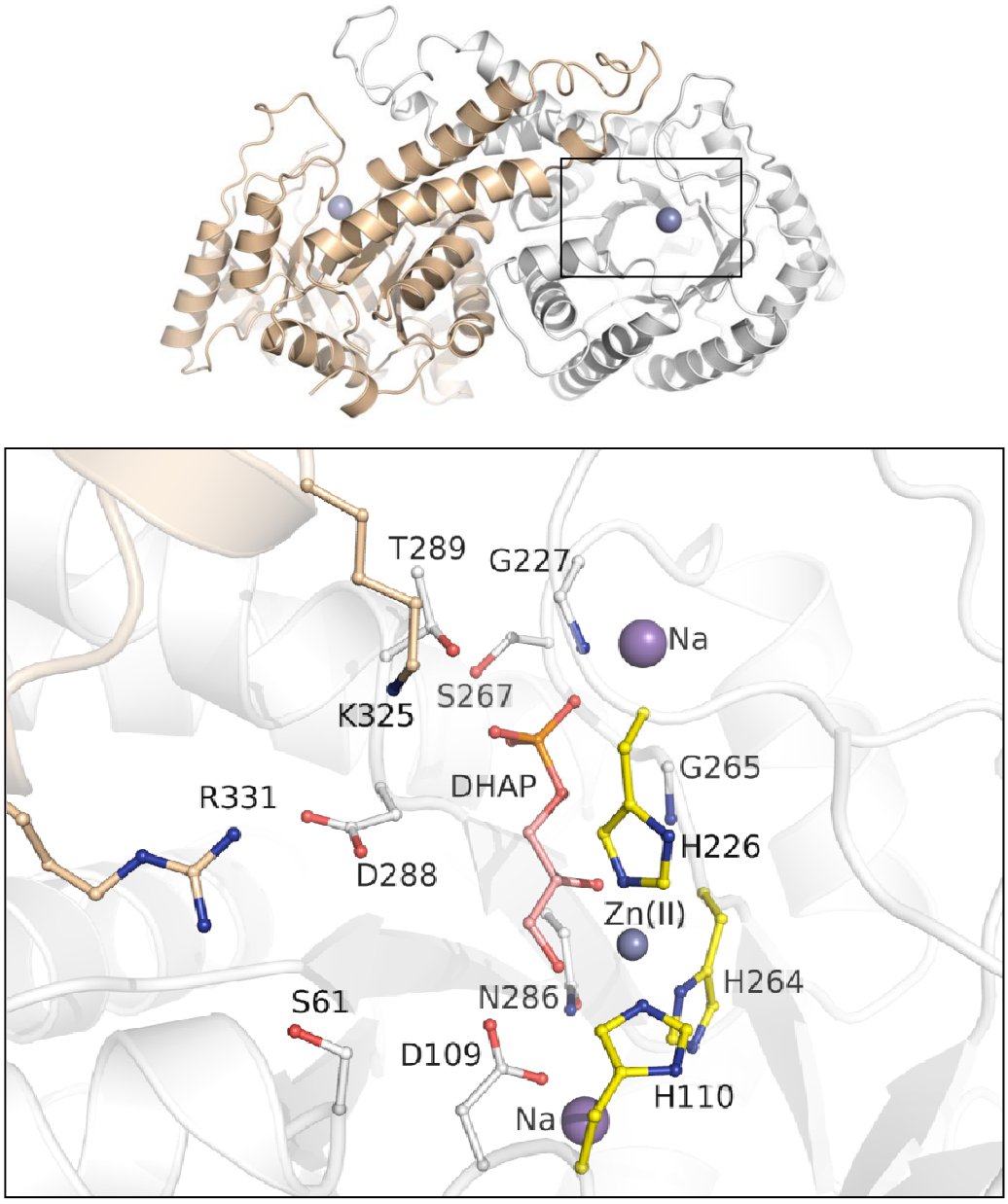

Figure 1-5. Présentation du site actif de la FBPA de classe II de *E. coli*

Haut. Vue complète de la structure du dimère. La chaîne A est colorée en blanc et la chaîne B en beige. Le zinc est représenté par des sphères grises. Bas. Site actif de la structure du complexe entre ecFBPA et le DHAP (rose). Les histidines coordonnant le zinc sont colorées en jaune.

1.2.1 Les premières bases biochimiques

1.2.1.1 La réaction est de type séquentielle ordonnée

C'est Allan Rose en 1965 (Rose, O'Connell, and Mehler, 1965) qui démontra le caractère « séquentiel ordonné » de la réaction, et ce chez les deux classes de FBPA. Ainsi le G3P ne peut se lier à l'enzyme qu'après la formation de l'intermédiaire énediolate à partir du DHAP.

1.2.1.2 Le rôle du métal et son implication dans la catalyse

Le rôle exact du métal a été étudié très tôt mais est encore aujourd'hui sujet à controverse.

Dès 1943, Otto Warburg (Warburg, 1943) proposa que l'aldolase de la levure soit activée par un métal car les agents chélateurs l'inactivaient. Ce métal est un cation divalent, généralement du zinc (Richards and Rutter, 1961; Rutter and Ling, 1958). Il est essentiel à l'enzyme (Horecker et al., 1963) et chaque sous-unité en contient un atome (Kobes et al., 1969).

Très tôt, William Rutter (Rutter, 1964) proposa que le zinc puisse polariser le DHAP par une liaison directe (figure 1-6).

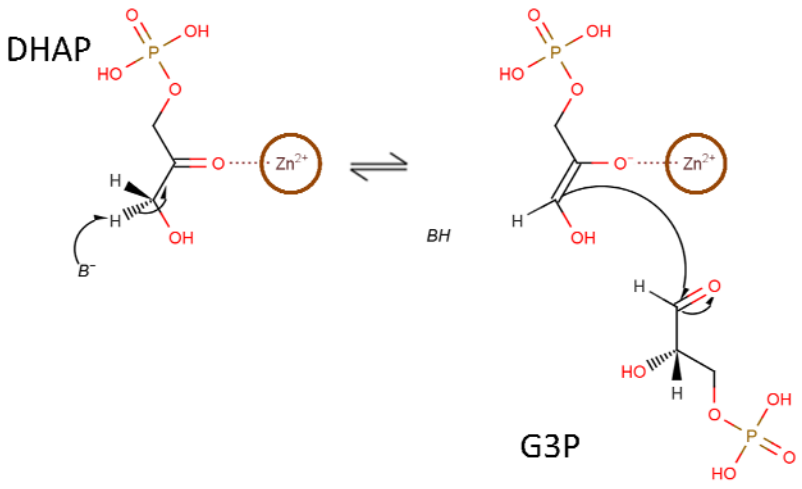

Figure 1-6. Rôle du zinc. Modèle proposé par Rutter *et al.* [3]

Gary Smith en 1980 (Smith, Mildvan, and Harper, 1980) réfuta cette hypothèse après avoir estimé par spectroscopie RMN (Résonance Magnétique Nucléaire) que la distance entre le métal et le ligand était trop importante. Il travaillait sur la FBPA de levure et avait remplacé le zinc par du magnésium pour avoir un signal détectable. Il identifia aussi un résidu, une histidine, pouvant relayer cette interaction (Smith and Mildvan, 1981) (figure 1-7). Plus tard, la mutation en alanine d'un tel résidu, His110, fut réalisé chez *E. coli.* Elle inactive l'enzyme et diminue presque totalement sa capacité à conserver le zinc, le dimère ne contenant plus que 0.15 atome de zinc au lieu de 2 (Berry and Marshall, 1993).

[3] Figures adaptées de la thèse de Matthieu Fonvielle Fonvielle, M. (2006). Synthèse et évaluation de nouveaux inhibiteurs sélectifs de la fructose-1,6-bisphosphate aldolase de classe II. Vers de nouveaux antibiotiques de synthèse. *Thèse*.

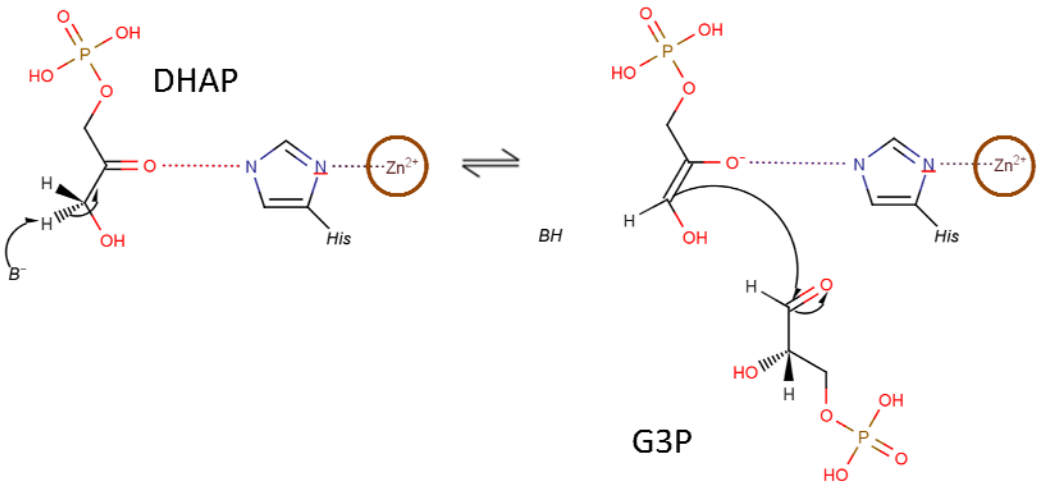

Figure 1-7. Rôle du zinc. Modèle proposé par Smith *et al.*

Trois ans plus tard et en s'appuyant sur des études par FTIR (spectroscopie InfraRouge par Transformée de Fourier), Joel Belasco (Belasco and Knowles, 1983) proposa que le zinc soit aussi impliqué dans la polarisation du G3P (figure 1-8). Ces auteurs concluent alors que l'obtention de structures cristallographiques est devenue une nécessité pour pouvoir poursuivre l'étude du mécanisme.

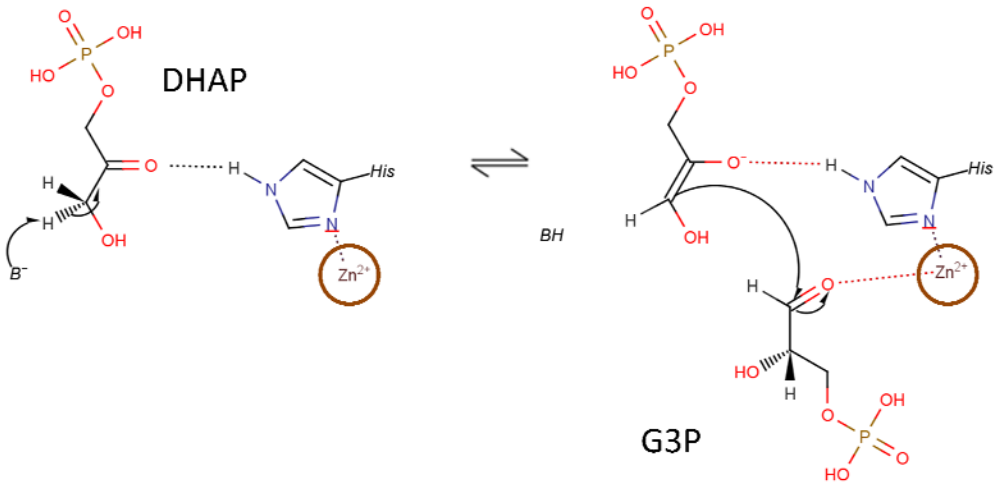

Figure 1-8. Rôle du zinc. Modèle proposé par Belasco *et al.*

1.2.2 De la structure à la fonction : un premier mécanisme catalytique

C'est à partir de l'obtention des premières structures en 1996 (Blom et al., 1996; Cooper et al., 1996) que des détails plus précis furent accessibles. En se basant sur la structure de la FBPA d'*Escherichia coli* en complexe avec le phosphoglycohydroxamate (PGH), un analogue de l'énediolate, le groupe de Allan Berry (University of Leeds, UK) proposa un premier mécanisme détaillé en synthétisant les résultats de plusieurs études (Berry and Marshall, 1993; Cooper et al., 1996; Hall et al., 1999; Plater et al., 1999; Zgiby et al., 2002). D'après leur modèle, la réaction est constituée de trois étapes impliquant un changement au niveau de liens covalents : 1) l'abstraction du proton *1-proS* du carbone C_3 du DHAP pour obtenir l'énediolate, intermédiaire réactionnel stable, 2) La formation d'un lien carbone-carbone entre le DHAP et le G3P puis 3) la protonation du groupement carboxyl C4=O en hydroxyle pour former le FBP. Ces différentes étapes sont détaillées ci-après.

1. Liaison du DHAP et changements conformationels

Dans les structures libres, le zinc est enfoui dans la protéine et est donc inaccessible aux ligands. Dans la structure du complexe avec le PGH, le zinc est exposé au site actif et est coordonné par le ligand. Les auteurs proposent donc que la liaison du ligand déclenche l'exposition du zinc, par un déplacement de 3.7 Å, ceci étant permis par la rotation des histidines le coordonnant (His110, His224 et His264). L'His224 se déplaçant de plus de 5 Å et la boucle qui la contient α6- β8, ainsi que la boucle α7- β9 subissent un réarrangement conformationel non négligeable.

2. L'abstraction du proton proS du DHAP / formation de l'énediolate

Par mutagénèse dirigée, des essais enzymatiques et des mesures d'effet isotopique, Zgiby *et al.* (Zgiby et al.2002) ont identifié le résidu Glu182 comme étant responsable de l'échange de proton sur le carbone C3 du DHAP. Ce résidu n'est pas visible dans les structures de FBPA non complexées mais se lie à Arg331 dans la FBPA *d'Escherichia coli* (ecFBPA) en complexe avec le

phosphoglycohydroxamate (PGH), et est donc relativement proche du site de liaison au DHAP. Ce positionnement au site actif après liaison d'un phosphate en P_1 est corrélé avec la relocalisation des boucles encadrant le site actif et plaide en faveur du rôle proposé. Sa liaison à l'Arg331 peut soit être un artefact cristallographique, soit avoir un réel rôle dans la catalyse. Les auteurs proposent que cette fermeture de la boucle puisse entrainer un changement d'environnement favorisant le déplacement des pKa des résidus impliqués dans les échanges de protons, tout en empêchant le G3P de se lier avant l'abstraction du proton et donc l'activation du DHAP en énediolate.

3. La liaison du G3P

Qamar *et al.* (Qamar, Marsh, and Berry, 1996) identifièrent par mutagénèse dirigée l'implication de Arg331 dans la liaison du phosphate du G3P, c'est à dire au locus dit P_6 en référence au phosphate 6 du FBP. Les résidus Ser61 et Asn35 (Zgiby et al., 2000) semblent également essentiels à la liaison du substrat. Cette dernière étude essaya sans succès d'identifier le ou les résidus responsables de la stéréospécificité de la condensation en FBP plutôt qu'en tagatose-1,6-bisphosphate.

4. La formation du lien C_3-C_4 et protonation de l'oxygène O_4

L'énediolate attaque le G3P (face *si* sur face *si*) après catalyse acide par l'Asp109. Ce résidu est aussi présenté (Plater et al., 1999) comme le résidu clef de la protonation de l'hydroxyle en C_4 du FBP.

Le FBP est alors formé et peut être libéré.

1.2.2.1 Apport des structures plus récentes

Deux groupes publièrent simultanément les premières structures de FBPA de classe II en complexe avec des substrats naturels.

Suite à un premier travail où un complexe avec le PGH fut obtenu chez *Giardia lamblia* (Galkin et al., 2007), Galkin *et al.* déposèrent une structure du mutant D83A,

équivalent du résidu Glu109 chez ecFBPA, en complexe avec le FBP. Le piégeage du substrat non clivé dans ce mutant et une perte d'activité non négligeable prêchent encore pour un rôle crucial de ce résidu. Une relocalisation du zinc dans cette structure a permis aux auteurs de proposer un mécanisme alternatif. Mais la flexibilité de la chaîne latérale de Glu83 requise pour ce mécanisme le rend très discutable. Par contre une structure du complexe avec le tagatose-1,6-bisphoshate (TBP), un des stéréoisomères du FBP, offre plusieurs informations intéressantes. Les deux isomères occupent le même site de liaison et aucun résidu ne semble être capable de discriminer entre les deux molécules. La spécificité n'est donc pas liée à la liaison substrat mais à l'activation de la réaction.

Le groupe d'Andrew Mesecar a cristallisé la FBPA de *Mycobacterium tuberculosis*, (Pegan et al., 2009) et obtenu des structures de complexes en présence de FBP, DHAP et des deux triose-phosphates à la fois. Dans les deux structures avec trioses, ils ont modélisé un mélange de DHAP avec son intermédiaire de haute énergie (HEI), possédant la même géométrie que l'énediolate. Cette interprétation est tout à fait possible mais repose sur l'existence d'une bosse de densité qui aurait demandé d'autres structures afin d'être identifiée, par exemple une structure sans ligand. S'appuyant sur le fait de travailler à pH acide (4.8), les auteurs expliquent le succès du piégeage du FBP. A ce pH, l'enzyme est inactive et donc le FBP n'est pas clivé. La diffraction de ces cristaux a permis d'obtenir une structure à 1.3 Å. À cette résolution, la densité électronique est d'excellente qualité et il parait étrange que les auteurs n'est pas remarqué que le phosphate P_1 du FBP ne semble pas être relié au reste de l'hexose. Les auteurs ne commentent pas non plus sur l'éloignement (3.7Å) entre l'Asp95, l'équivalent de l'Asp109 chez ecFBPA, et l'atome O4 du FBP. Cette distance peu propice à une déprotonation pourrait être due au pH acide utilisé. Mais alors la liaison du FBP pourrait aussi s'en trouver modifiée. Malgré ces nuances, ces structures offrent les premiers détails atomiques de la liaison au site de G3P et confirment l'identification des résidus identifiés par mutagénèse chez ecFBP

Ces deux études qui ont obtenu des vues atomiques de plusieurs étapes de la réaction, ne remettent pas fondamentalement en cause le mécanisme proposé par le groupe de Allan Berry mais ne le renforcent pas.

Deux études portant sur des bactéries thermophiles, *Thermus caldophylus* (tcFBPA) (Lee et al., 2006) et *Thermus aquaticus* (taFBPA) (Izard and Sygusch, 2004) ont fourni des structures de ces classes II tétramèriques. Bien que la conformation de la boucle catalytique soit mieux définie dans ces structures, les informations relatives au mécanisme sont surtout reliées à la spécificité de la réaction. Les acides aminés constituant le site de liaison au G3P diffèrent de celui des enzymes mésophiliques, augmentant le volume disponible et permettraient ainsi plusieurs orientations du G3P et des hexoses pouvant s'y lier. Il en résulte une moins bonne stéréospécificité qui explique la capacité de ces FBPA à aussi catalyser le clivage et la condensation du tagatose-1,6-bisphosphate.

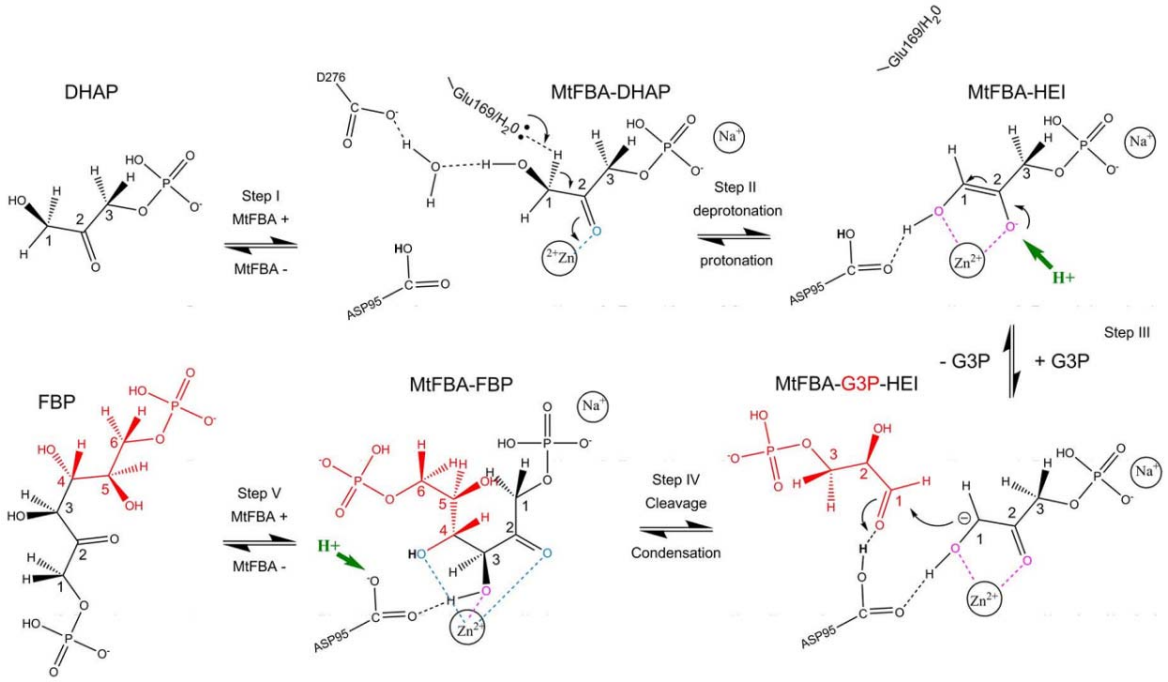

Figure 1-9. Modèle de mécanisme d'action des classes II FBPA

Tiré de Pegan *et al*. 2009 (Pegan et al., 2009)[4]

1.3 Les FBPA de classe II comme cible thérapeutique

La réalisation des fonctions cellulaires nécessite de l'énergie. Sans apport constant, une cellule ne peut croître ou même survivre. Les sucres, et en particulier le glucose, sont les nutriments les plus utilisés par les cellules. Vu la place centrale de la FBPA dans le catabolisme du glucose, il a été postulé que cette enzyme ubiquitaire pourrait être essentielle à la survie cellulaire et donc une cible de choix pour le développement de nouvelles molécules pharmacologiques.

---

[4] Reprinted from *J. Mol. Biol*., 386, Structural Basis for Catalysis of a Tetrameric ClassIIa Fructose-1,6-Bisphosphate Aldolase from *Mycobacterium tuberculosis*, 1038-1053, Copyright 2009, with permission from Elsviewer.

1.3.1 Des protéines essentielles…à la pathogénèse

Plusieurs indices laissent penser que cette enzyme peut être essentielle à la survie cellulaire.

D'une part, il ne semble pas possible de produire des mutants viables dépourvus de FBPA de classes II, suite à la délétion du gène ou à des insertions au sein de sa séquence. *Bacillus subtilis* (Commichau et al., 2009), *Candida albicans* (Rodaki, Young, and Brown, 2006), et même *Escherichia coli,* qui possède pourtant les deux classes[5] (Gerdes et al., 2003), sont des exemples d'organismes ne survivant pas sans le gène encodant pour les FBPA de classe II. Malheureusement, aucune de ces études n'a utilisé de plasmide à expression inductible portant le gène de la FBPA afin de prouver indubitablement son essentialité. D'autre part, l'utilisation d'ARN interférents chez *Giardia lamblia* permet de corriger ce manque de contrôle et conduit au même résultat (Galkin et al., 2007). Par contre, une étude chez *Helicobacter pylori* reposant sur l'utilisation de transposons afin de neutraliser l'expression du gène ne provoque pas la mort de la bactérie (Salama, Shepherd, and Falkow, 2004). Ici encore, un manque de contrôle ne permet pas vraiment de conclure puisque la position de cette transposition n'est pas connue et pourrait se faire par exemple à l'une des extrémités du gène et ainsi avoir peu d'effet.

Ainsi le caractère essentiel semble probable sans être indiscutable, de plus il est dépendant du métabolisme propre à chaque organisme. L'existence de plusieurs voies alternatives à celle d'« Embden-Meyerhof-Parnas » comme la voie Entner-Doudoroff ou celle des pentoses, ainsi que l'utilisation d'autres nutriments peuvent permettre à un organisme de survivre sans FBPA (figure 1-9). Néanmoins, plusieurs études (Banerjee, Darzins, and Maitra, 1987; Banerjee et al., 1985; Frey, Newlin, and Atherly, 1975; Lobo, 1984) montrent que l'absence ou la diminution d'activité des FBPA a un effet important sur la croissance des microorganismes ciblés. L'accumulation de FBP ou des trioses-

[5] Ce qui n'est pas vraiment surprenant lorsque l'on sait que la classe I n'est exprimée qu'en présence de certains substrats alors que l'expression de la classe II est constitutive. (Scamuffa, M. D., and Caprioli, R. M. (1980). Comparison of the mechanisms of two distinct aldolases from Escherichia coli grown on gluconeogenic substrates. *Biochim Biophys Acta* **614**(2)**,** 583-90.)

phosphates (G3P, DHAP) semble avoir soit un effet cytotoxique par elle-même (Bock and Neidhardt, 1966b), soit bloquer plusieurs voies de synthèse telles que celle des phospholipides (Su, Merlie, and Goldfine, 1975), des acides nucléiques (Bock and Neidhardt, 1966a; Mitchell et al., 1992) ou encore ralentir la synthèse protéique (Schwelberger, Kohlwein, and Paltauf, 1989). Sans tuer les cellules, l'inactivation des FBPA semble donc être néfaste à leur croissance.

Enfin comme nous l'avons vu ces enzymes sont essentielles à une infection efficace des bactéries pathogènes du genre *Neisseria* et *Streptococcus* et ont déjà servi à développer des vaccins contre *Candida albicans* (Fernandez-Arenas et al., 2004a) ou *Clostridium perfrigens* (Kulkarni et al., 2007). Ce dernier point n'est peut-être pas lié directement à leur activité catalytique mais seuls des tests d'inhibiteurs *in vivo* ou la détermination des zones d'interaction FBPA/cellule hôte pourront nous éclairer sur cette relation.

Figure 1-10. Quelques voies alternatives à la glycolyse

1.3.2 Des organismes cibles importants

Parmi toutes les cibles potentielles, seuls les organismes dont la structure de FBPA a été résolue au cours de mon doctorat seront présentés.

1.3.2.1 Helicobacter pylori

Ce spirochète d'environ 7µm de long infecte l'estomac de plus de la moitié de la population mondiale (Brown, 2000) et ce depuis plus de 58000 ans (Linz et al., 2007). La découverte de son implication dans le développement des problèmes gastriques et des ulcères de l'estomac a valu le prix Nobel de physiologie et de médecine à J. R. Warren et B. J. Marshall en 2005. Cette bactérie est associée à plus de 70% des cancers gastriques (adénocarcinomes) et augmenterait le risque d'en développer un par un facteur six (Fuccio et al., 2009a; Fuccio et al., 2009b). Il est d'ailleurs classé comme carcinogène de classe I (Vogiatzi et al., 2007) au même titre que la cigarette.

1.3.2.2 Mycobacterium tuberculosis

Ce bacille, appelé bacille de Robert Koch du nom de son découvreur aussi lauréat du prix Nobel de médecine et physiologie en 1905, infecte principalement les poumons et est l'agent de la tuberculose. Cette maladie tue près de deux millions de personnes par an (Dye, 2006) et est particulièrement mortelle chez les patients immunodéprimés (O'Brien and Nunn, 2001). Le développement de souches multi-résistantes aux antibiotiques (Gandhi et al., 2006) est un facteur alarmant qui a poussé l'Organisation Mondiale de la Santé à préconiser un traitement mondial intensif par l'utilisation simultanée de plusieurs antibiotiques afin de mettre fin à cette épidémie. L'application d'une telle méthode semble peu probable autant au niveau du coût que de la faisabilité. Par contre, le développement de nouveaux antibiotiques dit de « dernier recours » apparaît comme une nécessité (Cole and Alzari, 2007). Cette bactérie possède les deux classes de FBPA mais comme chez *E. coli* la classe I n'est pas exprimée de manière constitutive. De plus, la classe II semble essentielle (Sassetti and Rubin, 2003).

1.3.2.3 Magnaporthe grisea

Cet ascomycète infecte plusieurs plantes telles que le millet, l'orge ou le blé. Il cause en effet la pyriculariose (« rice blast desease ») qui déclenche la nécrose des tiges et conduit à la mort des plants de riz. Il est ainsi responsable de la perte d'environ 20% des récoltes de riz mondiales chaque année (Talbot, 2003). D'un point de vue humaniste, ces pertes sont préjudiciables car ce riz pourrait nourrir environ 60 millions de personnes. Mais la lutte contre cet agent pathogène intéresse surtout les compagnies agroalimentaires car les pertes s'élèvent pour eux à plus de 50 milliards de dollars par an.

1.3.3 Peu d'inhibiteurs connus

Pendant plus de trente ans, un seul inhibiteur des FBPA de classe II était disponible (Collins, 1974; Lewis and Lowe, 1977) , le phosphoglycolohydroxamate (PGH). Cet analogue du DHAP inhibe puissamment les classes II (Ki = 10 nM) mais a toutefois plusieurs défauts. Il est très peu spécifique des classes II vis-à-vis des aldolases de classe I (Ki = 1μM) et inhibe aussi plusieurs autres enzymes utilisant du DHAP comme par exemple la triose phosphate isomerase (TIM) (Fonvielle et al., 2004) , la L-rhamnulose-1-phosphate synthase (Kroemer, Merkel, and Schulz, 2003), la L-fuculose-1-phosphate aldolase (Joerger, Mueller-Dieckmann, and Schulz, 2000). De plus son hydrolyse produit un composé très cytotoxique, l'hydroxylamine.

Des dérivés de PGH ont été synthétisés pour pallier ses défauts. Le phosphoglycoloamidoxine (PGA) et le phosphoglycolohydrazide (PGHz) se sont révélés être plus spécifiques envers les classes II mais inhibent toujours la TIM (Gavalda et al., 2005). D'autres dérivés de phosphohydroxamate avec un groupement N-sulfonyle, n'inhibent que les aldolases mais sont à la fois moins puissants (Gavalda et al., 2005) et peu spécifique de la classe II (tableau 1-2).

Sans être de bonnes candidates pour le développement de molécules pharmacologiques, ces molécules ne sont toutefois pas sans intérêt.

Tableau 1-2. Structures et paramètres cinétiques des analogues de DHAP

	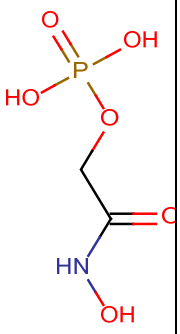 PGH	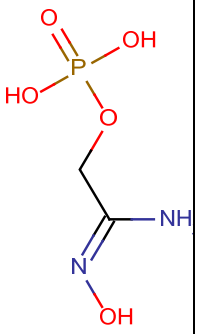 PGA	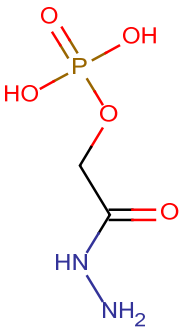 PGHz	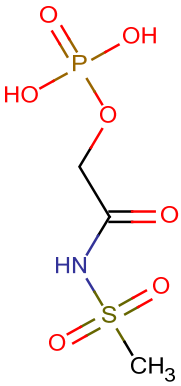 PGS_1	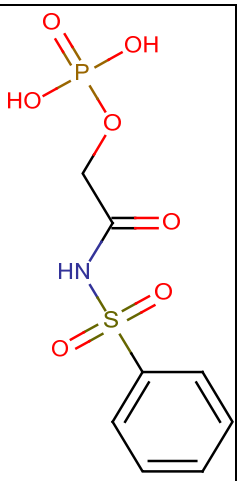 PGS_2
Inhibition classe II FBPA	Ki= 0,01 µM	Ki= 0,34 µM	Ki= 3,3 µM	Ki= 350 µM	Ki= 100 µM
Ki (classe I) / Ki (classe II)	100	1088	3320	28,6	100
Inhibition TIM	Ki= 3 µM	Ki= 4,5 µM	Ki= 111 µM	Ki > 3 000 µM	Ki > 3 000 µM

1.3.4 Les inhibiteurs comme outils d'étude

Les modes de liaison de composés non clivables ont un autre intérêt car ils permettent de figer la structure dans des états normalement non accessibles. On peut donc avoir accès à des conformations de l'enzyme qui normalement ne sont pas stabilisées. Des analogues d'états de transition sont ainsi utilisés régulièrement en cristallographie pour mimer ces états de haute énergie (Lolis and Petsko, 1990). De plus, ce sont ces mimes qui se révèlent souvent être les meilleurs inhibiteurs (Hiratake, 2005).

C'est l'utilisation du PGH qui a permis d'obtenir la première structure d'une FBPA de classe II complexée(Hall et al., 1999). On peut considérer que le PGH est plus un analogue de l'énediolate voir d'un intermédiaire de haute énergie que du DHAP. La structure obtenue peut donc être une vue proche d'un état conformationnel qui ne nous serait pas accessible sans l'utilisation d'un tel composé. Dans la structure de Hall *et al*, on peut d'ailleurs observer une partie de la boucle α7-β5 et le résidu catalytique Glu-142[6]. Bien entendu les conformations piégées peuvent être artificielles et ne pas exister avec les ligands naturels.

L'utilisation d'un analogue du FBP, l'hexitol-1,6-bisphosphate (HBP), chez l'aldolase de muscle de lapin (classes I), a apporté de nombreuses informations sur le mode de liaison de l'hexose et la réalisation d'une liaison spécifique au site actif (St-Jean et al., 2005). Chez les classes II, l'utilisation du tagatose-1,6-bisphosphate (TBP), un stéréoisomère du FBP, a permis de déterminer certaines interactions garantissant la réalisation d'une réaction stéréospécifique chez *Thermus caldophylus* (Galkin et al., 2009).

Développer d'autres analogues peut donc avoir une double utilité, obtenir des composés avec un potentiel antimicrobien non négligeable et fournir des outils supplémentaires afin de compléter l'étude structurale du cycle catalytique.

---

[6] Cette boucle est aussi visible dans une sous-unité de la FBPA de *Thermus caldophylus* (PDB : 2FJK) mais dans une conformation exposée au solvant et éloignée du site actif.

1.4 Objectifs du projet de recherche et justification des méthodes utilisées

1.4.1 Objectif général

L'objectif de mon doctorat était de détailler les événements moléculaires qui composent le cycle catalytique des fructose-1,6-bisphosphate aldolases de classe II. Les zoologistes du XIX^{ème} siècle se basaient sur des photographies afin de recomposer les diverses étapes des mouvements tels que la course ou le vol. De la même manière, nous allons essayer de reconstruire le film de notre mécanisme à partir d'un maximum de clichés des différentes étapes du cycle catalytique. Ces clichés sont nos structures cristallographiques.

Comme nous l'avons vu précédemment, un nombre important de données ont été accumulées par tous les groupes ayant étudié les classes II FBPA et ce par l'utilisation de diverses méthodes. Certaines questions restent néanmoins en suspens et des interprétations proposées nous semblent parfois fragiles puisqu'elles ne tiennent pas toujours compte de résultats déjà connus. Nous avons donc cherché à toujours confronter nos propres hypothèses et résultats aux données apportées pendant plus de 60 ans par ces recherches.

Comme souvent en recherche, nos découvertes et observations mais aussi les limites de nos méthodes d'études nous ont poussés à explorer des voies connexes. Ainsi, devant nos difficultés à piéger certains intermédiaires réactionnels, nous avons fait appel à des chimistes pour qu'ils nous fournissent de nouveaux inhibiteurs afin de mimer ces intermédiaires. L'utilisation de ces composés nous a permis d'obtenir des structures qui se sont révélées cruciales pour une interprétation argumentée et comparée de nos diverses structures. Parallèlement, ces structures ont offert une base solide à nos collaborateurs afin d'optimiser la sélectivité et la puissance inhibitrice de ces composés. Aussi une part non négligeable de ce doctorat touche au développement de nouveaux agents antimicrobiens.

Cette thèse est donc composée de trois volets qui sont étroitement imbriqués. Le premier porte sur la catalyse à proprement parler et repose sur la résolution de structures tridimensionnelles et d'études cinétiques. Le second volet présentera la mise au point d'un protocole de dynamique moléculaire; travail qui a d'abord été validé par des études sur le mode d'action d'inhibiteurs chez les classes I pour être ensuite appliqué à l'étude de la boucle catalytique. Enfin, le troisième volet porte sur la participation du laboratoire au « drug-design » chez les FBPA de classe II.

1.4.2 Objectifs spécifiques

1.4.2.1 Étude catalytique

1.4.2.1.1 Le rôle de Asp109 (ecFBPA)

Toutes les publications récentes présentent le résidu Asp109 comme effectuant l'abstraction du proton du FBP O4 lors du clivage, et la reprotonation du G3P O3 lors de la condensation aldolique. Cette identification repose sur des mesures d'activité après mutation de ce résidu en alanine et curieusement aucun commentaire n'est fait sur son orientation peu favorable à un tel rôle dans les structures cristallines déjà publiées. Bien que la perte d'activité puisse effectivement être due à un rôle direct de ce résidu lors de la catalyse, elle peut aussi être liée à un rôle plus structural. Dans ce cas une mutation iso-structurale aurait était plus appropriée et il est étrange que les auteurs n'aient pas simplement remplacé ce résidu aspartate par une asparagine, qui possède la même forme mais n'est plus capable d'abstraire un proton.

D'ailleurs, une étude réalisée en parallèle de cette thèse *(*Coincon et al., *In preparation*) nous a confortés dans notre a priori négatif vis-à-vis de ce type de mutation. La mutation d'un résidu du site actif, Glu42 en alanine, chez la pyruvate aldolase HpcH (HpaI) conduit ainsi à une perte totale de la géométrie du site actif alors que ce résidu n'est pas directement impliqué dans le mécanisme enzymatique de l'enzyme.

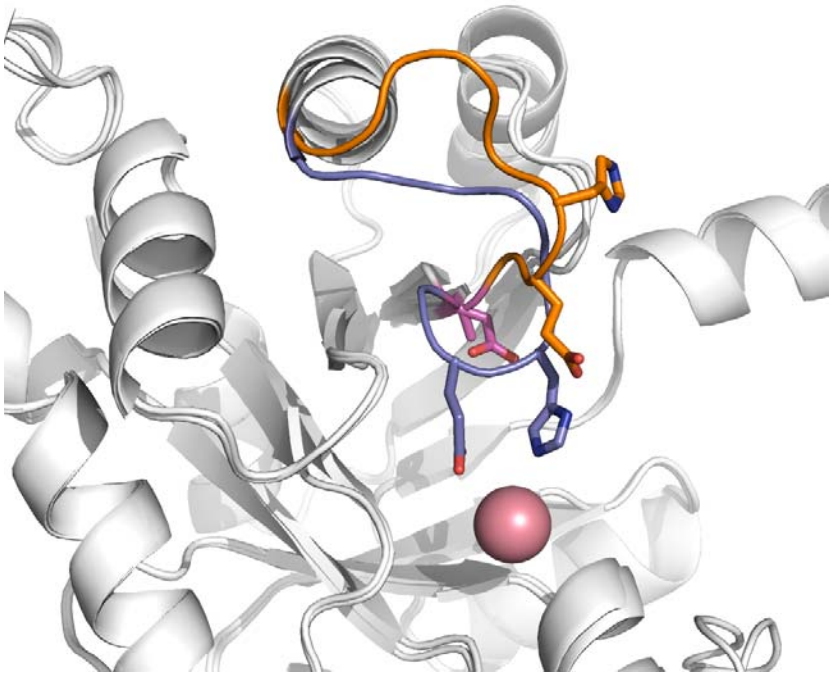

Figure 1-11 Perte de l'intégrité du site actif lors de la mutation E42A chez la HPA1 aldolase de *E. coli*.

La mutation (magenta) provoque la relocalisation d'une boucle chez le mutant (orange). Dans la protéine native, cette boucle (bleue) porte deux résidus qui coordonnent le métal catalytique (le cobalt est représenté en sphère). Le mutant est inactif bien que E42 ne soit pas directment impliqué dans la catalyse.

De plus, Plater *et al* (Plater et al., 1999) font le parallèle avec des études ayant identifié l'Asp33 de l'aldolase de muscle de lapin comme responsable de cette abstraction chez les classes I. Les études de Miguel St-Jean (St-Jean et al., 2005), au sein de notre laboratoire, ont montré que c'était un autre résidu, Glu187, qui était responsable de cet échange.

Nous avons donc décidé de réaliser la mutation en asparagine du résidu aspartate équivalent chez hpFBPA, Asp82, et de caractériser ce mutant par des études cinétiques et structurales.

1.4.2.1.2 Mobilité du zinc et des histidines le coordonnant

Le rôle du métal n'a pas été approfondi lors des récentes études structurales. L'enzyme présente pourtant une certaine originalité par sa capacité à enfouir et à exposer son zinc selon qu'elle accueille ou non un ligand. Alors que très tôt l'implication d' histidines dans la polarisation des substrats a été proposée, les papiers de Smith *et al* (Smith, Mildvan, and Harper, 1980) puis de Berry *et* al (Berry and Marshall, 1993) ont probablement découragé les études suivantes à examiner le rôle de ces résidus. Nous nous sommes donc penchés sur cette question en essayant de mettre en relation la flexibilité et la dynamique du site actif avec la réalisation de la catalyse.

1.4.2.1.3 Étude de la boucle catalytique α7-β5

La dynamique de notre enzyme est responsable de la difficulté à étudier l'échange stéréospécifique du proton sur le carbone C3 du DHAP. Le résidu responsable, Glu182, est porté par une boucle très flexible, la boucle α5-β7. Malheureusement cette boucle n'est pas visible dans les structures avec substrats naturels. Dans la structure en complexe avec le PGH chez ecFBPA, elle est présente mais n'interagit pas avec l'analogue du DHAP. Ceci permet tout de même de vérifier qu'elle est capable de se rendre au site actif. C'est par l'utilisation de nouveaux analogues du DHAP et du FBP mais aussi par des simulations de dynamique moléculaire que nous avons tenté de comprendre comment cette boucle pouvait amener ce résidu glutamate au site actif afin d'y échanger un proton.

1.4.2.2 Mise au point d'un protocole de dynamique moléculaire, modélisation de la boucle α7-β5 et simulation de la protéine

Sans être aisée, ni rapide, la réalisation d'un calcul de dynamique n'est pas le facteur limitant d'une telle étude. La mise au point d'un protocole de dynamique, son test puis l'analyse des simulations peuvent prendre beaucoup de temps.

Dans le cas de notre enzyme, nous souhaitons voir si une boucle mobile est capable de venir lier le DHAP fixé au site actif. Plusieurs problèmes se posent alors. Le zinc, sa coordination et nos substrats ne sont pas décrits ou optimisés dans les champs de forces des divers programmes existants. Il nous fallait donc créer leurs paramètres et les tester. De plus, l'échelle de temps d'un tel mouvement peut être supérieure à celle accessible par dynamique pour notre système (de l'ordre de dizaines de nano secondes).

Pour traiter un problème à la fois, nous avons mis au point notre protocole de simulation sur des aldolases de classe I qui sont dépourvues de métal. Nous y avons simulé des ligands déjà définis dans les champs de force, puis de nouveaux ligands dont nous avons créé les paramètres. La validation de ces dynamiques s'est faite par l'étude de la spécificité de molécules inhibitrices entre diverses FBPA de classe I et a conduit à deux publications.

Fort de ces résultats, nous nous sommes attaqués au problème du zinc. Plusieurs dynamiques furent obtenues. Leur analyse et surtout leur validation sont en cours mais nos résultats préliminaires seront exposés.

1.4.2.3 Développement d'antimicrobiens

Comme nous l'avons vu les FBPA de classe II sont des cibles thérapeutiques prometteuses. Deux caractéristiques sont importantes pour obtenir un inhibiteur efficace. Ce composé doit inhiber efficacement l'enzyme et lui être spécifique.

Notre principal rôle lors de ces études est d'obtenir des structures de complexes entre les FBPA de classe II et de nouvelles molécules candidates afin d'étudier leur mode

d'interaction. C'est en corrélant les donnés d'inhibition provenant d'essais cinétiques avec ces donnés structurales que nous guiderons l'optimisation de ces « drogues ».

L'utilité pharmacologique d'un composé est liée à plusieurs facteurs comme sa capacité à tuer ou ralentir la croissance des organismes pathogènes mais aussi à sa non toxicité vis-à-vis de l'organisme infecté et sa capacité à atteindre l'agent pathogène. Ces points sont en partie testés dans le cadre d'une collaboration avec un groupe de biologistes cellulaire et en testant nos inhibiteurs sur les aldolases de classes I afin de garantir leur spécificité.

Finalement, nous travaillons avec plusieurs FBPA, principalement celles d'*Helicobacter pylori* (classe IIB), de *Mycobacterium tuberculosis* et d'*Escherichia coli* (classe IIA). Nous pourrons ainsi étudier leurs différences et essayer de développer des antibiotiques encore plus spécifiques. Ceci pourra notamment réduire les effets secondaires de ces antibiotiques en épargnant la flore intestinale (*E. coli*), et limiter le développement de souches bactériennes résistantes. Si une bactérie est épargnée par la molécule, les souches présentant une résistance auront moins de chance d'être sélectionnées.

1.4.3 Justification des méthodes utilisées.

L'obtention de la structure tridimensionnelle d'une macromolécule biologique n'est pas une fin en soi puisque car c'est l'étude de cette structure, complétée et validée par d'autres méthodes, qui peut permettre de comprendre son organisation et son mode de fonctionnement.

Une structure ne représente pas une vue définitive de l'enzyme. Aussi l'analogie « clef-serrure » proposée par Fischer pour décrire l'interaction entre une enzyme et son substrat est une bonne approche didactique pour introduire l'enzymologie mais elle participe à donner une représentation figée de ce domaine. Dans son concept d'ajustement induit Koshland (Koshland, 1958; Koshland, Ray, and Erwin, 1958) a une vue plus dynamique en proposant que la protéine puisse s'adapter à la liaison de son substrat. On peut aussi imaginer que l'enzyme adopte librement plusieurs conformations et qu'une

d'entre elles est stabilisée par la liaison du substrat. La dynamique d'une catalyse est donc primordiale.

Nos études se basent principalement sur l'obtention de complexes par radiocristallographie. Mais comme il est peu probable de piéger toutes les étapes de notre catalyse, nous nous sommes aussi tournés vers la dynamique moléculaire.

La partie suivante décrit sommairement le principe de ces deux techniques et surtout justifie leur utilisation.

1.4.3.1 Obtention de structures macromoléculaires par radiocristallographie

Deux techniques permettent d'obtenir des structures tridimensionnelles de macromolécules à haute résolution. La spectroscopie par RMN et la radiocristallographie.

En raison des caractéristiques de notre système d'étude, nous avons uniquement utilisé la cristallographie par rayons X.

1.4.3.1.1 Présentation

La radiocristallographie ou cristallographie par diffraction aux rayons X est un type de microscopie dans lequel les lentilles optiques sont remplacées par une transformation mathématique, la transformée de Fourier (TF). Cette dernière permet de recalculer l'image provenant de la diffraction de rayons X par un cristal à partir de la mesure de l'intensité des rayons ayant diffusés à travers lui. En effet, la diffraction est un cas particulier de diffusion à travers un objet périodique. Les ondes lumineuses sont réémises selon des directions privilégiées où leur intensité est la résultante d'interférences, constructives et destructives. Les rayons X peuvent avoir une longueur d'onde équivalente à la taille des liens chimiques, c'est à dire de l'ordre de l'angström (10^{-10} m), ils permettent ainsi d'aller chercher une résolution du même ordre.

La résolution d'une structure par radiocristallographie se fait en plusieurs étapes. Nous nous contenterons ici d'un bref survol. Des descriptions plus détaillées sont disponibles dans l'excellente thèse Vanessa Delfosse (Delfosse, 2008) ou encore dans le

livre Biomolecular Crystallography de Bernhard Rupp (Rupp, 2009). 1) On commence par produire un échantillon dont l'homogénéité et la pureté doivent être « quasi-parfaites ». 2) Ensuite on doit « faire pousser » un cristal exploitable. C'est-à-dire qui diffracte et dont la résolution est suffisante. C'est l'étape limitante car la découverte des conditions propices à la cristallogenèse n'est pas encore maîtrisée et repose sur l'utilisation de méthodes de criblage et d'optimisation semi-empiriques. 3) Une foi un tel cristal disponible, on le fait diffracter. Cette collecte de données s'effectue à l'aide d'une source de rayons X. L'idéal étant d'avoir accès à une source de type synchrotron. Le cristal tourne autour d'un axe afin de l'exposer complètement aux rayons X. Ces expositions nous fournissent des clichés de diffractions. 4) Le traitement de ces données de diffraction se fait en plusieurs étapes. On indexe notre jeu de données, c'est-à-dire que l'on détermine l'organisation cristalline dans laquelle notre protéine à cristallisée. Avec cette information, on intègre l'intensité des diverses taches de diffraction. Puis on met à l'échelle ces différentes données, c'est-à-dire que l'on homogénéise les différentes images et taches de diffractions les unes avec les autres. 5) Le phasage de notre jeu de données est l'étape suivante. Les ondes diffractées n'ayant pas toutes suivies le même chemin, il en résulte un déphasage. Les clichés de diffractions nous ont permis de mesurer les intensités des nombreuses diffractions, à présent on doit déterminer leur phases pour calculer notre transformée de Fourrier. Ces phases peuvent être obtenues de diverses manières (MIR, MAD, SAD, MIRAS, remplacement moléculaire). Dans notre cas toutes nos structures ont été phasées par remplacement moléculaire, méthode qui repose sur l'utilisation d'un modèle préalable. 6) Enfin on construit notre modèle en faisant correspondre la position de tous les atomes de notre protéine avec la densité électronique calculée à partir de nos données. C'est l'affinement de la structure.

1.4.3.1.2 Justification du choix de la radiocristallographie

La spéctroscopie par RMN est limitée par la taille des macromolécules étudiées qui doit généralement rester inférieure à 50kD. Par contre, elle permet d'étudier les protéines en solution. La résolution complète d'une structure par RMN nécessite le marquage

isotopique de certains atomes de la molécule (généralement par incorporation de ^{15}N et ^{13}C). Bien que coûteux, ce marquage est assez aisé à réaliser. Par contre, celui des substrats et inhibiteurs peut se révéler plus ardu. Néanmoins l'impossibilité d'étudier nos enzymes par RMN en raison de leur taille (la forme dimérique atteint un poids moléculaire supérieur à 70 kD) est dommageable car nos boucles flexibles seraient probablement visibles avec cette technique.

Étudier une protéine dans un état cristallin peut sembler problématique. Pourtant beaucoup d'a priori portant sur cette technique sont infondés. Les cristaux sont généralement constitués de 60% de solvant et la concentration de la protéine y est approximativement de 600 mg/mL. Cette concentration est plus proche de celle du cytoplasme, qui peut atteindre 400 mg/mL (Ellis, 2001), que celle utilisée dans la plupart des techniques biochimiques (de l'ordre de quelque mg/mL). Bien entendu les protéines sont contraintes dans leurs mouvements au sein d'un cristal. Mais le cytoplasme, souvent vu comme une « soupe », est plus proche d'un gel avec une viscosité non négligeable (Luby-Phelps, 2000) qui limite aussi la diffusion des molécules. Des contacts cristallins peuvent néanmoins engendrer la modification de la structure mais une observation méticuleuse doit permettre de nuancer toute interprétation qui pourrait s'en trouver biaisée. Enfin, une molécule vibre aussi au sein d'un cristal et des parties flexibles peuvent même se déplacer. C'est le cas de l'extrémité C-terminale de l'aldolase de muscle de lapin qui bien que toujours cristallisée avec la même maille cristalline, peut soit être libre et exposée au solvant ou bien arrimée au site actif dans le cas du mutant K147M (St-Jean and Sygusch, 2007). Aussi il ne faut pas voir un cristal comme une « roche » protéique. D'ailleurs, la plupart des structures ayant été résolues à la fois par RMN et par cristallographie sont identiques, ce qui valide ces deux méthodes.

1.4.3.2 Simulations de dynamique moléculaire

1.4.3.2.1 Présentation

La résolution d'une structure cristalline fournit un modèle qui contient les coordonnées cartésiennes (x,y,z) de chaque atome de la structure. La seule information dynamique fournie par la cristallographie se rapporte au facteur B, dit de Debye-Waller ou encore facteur de température :

$$B = \frac{8\pi^2}{3} < (\Delta r^2) >$$

$$< (\Delta r^2) > \text{étant le déplacement quadratique moyen de l'atome}$$

Ce facteur correspond à l'état d'agitation d'un atome. Plus il est bas, plus la position de l'atome et son pouvoir de diffraction (relié au nombre d'électrons) permettent d'expliquer la densité. Plus la position de cet atome au sein du cristal est variable (vibration, manque de stabilisation d'une chaîne latérale, mouvement d'une boucle, qualité du cristal) moins il diffractera (à cause d'une moins bonne sommation de la diffraction à partir de tous les atomes équivalents du cristal) et plus l'atome le représentant aura un facteur B élevé. Ce paramètre peut alors apporter des informations intéressantes mais se révèle tout de même assez difficile à exploiter.

La mécanique moléculaire décrit les interactions existant entre tous les atomes d'un système. Les interactions entre deux atomes pouvant être de types liées, si les deux atomes sont reliés par un lien covalent, ou non liées (par exemple les forces de Van der Waals ou les forces électrostatiques). L'ensemble de ces descriptions constitue un champ de force. Si l'on prend l'exemple du champ de force AMBER (Ponder and Case, 2003), on peut voir qu'il décrit les différentes forces existantes par des formules de mécanique physique. Ainsi, la force de la liaison entre deux atomes est décrite sur le modèle d'un ressort dont la longueur idéale est r_0 et dont la constante d'élasticité est k_r, si la longueur du lien, r, s'éloigne de cette valeur une pénalité énergétique est calculée. L'addition de toutes ces composantes énergétiques calculées pour tous les atomes permet d'évaluer l'énergie potentielle de notre système V_p.

$$\mathrm{Vp} = \sum_{\text{liaison}} \frac{1}{2}\,\mathrm{k_r}\,(\mathrm{r}-\mathrm{r_0})^2 + \sum_{\text{angles}} \frac{1}{2}\,\mathrm{k_\theta}\,(\theta-\theta_0)^2$$

$$+ \sum_{\text{diédres}} \frac{1}{2}\,\mathrm{V_n}(1+\cos(\mathrm{n}\varphi-\gamma)) + \sum_{\text{non liées}} \sum \left\{\left[\frac{A}{r^{12}}-\frac{B}{r^6}\right] + \frac{q_i q_j}{4\pi\varepsilon_0\, r_{ij}}\right\}$$

Selon le champ de force, d'autres termes supplémentaires peuvent exister pour tenir compte des angles impropres ou même de l'application d'un champ magnétique sur le système.

Chaque champ de force doit être paramétré, c'est-à-dire que l'on doit déterminer les valeurs des différentes constantes. Ces valeurs peuvent provenir de mesures physiques (thermodynamiques, structurales ou spectroscopiques) ou être déterminées empiriquement.

Si l'on connait la position des atomes de notre système et la description des forces qui le régissent, son étude dynamique devient possible. Les simulations de dynamique moléculaire (MD) produisent une succession de conformations au cours du temps que l'on appelle une trajectoire. Selon la seconde loi de Newton, pour un système fermé, la somme des forces appliquées sur un corps est égale au produit de sa masse par son accélération.

$$\sum \vec{F} = m\vec{a}$$

Nous connaissons la masse et la position de tous les atomes de notre système ainsi que la somme des forces décrite par notre champ de force. On considère que la position initiale (t=0) des atomes de notre système correspond aux coordonnées atomiques de notre modèle. Pour calculer une accélération il faut dériver une vitesse. Il suffit alors de générer des vitesses aléatoires afin de démarrer notre dynamique.

À partir de ce moment, on intègre notre équation sur un intervalle de temps Δt donné (c'est notre pas d'intégration qui est de l'ordre de 1à 2 femtosecondes). Et on réitère ce calcul de pas en pas. À chaque pas, on obtient de nouvelles vitesses mais surtout de nouvelles coordonnées qui forment notre trajectoire.

Le caractère fermé du système est garanti par l'application de conditions périodiques à ses frontières. Les objets et les forces qui « quittent le système par un coté, le réintègrent par le coté opposé ». On doit donc définir la géométrie de notre système, c'est la « boîte » de simulation.

1.4.3.2.2 La nécessité d'un contrôle rigoureux

La validité des techniques de modélisation repose sur la robustesse des approximations qui les composent mais surtout sur le nombre de corrélations positives entre leurs prédictions et des données réelles.

La dynamique moléculaire est une technique courante utilisée sur une base quasi-quotidienne par les biologistes structuraux. L'affinement des structures cristallines ou le calcul des modèles RMN sont basés en partie sur cette technique. Mais dans les deux cas, des données expérimentales guident cette dynamique, la densité électronique ou les distances tirées de l'analyse de l'intensité des signaux NOE (Nuclear Overhauser Effect).

Ce domaine s'est énormément développée depuis la première courte simulation (10 picosecondes) d'une petite protéine (500 atomes) en 1977 (McCammon, Gelin, and Karplus, 1977). Elle a permis de comprendre de nombreux phénomènes dynamiques impliqués dans les interactions protéine-protéine (Sinha and Smith-Gill, 2005), le repliement (Coincon et al., 2005) ou encore la catalyse enzymatique (Kamerlin and Warshel, 2010) et peut s'appliquer aujourd'hui à des systèmes de taille conséquente (Schaeffer, Fersht, and Daggett, 2008). Elle demande toutefois une puissance de calcul considérable qui nous est heureusement accessible par le biais du Réseau Québécois de Calcul Haute Performance.

Plusieurs facteurs témoignent de l'utilisation d'un protocole correct. On peut citer comme exemples, la conservation des structures secondaires et de la compacité de la protéine, la stabilité énergétique du système ou encore la relative constance du temps de relaxation et de la densité du modèle de solvant. Tous ces facteurs doivent être vérifiés lors de chaque simulation.

Tout comme lors de nos expériences *in vivo*, un maximum de contrôles sera utilisé à toutes les étapes de nos simulations. De plus, ces observations *in silico* on le plus souvent possible été valideés expérimentalement.

CHAPITRE II

Étude structurale du mécanisme catalytique des FBPA de classe II

"Les détails sont des petits importants qu'il faut mettre à la raison."

Jean Auguste Dominique Ingres.

2 Étude structurale du mécanisme catalytique des FBPA de classe II

La résolution de la structure tridimensionnelle d'une enzyme offre une vue détaillée de l'architecture du site actif mais aussi, dans le cas des complexes, des interactions entre la protéine et ses substrats. Ces informations permettent d'identifier les résidus impliqués dans le mécanisme catalytique et de leur attribuer un rôle spécifique. C'est complété par des études de mutagénèse ponctuelle et de cinétiques enzymatiques, que la résolution d'une douzaine de structures cristallographiques nous a permis de clarifier le mécanisme catalytique des FBPA de classe II. En particulier, nous avons pu détailler l'étape d'abstraction du proton situé sur l'hydroxyle en O4 du FBP.

Non seulement le grand nombre de structures résolues a permis de renforcer nos interprétations, mais, sans une étude comparée, nos conclusions auraient été faussées. En effet, le caractère dynamique de la catalyse a compliqué énormément son étude. Néanmoins c'est cette dynamique qui apporte toute l'originalité au mécanisme de ces enzymes.

Ces résultats sont présentés sous la forme d'un article scientifique prêt à être soumis à la revue *Journal of Biological Chemistry*. J'y ai conduit la réalisation de toutes les expériences et analyses ainsi que contribué grandement à la rédaction de l'article, le tout avec l'aide de mon Directeur de thèse.

2.1 Metal cofactor dynamics in reaction intermediates of fructose-bisphosphate class II aldolases: SUBSTRATE RECOGNITION AND CLEAVAGE

Mathieu Coinçon and Jurgen Sygusch

Department of Biochemistry/Medicine, University of Montréal, CP 6128, Station Centre Ville, Montréal, Québec, Canada H3C 3J4

En préparation

2.1.1 Abstract

Crystal structures of two bacterial metal dependent fructose-bisphosphate (FBP) aldolases in complex with substrate and analogue as well as triose-P reaction products have been determined to 1.8-2.6 Å resolution. Ligand recognition is metal cofactor independent as discriminatory hexitol-bisphosphate binding was observed in the *E. coli* apoenzyme. The enzyme substrate complex with FBP from *H. pylori* aldolase revealed substrate turnover in the crystalline state with C3-C4 bond cleavage that was not catalyzed directly by the metal cofactor. The zinc ion has an essential passive role in enediolate stabilization of the DHAP product. Conserved Asp82 ensures enediolate integrity through its interaction with the DHAP C3 hydroxyl as Asp82→Asn mutation promotes methylglyoxal release, derived from β-elimination of the DHAP phosphate in the enediol(ate). Substrate binding in the acyclic form initiates active site conformational changes triggered by P1-phosphate binding that liberates zinc chelating His180, allowing it to act as a general base to initiate proton abstraction at the C4-hydroxyl. A second zinc chelating residue His83 hydrogen bonds the substrate C4-hydroxyl and assists substrate cleavage by stabilising the developing negative charge on the C4-hydroxyl during proton abstraction. Electrostatic interaction by Asp82 orients His83 side chain and explains inhibition by tagatose-bisphosphate. Substrate cleavage is concerted with metal cofactor relocation from an interior to a surface exposed site thereby stabilising the nascent enediolate form and inhibiting aldol condensation. Exchange by the metal cofactor between energetically equivalent sites modifies its coordination geometry, essential for product/substrate release. Recognition and discrimination of the triose-Ps, glyceraldehyde-3-P and dihydroxyacetone-P, implicates charged hydrogen bonds made with respective C2 and C3 hydroxyls of the triose-Ps by conserved Asp82 and Asp255 in the *H. pylori* aldolase active site.

2.1.2 Introduction

Fructose-1,6-bisphoshate aldolases (Fba; E.C.4.1.2.13) are ubiquitous enzymes that catalyze the reversible transformation of fructose-1,6-bisphoshate (FBP) into

dihydroxyacetone phosphate (DHAP) and glyceraldehyde-3-phosphate (G3P) and play a major role during glycolysis, gluconeogenesis and Calvin cycle. A common feature of all class II aldolases is that they are metalloenzymes and use a transition metal ion (1) to facilitate retroaldol/aldol reactions. They are evolutionarily and mechanistically unrelated to class I aldolases which employ an active site lysine in Schiff base formation (2). Metalloaldolases are found predominantly in microorganisms including human pathogens such as *Mycobacterium tuberculosis; Pseudomona aeruginosa; Helicobacter pylori; Yersinia pestis; Clostridium difficile; Candida albicans; Giardia lamblia* as well as in plant pathogens such as *Magnaporthe grisea*. The enzyme is essential for survival of *E. coli* and *Streptomyces* (3,4,5,6) as well as protozoa such as *Giardi lamblia* (7) making it a promising target for the development of novel antimicrobial drugs.

The main steps of the aldol reaction catalyzed by class II aldolases are depicted in schema 1. The salient feature of class II enzymes is catalysis of aldol condensation by use of Zn^{2+} or Co^{2+} to polarize the DHAP carbonyl, shown in **1**, thereby facilitating stereospecific proton exchange at the α-carbon in **2** and nucleophilic addition by the enolate form of DHAP-3. Protonation of the DHAP carbonyl group may not be required as stabilization of anionic enediolate intermediate-**2** could be sufficient for condensation with G3P to yield FBP-**4**.

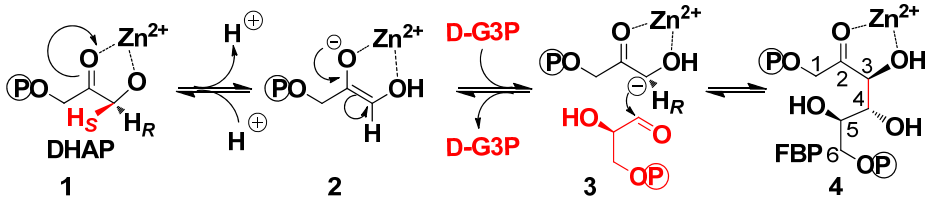

Scheme 2-1. . Intermediates of the catalytic mechanism in class II aldolases

Aldolase from both classes adopt the same 8-fold repeating α/β folding motif commonly referred to as a TIM-barrel; even though the enzymes share no sequence similarity and residues composing the active sites are completely dissimilar (8). The active site is surface exposed in class II aldolases and is situated on the carboxylate end of the β

strands comprising of β-barrel. In class II aldolases, Zn^{2+} ion coordinates the imidazole groups of three histidine residues and undergoes a conformational transition upon ligand binding in the active site (9). The rotational isomerisation of the histidine side chains allows the Zn^{2+} ion to migrate ~ 4 Å from an interior binding site where it interacts with an additional glutamate residue to a surface exposed site bringing it within coordination distance of C2 carbonyl and C3 hydroxyl of C1-phosphorylated ligands (7,9,10). The migration by the Zn^{2+} ion is concomittant with conformational changes in three loop regions that decreases their mobility and serves to stabilize attachment at the C1-phosphate binding locus (7,9,10,11).

The conformational changes induced by active site binding have stabilized enzymatic complexes formed with substrate (10,11), triose-P products (10) and various competitive inhibitors (7,9,12). In the majority of crystal structures of the enzymatic complexes, Zn^{2+} was coordinated with reactants in the active site as indicated in schema 1; however Zn^{2+} invariably coordinated most strongly with the C3 hydroxyl and to a lesser degree with the C2 carbonyl in all but one enzymatic complex that was formed with DHAP (10). In two catalytically incompetent complexes, Zn^{2+} was unexpectedly tightly coordinated with C3 and C4 hydroxyls and not the C2 carbonyl and alluded to a role by Zn^{2+} in substrate cleavage (11).

The Zn^{2+} metal ion readily accommodates different coordination geometries with ligands in enzyme active sites and makes mechanistic interpretation of the catalytic events based upon the structures of enzymatic complexes especially challenging. Zn^{2+} ion is frequently tetrahedrally coordinated in catalytic sites, although it may readily adopt penta- or hexacoordinate geometry (13). The coordination geometry depends on the type of ligand that is bound to Zn^{2+} and the solvent accessibility of the metal binding site (14). In the higher coordination geometry, oxygen dominates as the predominant ligand (15); however energy differences between corresponding four- to six- oxygen coordinated zinc complexes appear to differ by less than 0.4 kcal/mol (16). Such relatively low energy barriers to interconversion among Zn coordinated complexes could give rise to artefactual mechanistic

plasticity in Zn coordination due to crystallization conditions used to trap enzymatic complexes.

Evidence for an essential catalytic role by Zn^{2+} in the aldolase reaction mechanism comes from ^{13}C NMR study of *E. coli* FBP-aldolase showing Zn coordination promoted formation of the enediol or enediolate-intermediate-**2** from FBP (17). The intermediate formation was 50% of maximum at pH 8.0, with maximum at pH 9.0, and represents an extraordinarily large shift in pKa of the DHAP C3 α-carbon. Model compounds indeed corroborated that Zn^{2+} stabilizes the DHAP enolate-**2** by shifting the pKa of the C3 α-carbon by 10 pKa units to pKa ~ 8.4 (18).

Site-directed mutagenesis has identified two conserved residues, Asp-109 and Asn-286 in *E. coli* aldolase (19), and the equivalent Asp-83 in *G. lamblia* (20), whose mutations reduced catalysis by several orders of magnitude. Biophysical characterization implicated interaction by the conserved active site aspartate residue with the G3P carbonyl and suggested a catalytic role in aldol condensation (19). Support from structural studies however were inconclusive, as enzymatic complexes formed with FBP in *M. tuberculosis* class II aldolase did not indicate interaction by the C4 hydroxyl with the conserved aspartate residue, Asp-102 (10). Enzymatic complexes formed in the presence of triose-Ps also did not show interaction by the residue with G3P or DHAP (10). Biochemical characterisation of an alanine mutant of conserved residue Glu-182, situated on a highly mobile loop region in *E. coli* aldolase indicated a role by the residue in stereospecific proton exchange at the DHAP C3 α-carbon between intermediates 1 and 2, as depicted in scheme 1 (21). However, such a role by Glu-182 could not be immediately reconciled with structural data of an enzymatic complex formed with *E. coli* aldolase by the enediolate analogue, phosphoglycolohydroxamate, where a salt bridge between Glu-182 salt and Arg-331 would position Glu-182 ~7 Å from the exchangeable proton. Although the structural studies have revealed molecular detail of trapped enzymatic complexes they do not distinguish which structure, if any, of the enzymatic complexes represent an authentic intermediate in the reaction trajectory.

H. pylori is a human pathogen that colonizes the gastric mucosa, resulting in an acute inflammatory response and damage to epithelial cells and progressing to a number of disease states, including gastritis, peptic ulceration, and gastric cancer (22-27). In *H. pylori*, enzymes coding for either glycolytic pathway or pentose phosphate shunt are incomplete (28,29), the Entner-Doudoroff pathway being the only major route of sugar catabolism (30). Glucose catabolism, resulting in intracellular acid production, would be a potential burden on pH maintenance in *H. pylori,* which has to survive an external pH of 2–3 (31). By contrast, gluconeogenesis, which converts lactate and pyruvate into sugars required for nucleic acid and peptidoglycan biosynthesis, removes H+ from the cytoplasm, and is active in *H.pylori* (32) as enzymes of this pathway are fully present (29). The primary function of *H. pylori* aldolase is thus aldol condensation during gluconeogenesis.

In this study, we focus on FBP and triose-P recognition and the elementary rate step in retroaldol/aldol reaction, namely C-C bond cleavage/ formation catalyzed by class II aldolases. To elucidate the molecular details of the proton abstraction of the C4 hydroxyl of FBP, we conducted a crystallographic study using native *H. pylori* aldolase and flash cooled native aldolase crystals soaked in presence of saturating concentrations of FBP. To circumvent inhomogeneities in crystal quality that limit resolution of diffraction patterns and the resultant structural information, a shot gun strategy was employed to data collection. A large number of *H. pylori* aldolase crystals were screened that had been soaked under very similar conditions with a specific ligand and datasets were collected on only those crystal structures that diffracted to high resolution. Non-redundant crystal structures of trapped enzymatic complexes determined to highest resolution were collated and used to delineate the reaction trajectory catalyzed by the enzyme.

The slow turnover of FBP in the crystallized enzyme enabled trapping of both triose-Ps and FBP in the active site as reaction intermediates. The structures revealed continuous electron density corresponding to a conformationally driven relocation of Zn^{2+} ion between mutually exclusive states whereby the Zn metal cofactor coordinated with FBP or DHAP or was sequestered in the active site interior. Recognition of competitive

inhibitor, hexitol 1,6-bisphosphate, an FBP analogue, did not require Zn migration coordination. Crystal structures obtained by flash cooling of *E. coli* aldolase crystals soaked with obligate product DHAP or Zn depleted *E.coli* aldolase with hexitol 1,6-bisphosphate, corroborated Zn independent ligand recognition. The structural analysis indicates a canonical reaction mechanism by which class II aldolases reversibly cleave a C-C bond to form an enediolate intermediate. The crystal structure of an isosteric active site mutation of the conserved aspartate residue, D82N, soaked in presence of FBP, together with enzymological data corroborated the mechanistic interpretation and indicated the critical role for the residue in enediolate stabilization but not C-C bond formation, as well as fine tuning proton transfers that suppresses methylglyoxal synthetase activity by the enzyme. On basis of structural and site mutagenesis studies, His180, which one of the Zn chelating histidine residues, is proposed as the base responsible for proton abstraction at C4 hydroxyl, thereby initiating C-C bond cleavage.

2.1.3 Materials and Methods

2.1.3.1 Hexitol-bisphosphate preparation

HBP was prepared by NaBH4 reduction of FBP as described previously (33). This reaction produces a mixture of two diastereoisomers: (*2R*)-mannitol 1,6-bisphosphate (MBP) and (*2S*)-glucitol 1,6-bisphosphate (GBP).

2.1.3.2 Purification and crystallization of *H. pylori* aldolase

Plasmid pKK223-3 containing cloned *H.pylori* aldolase or D82N mutant were transformed and overexpressed in *E.coli* strain JM109. The recombinant protein was purified by a combination of anion exchange (DEAE), hydrophobic exchange chromatography (Phenyl-Sepharose) and size exclusion chromatography and was previously reported (9). Aldolase concentration was determined using the BCA Protein Assay Reagent (Pierce) with bovine serum albumin serving as standard. The purified protein was stored at 4° C in 85% saturating ammonium sulfate solution (25mM Tris/HCl

pH 8). *H. pylori* aldolase crystals were grown by vapour diffusion from a 1:1 mixture of protein solution (10 mg/ml initial protein concentration made up in 25 mM TrisHCl pH 8.0) and precipitant buffer (12% PEG 1000, 12% PEG 8000, 0.2 M calcium acetate, and 50 mM Tris/HOAc pH 8) and 4 μL drops were equilibrated at 23° C against 1 mL reservoirs of precipitant solution. Crystals grew in 2 weeks.

Purification and crystallization of *E.coli* aldolase was carried out as reported previously (8).

2.1.3.3 Data collection and processing

Aldolase crystals were soaked for 10 min in buffer containing saturation concentrations of ligand (mother liquor plus 5-10 mM ligand). In the case of *E.coli* aldolase crystals soaked with hexitol-1,6-bisphosphate, 10 mM EDTA was added to the mother liquor to chelate the Zn^{2+} metal ion. Prior to data collection, crystals were cryoprotected by transfer through a cryobuffer solution (ligand buffer plus 10% glycerol) and immediately flash cooled in nitrogen gaseous stream at 100°K. Diffraction data were collected at beamlines X8C, X12B, X25 and X29 of the National Synchrotron Light Source (Brookhaven National Laboratory, Upton, USA). A fluorescence energy scan, collected at beamline X8C by energy scanning about the Zn Kα edge (1.2818 Å), corroborated that the *H. pylori* aldolase crystals contained zinc, although no exogenous zinc was added during purification or crystallization of the protein. All data sets were processed with HKL2000 (34) and the results are summarized in Table 1.

Table 2-1. Data collection and refinement statistics

Part 1	hpFBPA-FBP	hpFBPA-DHAP	hpFBPA-triosePs	hpFBPA-HBP
Data Collection				
Resolution (Å)	39.80-2.04 (2.15-2.04)	39.48-1.85 (1.96-1.85)	33.4-2.26 (2.34-2.26)	29.6-2.2 (2.3-2.2)
Wavelength (Å)	1.0809	1.0809	1.0809	1.0809
Unique reflections /multiplicity	35664/3.5 (3573/2.9)	49870/2.6 (6572/2.4)	26901/3.5 (2015/2.6)	28070/1.4 (2364/1.5)
Completeness (%)	92.3 (63.9)	91.9 (89.4)	94.5 (70.7)	93.9 (63.6)
Average I/σ(I)	8.0 (3.2)	16.5 (3.3)	13.3 (2.4)	22.4 (6.1)
Rsym[†]	0.06 (0.19)	0.06 (0.21)	0.09 (0.32)	0.05 (0.19)
Space group	$P2_1$	$P2_1$	$P2_1$	$P2_1$
Unit cell parameters a (Å). b (Å). c (Å). α (°).β (°).γ (°)	39.4 87.4 100.0 90.0 100.2 90.0	39.5 88.0 90.8 90.0 100.4 90.0	39.3 87.0 91.0 90.0 100.2 90.0	39.2 85.4 90.4 90.0 100.6 90.0
Refinement				
Number of reflection used	35517	47842	24422	28006
Number of atoms				
Protein	4515	4520	4510	4491
Water	735	1043	371	859
Hetero	84	26	36	84
R_{cryst} (%)[‡]	15.5	15	19.3	16.8
R_{free} (%)[§]	20.5	19.7	23.5	21.9
Root mean square deviation				
Bond length (Å)	0.01	0.007	0.007	0.007
Bond angle (°)	0.96	1.08	0.69	0.74
Average B-factor (Å²) (rms bonded)	21.1 (4.8)	14.5 (5.1)	26.7 (2.8)	26.6 (4.7)
Ramachandran analysis[¶] (%)				
Favored regions	99.3	99.3	98.6	98.4
Allowed regions	100	100	100	100
Luzatti error in coordinates (Å)	0.19	0.16	0.19	0.24

Part 2	hpD82N-Methylglyoxal	hpD82N-triosePs	ecFBPA-DHAP	ecFBPA-HBP
Data Collection				
Resolution (Å)	30.2-1.94 (2.01-1.94)	35.83-2.63 (2.80-2.63)	39.87-1.70 (1.77-1.70)	29.01-1.65 (1.72-1.65)
Wavelength (Å)	1.0809	1.0809	0.99	0.99
Unique reflections /multiplicity	22209/3.6 (1756/3.3)	7579/2.5 (1100/2.0)	72711/3.5 (6944/3.0)	81553/5.7 (9156/2.4)
Completeness (%)	96.8 (84.3)	86.1 (78.8)	99.0 (95.0)	98.3 (89.1)
Average I/σ(I)	22.9 (6.1)	5.2 (2.1)	19 (1.7)	28.2 (2.3)
Rsym[†]	0.05 (0.19)	0.08 (0.13)	0.08 (0.60)	0.09(0.395)
Space group	C2	C2	$P2_1$	$P2_1$
Unit cell parameters a (Å). b (Å). c (Å). α (°).β (°).γ (°)	95.7 81.1 39.2 90.0 109.6 90.0	96.7 85.5 39.6 90.0 109.3 90.0	57.1 71.4 88.2 98.5 108.9 90.0	57.2 71.9 89.0 90.0 108.4 90.0
Refinement				
Number of reflection used	19619	8125	68483	78274
Number of atoms				
Protein	2280	2261	5307	36907
Water	256	264	1744	2783
Hetero	18	32	28	136
R_{cryst} (%)[‡]	15.7	20.9	14.7	15.4
R_{free} (%)[§]	20.5	24.6	17.2	18.3
Root mean square deviation				
Bond length (Å)	0.01	0.007	0.007	0.007
Bond angle (°)	0.98	0.72	1.23	1.05
Average B-factor (Å²) (rms bonded)	21.3 (3.9)	23.9 (3.6)	14.4 (5.0)	15.8 (3.6)
Ramachandran analysis[¶] (%)				
Favored regions	99	98.2	98.1	98.1
Allowed regions	1	100	100	100
Luzatti error in coordinates (Å)	0.18	0.3	0.16	0.15

*All values in parentheses are given for the highest resolution shell

†$R_{sym} = \sum_{hkl}\sum_i|I_i(hkl) - \bar{I}(hkl)| / \sum_{hkl}\sum_i\bar{I}(hkl)$, with i running over the number of independent observations of reflection hkl.

‡$R_{cryst} = \Sigma_{hkl}||F_o(hkl)| - |F_c(hkl)||/\Sigma_{hkl}|F_o(hkl)|$.

§$R_{free} = \Sigma_{hkl\in T}||F_o(hkl)| - |F_c(hkl)||/\Sigma_{hkl\in T}|F_o(hkl)|$, where T is a test data set randomly selected from the observed reflections prior to refinement. Test data set was not used throughout refinement and contained 10% of the total unique reflections.

¶Analyzed by Molprobity.

2.1.3.4 Structure solution and refinement

Crystal structures corresponding to FBP, DHAP or HBP soaked into *H. pylori* aldolase crystals were solved with the Phenix molecular replacement program (AutoMR) (35) using as reference model the structures of either native aldolase, phosphoglycolohydroxamic acid (PGH) bound to native aldolase or N-(3-hydroxypropyl)-glycolohydroxamic acid bis-phosphate (PGHPP) structure bound to native aldolase (PDB entry codes 3C4U, 3C52, and 3C56, respectively). The best solution was used as starting point for refinement. Each structure was advanced by iterative rounds of refinement using phenix.refine module (36,37) and model building in Coot (38). All structures reported belong to the monoclinic space group P21 and contain one aldolase homodimer in the asymmetric unit, consistent with the biologically active form of the enzyme. Molprobity server (39) and the Coot validating tools were used to optimize the structures during the refinement. Water molecules were automatically added by Phenix in initial rounds and manually near the end of refinement. Loop regions (residues 139-153) in each subunit were associated with regions of weak electron density. D82N mutant structures were solved using one subunit of DHAP bound dimer as the mutant protein crystallized in C2 space group and contained only one subunit per asymmetric unit. The orientation of Asn82 carboxamide was chosen in the electron density map to allow the carboxamide oxygen to hydrogen bond with its backbone amide, as was observed in all native structures. The alternate orientation would result in an unfavourable close contact with the both its backbone amide and a Na^+ ion bound in the TIM-barrel interior.

DHAP and FBP complex structure with *E. coli* aldolase was obtained and refined by same strategies using the *E. coli* aldolase structure in complex with PGH (PDB: 1B57) as molecular replacement template. Occupancy of active sites ligands was assessed on basis of B-factor agreement with adjacent active site residues using the Coot tool : colour by B-factor (45).

Ligand modeling was based on interpretation of electron density shapes of 2Fo-Fc and Fo-Fc annealed omit maps using phenix.elbow command for topology and parameters

generation. Binding by DHAP, G3P and HBP were readily discernable and were associated with clearly defined electron densities in the active site. Additional controls included B-factor coherence of equivalent atoms in different subunits, real space fit (RSR) or phenix ligandFit (40,41) and were used to discriminate between different ligands and their conformations.

Final model statistics, calculated with Phenix, Molprobity and SFCHECK (42), are shown in Table I. The coordinates and structure factors of *H. pylori* aldolase in complex with FBP, DHAP, triose-Ps and HBP have been deposited with the Protein Data Bank (43) (PDB entry codes[7] 1111, 2222, 3333, and 4444, respectively). D82N structures were deposited under PDB entry codes 5555 and 6666 for unbound and methylglyoxal liganded structures, respectively. Structures of *E. coli* aldolase in complex with DHAP and HBP were deposited under PDB entry code 7777 and 8888 respectively. The final structure models have Rcryst (Rfree) of 0.155 (0.205), 0.150 (0.197), 0.193 (0.235), 0.168 (0.219), 0.200 (0.259), 0.147 (0.172) and 0.154 (0.183), respectively. Ramachandran analysis with Molprobity placed at least 98 % of non glycine and non proline residues of the eight structures in the most favourable region and with the remainder found in allowed regions, attesting to good model geometry in the structures.

2.1.3.5 Comparisons

Superpositions were performed with the program PyMOL (44) or Coot using Cα atom coordinates of identical regions of amino acid sequences. Root mean square deviations (RMSD) are reported based on superposition of equivalent Cα atoms in different subunits. The enediolate plane was defined by least squares calculation with the LSQ Plane tool in Coot and used the Zn metal ion position and atom positions equivalent to C2-O2-C3-O3 in DHAP.

---

[7] Les structures seront déposées lors de la soumission de l'article.

2.1.3.6 Enzyme kinetics

Enzymatic activity was monitored by spectrophotometry using a coupled assay and following NADH oxidation at 340 nm (45). The rate of substrate cleavage was determined as a function of pH using 1 mL reaction solution containing 50 mM Tris-HCI, 1 mM FBP (Sigma), 0.3 mM NADH, 10 µg/mL glycerol-3-phosphate dehydrogenase / triose-phosphate isomerase (Sigma) at 25°C. NADH oxidation was monitored on a Cary 300 UV-Vis Spectrophotometer. Blanks used contained the entire assay system with aldolase being omitted. The kinetic constants, V_{max} and K_m, were determined from initial rate velocity measurements using GraFit 5.0 Data Analysing Software (46). Replicate errors in estimated kinetic parameters were ± 15% of estimated values. One unit of activity (U) corresponds to cleavage of 1 µmol of FBP per min. at 25°C. Enzyme concentration was determined by assuming an A280 of 0.221 for a 1 mg/mL aldolase solution.

2.1.3.7 pH profile assay

The following buffers (50 mM) were used to assay maximal velocities at the indicated pH values: PIPES (pH 6.0-7.5), Tris-HCl (pH 7.75-8.75), CHES (pH 9.0-9.75) and CAPS (10.0-11.0).

The pH data was fitted by non-linear regression in GraFit 5 to extract pKa of titratable groups where y represents catalytic activity.

2.1.3.8 Methylglyoxal detection

Methylglyoxal production was measured whereby 200 µM *H. pylori* aldolase (either wild-type or D82N) or BSA (negative control) were incubated with 10 mM FBP in PEG depleted crystallization buffer for 10, 30 and 60 min respectively after which time the protein was denatured and removed prior to dosage, as described previously (47). Supplementary controls were run using DHAP incubated in absence of enzyme to evaluate endogenous methylglyoxal release. DHAP released upon FBP cleavage was measured using the coupled enzyme assay described.

2.1.4 Results

2.1.4.1 *H. pylori* aldolase structure

H. pylori FBP aldolase aldolase exhibits a α/β8 -TIM barrel fold similar to the polypeptide fold described previously (9). The secondary structure elements assigned using PyMOL consist of twelve α-helices and eight β-strands. The native enzyme has two protomers in the asymmetric unit cell and arrangement of the protomers is best described in terms of a homodimer where each subunit displays identical tertiary structure (RMSD = 0.20Å). Size exclusion chromatography corroborated the dimeric quaternary structure of *H. pylori* aldolase, which elutes at relative molecular weight of 70 kD. The enzyme is globular with helices α11 and α12 of each subunit contacting the center of the TIM-barrel of the neighbouring subunit. The catalytic zinc ion is located in a shallow pocket in the β-barrel center and coordinated by residues His83 (Nε), His180 (Nε), His210 (Nδ), Glu134 and a water molecule. This coordination is strengthened by the interaction of His83 (Nδ) with Asp 82 and His210 (Nε) with Glu132. Additionally His210 and Glu134 interact with a monovalent cation (Na^{2+}) as do Gln47, Met102, Lys251 and Asn253. Weak density was found for residues 182-188 and 230-236 respectively located on loops β6-α8 and β7-α9 (corresponding to residues 175-192 and 210-237 respectively) and indicating conformational flexibility by these regions. No electron density was visible for residues 141-152 of loop β5-α7 (residues 136-156).

2.1.4.2 DHAP-enediolate

The structure of the enzymatic complex formed by soaking *H. pylori* aldolase crystals in the presence of DHAP is shown in figure 1A. Electron density corresponding to DHAP binding was continuous, readily interpreted as DHAP binding in the active site and exhibited full occupancy based on B-factor comparison with neighbouring residues.

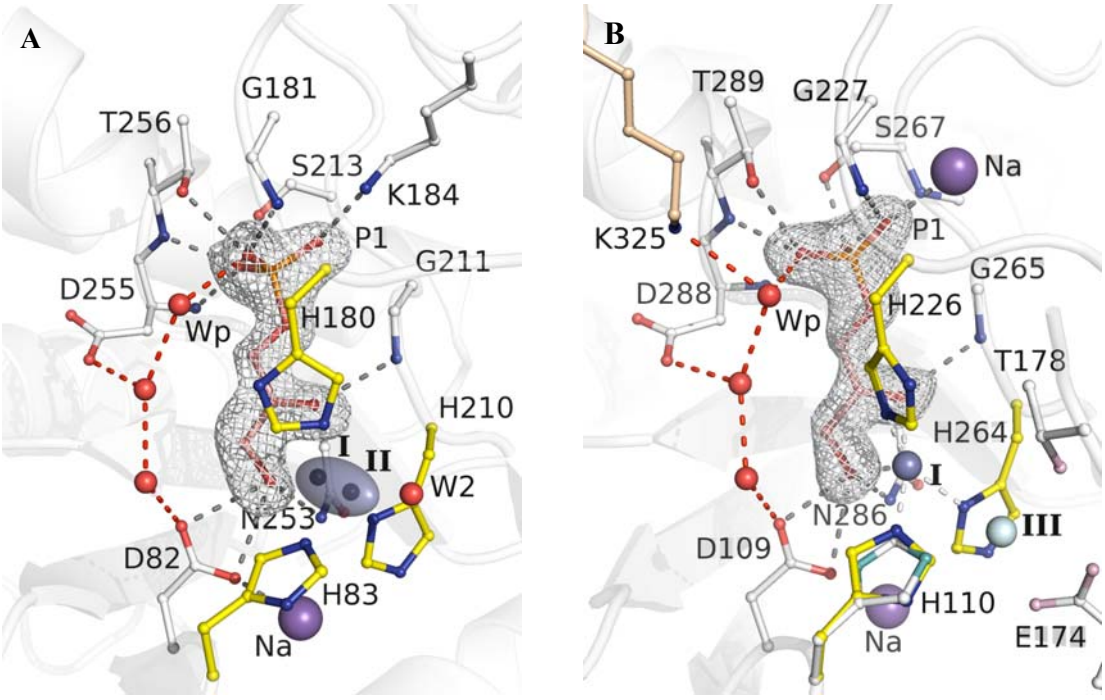

Figure 2-1. Electron density of trapped dihydroxyacetone-P intermediates in the active site of Class II aldolases.

Panels show **A-** dihydroxyacetone-P bound in active site of *H. pylori* aldolase and **B-** dihydroxyacetone-P bound in active site of *E. coli* aldolase. Electron densities encompassing dihydroxyacetone-P were calculated from a kicked Fo-Fc omit map and contoured at 3.5σ. The divalent zinc ion is depicted as an ellipsoid based on the anisotropic b-factor parameters in *H. pylori* aldolase and sites I and II are shown as small black spheres. Zinc ion is shown as blue and cyan spheres (sites I and III) in *E. coli* aldolase. Water molecules are shown as red spheres and sodium cation in purple. View is looking into the β-barrel from the carboxyl side of the β-strands.

DHAP interacts with a number of active site residues. The P1 phosphate binding locus comprises backbone interactions with amides of Gly181, Ser213, Asp255, Thr256 and side chain interactions with Lys184, Ser213 and Thr256 in which each oxygen participates in at least two hydrogen bonds. The DHAP molecule is further positioned by hydrogen bonds between Gly211 and its C2 carbonyl oxygen and a bidentate hydrogen bond between its C3 hydroxyl and Asp82 carboxylate. These interactions, except for the hydrogen bond with Lys184, are conserved in other class II aldolases (48). A spine of three water molecules outlines the distal side of DHAP where each water molecule interacts via a hydrogen bond to an adjacent water molecule. The line of water molecules are anchored by hydrogen bonds to the P1-oxyanion, and Asp-82, while the central water molecule interacts with Asp255. Remarkably, no residue in the structure is vicinal to the C3 atom of DHAP that would promote proton exchange at C3 resulting in enediolate formation.

A continuous anisotropic electron density was interpreted as the Zn^{2+} metal ion binding site, shown in figure 1. The interpretation of the elongated electron density corresponding to Zn^{2+} metal binding site was corroborated by a difference electron density map calculated based on the anomalous Zn signal and whose electron density showed the same elongated form (figure 2) thereby corroborating our interpretation and justified anisotropic refinement of the Zn ion position. Refinement of the Zn metal ion in two mutually exclusive positions, each at partial occupancy and 1.4 Å apart, corresponding to an exterior site (referred to as site I) and an interior site (site II), also satisfactorily explained the observed electron density. Residual continuous density not coincident with the Zn binding site but extending beyond the Zn binding site towards the active site interior was interpreted as a tightly bound water molecule, Wb, shown in figure 1, on the basis of the associated B-factor at full occupancy. The associated water molecule is well positioned to form a covalent bond with the Zn metal ion at site II. The Zn metal histidine chelating residues 83 and 210 could be satisfactorily positioned with respect to the Zn metal ion independently of whether the Zn metal ion position refinement was conducted anisotropically or in terms of two sites. Electron density for the side chain of the chelating

histidine residue 180 was weak independent of the mode of Zn position refinement and could not be reconciled with an optimal Zn bonding geometry. Superposition of the *H. pylori* DHAP structure with structures of *M. tuberculosis* and *G. lamblia* aldolase in complex with active site ligands, DHAP and TBP (RMSD 0.93 Å and 0.68 Å, respectively) coincides the exterior site I with that of the Zn metal ion binding in these structures and it is this site which interacts with the active site ligands. The absence of direct DHAP interaction with the Zn metal ion at site II indicates that the Zn metal ion is not required for DHAP binding.

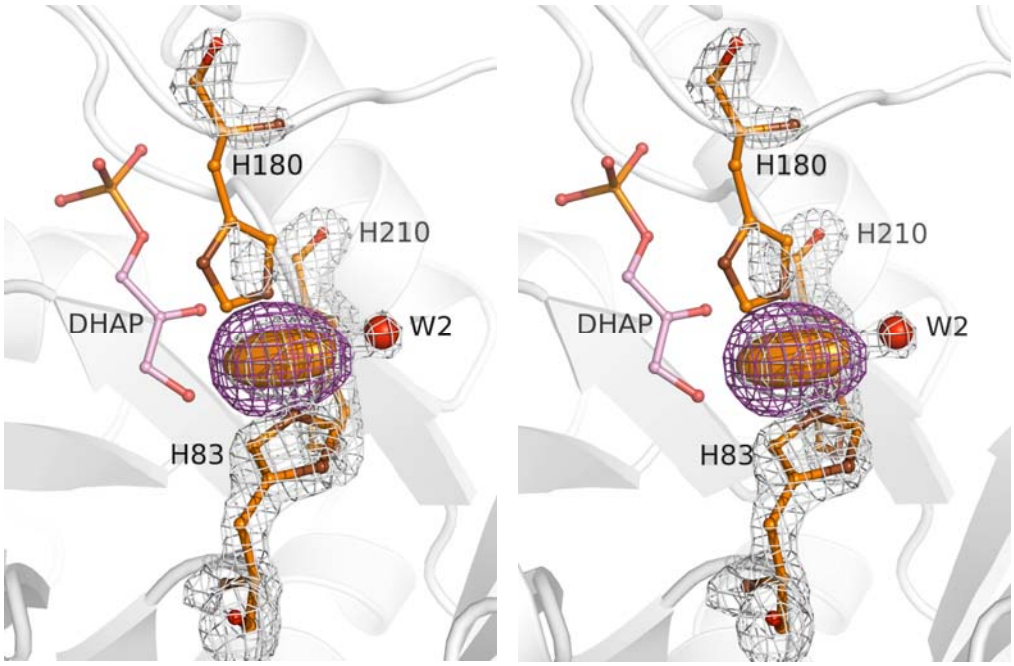

Figure 2-2. Stereo image of kicked omit map (white) and anomalous difference map (violet) in *H. pylori* aldolase structure in complex with DHAP.

Zn metal ion chelating residues His83 and His226 show good fit into the electron density difference map while difference electron density corresponding to the imidazole side chain of His180 fits into comparatively weak density even though of its backbone trace is unambiguous.

Table 2-2. Deviation of metal atoms from enediolate plane in structures of *E. coli* and *H.pylori* aldolases in complex with DHAP, DHAP + G3P and phosphoglycolohydroxamate (PGH).

Deviations are shown in absolute values Å and are averaged over respective subunits of the dimeric enzymes. * Calculation based on PDB entry code 1B57

E. coli	DHAP	0.19
	PGH*	0.20
H. pylori	DHAP	0.14
	DHAP & G3P	0.10
	PGH	0.07

At site I, the Zn^{2+} metal cofactor interacted with DHAP contacting the C2 carbonyl group (2.55 ± 0.08Å) and coordinating the C3 hydroxyl group (2.33 ± 0.02Å), similar to that reported for M. tb aldolase in complex with DHAP (10). Coplanarity of DHAP C1, C2, O2, C3 and O3 atoms, a requisite structural feature in the enediolate intermediate, lends support to identification of the intermediate as the enediolate and would suggest binding by DHAP as the enediolate intermediate when the Zn metal ion occupies site I. This interpretation is supported by the small deviation of the Zn metal ion, < 0.2 Å, out of the putative enediolate plane, tabulated in Table 2 and is comparable in magnitude to the estimated errors in the atomic coordinates shown in Table 1. A similar slight offset, shown in Table 2, is noted for phosphoglycolohydroxamate (PGH) which is a stable analogue of a transiently occurring dihydroxyacetone phosphate-derived enolate in enzymatic catalysis (49) corroborates the identification of DHAP binding mode by *H. pylori* aldolase as consistent with the cis-enediolate transition state.

The structure of the same enzymatic complex formed by soaking *E. coli* aldolase crystals in the presence of DHAP is shown in figure 1B. Electron density corresponding to DHAP binding was continuous, readily interpreted as DHAP binding in the active site and exhibited full occupancy based on B-factor comparison with neighbouring residues. Superposition of the *E. coli* aldolase complex with the same *H. pylori* aldolase complex (RMSD = 0.99 Å) showed the DHAP binding mode to be identical and active site interactions implicating the same conserved residues. The notable exception was the interaction of the P1-phosphate that in *H. pylori* aldolase implicated Lys184 and was replaced by a Na ion in *E. coli* aldolase. Different from *H. pylori* aldolase, the Zn metal cofactor in *E. coli* aldolase was refined using an isotropic B-factor occupying two distinct yet partially populated sites, corresponding to site I in H pylori aldolase and site III which is the buried site corresponding to the Zn metal ion binding site in the native enzyme. No evidence for Zn binding at the equivalent site II in *H. pylori* aldolase was found in electron density difference maps.

2.1.4.3 Substrate trapped in active site

Soaking of FBP into *H. pylori* aldolase crystals generated a series of electron density maps allowing trace of the substrate cleavage trajectory. Electron density interpretation was performed using the following protocol: structures were refined using composite models of reactant and products binding into the active site. In figures 4A and 4B are shown the resultant electron density difference omit maps, corresponding to subunit A and B of *H. pylori* aldolase respectively, and showing trapping of FBP and triose-Ps in the active site. Occupancies of triose-Ps and FBP were refined and validated in terms of B-factor similarity with contacting residues that provided structures consistent with both reactant and product binding. Cleavage of FBP in subunit B (figure 4B) is more advanced than in subunit A (figure 4A). In another *H. pylori* aldolase crystal complete cleavage of FBP has occurred in subunit A, shown in figure 3 while in subunit B, G3P has dissociated from the active site leaving only DHAP bound identically as in the crystal soaking experiments using only DHAP. In other soaking experiments with FBP, only DHAP was trapped in the active site indicating crystallization of a catalytically competent conformer that is consistent with preferential stabilization of the enediolate form of DHAP by the enzyme. Enzymatic turnover in the crystalline state based on the time course of substrate cleavage is estimated at ~ 0.1 min^{-1}. In each structure, the relative disposition of G3P and DHAP in the active site is consistent with the enediolate si face being subjected to a nucleophilic attack by the si face of the G3P aldehyde that yields the expected (3S,4R)-ketose 1,6-phosphate diastereoisomer.

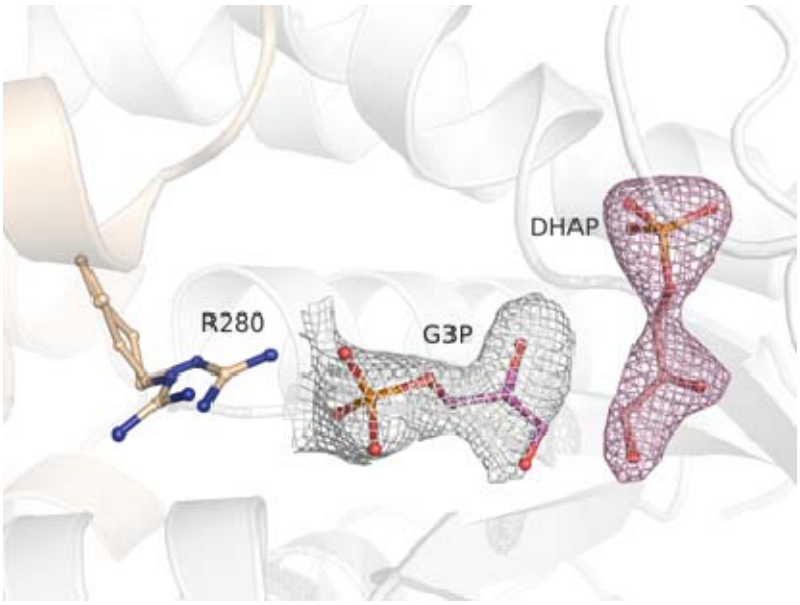

Figure 2-3. An electron density map indicating extensive substrate turnover into triose-Ps from another FBP soaking experiment.

Kicked Fo-Fc omit maps were calculated for either DHAP (pink) or G3P (magenta). Densities were contoured at 3.5σ around fully occupied DHAP (pink mesh) and at 1.9σ around G3P (white mesh) to take into consideration its half occupancies. Alternate conformations for Arg280 attest of partial binding of G3P. Arg280 repositioning is indicative G3P binding allowing it to interact with the G3P oxyanion.

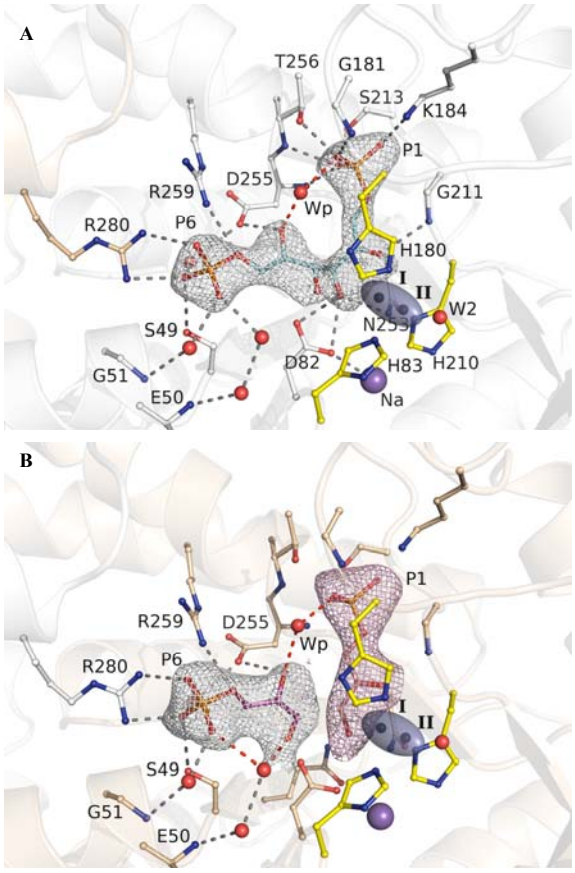

Figure 2-4. Electron density of trapped reaction intermediates in the active site of *H. pylori* aldolase.

Panels show **A-** fructose-1,6-P_2 trapped in active site of *H. pylori* aldolase and drawn in subunit corresponding to partial occupancy of 0.6 and **B-** glyceraldehyde-3-P and dihydroxyacetone-P also trapped in *H. pylori* aldolase and drawn in adjacent subunit and corresponding partial occupancies of 0.6. Electron density maps encompassing ligands were calculated from a kicked Fo-Fc omit map, only the ligand depicted was omitted for calculation. Densities have been drawn at 1.9σ to take into consideration the partial occupancies. Electron density surrounding dihydroxyacetone-P has been drawn in pink to emphasize cleavage of the C3-C4 bond in the substrate.

Superposition of DHAP and FBP structures (RMSD = 0.16 Å) indicates identical conformational responses to active site binding. Substrate attachment corresponds to an acyclic FBP conformation (50) that is stabilized through numerous interactions with active site residues (figure 4A). Interactions with P6-phosphate oxyanion includes hydrogen bonds to Ser49 and solvating water molecules as well as electrostatic interactions notably with Arg280 from the adjacent subunit, while apparently only hydrogen bonding to Arg259 via its bridging oxygen. Arg280 has been reported to bind the P6-phosphate in *E. coli* aldolase (Arg331) (51) and the side chain reorientation with respect to its native structure is consistent with binding at the P6 binding locus. The P6 binding mode uses identical residues to that reported for the FBP analog PGHPP in *H. pylori* aldolase (9). Interaction of active site residues with the P1-phosphate oxyanion are the same as described for DHAP binding including the keto oxygen hydrogen bonding with Gly211 backbone amide and C3 hydroxyl with Asp82. Attachment further conserves the water molecule, Wp, that interacts with the P1-oxyanion as seen in DHAP but different from DHAP, Wp, hydrogen bonds with the O5 hydroxyl of FBP. The only additional hexose interaction involves C5 hydroxyl with Asp255 and a close contact made by C4 hydroxyl with Asp82.

The electron density associated with the Zn metal ion was elongated as described for active site binding by DHAP and the same anisotropic refinement protocol was carried out for the Zn metal ion. Refinement was indistinguishable whether the Zinc metal ion was refined in terms of two mutually exclusive and partially occupied sites, I and II similarly disposed as for DHAP, or in terms of a single site corresponding to an anisotropic electron density. At site I, the Zn^{2+} metal cofactor would interact with FBP contacting the C2 carbonyl group at 2.6 Å and coordinating the C3 hydroxyl group at 2.3 Å that is similar to DHAP but different to that reported for *M. tuberculosis* aldolase in complex with DHAP (10). The absence of direct FBP interaction with the Zn metal ion at site II indicates that the Zn metal ion is not required for FBP binding. The refined occupancies of the Zn metal ion at sites I and II could be matched with the extent of substrate turnover in the two subunits supporting preferential association of site II with FBP binding and site I with substrate cleavage.

The interpretation of the electron density corresponding to substrate cleavage was based on a reduction in the electron density joining FBP C3 and C4 atoms in case of the partially cleaved complex trapped in the active site. An electron density map indicating extensive substrate turnover into triose-Ps from another crystal structure (figure 3) corroborated the interpretation of the electron density as a partially cleaved substrate complex. The binding mode of the phosphate oxyanions of the triose-Ps, DHAP and G3P, were coincident with that of the substrate while the aldehyde was slightly rotated from its nascent position in the substrate consistent with cleavage of the C3-C4 bond. Solvation of the aldehyde phosphate was indistinguishable to that of the FBP P6-oxynaion. G3P was bound as free aldehyde in the active site although G3P exists preponderantly in solution as the hydrated gem-diol form (52). Interpretation as the gem-diol form was not consistent with the electron density shown in figure 2b. The aldehyde carbonyl interacts with a water molecule that in turn hydrogen bonds its oxyanion. The hydrogen bonding interaction made by the C5 hydroxyl in FBP with Asp255 is also maintained in the aldehyde. An equivalent binding mode by DHAP would result in charged repulsion between the DHAP ketone carbonyl and Asp255 and indicates a key role by Asp255, a conserved active site residue, in discrimination of triose-P binding.

2.1.4.4 Hexitol bisphosphate

The electron density in Fig. 3 shows formation of a hexose-P2 adduct in the active site of *H. pylori* aldolase subunit that is consistent with the trapping of both (2R)-MBP and (2S)-GBP stereoisomers of HBP. Discrimination between the two stereoisomers was not possible on the basis of the electron density as both stereoisomers could be fitted in to the electron density map and were retained at equal relative occupancies throughout the refinement. Full occupancy was used for HBP in one subunit and occupancy was set to 0.5 in the other subunit. The only significant difference between the two stereoisomers is a hydrogen bond made by MBP C2 hydroxyl with Gly211 which is not made by the GBP C2 hydroxyl. This binding difference is substantiated by slightly tighter competitive inhibition in *H.pylori* aldolase by (*2R*)-MBP compared to (*2S*)-GBP (Ki = 73 μM vs 170 μM) (53).

Interactions made by both stereoisomers with active site residues, shown in Figure 5, include hydrogen bonds between C3 hydroxyl and Asp82, C4 hydroxyl with Asp255 and C5 hydroxyl with His83.

Superposition of FBP and HBP structures, (RMSD = 0.19 Å) shown in Figure 6 indicates identical binding modes by HBP and FBP phosphate moieties including their solvation by water molecules. Only the interactions made by C4 and C5 hydroxyls differ between FBP and the HBP stereoisomers and differentiates their binding modes. Whereas the C4 hydroxyl in both stereoisomers interacts with the same residue as does the C5 hydroxyl in FBP, the C5 hydroxyl interaction made with His83 in both stereoisomers is not present in the FBP adduct. Different from both FBP and DHAP structures, the zinc metal ion is not displaced from its buried position in the active site of the native enzyme (site III) where it interacts with two of its chelating residues, His83 and His210, Glu134 and a water molecule. Although refinement of the electron density of the metal ion position in the HBP structure was consistent with an anisotropic elongation of the zinc ion towards the direction of site II, consistent with limited overlap of the anisotropic electron densities corresponding to the Zn metal refinement between the two structures (region X in Fig. 5 and 6), HBP binding stabilizes the position of the imidazole side chain of zinc chelating residue His83 identically as in the native unbound enzyme and inhibits reorientation of the His83 side chain requisite for relocation of the metal ion. His180 in the HBP structure superimposes with the location of His180 in FBP and DHAP bound structures and therefore is not able to coordinate the zinc at the buried location where a water molecule replaces it in the metal coordination sphere. Active site recognition clearly does not require Zn ion involvement.

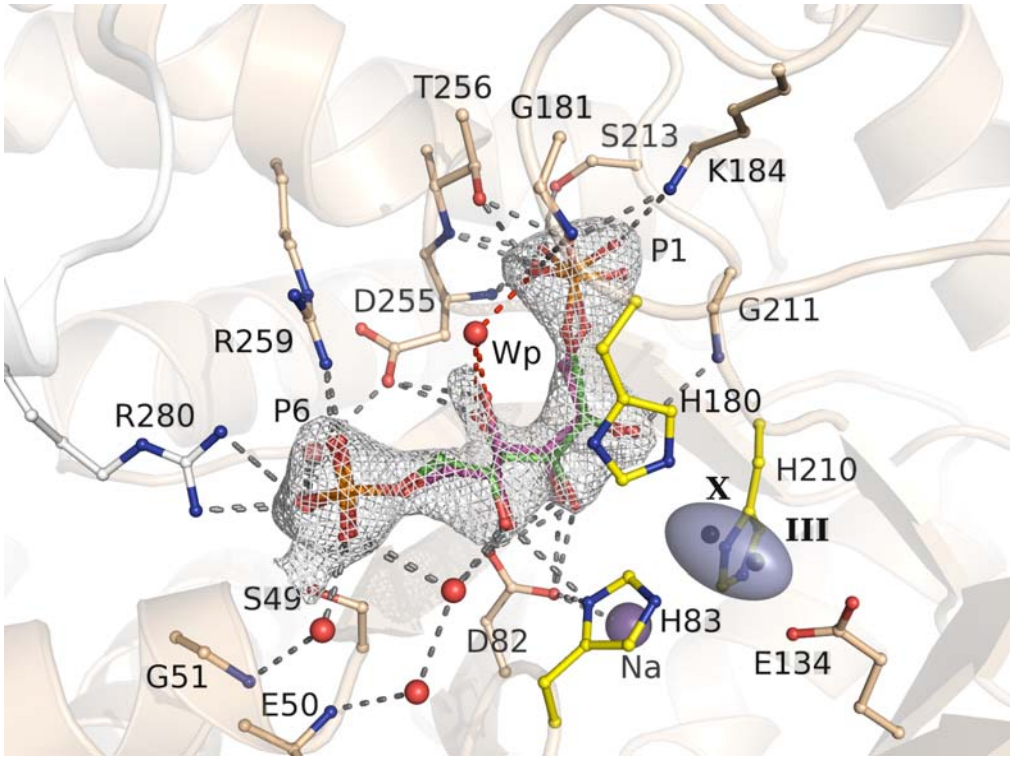

Figure 2-5. Electron density of trapped hexitol-bis-phosphate in the active site of *H. pylori* aldolase.

Mannitol-1,6-bisphosphate (magenta) and glucitol-1,6-bisphosphate (green) were modeled in the electron density map and refined at equal occupancies. Electron density maps encompassing ligands were calculated from a kicked Fo-Fc omit map. Density has been drawn at 3σ.

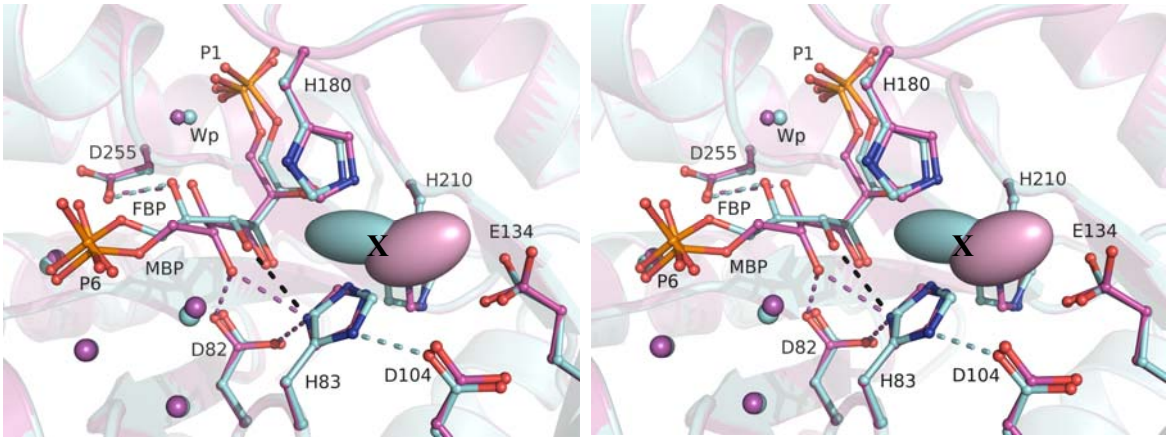

Figure 2-6. Stereo image of superimposition of MBP-hpFBPA (magenta) onto FBP-hpFBPA (cyan) complex structures.

The anisotropic B-factor refinement of the Zn metal ion positions in the two liganded structures resulted in common overlapping spatial region designated by X wherein the imidazole side chain of the chelating histidine residue 83 can rotate about its C_β-C_γ bond such that the imidazole $N_{\delta 1}$ engages in hydrogen bonding with Asp104 or Asp82. RMSD calculated on 534 equivalent C_α atoms between the two structures is 0.19 Å.

To test whether, the zinc metal ion is requisite for ligand binding; HBP was soaked into a crystal of the apoenzyme from *E.coli* and is shown in Figure 7. Structural determination corroborated the absence of zinc metal ion in the active site and showed preferential binding by (2R)-GBP with the concomitant displacement of the zinc chelating residue His226 equivalent to His180 in *H. pylori* aldolase. *E. coli* aldolase is a class IIa aldolase as is yeast aldolase (54) which has a 6.5-fold preference for (2R)-GBP instead of (2R)-MBP (Ki = 60 μM vs 400 μM) (59). Superposition of FBP and HBP structures from *H. pylori* aldolase with *E. coli* aldolase structure in complex with HBP showed superposition of phosphate moieties (RMSD calculated based on phosphate atom position < 0.3 Å) and a mode of binding by GBP in *E. coli* aldolase identical to FBP in *H. pylori* aldolase. Competent discriminatory active site binding therefore does not require interaction with or presence of the zinc metal ion.

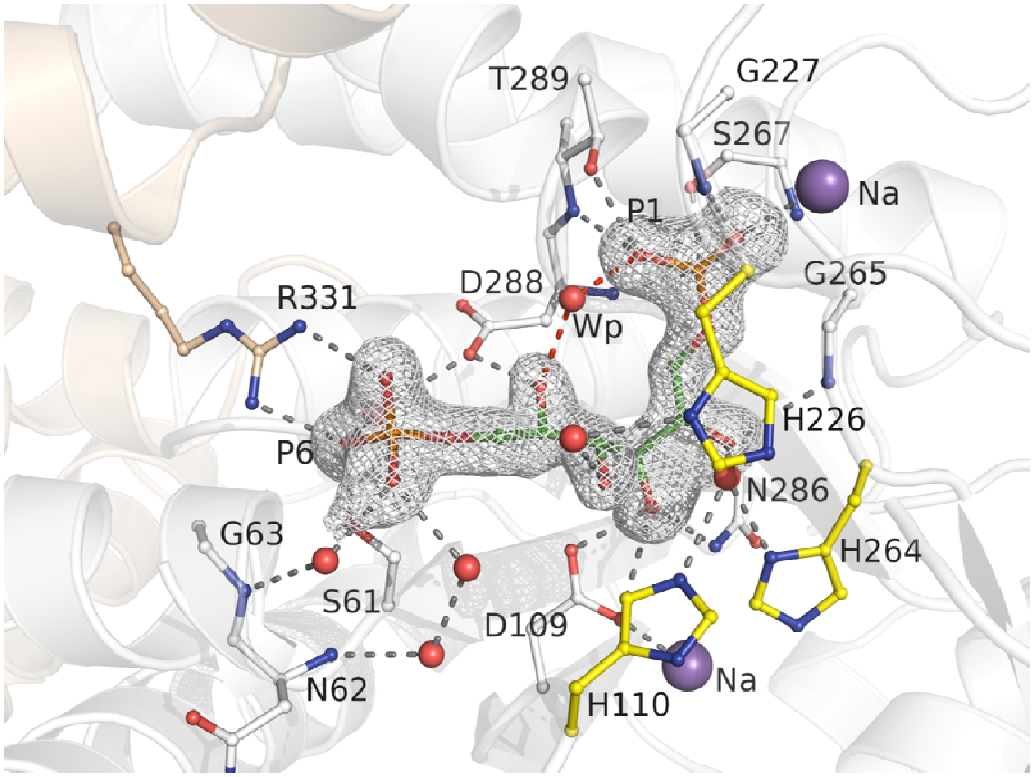

Figure 2-7. Electron density of glucitol-1,6-bisphoshate trapped after soaking of hexitol-1,6-bisphosphate into crystal of *E.coli* apo-aldolase. Electron density map encompassing the ligand was calculated from a kicked Fo-Fc omit map. Density has been drawn at 3.5σ. Notable is the absence of Zn cofactor in the active site.

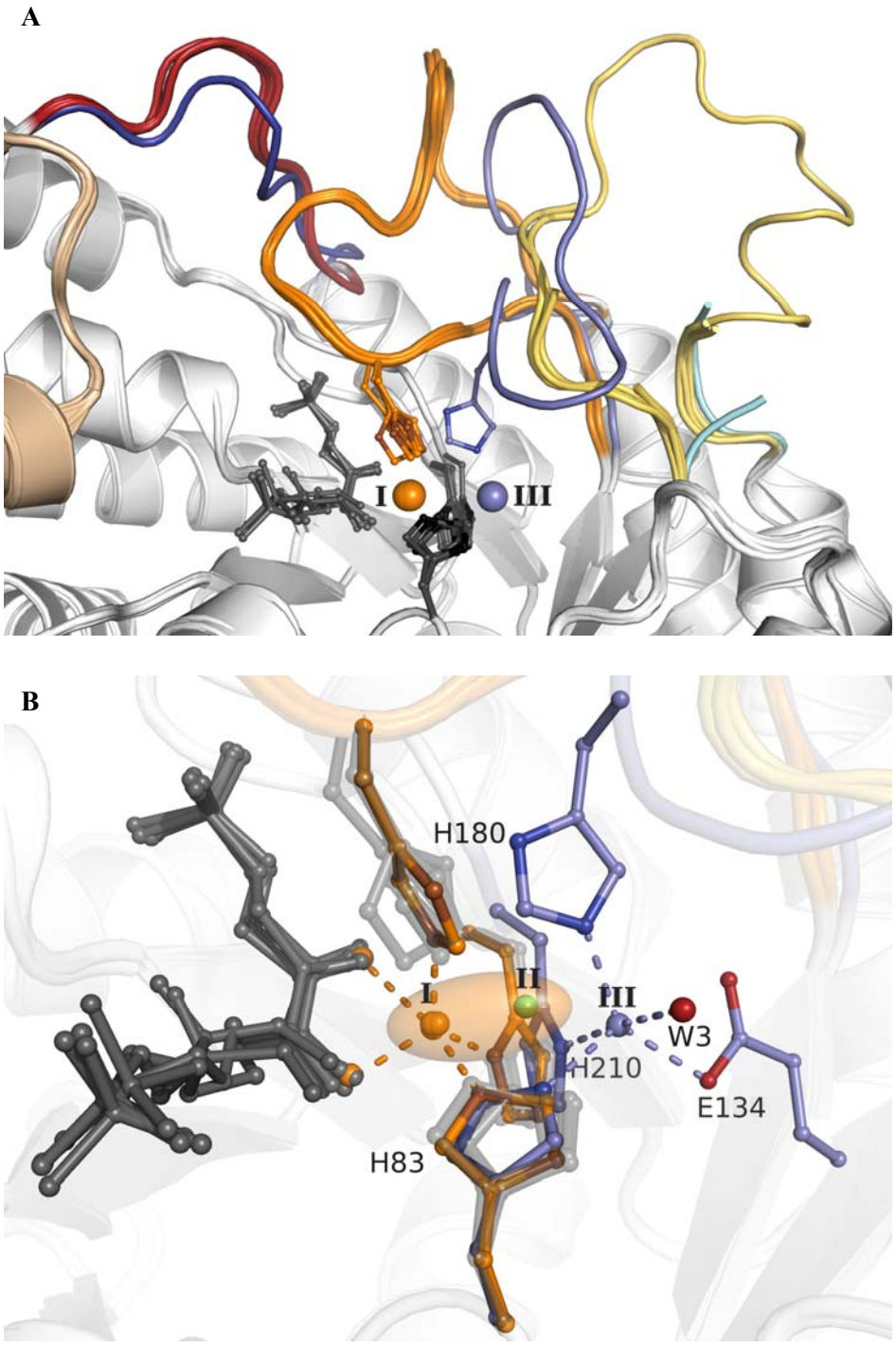
A
I
III
B
H180
I
II
III
W3
H210
E134
H83

(page précédente)

Figure 2-8. Conformational changes induced in *H. pylori* aldolase upon ligand binding.

Superimposition of DHAP, FBP, HBP, PGHPP, PGH and TD3 structures in complex with *H. pylori* aldolase (PDB entry codes: 1111, 2222, 4444, 3C56, 3C52 and 3N9R respectively). For the sake of clarity, ligands and Zn chelating histidine residues are shown in grey stick bonds except for His180 which undergoes significant conformational displacement. A. Residues from Loops β5-α7 (residues 136-156), β6-α8 (residues 175-192) and β7-α9 (residues 210-237) that undergo conformational changes in the bound structures are colored in red, orange and yellow respectively and shades of blue in the unbound hpFBPA structure. Loop β5-α7 is only fully traceable in the electron density map of the TD3-hpFBPA complex. B. Zn metal ion coordination is shown for surface exposed site I (orange) corresponding to binding by all ligands except for HBP which coordinates with the zinc metal ion at the buried site III (blue) of the native structure, the position of Zn metal binding site II is shown in green and a coordinating water molecule in red. Transparent ellipsoid represents the probability displacement calculated from the anisotropic B-factor of the zinc metal ion and was nearly identical for the FBP and DHAP complexed structures. Representative Zn chelating residues are also colored appropriately.

2.1.4.5 Open and closed conformation

Upon active site ligand binding, residues 182-188 and residues 230-236, respectively from loops β6-α8 and β7-α9, undergo significant conformational rearrangement (RMSD changes of 9.9±0.4 Å and 2.7±0.2Å, respectively), shown in Fig. 8a. The loop closure would afford active site access by loop β5-α7 (residues 136-156), although not visible in the electron density map contains a glutamate residue thought responsible for the proton exchange with the enediolate in *E. coli* aldolase (21). The loop closure correlates with P1-oxyanion binding in the active site. In the complexes formed between *H. pylori* aldolase and active site ligands, Lys184 in loop β6-α8 assists Ser213 and Thr256 and backbone amides of Gly181, Ser213 and Thr256 to grasp the P1 phosphate and stabilize the loop in a closed conformation. In the structures of *T. aquaticus* aldolase (55), *M. tuberculosis* aldolase (10) and *E. coli* aldolase (12), a monocation plays the equivalent the role of Lys184 in triggering the closure of the loop and/or stabilizing it once closed upon P1-oxyanion binding. Except for HBP, these movements are correlated with the relocation of the catalytic Zn^{2+} ion from its buried site III to the surface exposed site I, shown in Figure 8b.

2.1.4.6 Zinc relocation

For structure of *H. pylori* aldolase in complex with natural ligands, DHAP and FBP, the Zn metal ion position were refined using an anisotropic B-factor that corresponded to an ellipsoidal electron density indicating preferential positional displacement by the metal ion in the direction of the bound ligands, as seen in Figure 1a and 4a. Equivalent conventional refinement of the Zn metal cofactor position as two mutually exclusive yet partially occupied binding sites placed the metal cofactor, 2.4±0.2 Å and 3.8±0.1 Å away from the buried site, denoted by position I and II respectively in Fig. 6b. Metal cofactor coordination at these two sites engages the same three chelating histidines residues but necessitates rotations of His83 and His210 imidazole moiety by 176±3˚ and 37±8˚ respectively and a translational displacement of 4.82±0.4 Å of His180 (RMSD based on all residue atoms). At the surface exposed site I, the coordination is

completed by atoms from the ligands thereby stabilizing this conformation. Invariably, the metal cofactor interacts strongest with the ligand C3 hydroxyl by forming a bond while only making a close contact with the C2 carbonyl oxygen. At the intermediate location, site II, the metal cofactor is coordinated to the three histidine residues and to a well defined water molecule that in turn is hydrogen bonded to Glu134. Zn coordination at a position intermediate between these two Zn binding sites, coincident of greatest electron density by the Zn atom, is energetically unfavourable as it results in an unsatisfactory chelating geometry made by the metal cofactor with His180.

2.1.4.7 His180 side chain

His180 is situated at the juncture of the mobile β6-α8 loop and undergoes the largest displacement of all the metal chelating residues upon ligand binding. Simulated-annealing or kicked omit map encompassing all three chelating histidine residues and metal cofactor showed no clear density for the His180 side chain in all liganded structures even though the electron density map allowed unambiguous tracing its peptide backbone; the liganded structures included DHAP and HBP bound in both *H. pylori* and *E. coli* aldolase as well as FBP bound in *H. pylori* aldolase. A representative example can be seen in Figure 2. Clear electron density delineating the His180 side chain was only observed in the crystal structures for the tight binding competitive inhibitors, PGHPP and PGH (9) in *H. pylori* aldolase where the metal cofactor interacted only with ligands at site I. The structural data indicates that the Zn metal cofactor undergoes rapid exchange between the two coordination sites as the difference in the coordination geometries of the two sites is not significantly different and requires His180 to weaken its interaction with the metal cofactor during the exchange process.

2.1.4.8 Site-directed mutagenesis of active site residues

Michaelis-Menten kinetics were used to analyze initial rate velocities measured for site directed mutation of Asp82 proximal to the trapped intermediates and the corresponding kinetic parameters are shown in Table 2. The isosteric mutation Asp82 →

Asn sought to assess enediolate stability as Asp82 interacts with the DHAP C3 hydroxyl in the enediolate. The corresponding non-isosteric mutation of D82A in *G. lamblia* aldolase was however postulated to compromise substrate cleavage (11) by virtue of the binding geometry made with FBP in this mutant. The D82N mutation drastically reduced turnover but did not impact substrate binding consistent with a mechanistic role in catalysis. The considerable activity reduction by the D82N mutation corroborates activity reduction observed in the corresponding *E. coli* aldolase mutant D109A (56) and in *G. lamblia* aldolase mutant D83A (57).

Table 2-3. Kinetic parameters of native and D82N mutant in *H. pylori* aldolase.

Enzyme	**k_{cat} (s^{-1})**	**K_m (µM)**	**pKa_1**	**pKa_2**
Native	1.21	19.8	7.21	8.93
D82N	0.0007	7.38	9.61	-

The decrease in k_{cat} in the mutant could not be compensated for by changes in pH. The pH-activity profiles for the native and mutant enzyme are shown in Figure 9 and indicate with respect to native enzyme a consistent loss of catalytic activity by several orders of magnitude over the entire pH interval (pH 5 –10) and with maximal activity displaced to basic pH. The pH profile corresponding to the native displayed a bell shaped curve corresponding to two titratable groups that influence catalytic efficiency while mutation D82N displayed an S-shaped curve associated with a single titratable group. The pKas obtained for the native *H. pylori* enzyme where similar to values described for *G. lamblia* aldolase (62).

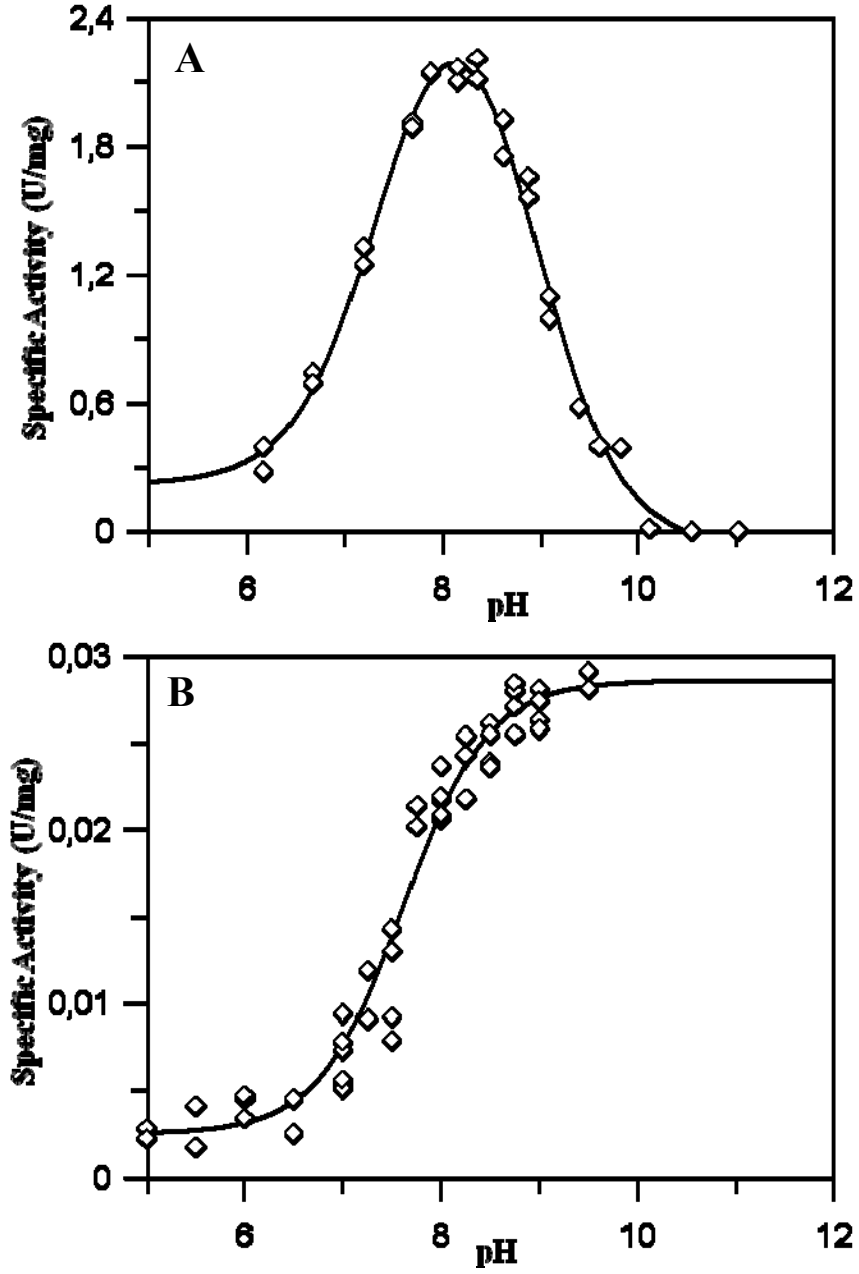

Figure 2-9. pH activity profiles for wild-type *H. pylori* aldolase and site-directed point mutations.

Panel A shows the pH profile for native enzyme, panel B to the mutation Asp82 → Asn.

2.1.4.9 D82N mutant structure

The significant reduction in catalytic activity by the isosteric D82N mutant prompted us to determine to the crystal structure of this mutant: a) in order to assess whether loss in active site integrity could explain the activity reduction and/or b) to trap substrate in the active site and thus test whether this mutation compromises substrate cleavage as was suggested (11). The crystal structures of unbound and FBP soaked D82N *H. pylori* aldolase identified the metal cofactor as bound exclusively at the surface site I and Zn metal cofactor position was refined using anisotropic B-factor refinement (figure 11). The β6-α8 loop residues 181-188 which are implicated in P1-phosphate binding could not be traced in the unbound crystal structure while in the structure corresponding to soaking of D82N crystals with FBP the same residues could be traced through a region of albeit weak density.

Surprisingly, soaking of FBP in the D82N crystals did not lead to observation of a hexose-bisphosphate molecule bound in the active site. Turnover of the D82N mutant calculated for a 10 minutes soak was < 0.5 FBP molecules cleaved which should have resulted in significant quantity of FBP trapped in the active site, especially in view of the slower turnover in the crystalline state of the native enzyme. Although phosphate binding could be identified at the P1-binding locus, continuous electron density extending to the metal cofactor as in DHAP was not observed, rather a compact density feature was observed associated with the metal cofactor in the same position as a molecule bound in the unliganded D82N structure, shown in Figure 8. The compact electron density feature was interpreted as methylglyoxal, derived through β-elimination of the DHAP phosphate (58). The methylglyoxal molecule and phosphate oxyanion were refined and on basis of electron density difference maps, their occupancies were set to 0.7 and 0.5, to take in account water molecules that occupy similar binding loci in the unliganded D82N structure, shown in Figure 10. The reduced occupancy by the phosphate oxyanion in the P1-phosphate binding site correlated with the observed weak density for the residues 181-188. Lys184 by interacting with the P1-phosphate orders this loop and the partial occupancy would weaken

the electron density associated with the loop. A notable feature in the unbound mutant structure and different from the native structure is the location of the Zn metal cofactor at surface site I in absence of P1-phosphate binding while in the native structure the Zn metal cofactor is bound at the buried site III. The mutation Asp82 → Asn weakens the hydrogen bonding capability between residue 82 and His83 existing in the native enzyme that allows Asp104 to compete for hydrogen bonding with His83 indicating that Zn relocation dynamics can be modulated by small differences in energy.

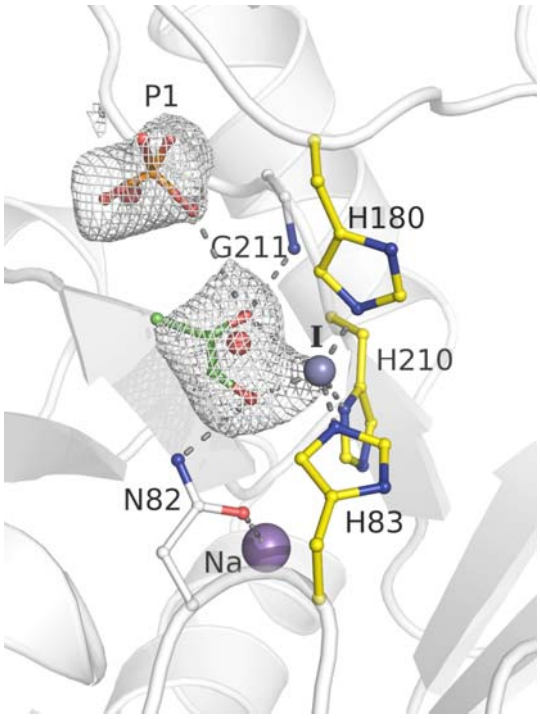

Figure 2-10. Electron density of trapped methylglyoxal in the active site of *H. pylori* aldolase D82N mutant.

Electron density encompassing methylglyoxal (white) and phosphate at site P1 was calculated from a kicked Fo-Fc omit map and contoured at 1.9σ to take into consideration the half occupancies of these ligands. Water molecules in alternate with methylglyoxal and phosphate are shown as red spheres and were not omitted during the calculation of the map.

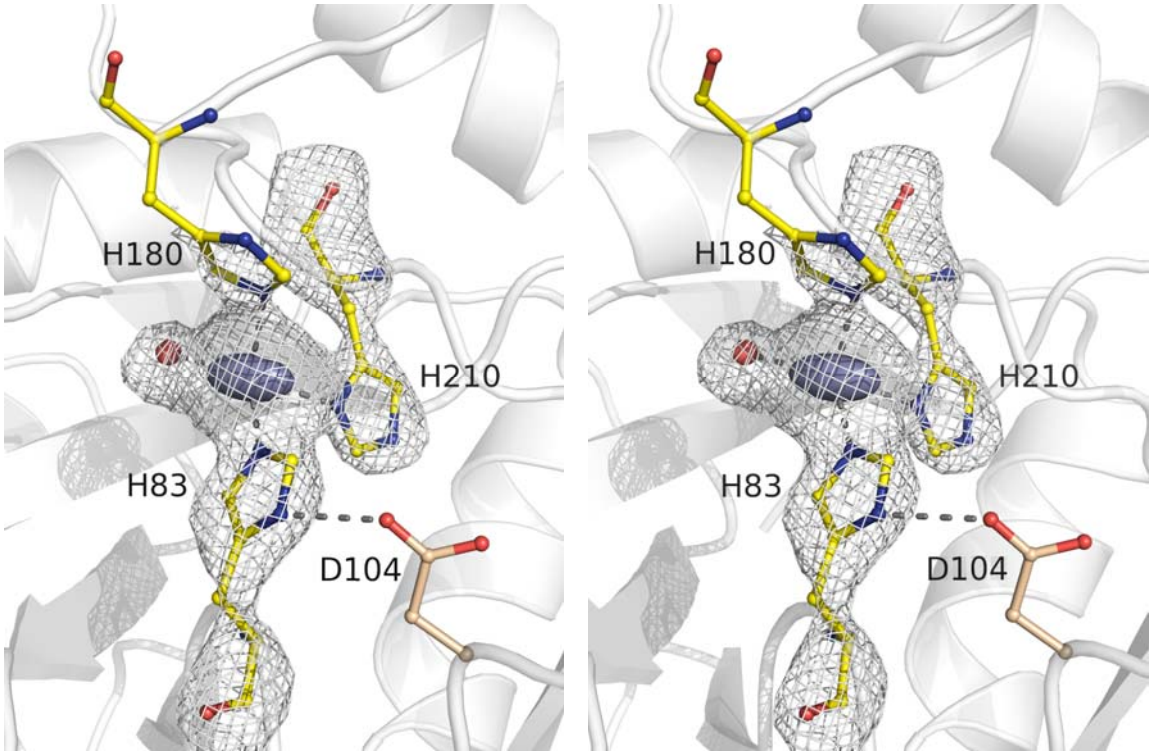

Figure 2-11. Stereo image of native D82N mutant structure of H. pylori aldolase showing zinc metal cofactor binding at site I in absence of ligand.

The zinc metal cofactor (ellipsoid) is coordinated by histidine chelating residues and a water molecule at the active site surface. The central position of the zinc ion is equivalent to site I.

2.1.4.10 Methylglyoxal detection

To corroborate the structural findings of methylglyoxal trapped in the active site of the D82N mutant, release of methylglyoxal was monitored using an enzymatic assay specific for methylglyoxal detection and is shown in Table 4. Methylglyoxal was generated by the D82N mutant following 10 min incubation at an estimated rate of 0.0008 s^{-1} that was equivalent to substrate turnover (kcat = 0.0007 s^{-1}) using a coupled enzymatic assay that detects triose-P release. In controls with BSA and wild-type recombinant enzyme, no methylglyoxal was detected. For longer incubation, methylglyoxal release decreased to 0.0003 s^{-1} when evaluated using measured levels shown in Table 4 at 30 and 60 min and suggests that methylglyoxal release from the enzyme has become rate-limiting. β-elimination from DHAP in solution was not the source of methylglyoxal release as methylglyoxal was not detected in controls using solution DHAP concentrations corresponding to those obtained from substrate turnover in the D82N mutant.

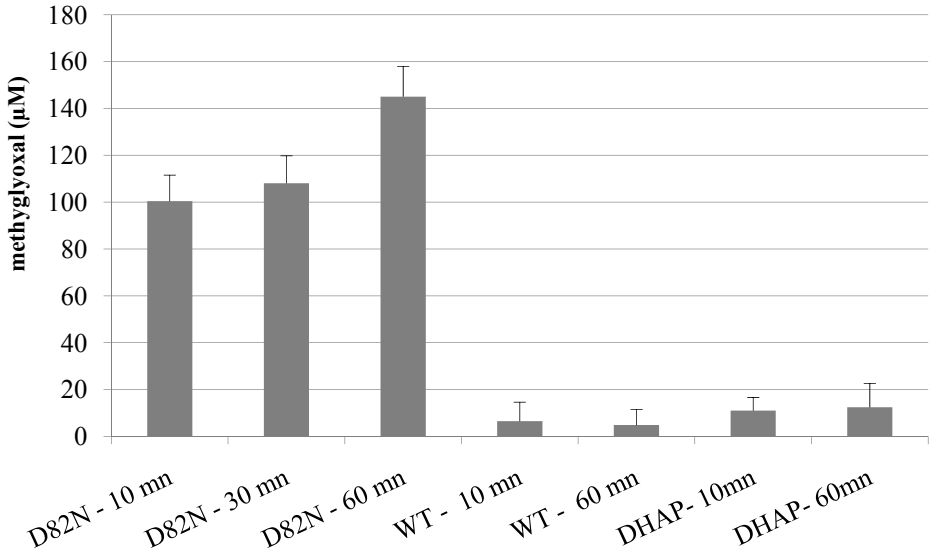

Table 2-4. Methylglyoxal detection in D82N mutant.

Columns represent level of methylglyoxal detected after incubations of 10 mM FBP with 200µM of D82N mutant, 200µM of native recombinant enzyme (WT), 84 µM and 252 µM of soluble DHAP (DHAP-10mn and DHAP-60mn respectively).

2.1.5 Discussion

The ability to cryotrap reaction intermediates in the crystalline state provided a unique opportunity to delineate the essential mechanistic features associated with proton transfers during substrate turnover and concomitant triose-P discrimination. Partial cleavage of the FBP substrate in *H. pylori* aldolase crystals indicates that turnover in crystalline state is slower (minutes) with respect to turnover predicted by kinetics in solution (7 s^{-1}). The slow turnover enabled cryotrapping of enzymatic complexes undergoing substrate cleavage. The structures of the enzymatic intermediates could be associated with substrate binding, substrate cleavage and triose-P recognition that afforded detailed insight into the catalytic cycle of class II aldolases at the molecular level. The concurrent conformational changes associated with substrate turnover revealed how dynamics is harnessed to perform enzyme catalysis in class II aldolases.

2.1.5.1 Enediolate trapping

The trapping of the DHAP enzymatic intermediate delineated the active site residues that are responsible for stabilization of the enediolate intermediate. Binding involves recognition of the DHAP in carbonyl form as binding by the gem-diol form of DHAP was not observed and is consistent with NMR analysis of DHAP binding in *E. coli* aldolase showing primarily or exclusive binding by the carbonyl form (17). Upon attachment the P1-oxyanion triggers a cascade of conformational changes to firmly grasp the active ligand. The structural characterisation identified Asp82 as the residue that guides the DHAP molecules in the active site which coordinates with the Zn metal ion to form the enediolate intermediate at site I. Formation of the enediolate intermediate is consistent with the high degree of coplanarity by the Zn ion with the C2-O2-C3-O3 plane in DHAP, calculated in Table S2, and which is indistinguishable from that of PGH, a putative transition state analogue (55). The low pKa ~ 8.0 determined for the enediolate intermediate in *E. coli* aldolase by NMR analysis (17) and in model compounds (18) supports trapping of DHAP in enediolate under crystallization conditions whose pH is 8 (Fig.1a). The C3 hydroxyl of the enediolate intermediate is coordinated by the Zn metal ion

while its C2 carbonyl only engages in close contact. Although the ^{13}C MR data clearly showed a significant shift by [2-^{13}C] DHAP carbonyl upon Zn metal coordination, it could not distinguish whether interaction by the Zn metal ion with the DHAP carbonyl was direct or indirect. Our structural data clarifies this interpretation and indicates an indirect interaction by Zn coordination with the C3 hydroxyl that is transmitted via intervening bonds to the C2 carbonyl. The supplementary interaction of the DHAP C2 carbonyl with the backbone amide of Gly211 would further polarize the keto function in leading to electronic rearrangement and enediolate formation.

Competent active site DHAP binding does not entail interaction with the Zn metal cofactor in both *H. pylori* and *E. coli* aldolase. The metal cofactor has significant occupancy at an additional site in both *H. pylori* and *E. coli* aldolase, distal to the enediolate, (site II – *H. pylori* aldolase and site III – *E. coli* aldolase) and where direct interaction cannot take place with DHAP by the metal cofactor. NMR data from *E. coli* aldolase incubated with DHAP indicates both the carbonyl form of DHAP and the resultant enediolate intermediate bound by the enzyme indicates exchange between the two sites in *E. coli* aldolase in agreement with sites I and III observed in the structural data. Nuclear relaxation studies using paramagnetic metal cofactors with acetol-phosphate in class II yeast aldolase yielded a binding geometry where the metal cofactor did not interact with acetol phosphate (59). The [2-13C] enriched acetol phosphate exhibited only a 13C resonance corresponding to carbonyl formation that would exclude ligand binding at site I. The relocation of the metal cofactor from site III to I thus serves to stabilize DHAP in its enediolate form. The barrier between Zn cofactor relocation between sites I and III is relatively low given that both sites have similar occupancies from the structural data and is corroborated by similar populations for DHAP carbonyl and enediolate forms in the NMR data (17).

2.1.5.2 Substrate reaction intermediate

Substrate recognition does not appear to require the presence of the zinc metal cofactor. This interpretation is supported by binding of the substrate analogue HBP which

does not entail interaction with the zinc metal cofactor in *H. pylori* aldolase, seen in Figure 5, and is further underscored in *E. coli* aldolase where binding takes place in absence of the metal cofactor (Figure 7). Superimposition of hexitol-P2 bound structure onto the FBP bound structure shows His83 in the HBP bound structure capable of hydrogen bonding with the C4 hydroxyl of FBP, seen in Figure 6. In Figure 4a, binding by FBP however suggests the contrary of not involving interaction with the His83 imidazole side chain by virtue of its side chain flip in the FBP bound structure corresponding to nearly a 180° rotation about its Cβ-Cγ bond in order to efficiently chelate the metal cofactor. The anisotropic B-factor refinement of the Zn metal ion position in the two liganded structures identified a common overlapping spatial region in Figure 6 that corresponds to a zinc coordination geometry which can be satisfied by the chelating histidine residues having H83 oriented in either direction. The energy penalty corresponding to this structural transition is minimal as it involves an exchange in hydrogen bonding partners made by the H83 imidazole Nδ1 with Asp82 and Asp104, shown in Figure 6. Different from HBP, strong second sphere coordination with the FBP C2 carbonyl oxygen by the zinc ion drives relocation to site I, being energetically more favourable than it would be with the HBP C2 hydroxyl due to the greater electronegativity of the carbonyl. However the energy gain by metal cofactor relocation to site I is partially offset by a resulting close contact made between His83 Cδ2 and FBP C4 hydroxyl. This close contact can be relieved upon metal cofactor migration to site II, increasing the distance from 2.8Å to 3.2Å, and a concomitant reduction in second sphere coordination energy due to an increase in Zn-FBP O2 distance from 2.7Å to 3.7Å. This interpretation of the structural data indicates transient substrate recognition in the native enzyme when the zinc ion is initially sequestered at site III. The interaction energy associated with hydrogen bond formation with His83 in substrate recognition is overcome by a gain in second sphere coordination between substrate and zinc metal cofactor at site I. This gain is mitigated by a close contact involving the chelating His83 and the FBP C4 hydroxyl which can be relieved. Zinc relocation among the binding sites in *H. pylori* aldolase involves a trade-off of competing interactions resulting in binding geometries of fairly similar stabilities.

FBP soaking into *H. pylori* aldolase crystals resulted in trapping of both triose-Ps, DHAP and G3P as free carbonyl forms, consistent with substrate turnover in crystals. G3P release from the active site prior to DHAP agrees with the obligate binding sequence in class II aldolases where G3P release precedes DHAP (60). Interactions made by G3P with the active site are fewer than with DHAP whereas there are 9 hydrogen bonds made by active site residues with the phosphate oxyanion in DHAP only 5 such interactions made interactions in G3P, seen in Figure 4b. More important, the zinc metal cofactor does not interact with G3P consistent with a lower intrinsic active site affinity by the free carbonyl form of G3P compared to DHAP in *H. pylori* aldolase that would result in G3P dissociation preceding DHAP (60). G3P release is further assisted by enediolate formation implicating Zn relocation to site I. In the FBP bound structure, Zn relocation would result in His83 Cδ2 making a steric clash with the FBP C4 hydroxyl and which is relieved in the triose-P structure where G3P pivots about its P6-phosphate binding site to minimize the contact by the nascent G3P aldehyde moiety thereby inhibiting aldol condensation. This interpretation of the structural data implies that aldol condensation involves a different binding geometry for G3P than is observed in Figure 4b.

H. pylori aldolase binds primarily (or exclusively) the acyclic carbonyl form of FBP based on the structural data. Specificity for the acyclic or cyclic enzyme form varies among class II aldolases. The *E. coli* enzyme has an absolute specificity for the acyclic form (17), while the class II yeast aldolase acts on both the cyclic and acyclic forms even as an apoenzyme (61). The bound geometry of the acyclic form of FBP has a number of structural features favourable for promoting catalysis of furanoside ring closure in the active site of *H. pylori* aldolase. Activation of the structurally invariant water molecule, Wp, shown in Figure 4a, by the P1-phosphate to which it is hydrogen bonded can in turn activate the C5 hydroxyl for nucleophilic attack on the C2 carbonyl. A mechanism of substrate assisted catalysis involving proton transfers has been described in class I rabbit muscle aldolase to explain enamine-Schiff base interconversion catalyzed by the DHAP P1-phosphate oxyanion and involved an intervening water molecule (62). Furthermore, hydrogen bonding by the FBP carbonyl with Gly211 backbone amide and the proximity of

Zn metal ion at site I would render the FBP C2 strongly electrophilic and making it favourable for nucleophilic attack. The charged hydrogen bond made by C5 hydroxyl with conserved Asp255 would guide the nucleophilic attack on C2 thereby ensuring cyclization. Relocation of the metal cofactor to site II would facilitate FBP release allowing for protonation of the C2 hydroxide.

2.1.5.3 Conformational transitions and zinc metal cofactor mobility

In E.coli and *H. pylori* aldolase, the relocation of the zinc metal cofactor is induced by ligand attachment at the P1-phosphate binding site that remodels the active site. The metal cofactor relocalizes from the interior site III in the active site to a surface accessible site I whereby the zinc metal cofactor can interact with the ligand. The conformational process driving the zinc ion relocation is the ordering of loops β6-α8 that stabilizes P1-phosphate binding, shown in Figure 8a for *H. pylori* aldolase. His226 in *E. coli* aldolase and equivalent His180 in *H. pylori* aldolase which are located at the inception of this loop also undergo a conformational displacement in their respective Cα atoms of 4.01 ± 0.02 Å and 4.97 ± 0.03 Å that disrupts their ability to chelate the zinc metal cofactor. Concomitant with the β6-α8 loop ordering, Thr 178 in *E. coli* aldolase and Leu138 in *H. pylori* aldolase which are at the inception of loop β5-α7 (residues 176-198 in *E. coli* aldolase and residues 136-156 in *H. pylori* aldolase) become ordered and their side chains point towards the former side chain position of His 226/His180 in the native enzyme, and is shown in Figure 12. In *E. coli* aldolase, Thr178 occupies the same physical space as His226 and enabling it to chelate the zinc metal cofactor identically to His226 at site III, seen in Figure 12a. In *H. pylori* aldolase, the pocket is larger owing to the larger displacement of His180 enabling Leu138 to swing into the pocket created by His180 displacement and enables of water molecule W2 to chelate with the metal cofactor at site II, shown in Figure 12b. Relocation of the zinc metal cofactor to site III in *H. pylori* aldolase would be unfavourable as it would result in a loss of coordination energy due to the expulsion of the water molecule W2 and the inability of His180 which is too distant to coordinate with the zinc metal factor at site III in presence of ligand. Relocation of the metal cofactor between site I and III in *E. coli*

aldolase occurs even in absence of active ligands however this relocation mechanism differs involving solely side chain rotations of the chelating histidine residues (8). The similar occupancies in *E. coli* aldolase of the metal cofactor at site I and III, and in *H. pylori* aldolase at site I and II indicates similar stabilities of the binding geometry at these two sites.

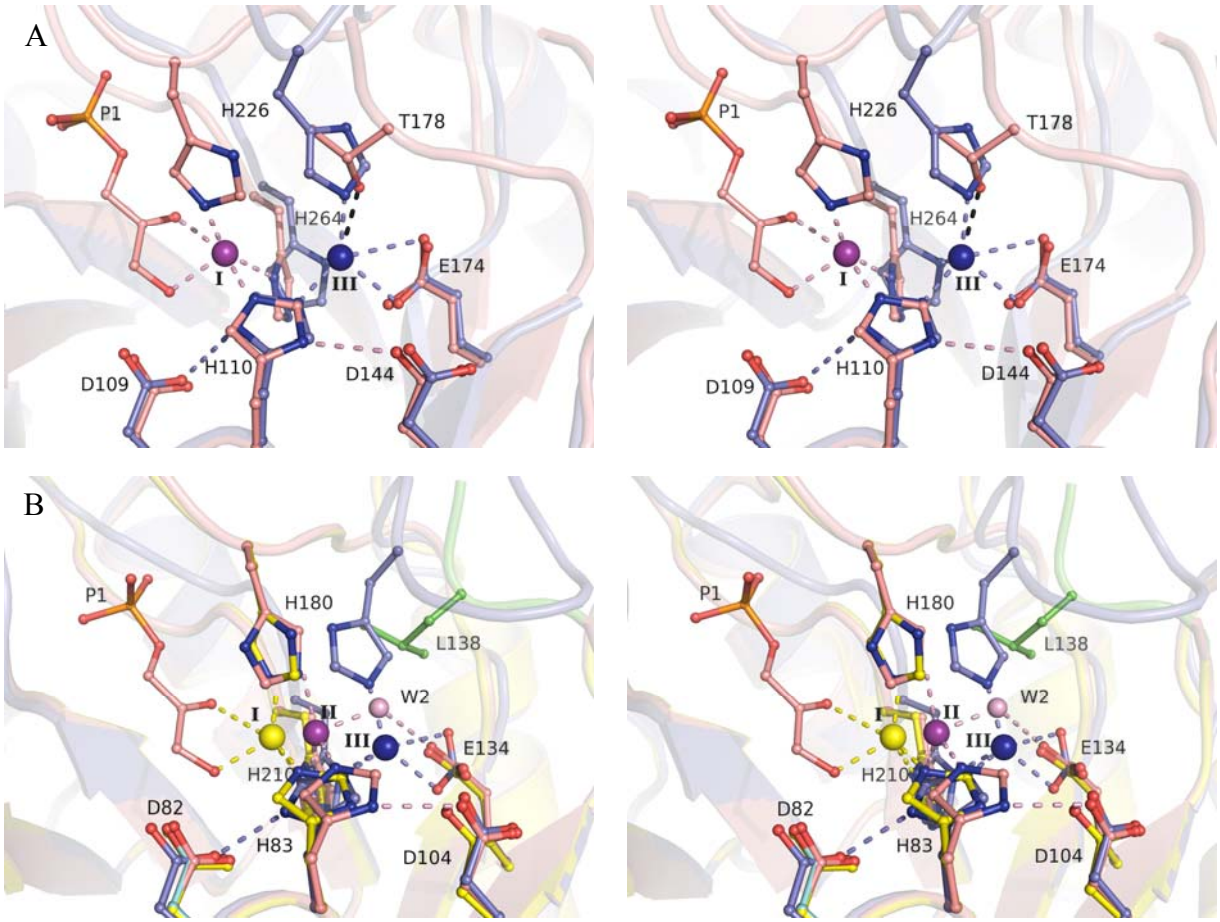

Figure 2-12. Stereo images of the superposition of structures of native class II aldolases and the corresponding structures of their bound DHAP intermediate.

Panel A compares conformational changes occurring upon DHAP binding in *E. coli* aldolase and panel B show the conformational changes occurring upon DHAP binding in H. pylori aldolase. In both panel, unbound structure is colored in blue while DHAP_FBPA complex structure is colored in pink and yellow.

Intriguingly, the substitution of Val for Thr178 in *M. tuberculosis* aldolase, also a member of class IIa aldolases would interfere with zinc ion relocation to site III as Val could not participate in Zn metal cofactor chelation. Superposition of the DHAP structure in *E. coli* aldolase with the structure of the DHAP complex formed in *M. tuberculosis* aldolase (RMSD = 0.94 Å) resulted in complete overlap by Thr178 in *E. coli* aldolase with Val165 in *M. tuberculosis* aldolase and by the Zn metal cofactors corresponding to site I in *E. coli* aldolase. Indeed, metal cofactor binding was not observed elsewhere in the active site of the *M. tuberculosis* enzyme. In the structure of *H. pylori* aldolase crystals soaked with very potent hydroxamate nanomolar inhibitors (9,48), Leu138 reorganizes and points into pocket displacing the water molecule W2 and metal cofactor binding is only observed at site I. In these structures, the previously disordered loops become almost fully traceable in the electron density. Sequestration of the metal cofactor at site I thus rigidifies the tertiary structure and is consistent with the similar observation in *G. lamblia* aldolase complexed with tight binding inhibitor tagatose 1,6-phosphate that resulted in nearly complete tracing of the polypeptide sequence through the electron density and with the Leu139 (Leu138 in *H. pylori* aldolase) pointing into the pocket (11). Catalysis is thus intimately linked to interconversion between binding geometries that are of similar stability and necessitating relocation of the zinc metal cofactor position in the active site.

2.1.5.4 Reversible substrate cleavage

A catalytic mechanism by which to promote cleavage of the C-C bond in class II FBP aldolases integrating kinetic and structural data is shown in Figure 14. A key feature is the interconversion among binding geometries of similar stabilities that promote cleavage of the C3-C4 bond in FBP. The catalytic cycle commences by FBP binding and entails recognition of two key substrate features. P1-phosphate oxyanion binding induces conformational changes whereby the β6-α8 loop in both *E. coli* aldolase and in *H. pylori* aldolase provoke a displacement of the zinc chelating histidine residue His226 in *E. coli* aldolase and His180 in *H. pylori* aldolase that is situated at the loop inception. His226/His180 displacement provokes bond rupture made between the metal cofactor and

the chelating histidine residue at site III. Secondly, competent active site binding by FBP is achieved via the second chelating histidine (His110/His83) by making a charged hydrogen bond with the FBP C4 hydroxyl, shown in Figure 14. The first chelating histidine no longer coordinated to the metal cofactor is free to interact with the FBP C4 hydroxyl as shown in Figure 14. Proton abstraction of the C4 hydroxyl initiates a rearrangement resulting in cleavage of the substrate C3-C4 bond. The mechanism is consistent with a trajectory of least atomic motion requiring only slight torsional librations by His226/His180 involving primarily rotational motions of its side chain position. The catalytic mechanism of substrate cleavage is concerted with metal cofactor relocation from site III to site I.

In both bacterial aldolases, rupture of zinc metal bond with His226/His180 is critical in order for this residue to act as general base at physiological pH. His residues coordinated to Zn^{2+} ion have a pKa ~ 13 (63) inhibiting their role as a general base at physiological pH. In contrast, the second chelating histidine, His110/His83, by virtue of the high pKa would stabilize the resultant negative charge created on the C4 hydroxyl ion in the transition state by electrostatic interaction. Charge stabilization by His110/His83 is assisted through electrostatic interaction with Asp109/Asp82 (Figure 14) that aligns the orientation of the histidine side chain maximizing the electrostatic interaction of His110/His83 with the developing negative charge on the C4 hydroxyl ion.

The superposition of the TBP inhibitor onto the FBP substrate in the catalytic mechanism proposed for C3-C4 bond cleavage is shown in Figure 13 and supports the proposed catalytic mechanism. Notable is the loss of His226/His180 interaction made with (4R)-FBP that is not possible with the C4 hydroxyl in (4S)-TBP. The loss of this interaction in TBP precludes efficient stabilization of the negative charge developed during proton abstraction thereby inhibiting substrate turnover.

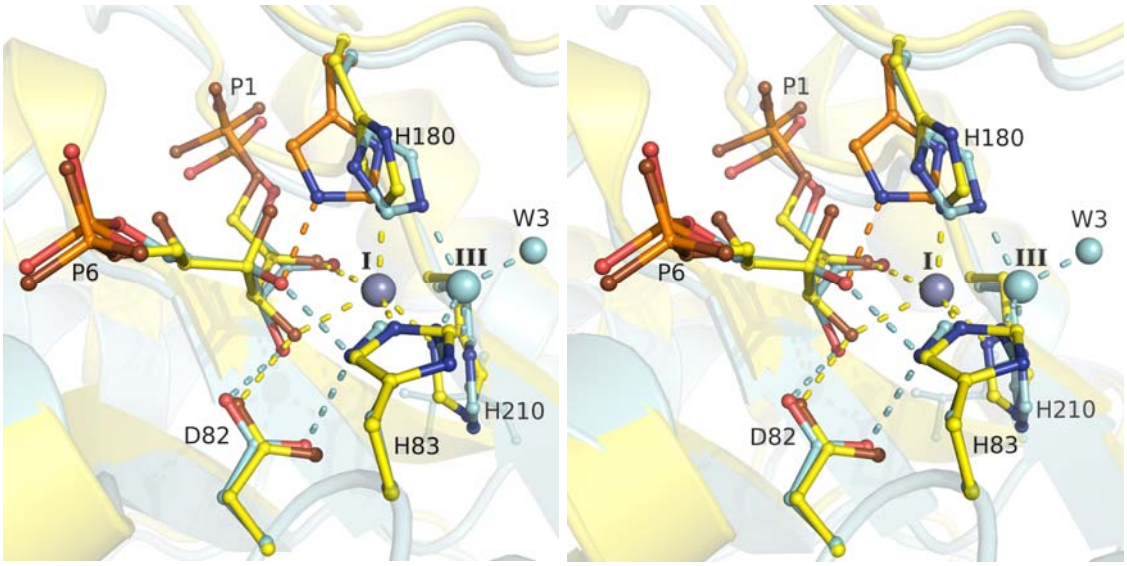

Figure 2-13. Stereo image showing superimposition of TBP-glFBPA complex (yellow), PDB: 3GAY, on FBP-hpFBPA complex (cyan).

Conformation of hpFBPA His180 (orange) is taken from the model of proton abstraction (figure 14A). RMSD calculated on 464 equivalent Cα atoms between the two structures is 0.67 Å.

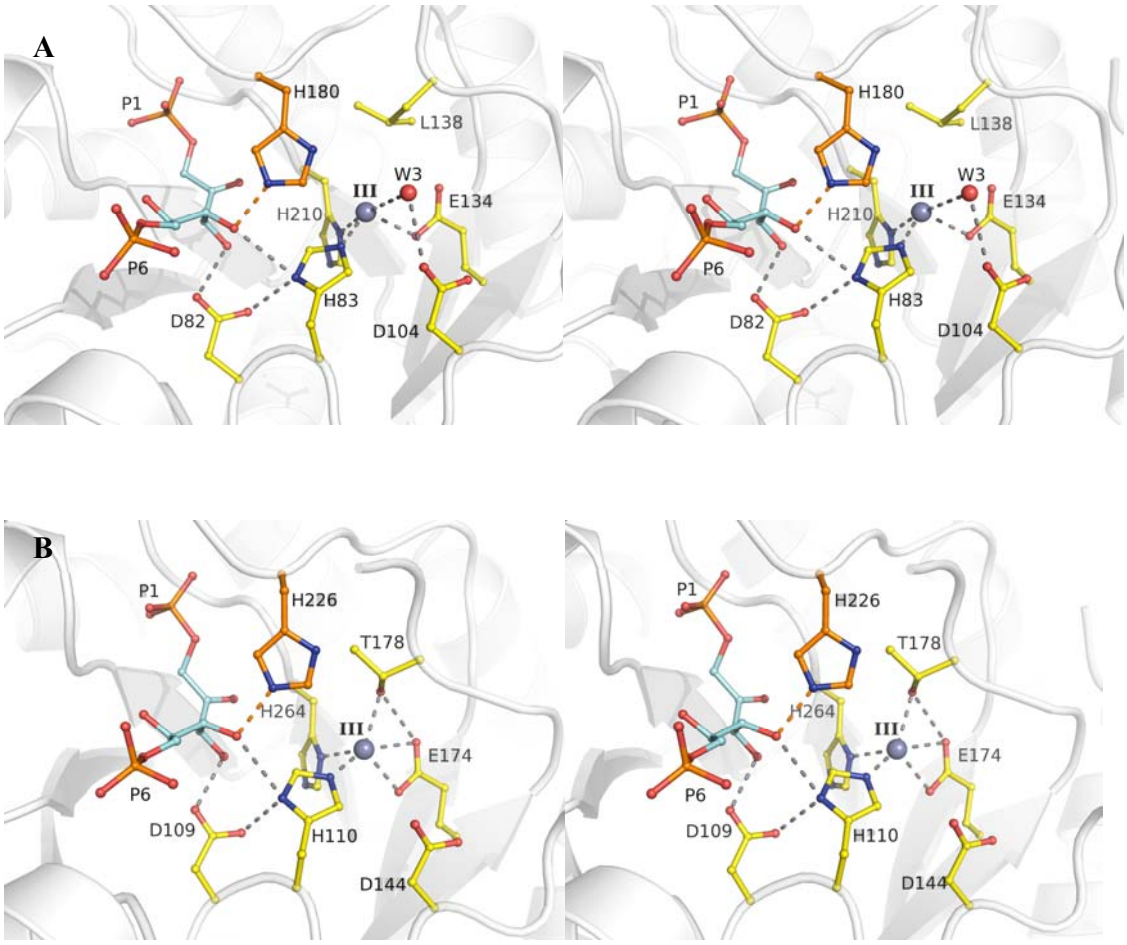

Figure 2-14. Stereo image of reaction mechanism depicting proton abstraction that initiates substrate cleavage in H. pylori (panel A) and *E. coli* (panel B) aldolases.

Stereo image shows incipient proton abstraction of the C4 hydroxyl by His180/His226 (orange) that is facilitated by the charged hydrogen bond made by His83/His110 (orange) and the substrate C4 hydroxyl. In this state, His83/His110 is no longer bonded to the Zn metal ion whereby its imidazole Nε2 acts as a proton acceptor catalyzing proton abstraction at the C4 hydroxyl. Yellow residues and white fold were extracted from HBP-FBPA complex structures. β7-α5 loop were extracted from DHAP-FBPA complex structures. His180/H226 were modeled in order to orient their Nε2 atom towards O4 forming an angle Nε2-O4-C4 of approximately 109° with a distance Nε2-O4 of 2.3 Å.

2.1.5.5 Asp109/Asp82

Cleavage of the substrate C3-C4 bond results in enediolate formation that is stabilized by migration of the metal cofactor to site I in order to coordinate the DHAP C3 hydroxyl. In the wild-type enzyme, the DHAP C3 hydroxyl by donating its hydrogen bond to Asp109/Asp83 maximizes its interaction with the metal cofactor as the two lone pairs of the C3 hydroxyl are directed towards the bonding Zn ion. In the D82N mutation, Asn82 acts as a hydrogen bond donor instead of an acceptor resulting in competition by Asn82 and the Zn ion for the *sp3* lone pairs of the C3 hydroxyl. The reduction in the number of electrons capable of coordinating with the Zn metal cofactor decreases bond strength. This interpretation is consistent with interaction of the DHAP C2 carbonyl with the metal cofactor that results in a longer bond length of 2.55 ± 0.08Å rather than 2.33 ± 0.02Å observed with DHAP C3 hydroxyl. Hybridization at the DHAP carbonyl oxygen is *sp2* and the C2 oxygen donates one lone pair to interact with the Gly211 backbone amide while leaving the other lone pair available for metal coordination while at the DHAP C3 hydroxyl both oxygen lone pairs are available for metal coordination. Competition for the DHAP C3 hydroxyl lone pairs by Asn82 would thus weaken metal cofactor coordination of the DHAP C3 hydroxyl and reduce stabilization of the enediolate form.

The significant shift in the pH activity for the D82N mutant of 2.5 pH units with respect to the native enzyme is consistent with a loss in enediolate stabilization in this mutant and suggests a pKa = 7.2 for the enediolate form in the native enzyme. A slightly higher pKa of ~ 8.0 estimated for the enediolate form in *E. coli* aldolase by NMR (17) is not inconsistent with the lower extent of the enediolate coordination by the metal cofactor. Although in both *E. coli* and *H. pylori* enzymes, the metal cofactor relocalizes between two sites with similar occupancy, in *H. pylori* aldolase, site II allows for second sphere coordination, albeit weak, by the DHAP C3 hydroxyl with the metal cofactor which is not possible at site III in *E. coli* aldolase.

A further consequence of the D82N mutation is that the hydrogen of the DHAP C3 hydroxyl is no longer contained in the enediolate plane and overlaps with the conjugating

π-electron system. This stereoelectronic factor promotes hydrogen acidity of the C3 hydroxyl hydrogen and enhances the propensity for β 1,4-elimination of the DHAP phosphate resulting in methylglyoxal formation (58). The detection of methylglyoxal formation in the D82N mutant is fully consistent with this interpretation and supports the identification of active site ligands as phosphate and methylglyoxal in the D82N mutant crystal structure. The structural and enzymological data thus supports an essential role by Asp82 in ensuring integrity of the enediolate intermediate. A significant role is unlikely for this residue in substrate cleavage. Substrate trapping was not observed in D82N mutant crystals indicating that the substantial activity reduction did not make substrate turnover rate limiting for this mutant.

2.1.5.6 Triose-P recognition

Recognition and discrimination of the triose-P substrates is critical in *H. pylori* aldolase whose primary function is FBP synthesis by condensation of G3P and DHAP during gluconeogenesis. The triose-Ps, DHAP and G3P, although chemically different are structurally very similar and, contrary to triose-P isomerase, for aldol condensation to occur requires each triose-P to interact at a different binding locus in aldolase. Indiscriminate attachment by DHAP and G3P at either triose-P binding locus is precluded in the active site of *H. pylori* aldolase. The enzymatic mechanism capable of explicitly recognizing and discriminating the cognate triose-Ps, G3P and DHAP, makes use of differences at the level of donor/acceptor hydrogen bonds by respective carbonyl and hydroxyl oxygens of the triose-P molecules. The carboxylate moiety of conserved active site residue Asp82 by making a charged hydrogen bond with the DHAP C3 hydroxyl, shown in Figure 4b, discriminates against aldehyde triose-P binding as the equivalent G3P O1 carbonyl interaction would be repulsive. Furthermore, keto moieties are considered stronger hydrogen bond acceptors than hydroxyls, thus binding by DHAP keto O2 with backbone amide Gly211 would provide an additional level of discrimination. The binding locus corresponding to the cognate aldehyde, G3P, specifically discriminates against DHAP

through the charged hydrogen bond made by Asp255 with the G3P O2 hydroxyl, shown in Figure 4b, as the equivalent DHAP O2 carbonyl interaction would be repulsive.

Different from *H. pylori* aldolase, G3P discrimination was not observed at the DHAP binding site in the crystal structure of *M. tuberculosis* aldolase in complex with DHAP where the DHAP C3 hydroxyl either pointed out of the active site interacting with a water molecule or interacted with the catalytic zinc metal ion (10) and did not interact with Asp95 (Asp82). Additionally, DHAP keto O2 did not interact with the equivalent backbone amide Gly253/Gly211 as observed in *H. pylori* aldolase. Although reduced triose-P discrimination could be a catalytic feature of *M. tuberculosis* aldolase, the crystallization of the enzyme at pH 4.8 would preclude formation by Asp95 of a charged hydrogen bond with the DHAP C3 hydroxyl thereby increasing competition for the C3 hydroxyl by the metal ion that reorganizes active site interactions made with DHAP. Unambiguous assignment of the G3P binding site in the crystal structure of *M. tuberculosis* aldolase was also compromised, as the interaction made by Asp276 (Asp255) at pH 4.8 with the G3P O2 hydroxyl could be accommodated by the DHAP carbonyl O2. At physiological pH where Asp95 and Asp276 are fully ionized, *M. tuberculosis* aldolase would however be fully competent to recognize and discriminate cognate triose-P binding and the discriminatory mechanism becomes identical to that in *H. pylori* aldolase.

Our structural analysis is comprehensive examining catalysis in two bacterial aldolases that belong to two distinct subfamilies of class II FBP aldolase genes in eubacteria (54). Members belonging to each family are observed to exhibit 40% sequence similarity, with 25%–30% sequence similarity among all class II FBP aldolases. However active site residues capable of interacting with active site ligands are conserved and suggest that the same catalytic mechanism of reversible aldol condensation is exploited by all class II FBP aldolases. The only variability in active site residues is at the level of metal cofactor mobility in the active site. Relocation of the metal cofactor in the active site upon ligand binding depends on the chelating ability and conformational dynamics of a homologous side chain adjacent to the active site. It is intriguing that in *E. coli* aldolase, site I and site III

are 3.5 Å apart, a distance frequently encountered in metalloenzymes that use dual zinc ions in the active site. It is intriguing to speculate that evolutionary rigidification of site I and site III in *E. coli* aldolase would represent a simple mechanism by which to create dizinc binding enzyme.

2.1.6 Footnotes

The atomic coordinates and structure factors (code … and …) have been deposited in the Protein Data Bank, Research Collaboratory for Structural Bioinformatics, Rutgers University, New Brunswick, NJ (http://www.rcsb.org/).

Research was supported by funding to JS from Natural Science and Engineering Research Council (Canada) and Canadian Institutes for Health Research.

We thank Paul Heron and Oktavian Toka for their assistance in the kinetic characterisation of native and mutant *H. pylori* aldolases. Work was carried out in part at beamlines X12B, X25 and X29 of the National Synchrotron Light Source. Financial support comes principally from the Offices of Biological and Environmental Research and of Basic Energy Sciences of the US Department of Energy, and from the National Center for Research Resources of the National Institutes of Health. Assistance by beamline personnel, Drs L. Flaks, D.K. Schneider, A. Soares, A. Héroux and H. Robinson, is gratefully acknowledged.

The abbreviations used are: DHAP, dihydroxyacetone phosphate; FBP, fructose-1,6-bis(phosphate); GBP, (*2S*)-glucitol-1,6-bis(phosphate); G3P, glyceraldehyde 3-phosphate; HBP, hexitol-1,6-bis(phosphate); MBP, (*2R*)-mannitol-1,6-bis(phosphate); NADH, nicotinamide adenine dinucleotide PGH, phosphoglycolohydroxamate; PGHPP, N-(3-hydroxypropyl)-glycolohydroxamic acid bis-phosphate; TBP, tagatose-1,6-bis(phosphate); TIM, triose phosphate isomerase; RMS, root mean square.

2.1.7 Acknowledgements

This work was supported by Discovery Grant from the National Science and Engineering Research Council of Canada and by a grant from the Canadian Institutes for Health Research to JS. Work was carried out in part at the National Synchrotron Light Source, Brookhaven National Laboratory, which is supported by the U.S. Department of Energy, Division of Materials Sciences, and Division of Chemical Sciences under contract number DE-AC02-98CH10886.

2.1.8 References

1. Kobes RD, Simpson RT, Vallee RL, and Rutter WJ. (1969) A functional role of metal ions in a class II aldolase. Biochemistry 8, 585–588

2. Rutter WJ. (1964) Evolution of Aldolase. Fed. Proc. 23, 1248–1257

3. Gerdes SY, Scholle MD, Campbell JW, Balázsi G, Ravasz E, Daugherty MD, Somera AL, Kyrpides NC, Anderson I, Gelfand MS, Bhattacharya A, Kapatral V, D'Souza M, Baev MV, Grechkin Y, Mseeh F, Fonstein MY, Overbeek R, Barabási A.-L, Oltvai ZN, Osterman AL. (2003) Experimental determination and system level analysis of essential genes in Escherichia coli MG1655. J. Bacteriol. 185, 5673-5684.

4. Wehmeier, UF. (2001) Molecular cloning, nucleotide sequence and structural analysis of the Streptomyces galbus DSM40480 fda gene: the S. galbus fructose-1,6-bisphosphate aldolase is a member of the class II aldolases. FEMS Microbiol. Lett. 197, 53-58.

5. Singer M, Rossmiessl P, Cali BM, Liebke H, Gross CA. (1991) The Escherichia coli ts8 mutation is an allele of fda, the gene encoding fructose-1,6-diphosphate aldolase. J. Bacteriol. 173, 6242-6248.

6. Singer M, Walter WA, Cali BM, Rouviere P, Liebke HH, Gourse RL, Gross CA. (1991) Physiological effects of the fructose-1,6 diphosphate aldolase ts8 mutation on stable RNA synthesis in Escherichia coli. J. Bacteriol. 173, 6249-6257

7. Galkin A, Kulakova L, Melamud E, Li L, Wu C, Mariano P, Dunaway-Mariano D, Nash TE, Herzberg O. (2007) Characterization, kinetics, and crystal structures of fructose-1,6-bisphosphate aldolase from the human parasite, Giardia lamblia. J Biol Chem. 282(7):4859-67.

8. Blom NS, Tétreault S, Coulombe R, Sygusch J. (1996) Novel active site in Escherichia coli fructose 1,6-bisphosphate aldolase. Nat. Struct Biol. 3(10):856-62.

9. Fonvielle M, Coinçon M, Daher R, Desbenoit N, Kosieradzka K, Barilone N, Gicquel B, Sygusch J, Jackson M and Therisod M. (2008) Synthesis and Biochemical Evaluation of Selective Inhibitors of Class II Fructose bis-Phosphate Aldolases: Towards New Synthetic Antibiotics. Chem. 14, 8521-8529.

10. Pegan SD, Rukseree K, Franzblau SG, Mesecar AD. (2009) Structural basis for catalysis of a tetrameric class IIa fructose 1,6 bisphosphate aldolase from Mycobacterium tuberculosis. J Mol Biol. 386(4):1038-53.

11. Galkin A, Li Z, Li L, Kulakova L, Pal LR, Dunaway-Mariano D, Herzberg O. (2009) Structural insights into the substrate binding and stereoselectivity of Giardia fructose-1,6-bisphosphate aldolase. Biochemistry. 48(14):3186-96.

12. Hall DR, Leonard GA, Reed CD, Watt CI, Berry A, Hunter WN. (1999) The crystal structure of Escherichia coli class II fructose-1, 6-bisphosphate aldolase in complex with phosphoglycolo-hydroxamate reveals details of mechanism and specificity. J Mol Biol. 287(2):383-94.

13. Dudev T, Lin YL, Dudev M, Lim C. (2003) First-second shell interactions in metal binding sites in proteins: a PDB survey and DFT/CDM calculations. J Am Chem Soc. 125(10):3168-80

14. Dudev T, Lim C. (2002) Factors governing the protonation state of cysteines in proteins: an Ab initio/CDM study. J Am Chem Soc. 124(23):6759-66

15. Glusker JP, Katz AK, Bock CW. (1999) Metal ions in biological Systems. The Rigaku Journal, 16(2):8-16.

16. Bock CW, Katz AK, and Glusker JP. (1995) Hydration of Zinc Ions: A Comparison with Magnesium and Beryllium Ions, J. Am. Chem. Soc. 117, 3754-3765

17. Szwergold BS, Ugurbil K, Brown TR. (1995) Properties of fructose-1,6-bisphosphate aldolase from Escherichia coli: an NMR analysis. Arch Biochem Biophys. 317(1):244-52.

18. Kimura E, Gotoh T, Koike T, and Shiro M. (1999) Dynamic Enolate Recognition in Aqueous Solution by Zinc (II) in a Phenacyl-Pendant Cyclen Complex: Implications for the Role of Zinc(II) in Class II Aldolases J. Am. Chem. Soc., 121 (6), 1267-1274.

19. Plater AR, Zgiby SM, Thomson GJ, Qamar S, Wharton CW, Berry A. (1999) Conserved residues in the mechanism of the *E. coli* Class II FBP-aldolase.. J Mol Biol. 285(2):843-5.

20. Galkin A, Kulakova L, Melamud E, Li L, Wu C, Mariano P, Dunaway-Mariano D, Nash TE, Herzberg O. (2007) Characterization, kinetics, and crystal structures of fructose-1,6-bisphosphate aldolase from the human parasite, Giardia lamblia. J Biol Chem. 282(7):4859-67

21. Zgiby S, Plater AR, Bates MA, Thomson GJ, Berry A. (2002) A functional role for a flexible loop containing Glu182 in the class II fructose-1,6-bisphosphate aldolase from Escherichia coli. J Mol Biol. 315(2):131-40

22. Marshall BJ. (2001) One hundred years of discovery and rediscovery of Helicobacter pylori and its association with peptic ulcer disease. In H. L. Mobley, G. L. Mendz, and S. L. Hazell (ed.) Helicobacter pylori: physiology and genetics. p. 19-24. ASM Press, Washington, D.C.

23. Mitchell HM. (2001) Epidemiology of infection. In H. L. Mobley, G. L. Mendz, and S. L. Hazell (ed.), Helicobacter pylori: physiology and genetics. p. 7-18. ASM Press, Washington, D.C.

24. Motta CR, Cunha MP, Queiroz DM, Cruz FW, Guerra EJ, Mota RM, Braga LL. (2008) Gastric Precancerous Lesions and Helicobacter pylori Infection in Relatives of Gastric Cancer Patients from Northeastern Brazil. Digestion. Aug 11;78(1):3-8

25. Lee YC, Lin JT, Chen TH, Wu MS. (2008) Is Eradication of Helicobacter pylori the Feasible Way to Prevent Gastric Cancer? New Evidence and Progress, but Still a Long Way to Go. J Formos Med Assoc. 107(8):591-9.

26. Fukase K, Kato M, Kikuchi S, Inoue K, Uemura N, Okamoto S, Terao S, Amagai K, Hayashi S, Asaka M; Japan Gast Study Group. (2008) Effect of eradication of Helicobacter pylori on incidence of metachronous gastric carcinoma after endoscopic resection of early gastric cancer: an open-label, randomised controlled trial. Lancet. 372(9636):392-7.

27. Talley NJ. (2008) Is it time to screen and treat H pylori to prevent gastric cancer? Lancet. 372(9636):350-2.

28. Doig P, de Jonge BL, Alm RA, Brown ED, Uria-Nickelsen M, Noonan B, Mills SD, Tummino P, Carmel G, Guild BC, Moir DT, Vovis GF, Trust TJ (1999) Helicobacter pylori physiology predicted from genomic comparison of two strains. Microbiol Mol Biol Rev. 63(3):675-707. Review

29. Marais A, Mendz GL, Hazell SL, and Megraud F. (1999) Metabolism and genetics of Helicobacter pylori: the genomic era. Microbiol. Mol. Biol. Rev. 63:642–674

30. Chalk PA, Roberts AD, and Blows WM. (1994). Metabolism of pyruvate and glucose by intact cells of Helicobacter pylori studied by 13C NMR spectroscopy. Microbiology 140:2085-2092.

31. Stingl K, Uhlemann Em EM, Deckers-Hebestreit G, Schmid R, Bakker EP, Altendorf K. (2001) Prolonged survival and cytoplasmic pH homeostasis of Helicobacter pylori at pH 1. Infect Immun. 69(2):1178-80.

32. Hoffman PS, Goodwin A, Johnsen J, Magee K, Veldhuyzen van Zanten SJO. (1996) Metabolic activities of metronidazole-sensitive and -resistant strains of Helicobacter pylori: repression of pyruvate oxidoreductase and expression of isocitrate lyase activity correlate with resistance. J Bacterial. 178:4822–4829.

33. Ginsburg A, and Mehler, AH. (1966) Specific anion binding to fructose diphosphate aldolase from rabbit muscle, Biochemistry 5, 2623-2634.

34. Otwinowski Z, Minor W (1997) Processing of X-ray Diffraction Data Collected in Oscillation Mode. Methods in Enzymology. 276, 307-326.

35. Zwart PH, Afonine PV, Grosse-Kunstleve RW, Hung LW, Ioerger TR, McCoy AJ, McKee E, Moriarty NW, Read RJ, Sacchettini JC, Sauter NK, Storoni LC, Terwilliger TC, Adams PD. (2008) Automated structure solution with the PHENIX suite. Methods Mol Biol. 426:419-35

36. Afonine PV, Grosse-Kunstleve RW. & Adams PD. (2005). CCP4 Newsl. 42, contribution 8

37. Adams PD, Grosse-Kunstleve RW, Hung L-W, Iorger TR, McCoy AJ, Moriarty NW, Read RJ, Sacchetini JC, Sauter NK, Terwilliger TC (2002) PHENIX: building new software for automated crystallographic structure determination. Acta Crystallogr. Sect D. 58, 1948-1954.

38. Emsley P, Cowtan K. (2004) Coot: model-building tools for molecular graphics. Acta Crystallogr. Sect D., 60, 2126-2132.

39. Lowell SC, davis IW, Arendall III WB, de Bakker PIW, Word JM, Prisant MG, Richardson, JS, Richardson DC (2003) Structure validation by C-alpha geometry: phi, psi, and C-beta deviation. Protein Struct. Funct. Genet. 50, 437-450.

40. Terwilliger TC, Adams PD, Moriarty NW, Cohn JD (2007) Ligand identification using electron-density map correlations. Acta Crystallogr D Biol Crystallogr. 63(Pt 1):101-7.

41. Terwilliger TC, Klei H, Adams PD, Moriarty NW, Cohn JD (2006) Automated ligand fitting by core-fragment fitting and extension into density. Acta Crystallogr D Biol Crystallogr. 62(Pt 8):915-22.

42. Vaguine AA, Richelle J, Wodak SJ. (1999) SFCHECK: a unified set of procedures for evaluating the quality of macromolecular structure-factor data and their agreement with the atomic model. Acta Crystallogr D Biol Crystallogr. 55(Pt 1):191-205.

43. Protein Data Bank, research collaboratory for structural bioinformatics, Rutgers University, New Brunswick, NJ. http://www.rcsb.org/

44. DeLano, W. L. (2004) The PyMOL Molecular Graphics System, DeLano Scientific LLC, San Carlos, CA.

45. Racker E. (1949) Aldehyde dehydrogenase, a diphospho-pyridine nucleotide-linked enzyme. J Biol Chem. 177(2):883-92.

46. Leatherbarrow, R.J. (2001) GraFit Version 5, Erithacus Software Ltd., Horley, UK.

47. Davis KA, Williams GR (1969) Glyoxalase I, a lyase or an oxidoreductive isomerase? Can. J. Biochem. 47, 553-556.

48. Daher R, Coinçon M, Fonvielle M, Gest PM, Guerin ME, Jackson M, Sygusch J, Therisod M (2010) Rational design, synthesis and evaluation of new selective inhibitors of microbial class II (zinc dependent) fructose bis-phosphate aldolases. J. Med. Chem (in press)

49. Collins KD. (1974) An activated intermediate analogue. The use of phosphoglycolohydroxamate as a stable analogue of a transiently occurring dihydroxyacetone phosphate-derived enolate in enzymatic catalysis. J Biol Chem. 249:136–142

50. Midelfort CF, Gupta BK, Rose IA (1976) Fructose 1,6-bisphosphate: isomeric composition, kinetics, and substrate specificity for Aldolases. Biochem 15, 2178-85.

51. Qamar S, Marsh K, Berry A. (1996) Identification of arginine 331 as an important active site residue in the class II fructose-1,6-bisphosphate aldolase of Escherichia coli. Protein Sci. 5(1):154-61.

52. Trentham DR, McMurray CH, Pogson CI (1969) Active Chemical State of D-Glyceraldehyde 3-Phosphate in its Reactions with D-Glyceraldehyde 3-Phosphate Dehydrogenase, Aldolase, Triose Phosphate Isomerase. Biochem J. 114,19-24

53. Mabiala-Bassiloua CG, Zwolinska M, Therisod H, Sygusch J, Therisod M. (2008) Separate synthesis and evaluation of glucitol bis-phosphate and mannitol bis phosphate, as competitive inhibitors of fructose bis phosphate aldolases. Bioorg Med Chem Lett. 18(5):1735-7.

54. Plaumann M, Pelzer-Reith B, Martin WF & Schnarrenberger C. (1997) Multiple recruitment of class-I aldolase to chloroplasts and eubacterial origin of eukaryotic class-II aldolases revealed by cDNAs from Euglena gracilis. Curr. genet. 31, 430-438.

55. Izard T, Sygusch J. (2004) Induced fit movements and metal cofactor selectivity of class II aldolases: structure of Thermus aquaticus fructose-1,6-bisphosphate aldolase. J Biol Chem. 279(12):11825-33.

56. Plater AR, Zgiby SM, Thomson GJ, Qamar S, Wharton CW, Berry A. (1999) Conserved residues in the mechanism of the *E. coli* Class II FBP-aldolase. J Mol Biol. 285(2):843-55.

57. Galkin A, Kulakova L, Melamud E, Li L, Wu C, Mariano P, Dunaway-Mariano D, Nash TE, Herzberg O. (2007) Characterization, kinetics, and crystal structures of fructose-1,6-bisphosphate aldolase from the human parasite, Giardia lamblia. J Biol Chem. 282(7):4859-67.

58. Iyengar R, Rose IA. (1981) Concentration of activated intermediates of the fructose-1,6-bisphosphate aldolase and triosephosphate isomerase reactions. Biochemistry. 20(5):1223-9.

59. Smith GM, Mildvan AS, Harper ET. (1980) Nuclear relaxation studies of the interaction of substrates with a metalloaldolase from yeast. Biochemistry. 19(6):1248-55.

60. Rose IA, O'Connell EL, Mehler AH. (1965) Mechanism of the Aldolase Reaction. J Biol Chem. 240:1758-65.

61. Schray KJ, Fishbein R, Bullard WP, Benkovic SJ. (1975) The anomeric form of D-fructose 1,6-bisphosphate used as substrate in the muscle and yeast aldolase reactions. J Biol Chem. 250(13):4883-7.

62. St-Jean M, Sygusch J. (2007) Stereospecific proton transfer by a mobile catalyst in mammalian fructose-1,6-bisphosphate aldolase. J Biol Chem. 282(42) :31028-37.

63. Martin RB. (1974) Pyrrole hydrogen ionization of imidazole derivatives in metal ion complexes and carbonic anhydrase. Proc Natl Acad Sci U S A. 71(11):4346-7.

CHAPITRE III

Mise au point d'un protocole de dynamique moléculaire :

Tests et applications

" En essayant continuellement on finit par réussir. Donc plus ça rate, plus on a de chance que ça marche."

Devise Shadock

3 Mise au point d'un protocole de dynamique moléculaire: tests et applications

La mise au point d'un protocole de dynamique moléculaire est un processus relativement aisé lorsque l'on s'attaque à des systèmes déjà étudiés ou du moins dont les composantes ont été paramétrées pour le champ de force choisi. Ce processus peut devenir beaucoup plus ardu et long lorsque le système d'intérêt est plus complexe ou original.

Aussi deux études portant sur des FBPA de classe I ont abouti aux publications présentées dans ce chapitre avant que nos premiers essais de simulation de FBPA de classe II soient fructueux.

La première étude (Dax et al., 2005) porte sur le HNA-P, un inhibiteur des FBPA de classe I dont nos collaborateurs montrent qu'il se lie lentement (« slow binding ») et de manière stable à une lysine du site actif de l'aldolase de muscle de lapin. Nos simulations des deux types de complexe, non covalent et covalent, ont permis d'illustrer et d'expliciter ces deux caractéristiques cinétiques de l'inhibiteur.

Dans la deuxième étude (Dax et al., 2006), la spécificité d'un inhibiteur envers la FBPA de *Trypanosoma brucei* par rapport à celle du muscle de lapin a pu être expliquée par nos simulations.

Lors de ces deux études, j'ai conduit la réalisation de l'étude par modélisation des interactions protéines-ligands. Ceci a demandé la paramétrisation du système et en particulier la mise au points des descriptifs topologiques des inhibiteurs, mais aussi la conduite de nombreuses simulations de test. J'ai donc rédigé la partie des résultats et des matériels et méthodes portant sur ces simulations.

En 2006, la première publication portant sur la simulation d'une métalloprotéine à zinc a été publiée (Bianchini et al., 2006). C'est en nous basant sur cet article que nous avons réussi à traiter correctement la coordination du métal au cours des dynamiques. Nous

avons donc commencé à accumuler des résultats que nous présenterons dans la troisième partie de ce chapitre.

3.1 Hydroxynaphthaldehyde Phosphate Derivatives as Potent Covalent Schiff Base Inhibitors of Fructose-1,6-bisphosphate Aldolase

Chantal Dax, Mathieu Coinçon, Jurgen Sygusch, and Casimir Blonski,

Groupe de Chimie Organique Biologique, LSPCMIB UMR CNRS 5068, Université Paul Sabatier, Bâtiment IIR1, 118 Route de Narbonne, 31062 Toulouse Cedex 4, France, and Department of Biochemistry/Medicine, University of Montréal, CP 6128, Station Centre Ville, Montréal, Québec, Canada H3C 3J4

Biochemistry **2005,** *44,* 5430-5443

3.1.1 Abstract

Interactions of phosphate derivatives of 2,6-dihydroxynaphthalene (NA-P_2) and 1,6-dihydroxy-2-naphthaldehyde (HNA-P, phosphate at position 6) with fructose-1,6-bisphosphate aldolase from rabbit muscle were analyzed by enzyme kinetics, difference spectroscopy, site-directed mutagenesis, mass spectrometry, and molecular dynamics. Enzyme activity was competitively inhibited by NA-P_2, whereas HNA-P exhibited slow-binding inhibition with an overall inhibition constant of ~24 nM. HNA-P inactivation was very slowly reversed with $t_{1/2}$ ~10 days. Mass spectrometry and spectrophotometric absorption indicated that HNA-P inactivation occurs by Schiff base formation. Rates of enzyme inactivation and Schiff base formation by HNA-P were identical and corresponded to ~4 HNA-P molecules bound par aldolase tetramer at maximal inhibition. Site-directed mutagenesis of conserved active site lysine residues 107, 146, and 229 and Asp-33 indicated that Schiff base formation by HNA-P involved Lys-107 and was promoted by Lys-146. Titration of Lys-107 by pyridoxal 5-phosphate yielded a microscopic pK_a ~8 for Lys-107, corroborating a role as nucleophile at pH 7.6. Site-directed mutagenesis of Ser-271, an active site residue that binds the C_1-phosphate of dihydroxyacetone phosphate, diminished HNA-P binding and enabled modeling of HNA-P in the active site. Molecular dynamics showed persistent HNA-P phosphate interactions with the C_1-phosphate binding site in the noncovalent adduct. The naphthaldehyde hydroxyl, ortho to the HNA-P aldehyde, was essential for promoting carbinolamine precursor formation by intramolecular catalysis. The simulations indicate a slow rate of enzyme inactivation due to competitive inhibition by the phenate form of HNA-P, infrequent nucleophilic attack in the phenol form, and significant conformational barrier to bond formation as well as electrostatic destabilization of protonated ketimine intermediates. Solvent accessibility by Lys-107 Nz was reduced in the covalent Schiff base complex, and in those instances where water molecules interacted with Lys-107 in the simulations, Schiff base hydrolysis was not mechanistically favorable. The findings at the molecular level corroborate the observed

mechanism of slow-binding tight inhibition by HNA-P of muscle aldolase and should serve as a blueprint for future aldolase inhibitor design.

3.1.2 Introduction

Fructose-1,6-bisphosphate aldolase (EC 4.1.2.13) is situated at the junction of the hexose and triose branches in the glycolytic pathway where it catalyzes the reversible cleavage of fructose 1,6-bisphosphate [Fru(1,6)P_2] to dihydroxyacetone phosphate (DHAP) and glyceraldehyde 3-phosphate (*1, 2*). There are two distinct classes of aldolases: class I aldolases, found in eucaryotes and higher plants, are characterized by formation of a protonated imine (Schiff base) intermediate with substrates, DHAP or Fru(1,6)P_2, and the ε-amino group of an active site lysine residue (Lys-229) while class II aldolases, found in eubacteria and lower eucaryotes, require a divalent metal ion as a cofactor to polarize the ketose carbonyl oxygen and stabilize the enolate intermediate (*3*). The reversible aldol reaction catalyzed by class I aldolases, typified by the mammalian enzyme from rabbit muscle, proceeds by an ordered uni-bi mechanism. The multistep reaction sequence, which is supported by enzymological studies, includes formation of several distinct enzyme−substrate intermediate species. In presence of substrate, carbinolamine, imine (Schiff base), and enamine (carbanion) intermediates have been detected (*4*).

Three-dimensional crystal structures of class I aldolases have been determined from vertebrates including that of muscle (*5*−*7*), liver (*8*), insect (*9*), and parasitic protozoa (*10, 11*). With the exception of the last 20 amino acid residues comprising the C-terminal region, the molecular architecture of these isoenzymes has been highly conserved. The polypeptide fold of each 40 kDa aldolase subunit of the homotetramer corresponds to that of a β-barrel, with the active site located in the β-barrel center. The active site is composed of a substantial number of potentially charged and polar amino acid residues, which include Asp-33, Lys-107, Lys-146, Glu-187, Lys-229, and Ser-271 and which are conserved among all class I aldolases sequenced to date.

The development of active site-directed inhibitors for class I aldolases is of interest both from a mechanistic perspective (*12*−*17*) and in clinical applications. The design of pharmacologically active drugs targeting class I aldolases would be useful against microorganisms or cells where glycolysis represents the unique or primary energy source, such as in parasitic protozoa, for example, *Trypanosoma brucei*, the causative agent of African sleeping sickness (bloodstream form) (*18, 19*), or in cancer cells (*20*). Although glycolytic aldolases have been extensively investigated, the reaction trajectory has yet to be delineated in terms of the functional roles of specific active site residues, and despite the large number of inhibitors that have been investigated none have proven particularly useful as reversible or irreversible inhibitors (*12*). Therefore, we considered the possibility of using time-dependent reversible inhibitors (slow binding) (*21, 22*) targeting active site lysine residues (vide supra). Chemical modification (*15*,*23*−*25*) site-directed mutagenesis (*15, 26*) of active site lysine residues has been shown to result in the loss of enzyme activity. In a previous study (*15*), the aromatic compound 2-hydroxybenzaldehyde 4-phosphate inhibited aldolase activity by slow and reversible Schiff base formation with Lys-146 and suggested a design for novel slow-binding inhibitors of this enzyme.

In the present paper we describe the synthesis of aromatic substrate analogues of aldolase possessing a naphthyl moiety, namely, naphthyl 2,6-bisphosphate (NA-P_2) and 1-hydroxy-2-naphthaldehyde 6-phosphate (HNA-P). The mode of interaction by which the latter compound inhibits aldolase from rabbit muscle, taken as a model for class I aldolase, was determined by enzyme kinetics, UV/visible difference spectroscopy, electrospray mass spectroscopy, and site-directed mutagenesis of the active site residues. Unlike NA-P_2, which is a competitive inhibitor, time-dependent inhibition takes place in the presence of HNA-P and is concomitant with Schiff base formation between the inhibitor aldehyde and active site residue, Lys-107. Enzyme activity was only very slowly recovered upon incubation of the aldolase−inhibitor complex in a solution devoid of HNA-P. Furthermore, inhibition studies using the active site point mutant, S271A, shows that binding of the phosphate moiety of HNA-P involves the DHAP phosphate binding site. Consistency with molecular dynamics modeling studies was used to corroborate these interactions as well as

examine additional interactions between HNA-P and aldolase. A mechanism for the observed slow-binding inactivation is proposed on the basis of the modeling studies.

3.1.3 Materials and Methods

3.1.3.1 Materials

Fru(1,6)P_2 (sodium salt), NADH, glycerol-3-phosphate dehydrogenase (EC 1.1.1.8), and triose-phosphate isomerase (EC 5.3.1.1) were purchased from Boehringer Mannheim, dihydroxyacetone phosphate (lithium salt) was from Sigma, pyridoxamine 5-phosphate was from Fluka, and other chemicals were from Aldrich. Hexitol 1,6-bisphosphate (hexitol-P_2) was prepared from Fru(1,6)P_2 by the procedure of Ginsburg and Melher (*27*).

3.1.3.2 Activity Assays

Aldolase activity was measured using a coupled assay system triose-phosphate isomerase and glycerol-3-phosphate dehydrogenase (TIM/GDH) by following NADH oxidation at 340 nm using a Safas spectrophotometer thermostated to 25 °C (*28*). Assays were initiated by the addition of substrate [Fru(1,6)P_2, 1 mM final concentration] to complete a solution containing aldolase made up in triethanolamine (TEA) buffer (100 mM TEA/HCl, pH 7.6, 50 mM NaCl, 1 mM EDTA, ionic strength 0.15) and 0.42 mM NADH and containing coupling enzymes (10 μg/mL GDH and 1 μg/mL TIM) to a final volume of 1 mL. The rate of substrate cleavage was determined by measuring the decrease in absorbance per minute at 340 nm. Aldolase was dialyzed overnight at 4 °C against TEA buffer before use, and the protein concentration was determined spectrophotometrically using an extinction coefficient of $\varepsilon_{280} = 0.91$ mL·mg^{-1}·cm^{-1} (*29*). The subunit concentration was determined on the basis of a molecular weight of 159000 for the aldolase tetramer (*30*).

The inhibition constant (K_i) for NA-P_2 was determined from double-reciprocal plots of initial rates measured in the presence of 10−100 μM Fru(1,6)P_2 and 0.5−1.5 μM inhibitor at constant enzyme concentration (2 μg/mL). For point mutation, K107M, assays were

performed at an enzyme concentration of 30 μg/mL in the presence of 0.03−1 mM Fru(1,6)P_2 and 5−30 μM inhibitor.

3.1.3.3 Reduction by Sodium Borohydride.

Sodium borohydride reduction of the aldolase−HNA-P complex (TEA buffer) was performed using a technique described previously (*15*).

3.1.3.4 Kinetic Methods

Slow-binding inhibition (*21, 22*) involves rapid equilibrium formation between enzyme E and inhibitor I, followed by the initial complex EI undergoing a slow and reversible isomerization to a kinetically more stable complex form, EI*, as shown in Scheme 1

For this kinetic sequence, K_i* represents the overall inhibition constant, K_i the dissociation constant for the Michaelis complex EI, and K_d the dissociation constant for the EI* complex.

(A) Characterization of Slow-Binding Inhibition. In the absence of substrate, the apparent first-order rate constant (k_{app}) describing the formation of EI* is defined by eq 1 (*31*) and exhibits saturating kinetics at increasing inhibitor concentrations ([I]) corresponding to lower and upper limits of k_{-2} and $k_2 + k_{-2}$, respectively. In the extreme situation where k_{-2} tends to zero, a slow-binding inhibitor becomes an active site-directed irreversible inhibitor.

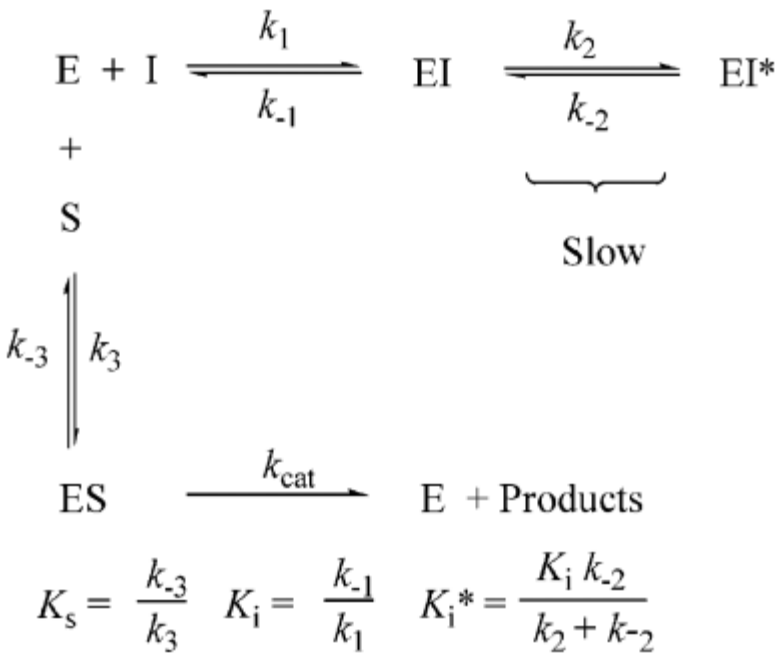

Scheme 3-1. Slow-binding inhibition

At this kinetic limit, eq 1 can be rearranged to the corresponding eq 2 described by Meloche (*32*) for this type of inhibition. The half-life of enzyme inactivation ($t_{1/2}$) plotted as a function of reciprocal inhibitor concentration then represents a straight line that intercepts the ordinate at ln $2/k_2$ and the abscissa at $-1/K_i$.

$$k_{app} = k_{-2} + \left[k_2 \frac{[I]/K_i}{1 + [I]/K_i}\right] \qquad (1)$$

$$t_{1/2} = \frac{\ln 2}{k_2}\left[1 + \frac{K_i}{[I]}\right] \qquad (2)$$

3.1.3.5 Time-Dependent Reversible Inhibition Studies.

Native recombinant aldolase (5 μM subunit) was incubated in the presence of HNA-P (0.05−1 mM) in TEA buffer. The enzymatic activity was assayed as a function of time with 10 μL aliquots. Inactivation kinetics followed a pseudo-first-order mechanism, and kinetic parameters K_i and $k_2$were determined using eq 2.

To determine the rate of reactivation, aldolase (25 μM subunit in TEA buffer) was incubated with 500 μM HNA-P until 90% inactivation was attained. Excess inhibitor was removed by ultrafiltration using a PM-30 membrane (Millipore), and the enzyme−inhibitor complex was incubated in TEA buffer (15 μM subunit final concentration) containing hexitol-P_2 (10 mM). Aliquots (10 μL) were withdrawn at various times for determination of aldolase activity. Controls consisted of identical protocols without HNA-P. Enzyme activity monitored over 10 days period lost ~5% of initial activity. The reactivation process was analyzed in terms of a first-order reaction.

3.1.3.6 UV/Visible Difference Spectroscopy

Absorbance spectra were measured using a Cary 1E Varian spectrophotometer at 25 °C. The same TEA buffer was used in both titration and activity assays. Absorbance spectra were measured by two different methods described elsewhere (*15*). For method A, absorption spectra were scanned either between 250 and 500 nm or at wavelengths corresponding to the maximum or minimum absorption and recorded as a function of time. Measurements were initiated by the addition of HNA-P at various final concentrations (0.1−1 mM) to TEA buffer containing a fixed concentration of aldolase (10 μM subunit). The measured absorption spectra of the enzyme complex were corrected for absorption by buffer, HNA-P, and enzyme alone. The resulting difference absorption spectra were used for determination of the rate constants describing the formation of the aldolase−HNA-P complex. Method B was used for the titration of HNA-P by aminocaproic acid. In each assay, aminocaproic acid was added at different final concentrations (0.01−0.2 M) to TEA buffer containing a fixed concentration of HNA-P (10 μM). Difference absorption spectra,

corresponding to Schiff base formation, were recorded at timed intervals and corrected for absorption by buffer, aminocaproic acid, and HNA-P alone.

Apparent first-order rate constants (k_{app}) and maximal absorption differences (ΔA_{max}) were obtained for each assay by fitting the time-dependent absorption data to a first-order kinetic equation (or the sum of two first-order kinetic processes). The dissociation constant (K_d) of the Schiff base formed between HNA-P and aminocaproic acid was obtained from maximal absorption differences determined using eq 3.

$$\Delta A = \frac{\Delta A_{max}[\text{HNA-P}]}{K_d + [\text{HNA-P}]} \qquad (3)$$

The dissociation constant (K_i) for the rapidly formed aldolase−HNA-P complex (EI) and rate constant k_2 corresponding to the slow formation of the EI* complex were derived from analysis of apparent first-order rate constants using eq 1 or 2.

All UV/visible difference spectroscopy experiments using aldolase mutants (10 μM subunit) were performed using method A.

3.1.3.7 Electrospray Ionization Mass Spectrometry (ESI/MS)

Electrospray ionization mass spectra were obtained in the positive mode with a TSQ700 Finnigan Mat triple quadrupole mass spectrometer. Aldolase (50 μM subunits in TEA buffer) was incubated with 500 μM HNA-P until 60 ± 5% inactivation was attained, and excess inhibitor was removed by ultrafiltration using ammonium acetate buffer (10 mM, pH 5.5). The samples were prepared at ~10 pmol/μL in H_2O/methanol (1:1 v/v) with a final concentration of 1 mM ammonium acetate and 0.5% acetic acid. Samples were infused into the source of the mass spectrometer at a continuous flow rate of 4 μL/min. Protein data were acquired over a wide scan range of m/z 500−2000 at a scan rate of 3 s per scan with a scan duration of 1 min. Spectra were transformed using the Excalibur program. The mass spectrometer was calibrated using myoglobin from horse heart (Sigma) as the standard.

3.1.3.8 Determination of Lys-107 pKa

(A)Model Compound Titration (PMP). Pyridoxamine 5-phosphate (PMP) was used to model the adduct formed between active site Lys-107 and pyridoxal 5-phosphate (PLP) following sodium borohydride reduction (*25*). UV/visible spectra were taken at pH values ranging from 6 to 12 to confirm reported ionization potentials of the pyridine nitrogen and amino nitrogen of PMP (*33*). The pK_a's were determined from analysis of absorbance data at 325 nm that were fitted against a double pK_a equation using the program Graphit (Sigma).

(B) Labeling of Aldolase with PLP. Aldolase labeled at Lys-107 (aldolase−PMP) was prepared according to Anai et al. (*25*) except that the aldolase−PMP complex was extensively dialyzed against Tris−acetate buffer (0.1 M, pH 7.0) prior to use rather than precipitated. Residual activity of the modified aldolase was ~30% of initial activity.

(C) Titration of Aldolase−PMP. UV/visible spectra were obtained as a function of pH (5.5−10.6) for the aldolase−PMP adduct (1 mg/mL in Tris−acetate buffer). Absorbance data of the complex were measured at 329 nm, and pK_a's were determined by the same procedure as that used for the PMP model compound. Extinction coefficient values were determined assuming an 1:1 stoichiometry of the aldolase−PMP complex.

3.1.3.9 Molecular Modeling

Molecular dynamics, using the GROMACS (*33*) package and the all-atom force field GROMOS96, was undertaken to study Michaelis and covalent complex formation with HNA-P. A high-resolution X-ray structure of tetrameric aldolase wherein DHAP was noncovalently bound in the active site (*6*) was used as template for inhibitor modeling.

In noncovalent forms of the complex, the HNA-P molecule was manually docked in the active site cleft by first superimposing its phosphate moiety onto the phosphate binding site (binding mode A) in a manner that preserves the same hydrogen-bonding pattern including the oxyanion interaction with Ser-271. The HNA-P aldehyde function was then aligned such that it would be capable of hydrogen bonding with Lys-107 by adjusting

torsion angles about the P−O ester bond, ω_1, and the ester oxygen C_6 carbon bond, ω_2. Hydrogen bonding by the oxygen aldehyde with Lys-107 resulted simultaneously in contacts between C_1−OH and Lys-146 as well as Asp-33.

To explore conformations suitable for Schiff base formation with Lys-107, simulations were conducted using the nucleophilic form of Lys-107. The naphthyl C_1−OH has a pK_a of 8.0 (*34*), such that at pH 7.6 used for inactivation, both phenol and phenate forms are present in sufficient concentrations, and simulations were performed wherein each phenolic species was used. Asp-109 OD2 was protonated to mimic proton transfer from Lys-107 and to reduce electrostatic interaction with the C_{11} carbonyl oxygen of the aldehyde moiety. The C_{11}carbonyl was chosen oriented cis with respect to the C_1−O_1 bond in the phenol form, maximizing its hydrogen-bonding interaction with the O_1 hydroxyl. In case of the phenate form, the C_{11} carbonyl was oriented trans with respect to C_1−O_1 bond to minimize repulsion with the O_1 hydroxyl ion. These two orientations represented all conformations found for *o*-hydroxybenzaldehyde molecular fragments in the Cambridge Structural Database.

Covalent complexes were modeled as protonated imines having the Lys-107 Nz atom covalently bound to the C_{11} atom of HNA-P. Steric clashes narrowed the model building of the HNA-P covalent complex to a conformation wherein HNA-P occluded the active site, allowing the phosphate oxyanion to potentially interact with Ser-38 as well as the charge cluster formed by Lys-41, Arg-42, and Arg-303.

The force field parameters for HNA-P were chosen on the basis of similar chemical moieties parametrized in the GROMOS96 force field (parameter set 43a1). All constructs were immersed in a dodecahedron box filled with SPC (simple point charge) water molecules imposing a minimum solute-wall box of 10 Å surrounding the aldolase subunit.

Simulations were performed with periodic boundary conditions at constant *T* (300 K) and *p* (1 bar) using the Berendsen method (*33*) with a coupling constant of 0.1 ps for temperature and 0.5 ps for pressure. The time step for dynamics was 2 fs using the LINCS algorithm (*34*). A twin-range cutoff method was used for nonbonded interactions. The

electrostatic interactions were calculated by the particle mesh Ewald (*35*) method with a 9 Å cutoff for electrostatic interactions and the Lennard-Jones interactions with a 14 Å cutoff. The pair list of atoms interacting together was updated every five steps and kept constant between updates.

Close contacts in the initial model, if any, were relieved by 600 cycles of steepest descent energy minimization and an additional 1000 cycles of conjugated gradient energy minimization. Minimizations were followed by a 20 ps molecular dynamics with positional restraints on protein non-hydrogen atoms to relax water molecules around the subunit; this was followed by an additional 200 ps of molecular dynamics without restraints to allow for system equilibration. The protocol yielded RMS values for energy derivatives as a function of the C_α position that were less than 1.8 Å with respect to the crystallographic coordinates of the subunit.

Simulations of 5 ns duration were conducted for each modeled structure. Atomic coordinates generated by the dynamical simulations were sampled at a frequency of 1 ps. The atomic coordinate frames and corresponding potential energies were then used to calculate appropriate model conformational statistics. A unit-weighting scheme was employed for calculation of time averages and corresponding standard deviations. Standard deviations are reported using the symbol ±. The larger the standard deviation, compared to the statistical average, the greater the configurational heterogeneity.

Geometry conducive for incipient formation of the carbinolamine precursor was used to filter configurations generated in the simulations. Candidate geometry competent for attack was analyzed whenever the attacking nucleophile, Lys-107 Nz atom, was less than the van der Waals distance from the electrophilic aldehyde C_{11} carbon. The angle of attack was calculated as the direction defined by the Lys-107 Nz atom and C_{11} carbon and the normal to the hybridization plane containing the aldehyde C_{11} carbon.

3.1.3.10 Aldolases

Expression and purification of recombinant rabbit muscle aldolases were as reported previously (*36, 37*). Purification was based on substrate affinity elution from the carboxymethyl-Sepharose stationary phase and using gel filtration for protein cleanup.

3.1.3.11 Chemical Syntheses

The NMR spectra were recorded in $CDCl_3$, CD_3OD, or D_2O with a Bruker AC200 (200 MHz ^1H NMR, 50 MHz ^{13}C NMR, and 81 MHz ^{31}P NMR), a Bruker AC250 (250 MHz^1H NMR, 62 MHz ^{13}C NMR), or a Bruker ARX400 (400 MHz ^1H NMR, 100 MHz ^{13}C NMR) spectrometer. All chemical shifts are reported in parts per million with respect to TMS for ^1H and ^{13}C NMR spectra and H_3PO_4 for ^{31}P NMR spectra as internal standards. Naphthyl 2,6-bisphosphate (NA-P_2) was prepared as described previously (*38*) and HNA-P according to Scheme 2.

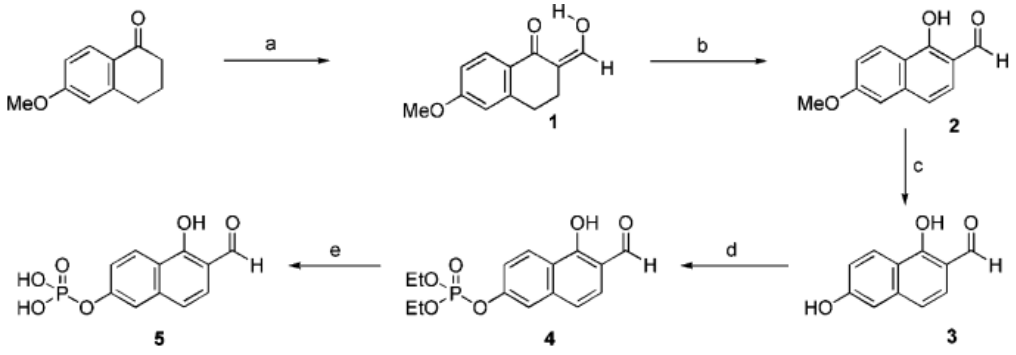

Scheme 3-2. Synthetic Scheme for the Synthesis of HNA-P (5)

Conditions: (a) MeONa, ethyl formate, benzene, room temperature; (b) DDQ, dioxane, room temperature; (c) BBr3, CH2Cl2, −40 °C; (d) (EtO)3P, pyridine, I2, CH2Cl2 ; (e) Me3SiBr, CH2Cl2, room temperature, H2O.

*(A) 2-[(Z)-1-Hydroxymethylidene]-6-methoxy-1,2,3,4-tetrahydro-1-naphthalenone (**1**)*. To a mixture of sodium methoxide (11.1 g, 205.6 mmol) and ethyl formate (9 mL, 111.4 mmol) in dry benzene (70 mL) at room temperature was added dropwise a solution of 6-methoxy-1-tetralone (8.4 g, 47.6 mmol) in dry benzene (40 mL). After addition, the reaction mixture was stirred at room temperature for 4 h. Et_2O (50 mL) was added, and the resulting mixture was washed with water, pH = 12. The pH of the aqueous layer was adjusted to 4 and extracted with Et_2O. The organic layer was washed with water and brine, then dried over $MgSO_4$, and evaporated under reduced pressure to yield **1** as a brownish powder (9.22 g, 95%).^{1}H NMR (250 MHz, $CDCl_3$): δ 2.54 (m, 2H, H3), 2.86 (m, 2H, H4), 3.94 (s, 3H, OCH_3), 6.61 (d, $^4J_{H5\text{-}H7}$= 2.50 Hz, 1H, H5), 6.82 (dd, $^4J_{H5\text{-}H7}$= 2.50 Hz, $^3J_{H7\text{-}H8}$= 8.50 Hz, 1H, H7), 7.92 (d, $^3J_{H8\text{-}H7}$ = 8.50 Hz, 1H, CH8), 9.88 (s, 1H, CH), 12.28 (br, 1H, OH). ^{13}C NMR (62 MHz, $CDCl_3$): δ 23.3 (C4), 29.37 (C3), 55.51 (OCH_3), 108.21 (C_2), 112.67 (C5), 113.05 (C7), 126.22 (C10), 128.82 (C8), 144.49 (C9), 163.4 (C6), 175.12 (CHOH), 208.07 (C1). Mass spectrometry (DCI/NH_3): 204 ($M + H^+$, 100%), 222 ($M + NH_4^+$, 15%).

*(B) 1-Hydroxy-6-methoxy-2-naphthaldehyde (**2**)*. A mixture of naphthalenone (**1**) (4.2 g, 20.74 mmol) and dichloro-2,3-dicyano-5,6-benzoquinone (5.20 g, 22.92 mmol) in dioxane (90 mL) was stirred at room temperature for 1 h. The hydroquinone was filtered off, and the solvent was removed under reduced pressure. The remaining product was purified by flash chromatography (CH_2Cl_2) to yield **2** as an yellow powder (4.1 g, 98%). ^{1}H NMR (200 MHz, $CDCl_3$): δ 3.91 (s, 3H, OCH_3), 7.01 (d, $^4J_{H5\text{-}H7}$ = 2 Hz, 1H, H5), 7.13 (dd, $^3J_{H5\text{-}H7}$ = 2 Hz,$^3J_{H7\text{-}H8}$ = 7.3 Hz, 1H, H7), 7.17 (d, $^3J_{H8\text{-}H7}$ = 7.3 Hz, 1H, H8), 7.36 (d, $^3J_{H3\text{-}H4}$ = 7.3 Hz, 1H, H3), 9.84 (s, 1H, CHO), 12.67 (s, 1H, OH). ^{13}C NMR (50 MHz, $CDCl_3$): δ 55.44 (OCH_3), 106.34 (C4), 113.28 (C2), 116.23 (C3), 116.43 (C8), 119.04 (C10), 126.12 (C5), 127.51 (C7), 139.62 (C9), 161.55 (C6), 162.03 (C1), 195.62 (CHO). Mass spectrometry (DCI/NH_3): 203 ($M + H^+$, 100%), 220 ($M + NH_4^+$, 17%).

*(C) 1,6-Dihydroxy-2-naphthaldehyde (**3**) (DHNA)*. A 1.0 M solution of boron tribromide in CH_2Cl_2 (15 mL, 15 mmol) was added dropwise to a stirred solution of

compound **2** (0.577 g, 2.85 mmol) in dry CH_2Cl_2 (120 mL) at −40 °C. The resulting mixture was stirred additionally for 1 h at −40 °C and then allowed to warm to room temperature. Water (20 mL) was added. The organic layer was washed by water (20 mL) and brine (20 mL) and dried over $MgSO_4$, and the solvent was evaporated under reduced pressure. The crude residue was purified by flash chromatography (CH_2Cl_2 to CH_2Cl_2/Et_2O, 1:1) to yield **3** as an orange powder (0.314 g, 59%).^{1}H NMR (400 MHz, CD_3OD): δ 7.03 (d, $^4J_{H5\text{-}H7}$ = 2.37 Hz, 1H, H5), 7.07 (dd, $^4J_{H5\text{-}H7}$ = 2.40 Hz, $^3J_{H7\text{-}H8}$ = 9 Hz, 1H, H7), 7.13 (d, $^3J_{H4\text{-}H3}$ = 8.49 Hz, 1H, H4), 7.40 (d, $^3J_{H4\text{-}H3}$ = 8.50 Hz, 1H, H3), 8.21 (dd, $^3J_{H8\text{-}H7}$ = 9 Hz, $^4J_{H8\text{-}H5}$ = 0.50 Hz, 1H, H8), 9.91 (s, 1H, CHO).^{13}C NMR (100 MHz, CD_3OD): δ 110.65 (CH5), 114.23 (C2), 119.06 (CH7), 119.23 (CH4), 119.40 (C9), 127.18 (CH8), 128.48 (CH3), 141.68 (C10), 161.28 (C6), 163.05 (C1), 197.44 (CHO). Mass spectrometry (DCI/NH_3): 189 ($M + H^+$, 100%), 206 ($M + NH_4^+$, 32%).

*(D) 1-Hydroxy-2-naphthaldehyde 6-Diethyl Phosphate (**4**).* To a solution of compound **3** (0.21 g, 1.1 mmol) in CH_2Cl_2 (34 mL) was added dry pyridine (0.1 mL, 1.24 mmol) at 0 °C, followed by the addition of a mixture of iodine (0.31 g, 1.2 mmol) and triethyl phosphite (0.23 mL, 1.32 mmol) in CH_2Cl_2 (10 mL). The resulting mixture was stirred for 1 h at 0 °C and allowed to warm to room temperature. Water (20 mL) was added, the organic layer was washed by brine and dried over $MgSO_4$, and the solvent was removed under reduced pressure. The remaining product after flash chromatography (CH_2Cl_2) yielded compound **4** as a yellow oil (0.11 g, 31%). ^{1}H NMR (200 MHz, $CDCl_3$): δ 1.34 (t, $^3J_{H\text{-}H}$ = 7 Hz, 6H, CH3), 4.24 (q, $^3J_{H\text{-}H}$ = 7 Hz, 4H, CH2), 7.26 (d, $^3J_{H3\text{-}H4}$ = 8.59 Hz, 1H, H3), 7.35 (dd, $^4J_{H7\text{-}H5}$ = 2.27 Hz, $^3J_{H7\text{-}H8}$ = 9.10 Hz, 1H, H7), 7.44 (d, $^3J_{H4\text{-}H3}$ = 8.59 Hz, 1H, H4), 7.59 (se, 1H, H5), 8.37 (d, $^3J_{H8\text{-}H7}$ = 9.10 Hz, 1H, H8), 9.91 (s, 1H, CHO). ^{13}C NMR (50 MHz, $CDCl_3$): δ 16.11 (d, $^3J_{C\text{-}P}$ = 6.40 Hz, CH3), 64.9 (d, $^2J_{C\text{-}P}$ = 6.10 Hz, CH2), 114.11 (C10), 116.36 (d, $^3J_{C\text{-}P}$ = 4.70 Hz, C5), 118.99 (C3), 119.90 (d, $^3J_{C\text{-}P}$ = 5.70 Hz, C7), 126.75 (C4), 127.69 (C8), 138.83 (C2), 152.27 (d, $^2J_{C\text{-}P}$ = 6.95 Hz, C6), 161.70 (C1), 196.10 (CHO). ^{31}P NMR (81 MHz, $CDCl_3$): δ −6.80. Mass spectrometry (DCI/NH_3): 325 ($M + H^+$, 56%), 342 ($M + NH_4^+$, 100%).

*(E) 1-Hydroxy-2-naphthaldehyde 6-Phosphate (Sodium Salt) (**5**) (HNA-P).*Bromotrimethylsilane (0.15 mL, 1.1 mmol) was added slowly with stirring to a solution of protected phosphate **4** (0.054 g, 0.17 mmol) in dry CH_2Cl_2 (200 μL) under nitrogen atmosphere. The resulting mixture was stirred for 3 h at room temperature (the progress of the reaction was monitored by ^{31}P NMR). Then Et_2O/H_2O (10:1) was added, and the organic layer was washed by water (10 mL). The pH of the aqueous layer was adjusted to 7.6 with aqueous NaOH (1 M); the solution was freeze-dried to yield **5** as a white powder (0.050 g, 96%). ^1H NMR (250 MHz, D_2O): δ 7.11 (d, $^3J_{H3-H4}$ = 8.50 Hz, 1H, H3), 7.34 (d, $^3J_{H7-H8}$ = 8.00 Hz, 1H, H7), 7.41 (se, 1H, H5), 8.24 (d, $^3J_{H4-H3}$ = 8.50 Hz, 1H, H4), 9.84 (d, $^3J_{H8-H7}$ = 8.00 Hz, 1H, H8), 9.91 (s, 1H, CHO). ^{13}C NMR (50 MHz, D_2O): δ 114.73 (C2), 116.93 (C10), 118.32 (d, $^3J_{C-P}$ = 3.57 Hz, C5), 120.13 (C8), 123.36 (d, $^3J_{C-P}$ = 5.00 Hz, C7), 123.42 (C9), 126.72 (C3), 128.31 (C4), 142.35 (C1), 158.49 (d, $^2J_{C-P}$ = 6.00 Hz, C6), 198.32 (CHO). ^{31}P NMR (81 MHz, D2O): δ0.56. Mass spectrometry (FAB^-): 267. λ_{max}^{H2O} (pH 7.6): 392 nm (ε 5100 $M^{-1}\cdot cm^{-1}$), 277 nm (ε 4650 $M^{-1}\cdot cm^{-1}$).

3.1.4 Results

3.1.4.1 Competitive Inhibition of Rabbit Muscle Aldolase by NA-P2.

The Fru(1,6)P_2 analogue, NA-P_2, competitively inhibited the aldolase-catalyzed reaction consistent with an inhibition constant,K_i, of 0.28 ± 0.03 μM. The Michaelis constant (K_m) determined for Fru(1,6)P_2 as substrate was 13 ± 2 μM. Both K_i and K_m values increased to 13 ± 1 μM and 150 ± 15 μM, respectively, when the assays were performed with the K107M mutant. From differential protection experiments, Lys-107 has been shown to interact with the C_6 phosphate of Fru(1,6)P_2 (*25*). The decreased affinity, with respect to the wild-type enzyme for both inhibitor and substrate, by the point mutation Lys-107 to Met suggests that Lys-107 also interacts with a phosphate moiety on NA-P_2.

3.1.4.2 Time-Dependent Reversible Inhibition of Aldolase by HNA-P.

Table 3-1. Interaction of HNA-P with Aldolase

conditions[a]	specific acitvity (units/mg)[b]
enzyme alone	12.5 ± 0.5
enzyme + HNA-P	2.8 ± 0.3
enzyme + HNA-P + Fru(1,6)P_2	5.2 ± 0.4
enzyme + HNA-P + hexitol-P_2	9.9 ± 0.5
enzyme + DHNA	12.5 ± 0.5

[a] Native rabbit muscle aldolase (0.2 mg/mL) was incubated in the presence of a fixed concentration of HNA-P (250 μM) in TEA buffer (1 mL final volume, pH 7.6) with or without Fru(1,2)P_2 or hexitol-P_2 (1 mM). [b] Aliquots were analyzed after 80 min incubation time for enzymatic activity (see the Materials and Methods section). In control experiments performed with enzyme alone or in the presence of DHNA (250 μM), no loss of enzyme activity was detected.

Incubation of aldolase with HNA-P leads to a first-order loss of enzyme activity (kinetics not shown). Substrate Fru(1,6)P_2 and substrate analogue hexitol-P_2, a strong competitive inhibitor for the aldolase-catalyzed reaction (*27*), protected the enzyme against inactivation by HNA-P (Table 1), consistent with inactivation occurring at the active site. By contrast, under identical experimental conditions, described in Table 1, the nonphosphorylated hydroxynaphthaldehyde DHNA analogue (see Scheme 2) was completely inactive against aldolase, indicating a functional role for the phosphate group in mediating active site binding by HNA-P. The aldolase inactivation rate was saturating with respect to increasing HNA-P concentrations and was analyzed as an irreversible process (Scheme 1 with $k_{-2} = 0$). Kinetic parameters were derived from the apparent first-order rate constant (k_{app}) measured at different inhibitor concentrations (0.01−1.5 mM) according to eq 2 and are shown in Table 2.

Table 3-2. Kinetic Parameters Describing the Interaction of HNA-P with Aldolase in TEA Buffer (pH 7.6)

parameter	value
K_i (μM)	125 ± 25[a]
k_2 (min^{-1})	0.067 ± 0.03[a]
k_{-2} (min^{-1})	$(13 \pm 3) \times 10^{-6}$ [b]
K_i* (nM)	24 ± 5

[a] Calculated using eq 3. [b] Calculated from data corresponding to enzymatic activity recovered (see the Materials and Methods section).

Enzyme activity, representing 20 ± 5% of the initial value, was recovered after 10 days incubation of the inactivated enzyme in a solution devoid of HNA-P and containing a saturating concentration of hexitol-P_2. Recovery of enzyme activity, analyzed as a first-order process, furnished the microscopic rate constant [$k_{-2} = (1.3 \pm 0.3) \times 10^{-5}$ min^{-1}]. The recovery of enzymatic activity is 4 orders of magnitude smaller than the inactivation constant k_2, consistent with determination of k_2 using the kinetic approximation of irreversible inactivation. HNA-P, therefore, behaves as a slow-binding inhibitor, and from the values shown in Table 2, the overall dissociation constant K_i* was calculated to be 24 ± 5 nM. Moreover, enzyme activity could not be restored after treatment of the enzyme−inhibitor complex with sodium borohydride, suggesting that the mechanism of inhibition by HNA-P involves Schiff base formation with an active site lysine residue.

3.1.4.3 Interaction of HNA-P with Aminocaproic Acid.

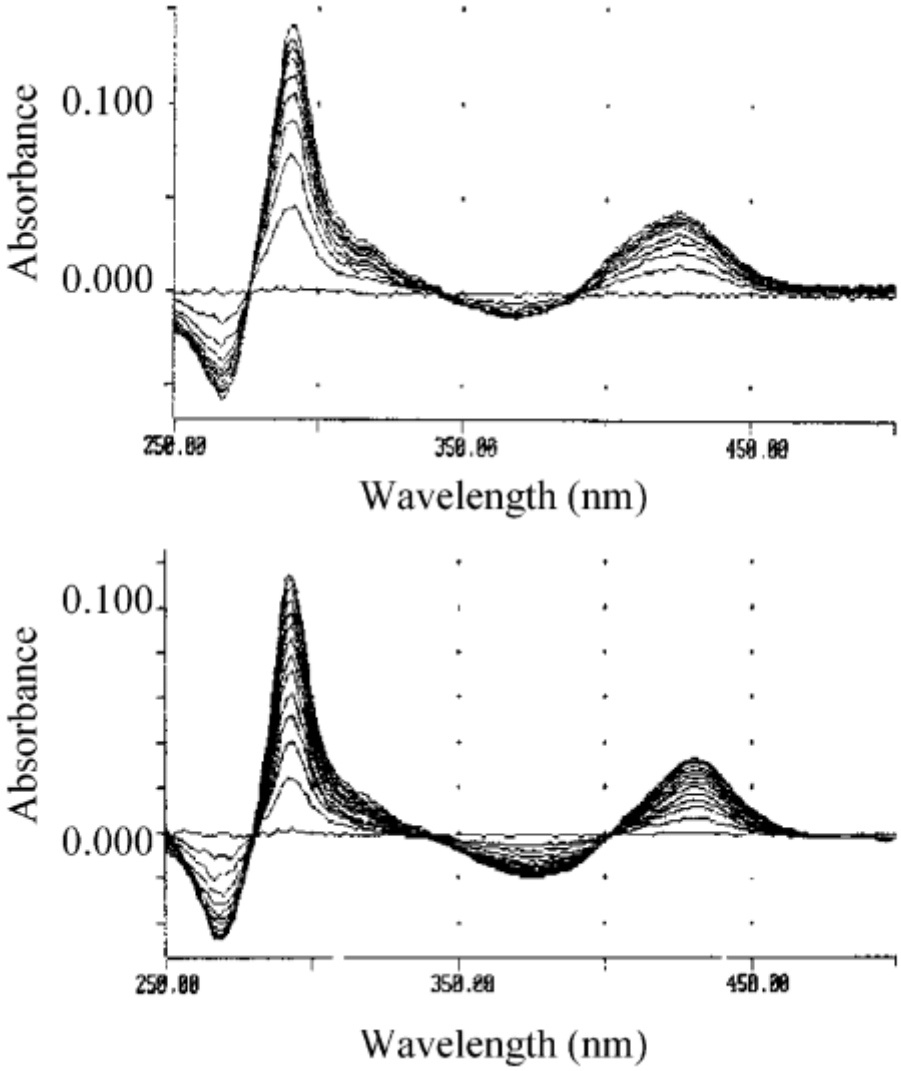

Figure 3-1. Interaction of HNA-P with aminocaproic acid and with native recombinant rabbit muscle aldolase.

Upper panel: UV/visible difference spectra of a mixture of 10 μM HNA-P and 200 mM aminocaproic acid in TEA buffer (1 mL, pH 7.6) with time (10 min intervals). Lower panel: UV/visible difference spectra of aldolase (10 μM subunits) and 250 μM HNA-P in the same buffer with time (interval of 5 min).

Schiff base formation between HNA-P and the ε-amino group of aldolase lysine residues was modeled using the reaction of HNA-P (10 μM) with aminocaproic acid (0.1−1 mM) as reference and was monitored by UV/visible difference spectroscopy (*15*). Schiff base formation between amino acids and aromatic hydroxyaldehydes such as pyridoxal or salicylaldehyde can be followed by difference spectroscopy and has been reported previously (*39*−*41*). The model reaction, shown in Figure 1 (upper panel), is characterized by changes in UV/visible absorbencies that correspond to two maxima at 425 nm (Δε 3730 ± 200 $M^{-1}\cdot cm^{-1}$) and 291 nm (Δε 13080 ± 700 $M^{-1}\cdot cm^{-1}$), which can be ascribed to Schiff base formation, and two minima at 367 nm (Δε −740 ± 50 $M^{-1}\cdot cm^{-1}$) and 267 nm (Δε −5050 ± 300 $M^{-1}\cdot cm^{-1}$) resulting from HNA-P consumption due to covalent complex formation. The presence of isosbestic points at 388, 343, and 276 nm indicates an absence of side reactions and no intermediate accumulation. Differential absorbance changes at equilibrium were found to be saturating with increasing aminocaproic acid concentrations (see Figure 2), and reaction kinetics for each aminocaproic acid concentration were consistent with a pseudo-first-order rate process for the reaction and corresponding to a second-order rate constant,k_{2nd}, of 0.12 ± 0.01 $M^{-1}\cdot min^{-1}$ at 25 °C. The value of the dissociation constant, K_d, for the HNA-P−aminocaproic acid adduct was 16 ± 3 mM (see Figure 2).

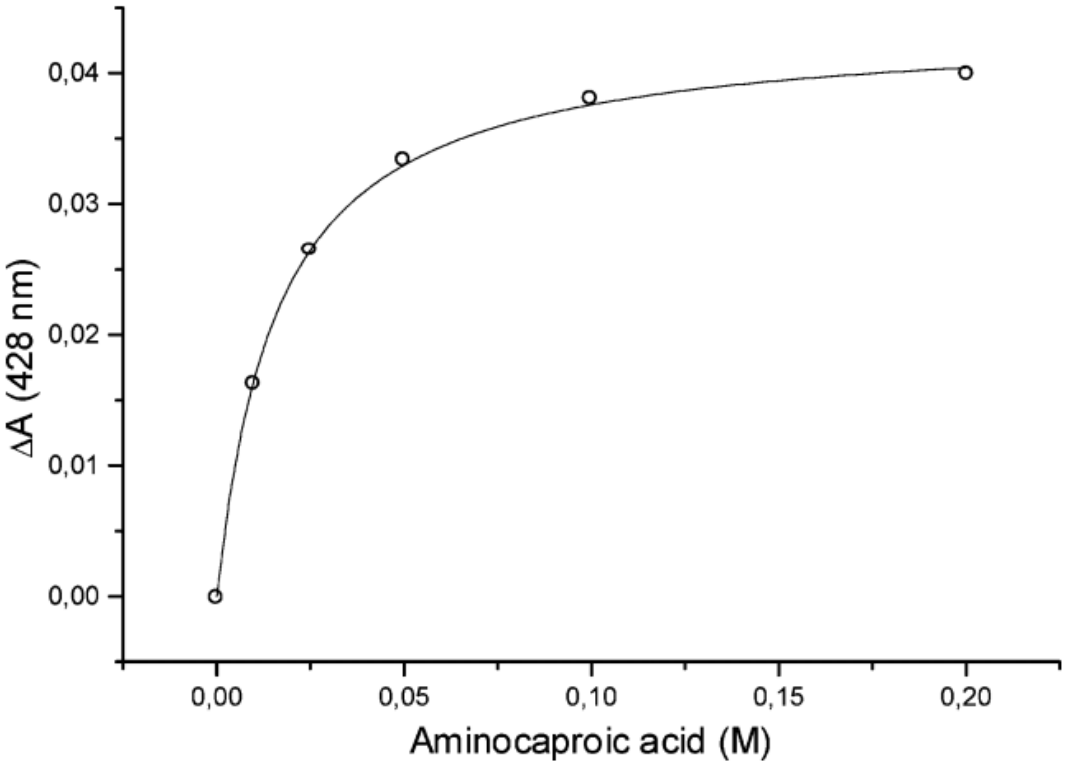

Figure 3-2. Change in differential absorbance as a function of aminocaproic acid concentration.

Differential absorbance at equilibrium was measured at 425 nm in TEA buffer (pH 7.6). The concentration of HNA-P was 10 μM. Data points are experimental, and the line represents the best fit of the data to eq 3. The Kd value determined was 16 ± 3 mM.

3.1.4.4 Interaction between HNA-P and Aldolase.

When HNA-P (0.1−1 mM, final concentration) was added to a solution containing native aldolase (10 μM subunits), the resulting UV/visible difference spectra have maxima at 431 and 293 nm and minima at 376 and 268 nm, with isosbestic points at 401 and 279 nm (Figure 1, lower panel). Slight differences in band positions with respect to the model reaction can be attributed to differences in the protein environment of HNA-P with respect to the model system and have been observed in other studies (*15, 39*). The progress of absorbance difference spectra was consistent with two distinct first-order rate processes. The rapid kinetic phase displayed the larger absorbance change and saturating behavior at high inhibitor concentrations and correlated with complete loss of enzyme activity and was made use of in the subsequent analyses. A slow kinetic phase was also observed when the assays were run in the presence of a saturating concentration of the protective substrate analogue hexitol-P_2 (10 mM). This slow kinetic phase, which corresponds to a 30 times smaller rate constant and contributes one-fourth of the final absorbance change, is not related to the observed inhibition and was not further analyzed. The same absorbance change at equilibrium (for the rapid kinetic phase) was observed over the entire range of inhibitor concentrations used. At these saturating concentrations, molar absorption coefficients for bound HNA-P were calculated by assuming that all four active sites of aldolase were occupied and yielded $\Delta\varepsilon_{431} = 3600 \pm 200\ M^{-1}\cdot cm^{-1}$, $\Delta\varepsilon_{376} = -2140 \pm 110\ M^{-1}\cdot cm^{-1}$, $\Delta\varepsilon_{293} = 12480 \pm 650\ M^{-1}\cdot cm^{-1}$, and $\Delta\varepsilon_{268} = -5080 \pm 250\ M^{-1}\cdot cm^{-1}$. The resulting stoichiometry of HNA-P bound to aldolase at maximal inhibition is consistent with differential molecular absorbencies derived from the aminocaproic acid−HNA-P complex given above, which predict an EI* complex having 3.9−4.2 mol of HNA-P bound/mol of tetrameric aldolase.

Kinetic parameters, K_i and k_2, describing EI* complex formation, were determined from data shown in Figure 3 according to eq 1 or 2 and yielded values of $K_i = 125 \pm 25$ μM and $k_2 = 0.067 \pm 0.004\ min^{-1}$, which are in good agreement with those determined kinetically (Table 2). The overall dissociation constant K_i* calculated from these results

corresponds to 24 ± 5 nM. Thus, the reactivity of HNA-P toward aldolase, as defined by (k_2/K_i), is about 4000-fold enhanced with respect to the reaction with model compound aminocaproic acid (k_{2nd}). Moreover, the dissociation constant of the HNA-P−aminocaproic acid complex is about 4×10^5-fold weaker than that of the aldolase−HNA-P complex. Thus, the aldolase active site contributes about 7.5 kcal mol^{-1} of binding energy to the Schiff base complex.

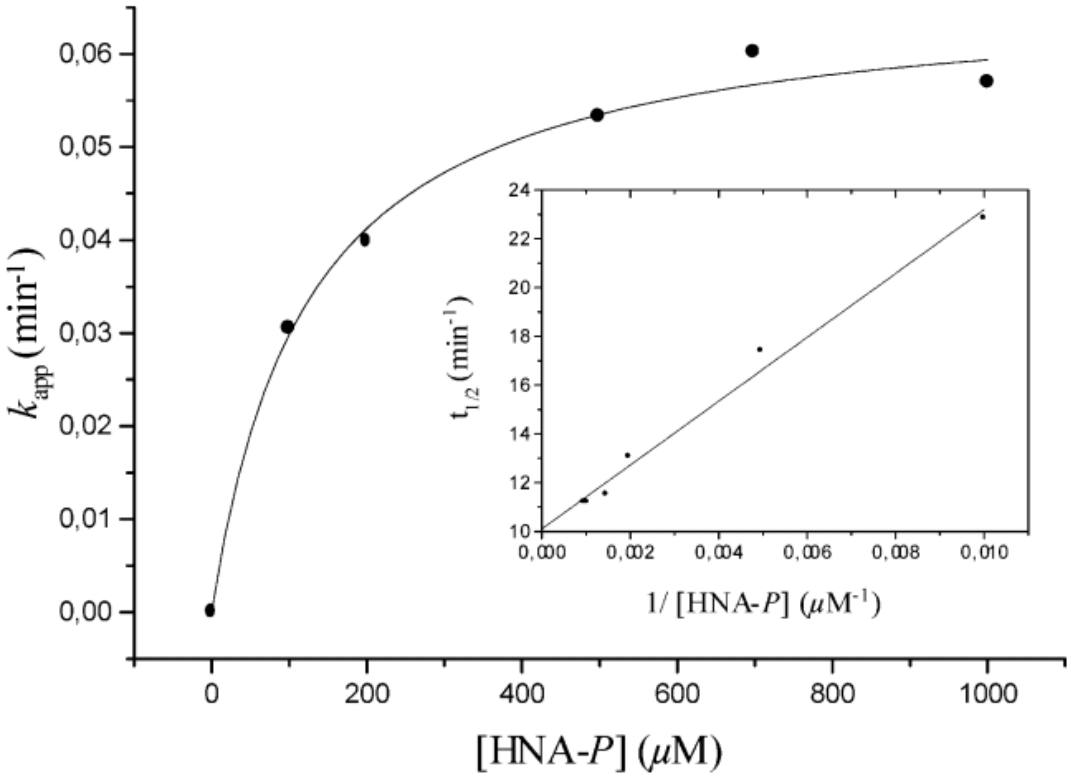

Figure 3-3. Saturation kinetics of the Schiff base formation between native recombinant rabbit muscle aldolase and HNA-P.

Shown is the variation of apparent first-order rate constant of Schiff base formation (kapp) between aldolase (10 μM subunits) and HNA-P at various concentrations in TEA buffer (pH 7.6). The line shown was derived from nonlinear regression of experimental data (symbols) analyzed according to eq 1. In the insert is shown the linear regression of the experimental data (t1/2) analyzed according to eq 2. The best fit corresponded to values of Ki = 125 ± 25 μM and k2 = 0.067 ± 0.003 min-1.

3.1.4.5 ESI/MS Analysis of the Aldolase−HNA-P Complex.

ESI analysis of an aldolase−HNA-P complex yielded molecular masses corresponding to a free aldolase monomer (39212 Da), a binary complex between an aldolase subunit and HNA-P (39457 Da), and a minor species consisting of a ternary complex between an aldolase subunit and two HNA-P molecules (39715 Da) (Figure 4) Observation of binary and ternary complexes is consistent with molecular masses that correspond to Schiff base complexes between an aldolase subunit and inhibitor at the expected stoichiometries of 1:1 and 1:2, respectively. The presence of both free and modified enzyme is compatible with UV/visible kinetic data and agrees with an observed 60% loss in initial activity.

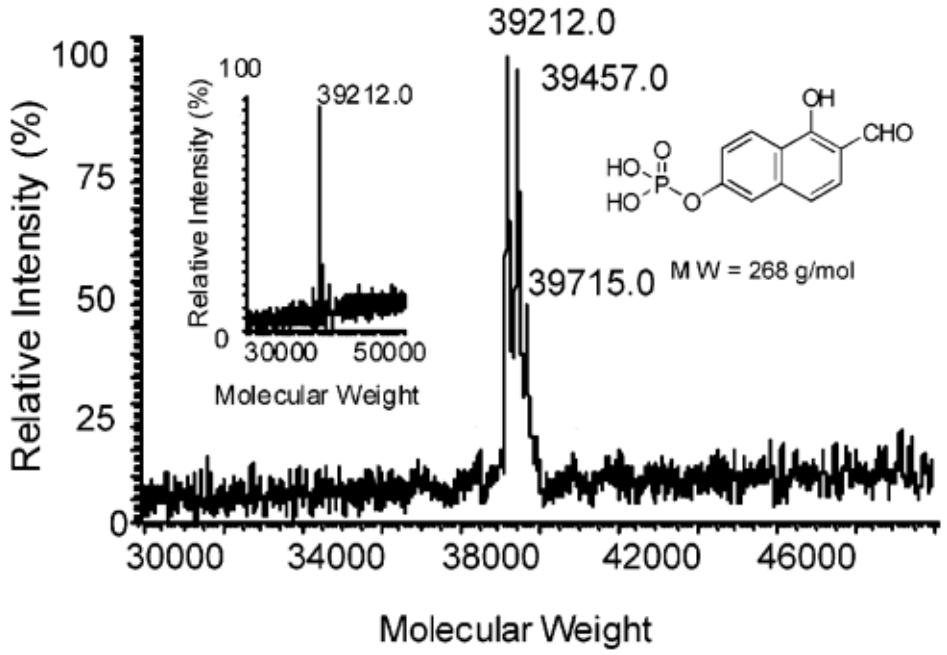

Figure 3-4. Deconvoluted electrospray ionization mass spectrum of the aldolase−HNA-P complex (40% residual activity).

Samples were prepared at 10 pmol/μL in 50% MeOH, 50% H2O, 1 mM ammonium acetate, and 0.5% acetic acid and were infused at 4 μL/min. Several scans (20) from m/z 500 to m/z 2000 at a scan rate of 3 s per scan were summed to yield the final profile spectrum prior to deconvolution. In the insert is shown the deconvoluted electrospray ionization mass spectrum of native recombinant aldolase prior to inhibition.

3.1.4.6 Interaction between Aldolase Mutants and HNA-P.

(A) Lysine Mutants. Lysine residues 107, 146, and 229 are located in the aldolase active site and thus are candidates for mediating inactivation through Schiff base formation with HNA-P. To identify which lysine residue was responsible for the differential absorbencies observed in the presence of HNA-P, point mutations of these lysine residues were constructed, namely, K107M, K146M, and K229M. These active site mutants possess no charge, are isosteric, and are unable to participate in Schiff base formation. Comparison of atomic coordinates for K107M, K229M, and native enzyme[2] shows these mutant structures to be isomorphous with respect to wild-type enzyme (RMS deviations of atomic coordinates with respect to native aldolase are 0.41 and 0.48 Å for K107M and K229M structures, respectively). UV/visible difference spectroscopy (method A) was used to examine the formation of the enzymatic complex for each point mutation in the presence of a fixed HNA-P concentration (300 μM), and analysis of the resulting data at 431 nm is reported in Table 3

Difference spectra observed for the mutant K229M were identical to that observed with wild-type enzyme. The progress of the reaction could be accounted for by two distinct first-order processes. The kinetic parameters and the amount of EI* complex formed were identical with those of the wild-type enzyme and rule out Lys-229 as the lysine residue directly responsible for Schiff base formation.

In contrast, difference spectra of the K107M mutant plus HNA-P showed only a slow kinetic phase whose rate constant and maximal absorbance were identical to the values of the slow phase observed for the wild-type enzyme. The absence of a rapid phase together with the absence of enzyme inhibition is consistent with Lys-107 being responsible for the observed slow-binding inhibition.

Reaction of the K146M mutant with HNA-P resulted in an overall absorbance change at an equilibrium comparable with that observed for wild-type aldolase (Table 3). The kinetic phase associated with enzyme inhibition, although corresponding to a first-order rate process, differed from that observed in the wild-type enzyme, exhibiting very

slow Schiff base formation. The substitution of Lys-146 with Met thus results in a decrease in the rate of EI* complex formation, but it does not change the ability by the mutant to form the complex. Thus, Lys-146 is not required for Schiff base formation but merely facilitates it.

Similarly, reaction by D33N and D33S mutants resulted in an overall absorbance change at equilibrium similar to that of the wild-type aldolase (Table 3). The kinetic phase associated with enzyme inhibition corresponded to a first-order rate process and was consistent with diminished Schiff base formation. Different from other mutants, the very slow rate process was not observed, indicating that loss of the carboxylate moiety suppresses the HNA-P side reaction and implying that the side reaction depends on the integrity of the C_6-phosphate binding locus. The same carboxylate oxygen of Asp-33 interacts with both Lys-107 and Lys-146 in the active site of the native enzyme such that loss of Asp-33 negative charge as well as its interaction with the lysine residues in the point mutant D33S may destabilize Lys-107 and Lys-146 side chain conformations. Both Lys-107 and Lys-146 are responsible for promoting substrate C_6-phosphate binding in aldolases (*24*).

Table 3-3. Interaction of HNA-P with Recombinant Mutant Aldolases

aldolase	specific acitivity (units/mg)	residual specific activity (%)	analysis of k_{app} (min^{-1})	relative ΔA of resolved species at 431 nm (%)
native	12.5	nd	0.045(3)[b]	100[c]
			0.0015(3)	*25*
K229M	3×10^{-6}	nd	0.040(3)[b]	95[c]
			0.0015(3)	*25*
K146M	2×10^{-3}	nd	0.0050(5)[b]	98[c]
			0.0015(3)	*25*
K107M	0.7	95	0.0015(3)	30
D33S	2×10^{-3}	nd	0.0070(5)	97
D33N	3×10^{-3}	nd	0.023(2)	98

[a] Assays were performed in TEA buffer (pH 7.6) according to method A (see the Materials and Methods section) at fixed aldolase subunit concentrations (10 μM subunits) and HNA-P concentrations (300 μM). Rates of Schiff base formation were monitored at 431 nm and could be analyzed by two first-order processes. For these cases, the rapid phase displaying the larger absorbance change is correlated with the loss of enzyme activity. The results obtained for the slow process are indicated in italics. nd = not detectable. [b] Standard deviation given in parentheses and corresponds to last significant figure for each rate constant. [c] Relative amplitude for rapid phase.

(B) Ser-271 Mutant. The phosphate moiety of HNA-P is essential for aldolase interaction as the analogue DHNA, which lacks the phosphate moiety, is only a very weak inhibitor (Table 1). DHAP binding in rabbit muscle aldolase places the phosphate moiety of the reactant within hydrogen- bonding distance of Ser-271 (*6*), suggesting that this residue may participate in the binding and positioning of HNA-P in the active site. To examine this hypothesis, the active site mutant S271A, which is unable to participate in hydrogen bonding with the phosphate oxyanion, was employed.

The mutant S271A exhibited considerably lowered activity and affinity toward Fru(1,6)P_2(specific activity = 0.05 unit/mg and K_m = 1 mM), indicating a functional role for Ser-271 in catalysis. UV/visible difference spectra of the S271A mutant (10 μM subunits) in the presence of HNA-P (0.1−1.5 mM) were consistent with two distinct first-order kinetic processes, identical with those observed in the wild-type enzyme (see Figure 1). The stoichiometry of HNA-P binding to the S271A mutant corresponds under saturating conditions to an EI* complex wherein ~4 mol of inhibitor is bound per mole of tetrameric mutant aldolase. Kinetic analysis of data corresponding to EI* complex formation yielded values for K_i and k_2 of 1.3 ± 0.1 mM and 0.065 ± 0.006 min^{-1}, respectively. Thus, the mutation Ser-271 to Ala decreases by 1 order of magnitude the affinity of HNA-P for the aldolase active site but did not modify its ability to catalyze Schiff base formation. The contribution of the hydroxyl moiety of Ser-271 to binding energy of the HNA-P phosphate moiety in the aldolase-HNA-P complex is thus ~1.4 kcal·mol^{-1}.

3.1.4.7 Ionization Constant of the Amino Group of Lys-107.

PLP reacts covalently with muscle aldolase by Schiff base formation with Lys-107, which inhibits enzymatic activity (*25*). The resulting complex can be reduced in the presence of sodium borohydride ions, resulting in PMP becoming irreversibly bound to the ε-amino group of Lys-107. Bound PMP is spectrophotometrically detectable and thus useful as a "reporter group" (*42*) at the active site of the enzyme. By comparison of pK_a's of the substituted pyridine nitrogen and ammonium ion of the reporter group with those of

unbound PMP, the perturbation of the active site environment on the ionization potential can be estimated. The pK_a of the substituted phenol (pK_a ~3.7) was not used in this study due to poor stability of the enzyme at low pH.

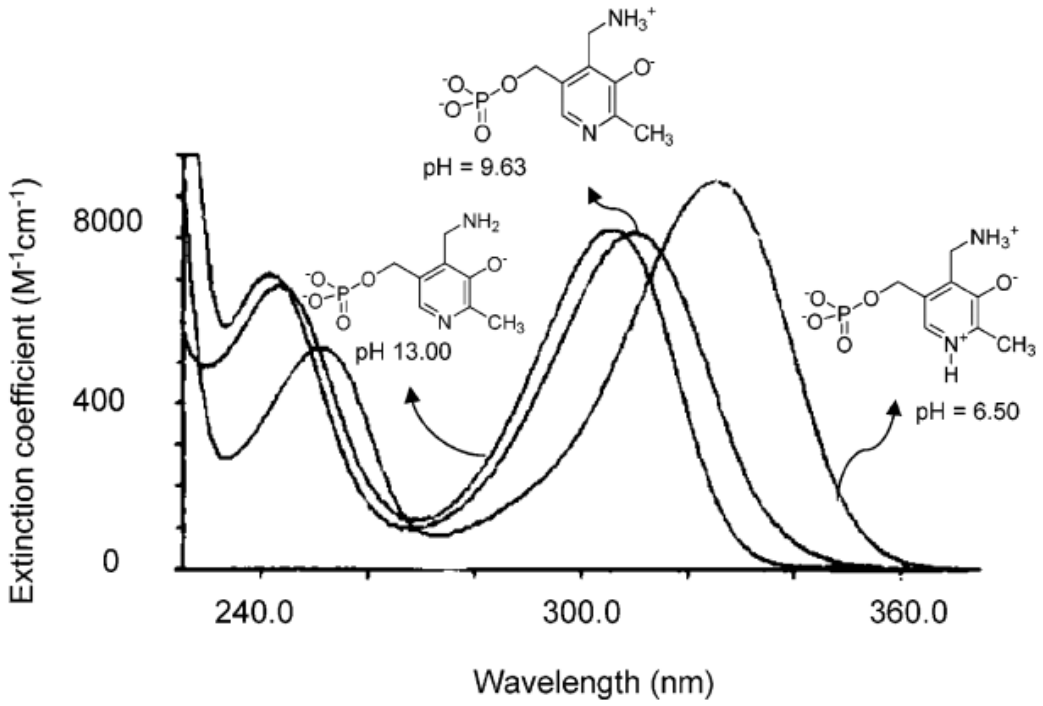

Figure 3-5. Absorption spectra of pyridoxamine 5-phosphate taken at pH 6.50, 9.63, 13.0. At the pH shown, the observed spectra arise predominantly from the indicated species.

(A) Model Compound. UV/visible spectra of PMP at pH 6.50, 9.63, and 13.0 are shown in Figure 5, and each absorption spectrum illustrated corresponds to the predominant species present at the given pH (*43*). Substantial spectral changes accompany titration of the substituted pyridinium ion (λ_{max} 325 nm) to the corresponding pyridine (λ_{max} 309 nm) while only a small but measurable spectral shift occurs upon neutralization of the ammonium salt group (λ_{max} 305 nm). The change in absorbance at 325 nm with pH was used for the determination of PMP pK_a's, shown Figure 6, and yielded two ionizations

constants of 8.75 ± 0.08 (pyridine nitrogen) and 10.5 ± 0.4 (amino nitrogen) that are in good agreement with those determined previously (*43*).

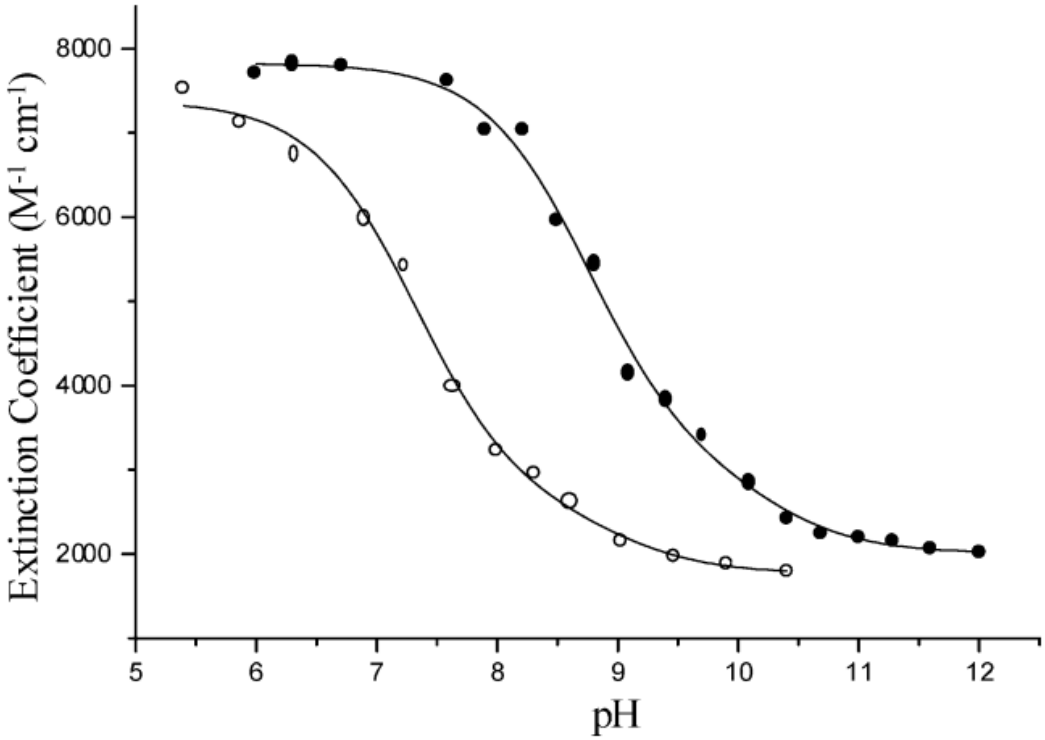

Figure 3-6. Absorption spectra of PMP at 325 nm (solid circles) and the PMP−aldolase complex at 329 nm (open circles) as a function of pH.

The best fit using the Graphit program (double pKa equation) corresponded to pKa values of 8.75 ± 0.08 and 10.5 ± 0.4 for PMP and 6.9 ± 0.1 and 8.3 ± 0.5 for the PMP−aldolase complex.

(B) Labeled Protein. The UV/visible spectra of the native and freshly prepared aldolase−PMP complex showed a slight shift of the maximal absorbance to 329 nm (pH 6.0) compared to the PMP model compound (not shown). The absorbance changes at 329 nm that would accompany the deprotonation of pyridium and ammonium ions yield pK_a's of 6.9 ± 0.1 and 8.3 ± 0.5, respectively, and are shown in Figure 6. This represents an

increase in acidity of ~2 pK units relative to the model compound and is not inconsistent with the presence of positively charged residues, such as Lys-146 that is adjacent to Lys-107. The proximity of two lysine residues in an active site has been shown to result in a pK_a decrease by several pK_a units (*44*). A lowered p$K_a$for Lys-107 would be mechanistically useful for nucleophilic attack on the carbonyl group of HNA-P during Schiff base formation.

3.1.4.8 Molecular Modeling of Aldolase−HNA-P Complexes.

Molecular dynamics simulations were conducted to explore active site HNA-P configurations consistent with covalent complex formation as well as to gain insight into the exceptional stability of the covalent adduct formed by HNA-P and aldolase. Control simulations were first carried out in an effort to reduce computational overhead. Simulations of 1 ns duration each were run, comparing conformations generated for the unbound aldolase tetramer and that of a single unbound aldolase subunit. RMS deviations of atomic coordinates generated in each frame were <1.5 Å (based on C_α atomic positions) in the simulations when compared with respect to the initial crystallographic model and were <1.6 Å when comparing coordinates generated in identical frames between each of the simulations. These deviations are comparable with those obtained in simulations described in the literature (*45, 46*) and warranted use of a single subunit in the molecular modeling of aldolase−HNA-P complexes.

(A) Noncovalent Aldolase−HNA-P Complex. Energy minimization yielded a stable HNA-P Michaelis complex, free of close contacts, filling the entire active site cleft and necessitated the expulsion of several water molecules in the crystal structure due to steric conflict. Simulation of 5 ns duration for phenol and phenate species showed the phosphate moiety to be persistently bound in its binding site. The oxyanion was anchored in its position by electrostatic interactions with Arg-303 and Lys-229 and by hydrogen bonds to backbone amides of Ser-271, Gly-272, Gly-302, and Arg-303 as well as with the Ser-271 side chain. Table 4 summarizes calculated distances and standard deviations of all oxyanion contacts made with active site residues.

In contrast, the orientations sampled for the naphthaldehyde moiety of HNA-P differed between the simulations for the phenol and phenate species. Torsional rotations in ω_1 and $\omega_2$resulted in the O_1 oxygen substituent for the naphthaldehyde moiety of HNA-P pointing in opposing directions that were approximately perpendicular with respect to its starting position within 200 ps of simulation. The ensemble of conformations sampled by the naphthaldehyde moiety resulted in few persistent hydrogen-bonding or electrostatic contacts with active site residues for the phenol species. Guanidinium moieties of Arg-42 and Arg-303, situated on opposite side of the naphthaldehyde moiety, participated in stacking interactions. The O_1hydroxyl interacted with either Ser-35, Arg-42, or Arg-148 side chains intermittently. The distance between the attacking Lys-107 Nz and aldehyde C_{11} carbon averaged over the entire simulation was 5.8 (±1.3) Å. In only 0.27% of all frames were the configurations of Lys-107 and aldehyde competent for attack, and the averaged distance and angle of attack were 3.48 (±0.06) Å and 36° (±8°), respectively. In these frames, the aldehyde O_{11} oxygen made a hydrogen bond with Ser-35 NH, 2.92 (±0.16) Å. The electrostatic interaction between the positive partial charges of the Lys-107 Nz hydrogens and negative partial charge of the aldehyde O_{11} oxygen influences the angle of attack and causes it to deviate from a value of 0° that would correspond to direct perpendicular attack of the Lys-107 Nz atom on the hybridization plane containing the aldehyde C_{11} carbon, an example of which is shown in Figure.

A more stable configuration was observed for the phenate species due to additional persistent contacts made with active site residues and resulted in a shorter averaged distance between the attacking Lys-107 Nz and aldehyde C_{11} carbon of 5.0 (±1.1) Å. Stabilizing electrostatic interactions involved the phenate O_1 oxygen with Lys-146 and Arg-148 side chains, averaged distances of 3.03 (±0.3) Å and 2.95 (±0.3) Å, respectively. In 80% of the frames, the aldehyde O_{11} oxygen interacted with an active site residue that was either Glu-34 NH, Ser-35 NH, Ser-35 side chain, or Ser-38 side chain. Geometries consistent with potential attack that had an angle of attack <20° were observed in 0.14% of the frames, <30° in 0.73%, and <40° in 1.7% of the frames. However, in no instance was the aldehyde O_{11} oxygen within close contact of a residue capable of acting as a general

acid in either species. Hydrogen bonding between Lys-107 and Lys-146 was not observed in geometries considered competent for attack. Distances between Lys-107 and Lys-146 were 6.5 (±0.1) Å and 7.3 (±1.1) Å for phenol and phenate species, respectively. Potential energies profiles for each species showed no trend with time and were statistically identical as the average energy difference between species was less than their respective standard deviations (~620 kJ/mol).

(B) Covalent Aldolase−HNA-P Complex. Formation of the covalent adduct necessitated a displacement of the HNA-P molecule toward Lys-107 for bond formation with the aldehyde and resulted in the HNA-P oxyanion no longer interacting with the DHAP P_1-phosphate binding locus as was used to model the HNA-P Michealis complex. Simulations of 5 ns duration for both phenol and phenate species yielded essentially similar configurations for the HNA-P moiety in the active site. For each species, the HNA-P adduct adopted a similar ensemble of conformations that was roughly perpendicular to the starting position attained during the equilibration and remained in this orientation for the duration of the simulation. The conformations adopted by HNA-P throughout the simulations differed somewhat from those of the noncovalent adduct in the active site. The HNA-P phosphate underwent a torsional rotation in ω_1 and ω_2 such that the oxyanion was consistently displaced by ~7 Å toward the active site surface with respect to the noncovalent adduct (shown in Figure 7). Simultaneously, the HNA-P naphthaldehyde moiety underwent a rotational displacement within the active site cleft, pivoting by ~30° about the O_1 position for covalent bond formation with Lys-107 and leaving the naphthaldehyde moiety more solvent exposed in the covalent adduct.

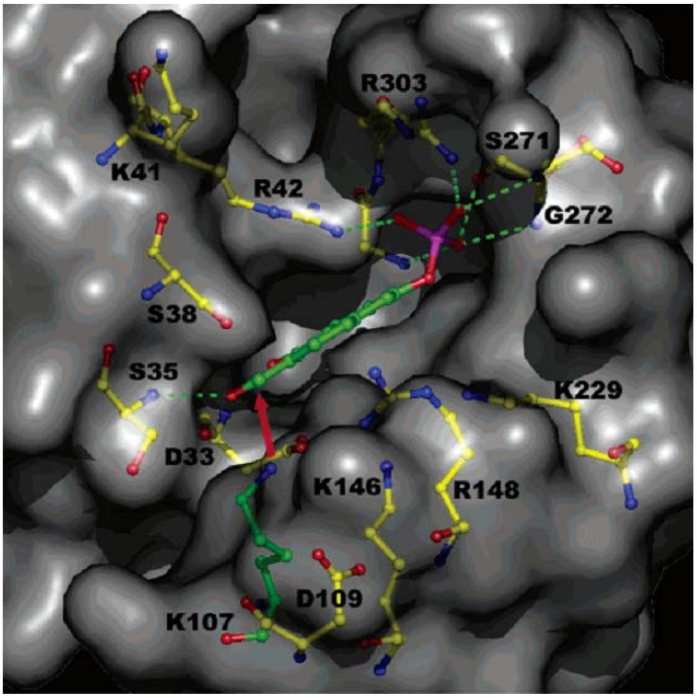

Figure 3-7. Frame generated by the simulation showing the Michaelis complex corresponding to the phenol species of HNA-P docked in the rabbit muscle aldolase active site cleft in a conformation competent for covalent bond formation.

The solvent-accessible surface of the protein is depicted in gray. Dotted lines represent hydrogen bonds or electrostatic interactions, and active site residues proximal to HNA-P are labeled. The arrow shows the presumed trajectory corresponding to nucleophilic attack on the electrophilic C11 aldehyde carbon by Lys-107 Nz, the atom which is within close contact of the C11 carbon. The phosphate oxyanion of the HNA-P inhibitor is bound at the C1-phosphate binding locus through hydrogen-bonding interactions with Lys-229, Ser-271, and Arg-303 as well as backbone amides that are maintained throughout the simulations. Guanidinium moieties of Arg-42 and Arg-303, situated on the opposite side of the naphthaldehyde moiety, make stacking interactions. The aldehyde O11 oxygen makes a hydrogen bond with Ser-35 NH in all frames competent for nucleophilic attack. Lys-146 is protonated and, although capable, does not hydrogen bond to the Lys-107 Nz nucleophile. The drawing was made with the program PyMOL [48].

To investigate the slow hydrolysis of the Schiff base, frames were analyzed as a function of water molecule accessibility with respect to the Schiff base formed and in particular hydrogen bonding by water molecules to Lys-107 Nz. A representative frame illustrated in Figure 8 shows the phenol species of the covalent adduct.

In both simulations, the phosphate oxyanion strongly interacted with Ser-38 and Lys-41, making hydrogen bonds in virtually all frames with averaged distances of 2.7 (±0.1) Å and 3.2 (±0.1) Å, respectively, for the phenol species and 2.7 (±0.5) Å and 3.0 (±0.2) Å for the phenate species. Hydrogen bonding by the oxyanion to Arg-303 was observed only in a minority of frames (29.3% for the phenol and 42.7% for the phenate) and occasionally to Arg-42 (18.9% for the phenol and 0.7% for the phenate) and never simultaneously to both residues. In the case of the phenate species, interaction of Asp-33 with O_1 is repulsive compared to the phenol species, shown in Figure 8, where the interaction is attractive [averaged distance 2.8 (±0.2) Å]), and resulted in a slight displacement of the naphthalene ring to minimize O_1 interaction with Asp-33. Potential energy profiles for both species showed no trend with time and were considered statistically identical, the average energy difference between the two species being less than their respective standard deviations (610 kJ/mol). In both instances, the covalent adduct occluded the active site residues Lys-146 and Lys-229 throughout the entire simulation.

(C) Water Molecule Interaction. In the majority of the frames (64% for phenol and 62% for phenate species), no water molecules bound to Lys-107 Nz compared to a control surface residue Lys-321, whose Nz atom bound water molecules in all frames, indicating reduced solvent accessibility for Lys-107 Nz. Hydrogen bonding of water molecules with Lys-107 Nz, as shown in Figure 8, was observed in only a minority of the frames. Water molecule (W_2) hydrogen bonding to Asp-33, Asp-109, Lys-146, and occasionally Arg-148 as well as Lys-107 was observed in 23% of the frames for the phenol simulation and 27% of the frames in the case of the phenate. Hydrogen bonding to Lys-107 Nz by the W_1 water molecule also shown in Figure 8 was observed in 13% (phenol) and 11% (phenate) of the frames. Variation in the position of the W_1 binding site was qualitatively considerably

larger than for W_2, which was essentially constant with respect to its interaction partners. Contrary to the W_2 molecule, the W_1 did not participate in any hydrogen bonds with amino acid side chains capable of acting as a general base. In only a minority of the frames (3% for phenol and 6% for phenate species) did two water molecules interact with Lys-107, as shown in Figure 8.

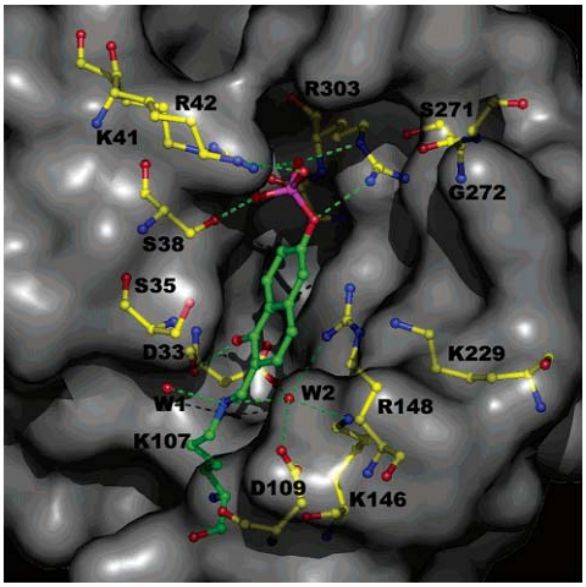

Figure 3-8. Snapshot from the dynamical simulation of the phenol species of the HNA-P covalent adduct formed with Lys-107 Nz of rabbit muscle aldolase.

The solvent-accessible surface of the protein is depicted in gray. Dotted lines represent hydrogen bonds or electrostatic interactions, and active site residues are labeled. The orientation was chosen to maximize positional overlap of Cα atom positions of active site residues common to both figures. In all simulations, the phosphate oxyanion no longer binds the C1-phosphate binding locus rather interacting with Ser-38 and Lys-41 and sometimes with Arg-303. Hydroxyl O1 interacts with the Asp-33 backbone in the phenol species. In the majority of frames for phenol and phenate species, water molecules do not hydrogen bond to Lys-107 Nz (not shown). In simulations with phenol and phenate species where water molecules hydrogen bond Lys-107 Nz via the binding locus designated W1, these water molecules do not interact with any amino acid capable of acting as a general base. For water molecules hydrogen bonding to Lys-107 Nz via the binding locus designated W2, activation is possible by either Asp-33 or Asp-109; however, electrostatic attraction of the resulting hydroxyl ion with Lys-146 and/or Arg-148, which are within hydrogen-bonding distance of W2, makes Schiff base hydrolysis unfavorable.

3.1.5 Discussion

3.1.5.1 NA-P2−Aldolase Interaction.

Aromatic bisphosphorylated substrate analogues of fructose-1,6-bisphosphate aldolases strongly interact with the enzyme active site and represent compounds of considerable interest. The naphthalenic derivative NA-P_2 (K_i = 0.28 μM) represents one of the most potent competitive inhibitors for rabbit muscle aldolase-catalyzed reaction. Similar trends were noted using inhibitors of rat muscle aldolase also possessing aromatic moieties (*38*). The rigid structure imposed by the aromatic rings compared to a compound, which is not conformationally restricted such as hexanediol 1,6-bisphosphate (K_i = 25 μM) (*47*), would suggest that a smaller configurational entropy loss upon active site binding by the rigid aromatic compound, compared to the conformationally mobile analogue, may contribute for the observed affinity differences in aldolase−inhibitor complex formation (*48, 49*).

Aldolase has two distinct binding sites for inorganic phosphate (*27*). From protection experiments, the higher affinity site corresponds to the C_1-phosphate binding site of Fru(1,6)P_2 while the second site, of lower binding energy, binds the C_6-phosphate and involves the participation of the Lys-107 residue to the binding (*25*). The fact that the mutation of Lys-107 to Met increases both K_m of the substrate Fru(1,6)P_2 and K_i of the inhibitor NA-P_2 argues in favor of the same binding site for the phosphate moiety of each compound and also the involvement of this lysine residue to binding. In the structure of rabbit muscle aldolase soaked with substrate, Lys-107 indeed interacts with the C_6-phosphate of Fru(1,6)P_2 (unpublished data). The above considerations are consistent with an inhibition scheme in class I aldolases where substitution of one of the phosphate groups of NA-P_2 by an aldehyde group results in Schiff base formation between Lys-107 and HNA-P. Enzyme inactivation by PLP through Schiff base formation at Lys-107 further corroborates our approach (*25*).

3.1.5.2 Aldolase Inhibition by HNA-P.

Incubation of aldolase with HNA-P leads to a time-dependent inhibition resulting in complete activity loss that is only very slowly reversed. The inactivation kinetics correspond to slow-binding inhibition consisting of a fast preequilibrium association followed by a slow and reversible rearrangement at the active site that results in enzymatic inactivation (*21, 22*). Although the structural change in going from NA-P_2 to HNA-P provoked a decrease in active site affinity (K_i = 125 μM for the fast process), HNA-P represents to date the most potent slow-binding inhibitor for a class I aldolase having an overall inhibition constantK_i* value of ~24 nM. This inhibition can be made irreversible upon treatment of HNA-P−enzyme complex with sodium borohydride, in agreement with an inhibition mechanism involving Schiff base formation with an active site lysine residue. Accessibility of the BH_4^- ion by the Lys-107 Nz atom is consistent with results from the dynamical simulations where the Lys-107 Nz atom is accessible to a water molecule, W_1.

3.1.5.3 Aldolase−HNA-P Interaction.

The reactivity of HNA-P toward aldolase was characterized and quantified by UV/visible difference spectroscopy (*15*) using the HNA-P reaction with aminocaproic acid as a reference system. The kinetics of aldolase−HNA-P complex formation differs from that of the model system where in the presence of aldolase two distinct first-order kinetic processes were observed: a rapid phase consistent with a stoichiometry of one HNA-P reacted with a single aldolase subunit and a slower reaction that results in a stoichiometry of ~2 molecules of HNA-P bound per aldolase subunit. Analysis of ESI/MS data is entirely consistent with the presence of these two adducts. The faster process, associated with the larger differential absorbance change, results in enzyme inhibition, and incubation with hexitol-P_2, which protects against inhibition, abolishes the rapid phase. Kinetic parameters derived from the faster rate process describing the Schiff base formation are in good agreement with those obtained from enzymatic inhibition studies, and both Schiff base formation and inhibition are maximal when approximately one molecule of HNA-P has been covalently bound per aldolase subunit.

There are three lysine residues, 107, 146, and 229, located in the active site of aldolase that each could give rise to Schiff base formation. Site-directed mutagenesis of these amino acid residues to neutral isosteric amino acids, K107M, K146M and K229M, yielded mutant proteins that displayed not only diminished catalytic activity but also modified Schiff base formation kinetics. The most significant change in HNA-P interaction with aldolase arose from the mutation K107M where the fast phase corresponding to Schiff base formation was suppressed and enzyme inactivation did not occur. The identification of Lys-107 as the residue responsible for the Schiff base formation is consistent with the results obtained from the other mutants. The UV/visible difference spectra from the K229M mutant does not differ from spectra observed for the wild-type enzyme, thus eliminating Lys-229 as a candidate amino acid implicated in enzyme inhibition. Although inhibition kinetics for the point mutant K146M were reduced from the wild-type enzyme in terms of rate of Schiff base formation, the point mutation did not modify the ability of the mutant to form this complex. From the rabbit muscle aldolase crystal structure (*5*), Lys-146 is proximal to Lys-107 such that the decrease in Schiff base formation is consistent with a role by Lys-146 in the inhibition mechanism pathway.

3.1.5.4 Slow Inactivation.

Enzymatic inactivation is 4000-fold more efficient compared to model compound formation. The HNA-P dissociation constant is micromolar, which is similar in value to dissociation constants of other monophosphorylated inhibitor compounds (*15*), suggesting that the rate of covalent bond formation may be at the origin for the slow-binding reaction. Schiff base formation with HNA-P requires that Lys-107 be present in sufficient concentration as a nucleophile. Electrostatic charge destabilization due to the presence of an adjacent positive charge has been reported as a mechanism for pK_a reduction of a lysine residue (*44, 50*). In rabbit muscle aldolase, although Lys-107 is adjacent to Lys-146, each participate in hydrogen-bonding interactions with water molecules that would mitigate their electrostatic repulsion and reduce charge destabilization. Hence, the observed pK_a reduction for Lys-107 of only ~2 units, and Lys-146 neutralization by mutation to Met that

diminishes only by 9-fold the rate of inactivation is consistent with the Lys-146 charge having a smaller destabilizing effect on the Lys-107 pK_a.

Other mechanisms of nucleophilic activation of Lys-107 cannot be ruled out as contributing factors. A pK_a of ~5 for the surface residue Asp-109 roughly matches that of Lys-107 (pK_a ~8) and would suggest that electrostatic interaction between Lys-107 and Asp-109 could favor proton transfer in a general base catalysis mechanism, thereby rendering Lys-107 nucleophilic and which would simultaneously diminish Asp-109 repulsion with the HNA-P aldehyde oxygen. The small overall reductions in k_{app}, shown in Table 3, for both D33N and D33S mutants tend to exclude Asp-33 as being implicated in activating Lys-107 for nucleophilic attack by a similar mechanism. At pH 7.6, concentration of the Lys-107 nucleophile appears to be sufficient for Schiff base formation not to be rate determining and thus would not explain slow inactivation.

The molecular dynamics simulations indicate a low concentration of HNA-P species competent for Schiff base formation with aldolase. The observed slow rate of aldolase inactivation is consistent with very infrequent occurrence of reaction geometries for both phenol and phenate species. Furthermore, carbinolamine formation depends on a general acid to facilitate protonation of the O_{11} oxygen, which in the phenol species can be performed via intramolecular proton transfer from the ortho C_1 hydroxyl, oriented cis to the reactive aldehyde. By contrast, no residue could be identified in the case of the phenate species that was within close contact distance and capable of general acid catalysis, making HNA-P inactivation due to the phenate species mechanistically unlikely. The additional stabilizing interactions made by the phenate species would then competitively inhibit binding of the phenol species and further decrease the rate of inactivation. A reduced rate of inactivation due to increased concentration of the incompetent phenate species at higher pH is not inconsistent with the slower inactivation observed in rabbit muscle aldolase for an *o*-hydroxybenzaldehyde phosphate analogue at alkaline pH (*16*).

The simulations clearly indicate that formation of the covalent bond between Lys-107 and HNA-P aldehyde requires a conformational rearrangement in the active site by

HNA-P. The conformational rearrangement involves breaking all six hydrogen bonds and one electrostatic interaction with the phosphate oxyanion in the noncovalent adduct (see Table 4), thereby creating a significant kinetic barrier to covalent bond formation. Formation in the covalent complex of fewer interactions by the phosphate oxyanion, one hydrogen bond with Ser-38 and a single electrostatic interaction with Lys-41, results in a contribution to the overall reaction that is energetically unfavorable. The increased solvent exposure by the aromatic naphthaldehyde moiety would further tend to increase the conformational barrier leading to covalent adduct formation.

Electrostatic destabilization, although advantageous as a mechanism for increasing the concentration of the attacking lysine nucleophile, would promote slow inactivation by heightening kinetic barriers in formation of protonated intermediates in the Schiff base reaction (*51*). Aldolase inactivation at pH 7.6 by HNA-P as well as by PLP through a Schiff base mechanism involves obligate formation of a protonated ketimine at Lys-107. The presence of an ionized Lys-146 amine vicinal to Lys-107 would tend to destabilize a protonated chemical species at Lys-107, increase the kinetic barrier to protonated ketamine formation, and consequently diminish the rate of Schiff base formation. Such a mechanism, although feasible, may be of less importance in the case of aldolase inactivation by HNA-P as Lys-146 neutralization only modestly decreases the inactivation rate and only a slight reduction in Lys-107 pK_a is observed, presumably because the lysine residues do not engage in hydrogen bond formation in the presence of HNA-P as seen in the simulations. The slow inactivation rate thus stems from a number of factors that cumulatively make covalent bond formation kinetically unfavorable, including competitive inhibition by the phenate species, infrequent occurrence of competent reaction geometries, a substantial conformational barrier to covalent adduct formation, and, to a lesser extent, destabilization of the protonated ketimine in the adduct.

3.1.5.5 Tight-Binding Reversible Inhibition.

Very slow dissociation of the covalent complex implies significant complex stability, due to inhibition of Schiff base hydrolysis that renders covalent bond formation

quasi-irreversible. In the majority of the configurations generated during the simulations, Schiff base hydrolysis would not be possible because no water molecules associated with the Lys-107 Nz atom in the covalent adduct. In those frames where water molecules were found within hydrogen-bonding distance of Lys-107, as shown in Figure 8, hydrolysis of the Schiff base is not mechanistically feasible. Either activation of the water molecule is not possible due to the absence of a conjugate base, as in the case of W_1, or, if activated, as in the case of W_2, the resultant electrostatic attraction by the OH^- ion with either protonated Lys-146 or Arg-148 or both would substantially reduce the frequency of attack on the Lys-107 ketimine. Furthermore, activation of W_2 would be even more unfavorable in the case of the phenate species due to the negative charge on O_1.

An alternate mode of attachment by the HNA-P phosphate at the substrate C_6-phosphate binding locus cannot be excluded and could give rise to the observed side reaction. Lys-41 and Lys-152 are surface residues that are within an ~15 Å radius of Lys-107, and if the HNA-P phosphate binds to the substrate C_6-phosphate binding locus, either residue could participate in Schiff base formation with the HNA-P aldehyde. The higher pK_a of these lysine residues and weaker affinity of the C_6-phosphate binding site are consistent with the observed slow secondary reaction that is not maximal at the inhibitor concentrations used to inactivate the enzyme. Disruption of the C_6-phosphate binding site by the point mutations D33N and D33S is not inconsistent with a reduced affinity of the secondary binding site and rendering the secondary side reaction unobservable at the inhibitor concentrations employed in the study.

3.1.5.6 Implications for Drug Design.

The interaction of HNA-P with aldolase provides insights for the design of a new class of inhibitors for aldolase-catalyzed reactions. On the basis of our study, functional groups, including phosphate, aldehyde, and naphthol moieties, of the HNA-P molecule are important for tight binding and represent a blueprint for future inhibitor design. Phosphorylated inhibitors, whose phosphate moieties are able to recognize the aldolase C_1-phosphate binding site, represent a desirable design feature in a potential inhibition

strategy. Interaction with the substrate C_1-phosphate binding locus in the native enzyme involves not only hydrogen bonding with Ser-271, which is conserved in all class I aldolases, but also hydrogen bonding with backbone atoms of other active site residues making for a phosphate binding site that could be exploited in all class I isoenzymes. However, the presence of the phosphate group remains problematic in drug design because of the poor ability by phosphate monoesters to penetrate cell membranes. These impediments could be circumvented by synthesizing a prodrug that would mask the phosphate charges using an protecting group that can be enzymatically converted into the active phosphate monoester form once the prodrug has been internalized (*52, 53*).

3.1.6 Acknowledgment

We thank Christine Munger for skillful assistance in providing purified recombinant enzymes of both native and mutated aldolase.

3.1.7 References

1. Meyerhof, O., Lohman, K., and Shuster, Ph. (1936) Uder die Aldolase, ein Kohlenstoff-verknupfendes Ferment, Biochem. Z. 286, 301−331.

2. Horecker, B. L., Tsolas, O., and Lai, C. Y. (1972) Enzymes, 3rd Ed. 7, 213−258.

3. Rutter, W. J. (1964) Evolution of aldolase, Fed. Proc., Fed. Am. Soc. Exp. Biol. 23, 1248−1257.

4. Rose, I. A., Warms, J. V., and Kuo, D. J. (1987) Concentration and partitioning of intermediates in the fructose bisphosphate aldolase reaction. Comparison of the muscle and liver enzymes, J. Biol. Chem. 262, 692−701.

5. Sygusch, J., Beaudry, D., and Allaire, M. (1987) Molecular architecture of rabbit skeletal muscle aldolase at 2.7-Å resolution, Proc. Natl. Acad. Sci. U.S.A. 84, 7846−7850.

6. Blom, N., and Sygusch, J. (1997) Product binding and role of the C-terminal region in class I d-fructose 1,6-bisphosphate aldolase, Nat. Struct. Biol. 4, 36−39.

7. Gamblin, S. J., Davies, G. J., Grimes, J. M., Jackson, R. M., Littlechild, J. A., and Watson, H. C. (1991) Activity and specificity of human aldolases, J. Mol. Biol. 219, 573−576.

8. Dalby, A. R., Tolan, D. R., and Littlechild, J. A. (2001) The structure of human liver fructose-1,6-bisphosphate aldolase, Acta Crystallogr., Sect. D: Biol. Crystallogr. 57, 1526−1533.

9. Hester, G., Brenner-Holzach, O., Rossi, F. A., Struck-Donatz, M., Winterhalter, K. H., Smith, J. D. G., and Piontek, K. (1991) The crystal structure of fructose-1,6-bisphosphate aldolase from Drosophila melanogaster at 2.5 Å resolution, FEBS Lett. 292, 237−242.

10. Kim, H., Certa, U., Dobeli, H., Jakob, P., and Hol, W. G. (1998) Crystal structure of fructose-1,6-bisphosphate aldolase from the human malaria parasite Plasmodium falciparum, Biochemistry 37, 4388−4396.

11. Chudzik, D. M., Michels, P. A., de Walque, S., and Hol, W. G. (2000) Structures of type 2 peroxisomal targeting signals in two trypanosomatid aldolases, J. Mol. Biol. 300, 697−707.

12. Gefflaut, T., Blonski, C., Périé, J., and Willson, M. (1995) Class I aldolases: substrate specificity, mechanism, inhibitors and structural aspects, Prog. Biophys. Mol. Biol. 63, 301−340.

13. Blonski, C., Gefflaut, T., and Périé, J. (1995) Effects of chirality and substituents at carbon 3 in dihydroxyacetone-phosphate analogues on their binding to rabbit muscle aldolase, Bioorg. Med. Chem. 3, 1247−1253.

14. Gefflaut, T., Blonski, C., and Périé, J. (1996) Slow reversible inhibitions of rabbit muscle aldolase with substrate analogues: synthesis, enzymatic kinetics and UV difference spectroscopy studies, Bioorg. Med. Chem. 4, 2043−2054.

15. Blonski, C., De Moissac, D., Périé, J., and Sygusch, J. (1997) Inhibition of rabbit muscle aldolase by phosphorylated aromatic compounds, Biochem. J. 323, 71−77.

16. Blonski, C., Gefflaut, T., and Périé, J. (1998) Kinetic and spectroscopic study of slow-binding inhibition processes in aldolase, J. Phys. Org. Chem. 11, 793−802.

17. Page, P., Blonski, C., and Périé, J. (1999) Origin of the slow-binding inhibition of aldolase by d-glycero-tetrulose 1-phosphate (d-erythrulose 1-phosphate) from the comparison with the isosteric phosphonate analogue, Eur. J. Org. Chem. 1999, 28533−2857.

18. Opperdoes, F. R. (1987) Compartmentation of carbohydrate metabolism in trypanosomes, Annu. Rev. Microbiol. 41, 127−151.

19. Verlinde, C. L. M. J., Hannaert, V., Blonski, C., Willson, M., Périé, J., Fothergill-Gilmore, L. A., Opperdoes, F. R., Gelb, M. H., Hol, W. G. J., and Michels, P. A. M. (2001) Glycolysis as a target for the design of new anti-trypanosome drugs, Drug Resist. Updates 4, 50−65.

20. Schartz, D., and Beitner, R. (2000) Detachment of the glycolytic enzymes, phosphofructokinase and aldolase, from cytoskeleton of melanoma cells, induced by local anesthetics, Mol. Genet. Metab. 69, 159−164.

21. Morrison, J. F., and Walsh, C. T. (1988) The behavior and significance of slow-binding enzyme inhibitors, Adv. Enzymol. Relat. Areas Mol. Biol. 61, 201−300.

22. Schloss, J. V. (1988) Significance of slow-binding enzyme inhibition and its relationship to reaction-intermediate analogues, Acc. Chem. Res. 21, 348−353.

23. Hartman, F. C., and Brown, J. P. (1976) Affinity labeling of a previously undetected essential lysyl residue in class I fructose bisphosphate aldolase, J. Biol. Chem. 251, 3057−3062.

24. Gupta, S., Hollenstein, R., Kochlar, S., and Christen, P. (1993) Paracatalytic self-inactivation of fructose-1,6-bisphosphate aldolase. Structure of the crosslink formed at the active site, Eur. J. Biochem. 214, 515−519.

25. Anai, M., Lai, C. Y., and Horecker, B. L. (1973) The pyridoxal phosphate-binding site of rabbit muscle aldolase, Arch. Biochem. Biophys. 156, 712−719.

26. Morris, A. J., and Tolan, D. R. (1994) Lysine-146 of rabbit muscle aldolase is essential for cleavage and condensation of the C3−C4 bond of fructose 1,6-bis(phosphate), Biochemistry 33, 12291−12297.

27. Ginsburg, A., and Mehler, A. H. (1966) Specific anion binding to fructose diphosphate aldolase from rabbit muscle, Biochemistry 5, 2623−2634.

28. Racker, E. (1947) Spectrophotometric measurement of hexokinase and phosphohexokinase activity, J. Biol. Chem. 246, 7041−7050.

29. Baranowski, T., and Niederland, T. R. J. (1949) Aldolase activity of myogen A, J. Biol. Chem. 180, 543−551.

30. Kawahara, K., and Tanford, C. (1966) The number of polypeptide chains in rabbit muscle aldolase, Biochemistry 5, 1578.

31. Segel, I. H. (1975) Enzyme Kinetics: Behavior and Analysis of Steady-State and Rapid Equilibrium Enzyme Systems, Willey-Interscience, New York.

32. Meloche, H. P. (1967) Bromopyruvate inactivation of 2-keto-3-deoxy-6-phosphogluconic aldolase. I. Kinetic evidence for active site specificity, Biochemistry 6, 2273−2280.

33. Berendsen, H. J. C., van der Spoel, D., and van Drunen, R. (1995) GROMACS: A message-passing parallel molecular dynamics implementation, Phys. Commun. 91, 43−56.

34. Hess, B., Bekker, H., Berendsen, H. J. C., and Fraaije, J. G. E. M. (1997) LINCS: A linear constraint solver for molecular simulations, Comput. Chem. 18, 1463−1472.

35. Essman, U., Perela, L., Berkowitz, M. L., Darden, T., Lee, H., and Pedersen, L. G. (1995) A smooth particle mesh Ewald method, Chem. Phys. 103, 8577−8592.

36. Morris, A. J., and Tolan, D. R. (1993) Site-directed mutagenesis identifies aspartate 33 as a previously unidentified critical residue in the catalytic mechanism of rabbit aldolase A, J. Biol. Chem. 268, 1095−1100.

37. Berthiaume, L., Tolan, D. R., and Sygusch, J. (1993) Differential usage of the carboxyl-terminal region among aldolase isozymes, J. Biol. Chem. 268, 10826−10835.

38. Suh, B., and Barker, R. (1971) Fluorescence studies of the binding of alkyl and aryl phosphates to rat muscle aldolase, J. Biol. Chem. 246, 7041−7050.

39. Metzler, C. M., Cahill, A., and Metzler, D. E. (1980) Equilibriums and absorption spectra of Schiff bases, J. Am. Chem. Soc. 102, 6075−6085.

40. Johnson, R. J., and Metzler, D. E. (1970) Analyzing spectra of vitamin B6 derivatives, Methods Enzymol. 18A, 433−471.

41. Heinert, D., and Martell, A. E. (1963) Pyridoxine and pyridoxal analogs. VI. Electronic absorption spectra of Schiff bases, J. Am. Chem. Soc. 85, 183−185.

42. Burr, M., and Koshland, D. E., Jr. (1964) Use of “reporter groups” in structure−function studies of proteins, Proc. Natl. Acad. Sci. U.S.A. 52, 1017.

43. Williams, V. R., and Neilands, J. B. (1954) Apparent ionization constants, spectral properties and metal chelation of the cotransaminases and related compounds, Arch. Biochem. Biophys. 53, 56−70.

44. Highbarger, L. A., Gerlt, J. A., and Kenyon, G. L. (1996) Mechanism of the reaction catalyzed by acetoacetate decarboxylase. Importance of lysine 116 in determining the pKa of active-site lysine 115, Biochemistry 35, 41−46.

45. Baaden, M., Meier, C., and Sansom, M. S. (2003) A molecular dynamics investigation of mono and dimeric states of the outer membrane enzyme OMPLA, J. Mol. Biol. 331, 177−189.

46. Sulpizi, M., Rothlisberger, U., and Carloni, P. (2003) Molecular dynamics studies of caspase-3, Biophys J. 84, 2207−2215.

47. Harman, F. C., and Barker, R. (1965) An exploration of the active site of aldolase using structural analogs of fructose diphosphate, Biochemistry 4, 1068−1075.

48. Dudley, H. W., Searle, M. S., Mackay, J. P., Gerhard, U., and Maplestone, R. (1993) Toward an estimation of binding constants in aqueous solution: Studies of associations of vancomycin group antibiotics, Proc. Natl. Acad. Sci. U.S.A. 90, 1172−1178.

49. Schirmer, R. H., Müller, J. G., and Krauth-Siegel, R. L. (1995) Disulfide-reductase inhibitors as chemotherapeutic agents: The design of drugs for trypanosomiasis and malaria, Angew. Chem., Int. Ed. Engl. 34, 141−154.

50. Schmidt, D. E., Jr., and Westheimer, F. H. (1971) pK of the lysine amino group at the active site of acetoacetate decarboxylase, Biochemistry 10, 1249−1253.

51. Maurady, A., Zdanov, A., de Moissac, D., Beaudry, D., and Sygusch, J. (2002) A conserved glutamate residue exhibits multifunctional catalytic roles in d-fructose-1,6-bisphosphate aldolases, J. Biol. Chem. 277, 9474−9483.

52. Périgaud, C., Gosselin, G., Lefebvre, I., Girardet, J.-L., Benzaria, S., Barber, I., and Imbach, J.-L. (1993) Synthesis and antitumor activity of a new class of pyrazolo[4,3-e]pyrrolo[1,2-a][1,4]diazepinone analogs of pyrrolo[1,4]benzodiazepines, Bioorg. Med. Chem. Lett. 3, 2521−2526.

53. Farquhar, D., Khan, S., Srivasta, D. N., and Saunder, P. P. (1994) Synthesis and antitumor evaluation of bis[(pivaloyloxy)methyl] 2‘-deoxy-5-fluorouridine 5‘-monophosphate (FdUMP): a strategy to introduce nucleotides into cells, J. Med. Chem. 37, 3902−3909.

Abbreviations: DHAP, dihydroxyacetone phosphate; DHNA, 1,6-dihydroxy-2-naphthaldehyde; ESI, electrospray ionization; FAB, fast atom bombardment; Fru(1,6)P_2, fructose 1,6-bisphosphate; hexitol-P_2, hexitol 1,6-bisphosphate; GDH, glycerol-3-phosphate dehydrogenase; HNA-P, 1-hydroxy-2-naphthaldehyde 6-phosphate; MS, mass spectrometry; NA-P_2, naphthyl 2,6-bisphosphate; PDB, Protein Data Bank; PLP, pyridoxal

5-phosphate; PMP, pyridoxamine 5-phosphate; TEA, triethanolamine; TIM, triose-phosphate isomerase; Tris, tris(hydroxymethyl)aminomethane.

Atomic coordinates for the DHAP native complex and mutants K107M and K229M are available from the Research Collaboratory for Structural Bioinformatics Protein Databank (http://www.rcsb.org/pdb/) deposited under accession codes 1ADO, 1EWD, and 1EWE, respectively.

3.2 Selective Irreversible Inhibition of Fructose-1,6-Bisphosphate Aldolase from *Trypanosoma brucei*

Chantal Dax, Francis Duffieux, Nicolas Chabot, Mathieu Coincon, Jurgen Sygusch, Paul A. M. Michels, and Casimir Blonski

LSPCMIB, UMR-CNRS 5068, Groupe de Chimie Organique Biologique, Université Paul Sabatier, Bat. IIR1, 118 Route de Narbonne 31062, Toulouse Cedex 9, France, Department of Biochemistry, University of Montreal, Pavillon Roger Gaudry, CP 6128, Station Centre Ville, Montréal, QC, Canada, H3C 3J7, and Research Unit for Tropical Diseases, Christian de Duve Institute of Cellular Pathology, and Laboratory of Biochemistry, Université Catholique de Louvain, ICP-TROP 74-39, Avenue Hippocrate 74, B-1200 Brussels, Belgium

J. Med. Chem., **2006**, *49* (5), pp 1499–1502

3.2.1 Abstract

An irreversible competitive inhibitor hydroxynaphthaldehyde phosphate was synthesized that is highly selective against the glycolytic enzyme fructose 1,6-bisphosphate aldolase from*Trypanosoma brucei* (causative agent of sleeping sickness). Inhibition involves Schiff base formation by the inhibitor aldehyde with Lys116 followed by reaction of the resultant Schiff base with a second residue. Molecular simulations indicate significantly greater molecular geometries conducive for nucleophilic attack in *T. brucei* aldolase than the mammalian isozyme and suggest Ser48 as the Schiff base modifying residue.

3.2.2 Introduction

Among the many diseases that afflict humankindthose caused by pro, tozoan parasites occupy an important place because of the large number of victims, the lack of efficient therapy, and their continuing spread. The World Health Organization reported 55 000 deaths in 2002 out of 500 000 cases for sleeping sickness in sub-Saharan Africa, caused by infection with *Trypanosoma brucei*.[1] Trypanosomiasis also significantly affects human nutrition through their impact on food animals by killing 3 million cattle per year. A number of drugs have been used in the treatment of trypanosomal infections (Figure 9).

Suramin, pentamidine, and some arsenical drugs often induce severe toxic side effects, and resistance against these drugs is spreading.[2] The drug most recently introduced (early 1990s) against sleeping sickness is (*R*,*S*)-2-difluoromethylornithine (DFMO, initially developed as an anticancer drug[3]). However, this drug is only active against *Trypanosoma brucei gambiense*(prevalent in west and central Africa) whereas *T. b. rhodesiense* (prevalent in east and southern Africa) is insensitive to this compound.[4] An additional problem is that large amounts of DFMO are required to treat a patient.[5] The need for broad spectrum, inexpensive, highly efficient, and nontoxic drugs therefore remains a priority.

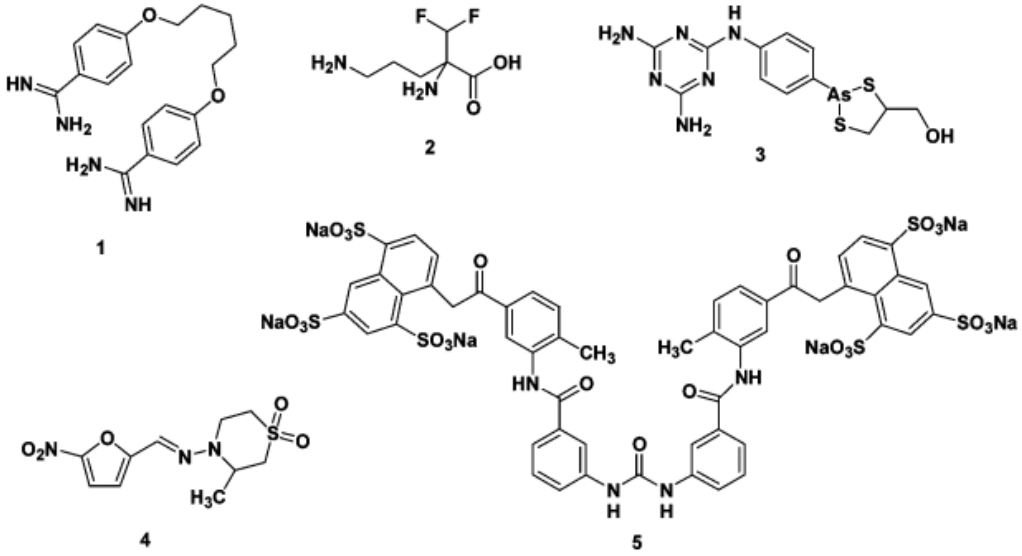

Figure 3-9. Drugs currently in use to treat trypanosomiasis

1, pentamidine; 2, difluoromethylornithine; 3, melarsoprol; 4, nifurtimox; 5, suramin, sodium salt.

Among the potential metabolic targets considered for the development of new drugs, glycolysis appears as a highly promising pathway, since it is the only ATP-generating process in the bloodstream form of *T. brucei*.[6] It has been shown that trypanosomal glycolysis contains several structural features distinct from the corresponding process in mammalian cells, which may allow for the design of selective compounds without liability in mammals.[7] The approach we considered was to inhibit a glycolytic enzyme with a compound targeting its active site. We chose the fourth enzyme in the cascade as the target, i.e., class I fructose 1,6-bisphosphate aldolase (EC 4.1.2.13). On the basis of the literature[8] and previous work from ourlaboratory,[9] we envisaged mimics of Schiff base formation (iminium ion) by use of phosphorylated naphthalene derivatives. Such derivatives feature an aldehyde group for Schiff base formation and whose resulting

iminium ion is stabilized by the presence of an OH group at the ortho position.[10] Permutation of the three functionalities (phosphate, aldehyde, and hydroxyl) on the naphthalene skeleton allows for the design of lead compounds with different functional topologies.

3.2.3 Results and Discussion

A number of such compounds were synthesized and assayed on both *T. brucei* and rabbit muscle aldolase. Synthesis of the most promising compound, **9** (TBK1) likely to form a Schiff base with one of the three lysyl groups of the active site (Lys116, -156, and -239 in *T. brucei*aldolase), is shown in Scheme 3

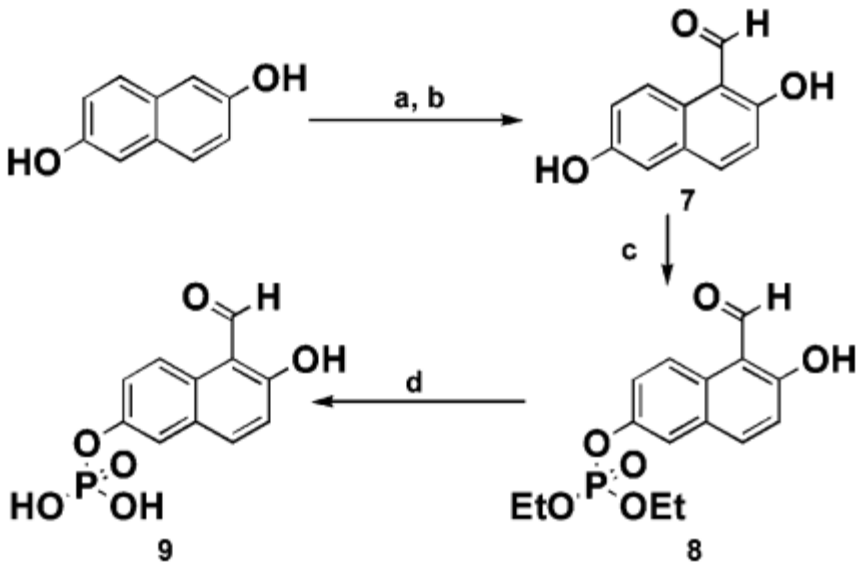

Scheme 3-3. Synthesis of *T. brucei* Aldolase Inhibitor 9a

Reagents: (a) biphenylformamidine, acetone, 82% (6; see Supporting Information); (b) H2SO4, H2O/ EtOH, 96%; (c) (EtO)3P, I2, pyridine, CH2Cl2/THF, 31%; (d) Me3SiBr, CH2Cl2, H2O, NaOH, 90%.

Synthesis of **9** required, as starting material, 2,6-dihydroxynaphthalene formylated at position 1 using diphenyl formamidine[11] followed by hydrolysis of the resulting Schiff base under acidic conditions to yield the aldehyde derivative **7**. The key step was selective monophosphorylation at position 6 of **7** to obtain the ester derivative **8** without a protecting group at position 2. This was performed using the triethyl phosphite/pyridine/iodine procedure.[12] Compound **9** was then obtained by the transesterification reaction of **8** using silyltrimethyl bromide and followed by routine hydrolysis.

The effect of **9** on aldolase can be summarized in six points.

(1) The inhibitory effect of **9** was investigated on mammalian and parasite aldolases. Standard conditions were employed for kinetic constant determination (see Supporting Information). A time-dependent inhibition of the *T. brucei* enzyme was observed at low concentration (20 μM) (Table 4) which could not be reversed upon dialysis (see Supporting Information).

Table 3-4. Interaction of TBK 1 with Rabbit Muscle (RM) and *T. brucei* (Tb) Class I Aldolase

incubation time (min)	**9** (mM)	enzyme (0.2 mg/mL)	residual activity (%)
5	1	RM	80
15			80
5	0.1	RM	100
15			100
5	0.5	Tb	<20
15			0
5	0.02	Tb	75
15			50

Rabbit muscle aldolase by comparison was not inhibited or only very weakly at high inhibitor concentration (1 mM). Compound **9** selectivity was further explored using aldolases from other sources, and the results are summarized in Table 5. In each case, **9** (100 μM) was incubated with enzyme at 0.2 mg/mL. No effect was observed on the mammalian enzymes (rabbit muscle and human liver), whereas the aldolases from three protozoan parasites (*T. brucei*, *Leishmania mexicana*, and *Plasmodium falciparum*) were inhibited, with the strongest effect on *T. brucei*aldolase.

Table 3-5. Selective Inhibition of Class I Aldolases by 9

enzyme (0.2 mg/mL)	residual activity (%)
Conditions: 100 μM **9**, 15 min	
rabbit muscle	100
human liver	100
Trypanosoma brucei	<0.5
Leishmania mexicana	15
Plasmodium falciparum	30

Compound **9** appears to be a very selective inhibitor of *T. brucei* aldolase. Further analyses (see Supporting Information) yielded inhibition constants K_i = 23.03 ± 2.31 μM and k_3 = 0.39 ± 0.04 min^{-1} with $k_4 \approx 0$, values indicating a quasi-irreversible behavior by **9** (Figure 2). We therefore concentrated our efforts on *T. brucei* aldolase.

$$\mathbf{E + I} \underset{\mathbf{k_2}}{\overset{\mathbf{k_1}}{\rightleftharpoons}} \mathbf{EI} \underset{\mathbf{k_4}}{\overset{\mathbf{k_3}}{\rightleftharpoons}} \mathbf{EI^*};\ \mathbf{K_i = \frac{k_2}{k_1}};\ \mathbf{k_4 = 0}$$

Figure 3-10. Scheme for the interaction kinetics of 9 with *T. brucei* aldolase.

(2) To determine the inhibition mode of **9**, we analyzed the protection of *T. brucei* aldolase against inhibition by its substrates fructose 1,6-P_2 (FBP) and dihydroxyacetone-P (DHAP) and by two strong competitive inhibitors, namely, hexitol-1,6-P_2 (HBP, an FBP analogue resulting from the reduction of the FBP carbonyl group, K_i = 0.45 μM)[13] and naphthalene-2,6-P_2 (NBP,K_i = 0.28 μM).[8] Compound **9** (100 μM) was incubated with *T. brucei* aldolase and in the presence of different concentrations of substrates (FBP, DHAP) or competitive inhibitors (HBP, NBP). The residual activity was determined after 5 and 15 min of incubation. The results are summarized in Table 6 and are consistent with active site binding. FBP and DHAP only partially protected the

enzyme against inhibition. By contrast, both competitive inhibitors, which cannot undergo a retro aldolization reaction, totally protected the enzyme.

Table 3-6. In Vitro Study of *T. brucei* Aldolase Protection against 9 Inhibition by Its Substrates and Competitive Inhibitors

compd	concn (mM)	residual activity (%) ± 5% at 5 min	residual activity (%) ± 5% at 15 min
none		15	0
DHAP	0.250	56	48
	0.500	63	44
	1	60	52
	10	80	70
FBP	1	80	51
	10	100	89
hexitol 1,6-bisphosphate (HBP)	1	100	100
	0.1	100	100
naphthyl 1,6-bisphosphate (NBP)	1	100	100

(3) To investigate the molecular process by which inhibition occurs, we used UV−vis difference spectroscopy to probe the aldolase−**9** interaction. The spectrum corresponding to the interaction of inhibitor with the *T. brucei* enzyme is shown in Figure 11 Compared to the spectrum of **9** reacting with a lysine mimic, ε-aminocaproic acid (Supporting Information), the spectrum for the reaction with the enzyme is different. In

both cases, however, the presence of isosbestic points in the spectra indicates that complex formation proceeds without accumulation of intermediates or side reactions.

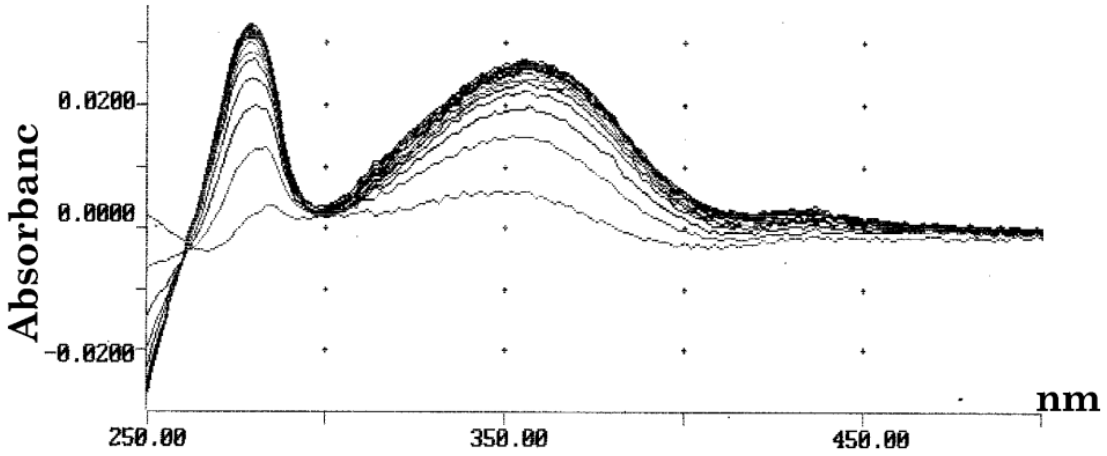

Figure 3-11. UV−vis difference spectrum of 9.

Reaction of *T. brucei* aldolase (0.2 mg/mL) and 9 (50 μM) in TEA buffer, pH 7, Δt = 2 min. Absorption spectrum has λmax = 278 and 356 nm with isosbestic point at 262 nm.

We hypothesized that **9** inhibition involves initial Schiff base formation with enzyme followed by a nucleophilic attack by a second active site residue. Such a reaction sequence was reported for naphthalene dicarboxaldehyde, which upon Schiff base formation reacts with a cysteine residue.[14] Similarly in the reaction of pyridoxal phosphate with ethane-1,2-diamine,[15] the resulting iminium ion undergoes an intramolecular nucleophilic attack by the second amino group to form a cyclic geminal diamine. To explore such a possibility, we examined the reaction of **9** with model compounds that are mimics of amino acid residues: ethanolamine as a serine analogue, cysteamine as a cysteine mimic, and ethane-1,2-diamine as a second lysyl group. The difference spectrum of the reaction with **9** by ethanolamine resembled closely the spectrum obtained with the enzyme that is shown in Figure 3; resultant absorption maxima (λ_{max} at 270 and 350 nm)

and isosbestic point (λ = 255 nm) were only slightly shifted (~7 nm) toward the UV. We therefore concluded that the amino acid reacting with the intermediate iminium ion formed between the enzyme and **9** is most likely a serine residue. Further support for this conclusion is not inconsistent with the observation below.

(4) The formation of enzyme−inhibitor complexes was studied by electrospray mass spectrometry with the recombinant *L. mexicana* aldolase, which exhibits the same inhibition pattern as the *T. brucei* enzyme (see point 1). Mass spectrometric analyses with the recombinant Trypanosoma protein were unsuccessful. The results obtained with the recombinant *L. mexicana* aldolase corresponded to an observed $\Delta m/z$ of 255 between the free enzyme and the **9**−enzyme complex (see Supporting Information) and indicate a single inhibitor molecule bound per subunit of enzyme. These data are not inconsistent with the formation of the iminium ion concomitant with the loss of a water molecule and that of the putative internal adduct because both have the same mass as the iminium ion intermediate.

(5) To determine which residue was involved in Schiff base formation, point mutations were made of active site lysine residues in the recombinant *T. brucei* enzyme. Active site lysine residues were mutated to methionine, yielding constructs K116M, K156M, and K239M. Compound **9** was incubated with each construct, and the corresponding UV−vis difference spectra were compared to that obtained with the wild-type (Figure 3). For mutants K156M and K239M, the spectra were identical to that of the wild-type enzyme. By contrast, K116M yielded a different spectrum, indicating that Lys116 is the active-site residue responsible for Schiff base formation. This result was corroborated by the observation that the K116M mutant was not inhibited by **9**.

(6) Finally, to gain insight into the preferential reactivity of **9** toward parasite aldolases, we docked it into the crystallographic structures of rabbit muscle and *T. brucei* aldolases, minimized the interaction energies of resulting complexes, and then compared the trajectories of the molecular dynamics simulations[16] using the minimized aldolase complexes as the starting point. Simulations sought to identify configurations of **9** in the active site that are consistent with incipient Schiff base formation,

using a protocol previously described to analyze the reactivity of a **9** isomer, HNA-P, with rabbit muscle aldolase.[10] For all simulations, the reactive lysine residue was modeled in its nucleophilic form consistent with a pK_a of ~8 for Lys107 in the mammalian aldolase.[10] Energy minimizations yielded a stable Michaelis complex with **9**, free of close contacts, filling the entire active site cleft and necessitated the expulsion of only several water molecules in the crystal structure. Simulations of 5 ns duration for the parasite and mammalian aldolases showed the phosphate moiety to be persistently bound in its binding site, making identical electrostatic and hydrogen-bonding interaction with active site residues in both isozymes. We then analyzed the trajectories generated by the simulation for coordinate frames whose geometries are conducive for nucleophilic attack in *T. brucei* and rabbit muscle enzymes.[10] Only 3% of the frames analyzed displayed geometries consistent with nucleophilic attack by Lys116 in the *T. brucei* enzyme (Supporting Information). A representative frame is shown in Figure 12.

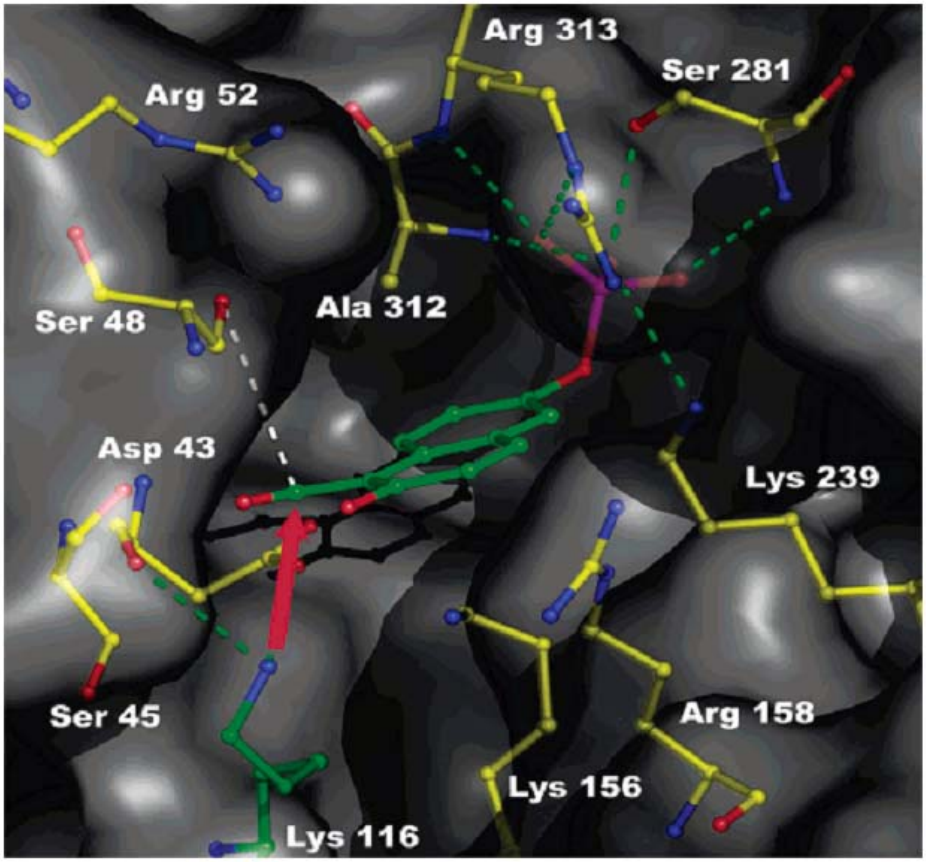

Figure 3-12. Michaelis complex formed in the *T. brucei* aldolase active site with 9 inhibitor.

The solvent-accessible surface of the protein is depicted in gray. Dotted green lines represent hydrogen bonds or electrostatic interactions, and active site residues proximal to 9 are labeled. The red arrow shows the presumed trajectory corresponding to nucleophilic attack by Lys116 Nz on the electrophilic C7 aldehyde carbon. Lys116 is oriented by two hydrogen bonds made by its Nz atom to carboxylate and backbone oxygens of Asp43 (one is hidden by the red arrow) and that is pointing its free electron pair in the direction of the 9 C7 atom. The white dotted line indicates the proximity of Ser48 to the C7 carbon of 9. The drawing was made with PyMOL (http://pymol.sourceforge.net/).

Notable is the reaction geometry in Figure 4 that places Lys116 nearly perpendicular to the aldehyde of **9** at a distance of 3.36 Å. This orientation is favorable for Schiff base formation in the first step of the inhibition mechanism. A similar percentage of frames (1.8%) suitable for nucleophilic attack by Lys107 was noted in the HNA-P Michaelis complex with mammalian aldolase.[10] Moreover, the intermolecular hydrogen bond between the hydroxyl and the aldehyde on the naphthalene skeleton of **9** (not shown in Figure 4) stabilizes the carbonyl group orientation for nucleophilic attack by Lys116. In model systems, the presence of a hydroxyl ortho to the aldehyde is important for formation and Schiff base stabilization.[10] Surprisingly, no frame was found suitable for nucleophilic attack in the rabbit muscle aldolase simulation of the Michaelis complex with **9** and is consistent with poor reactivity by **9** in the mammalian isozyme. Although active sites differ in one residue (Gly302 in the mammalian enzyme being replaced by a bulkier Ala312 in *T. brucei* aldolase), analysis of dynamical trajectories did not reveal conformational differences in the positioning of **9** with respect to C_α atoms of these residues, suggesting that this amino acid change may not account for the observed reactivity differences. Reaction of **9** with the malarial aldolase whose active site composition is identical to that of mammalian aldolase would corroborate this conclusion.

The reactant configuration in Figure 4 places the γ-OH of Ser48 within van der Waals contact of the **9** carbonyl. Intriguingly, Ser48 oriented opposite and nearly perpendicular to the aldehyde would be well-positioned to interact with the nascent iminium ion and could be the residue that reacts with the Schiff base, leading to the final intermediate in the slow binding inhibition mechanism.

In conclusion, we have synthesized a selective time-dependent inhibitor of *T. brucei* aldolase that does not significantly inhibit mammalian aldolase activity. We identified Lys116 as being responsible for Schiff base formation. Molecular dynamics suggest that differences in stabilization of reaction geometries are responsible for the differential reactivity of **9** with *T. brucei* aldolase compared to rabbit muscle aldolase and that Ser48 is most likely the reactive residue in the second step of the inhibition

mechanism. MS experiments performed on *L.mexicana* aldolase support these conclusions. Compound **9** and its "prodrug" analogues will be tested in in vitro cultures of *T. brucei* to determine if it causes growth retardation.

3.2.4 Acknowledgment

This work was funded by the European Commission, through its programs INCO-DC (Contract IC18-CT97-0220) and INCO-DEV (Contract ICA4-CT-2001-10075) to C.B. and P.A.M.M., and by a grant from the National Scientific Research and Engineering Council (NSERC) of Canada to J.S. We thank the Réseau Québécois de Calcul de Haute Performance (RQCHP) for computational resources for the molecular dynamical simulations. The authors are grateful to Professor J. Poupaert, Université Catholique de Louvain, Brussels, Belgium, for helpful discussions.

3.2.5 References

(1) World Health Organization report on Tropical Diseases Research (TDR) program (2002).

(2)(a) Howells, R. E. The modes of action of anti-protozoal drugs. Parasitology 1985, 90, 687−703.

(b) Neujean, G. Chemotherapy and chemoprophylaxis of sleeping sickness caused by Trypanosoma gambiense. Rev. Med. Liege 1959, 14, 5−13.

(3) Milord, F.; Pepin, J.; Loko, L.; Ethier, L.; Mpia, B. Efficacy and toxicity of eflornithine for treatment of Trypanosoma brucei gambiense sleeping sickness. Lancet 1992, 340, 652−655.

(4) Sjoerdsma, A.; Schechter, P. J. Chemotherapeutic implication of polyamine biosynthesis inhibition. Clin. Pharmacol. Ther. 1984, 35, 287−300.[PubMed], [ChemPort]

(5) Van Nieuwenhove, S. Clinical evaluation of eflornithine in Trypanosomiasis. Trans. R. Soc. Trop. Med. Hyg. 1985, 79, 692−696.

(6)(a) Visser, N.; Opperdoes, F. R. Glycolysis in Trypanosoma brucei. Eur. J. Biochem. 1980, 103, 623−632. (b) Verlinde, C. L.; Hannaert, V.; Blonski, C.; Willson, M.; Perie, J. J.; Fothergill-Gilmore, L. A.; Opperdoes, F. R.; Gelb, M. H.; Hol, W. G.; Michels, PAM. Glycolysis as a target for the design of new anti-trypanosome drugs. Drug Resist. Updates 2001, 4, 50−65.

(7) Opperdoes, F. R.; Baudhuin, P.; Coppens, J.; De Roe, C.; Edwards, S. W.; Weijers, P. J.; Misset, O. Purification, morphometric analysis and characterization of the glycosomes of the protozoan hemoflagallate Trypanosoma brucei. J. Cell Biol. 1984, 98, 1178−1184.

(8) Shu, B.; Barker, R. Fluorescence studies of the binding of alkyls and aryl phosphates to rat muscle aldolase. J. Biol. Chem. 1971, 246, 7041−7045.

(9)(a) Blonski, C.; Gefflaut, T.; Périé, J. Effects of chirality and substituents at carbon 3 in dihydroxyacetone-phosphate analogues on their binding to rabbit muscle aldolase. Bioorg. Med. Chem. 1995, 3, 1247−1253.

(b) Gefflaut, T.; Blonski, C.; Perie, J. Slow reversible inhibitions of rabbit muscle aldolase with substrate analogues: synthesis, enzymatic kinetics and UV difference spectroscopy studies. Bioorg. Med. Chem. 1996, 4, 2043−2054.

(c) Gefflaut, T.; Blonski, C.; Périé, J.; Willson, M. Class I aldolases: substrate specificity, mechanism, inhibitors and structural aspects. Prog. Biophys. Mol. Biol. 1995, 63, 301−340.

(10)(a) Blonski, C.; Moissac, D.; Perie, J.; Sygusch, J. Inhibition of rabbit muscle aldolase by phosphorylated aromatic compounds. Biochem. J. 1997, 323, 71−77.[

(b) Dax, C.; Coincon, M.; Sygusch, J.; Blonski, C. Hydroxynaphthaldehyde phosphate derivatives as potent covalent Schiff base inhibitors of fructose-1,6-bisphosphate aldolase. Biochemistry 2005, 44, 5430−5443.

(11)(a) Shoesmith, J. B.; Haldane, J. Condensation of diphenyl formamidine with phenol. Part I. A new synthesis of β-resorcy-aldehyde. J. Chem. Soc. 1923, 123, 2704−2707.[ChemPort] (b) Shoesmith, J. B.; Aldane, J. Condensation of diphenyl

formamidine with phenol. Part II. The general nature of the reaction. J. Chem. Soc. 1924, 125, 2405−2407.

(12)(a) Stowell, J. K.; Wildlanski, T. S. A new method for the phosphorylation of alcohols and phenols. Tetrahedron Lett. 1995, 36, 1825.

(b) Claustre, S.; Willson, M. Selective phosphorylation on primary alcohols of unprotected polyols. Phosphorus, Sulfur Silicon Relat. Elem. 2001, 174, 37−47.

(13) Ginsburg, A.; Mehler, A. H. Specific anion binding to fructose bisphosphate aldolase from rabbit muscle. Biochemistry 1966, 5, 2623−2634.

(14) McCurdy, C. R.; Le Bourdonnec, B.; Metzger, T. G.; El Kouhen, R.; Zhang, Y.; Law, P. Y.; Portoghese, P. S. Naphthalene dicarboxaldehyde as an electrophilic fluorogenic moiety for affinity labelling: application to opioid receptor affinity labels with greatly improved fluorogenic properties. J. Med. Chem. 2002, 45, 2887−2890.

(15)(a) Tobias, P. S.; Kallen, R. G. Kinetics and equilibria of the reaction of pyridoxal 5‘-phosphate with ethylenediamine to form Schiff bases and cyclic geminal diamines:evidence for kinetically competent geminal diamine intermediates in transimination sequences. J. Am. Chem. Soc. 1975, 97, 6530−6539.

(b) McQuate, R. S.; Leussing, D. L. Kinetic and equilibrium studies on the formation of zinc(II) salicylaldehyde Schiff base derived from ethylenediamine and 1,3-diaminopropane. J. Am. Chem. Soc. 1975, 97, 5117−5125.

(16)(a) Weiner, S. J.; Kollman, P. A.; Case, D. A.; Singh, U. C.; Ghio, C.; Alagona, G.; Profeta, S. J.; Weiner, P. A. New force field for molecular mechanical simulation of nucleic acids and proteins. J. Am. Chem. Soc. 1984, 106, 765−784.

(b) Weiner, S. J.; Kollman, P. A.; Nguyen, D. T.; Case, D. A. An all atom force field for simulation of proteins and nucleic acids. J. Comput. Chem. 1986, 7, 230−252.

3.2.6 Supporting Information

3.2.6.1 Synthesis

All reactions were carried out under an argon atmosphere with dried solvent: THF and ether were distilled over sodium/benzophenone, CH_2Cl_2 over P_2O_5, pyridine and triethyl amine over potassium hydroxide. HPLC solvents were used without distillation. ^{1}H, ^{13}C and ^{31}P NMR spectra were recorded using a Bruker AC 200 or AC 250 spectrometer. The values of the chemical shifts (δ) are given in ppm, as internal standards were used TMS for ^{1}H and ^{13}C, phosphoric acid for ^{31}P. Coupling constants (J) are in Hz. Progress of the reaction was monitored by TLC on silica gel plates (Merck 60-F254) at λ=254 nm and 366 nm. Merck silica gel (Merck-60, 230-400 mesh) was used for flash chromatography. Preparative and analytic HPLC used reverse phase (Macherey-Nagel polygoprep C18, 12-25 μm, 60 Å) with appropriate eluent. Mass electrospray spectra were acquired using a quadripolar Nermag R10-10 in DCI mode. Hexitol bisphosphate (HBP) was prepared from fructose bisphosphate (FBP) by the procedure of Ginsburg and Mehler.[1] All compounds yielded satisfactory NMR, ESMS and CH data.

3.2.6.1.1 1-[(phenylimino)methyl]naphthalene-2,6-diol (6):

This compound was synthesized by the procedure of Shoesmith et al.[2,3] A mixture of 5 g of 2,6-dihydroxynaphtalene (31.20 mmol) and 8.7 g of diphenyl formamidine (44.35 mmol) was stirred at 120°C under argon for 5 h. The progress of the reaction was monitored by TLC. The resulting mixture was cooled to room temperature and 30 ml of acetone were added, the resulting precipitate was filtered off and dried to give **6** as a red powder (6.74g; 82%). Compound **6** was used in the next step without other purification.

3.2.6.1.2 2,6-dihydroxy-1-naphtaldehyde (7):

A solution of **6** (6.0g, 22.8 mmole) in 5 ml of water and 4 ml of concentrated H_2SO_4 (96%) was put in a liquid-liquid extraction by upward displacement with ether during 4 days. Removal of the solvent under reduced pressure gave compound **7** as a yellow solid (4.12g; 96%).

^{1}H NMR (200 MHz, CD_3OD) : δ (ppm) : 7.02 (d, $^3J_{H4-H3}$= 9.1 Hz, 1H, H4) ; 7.10 (se, 1H, H5) ; 7.18 (dd, $^3J_{H7-H8}$= 9.10 Hz, $^4J_{H7-H5}$= 2.6 Hz, 1H, H7) ; 7.82 (d, $^3J_{H3-H4}$= 9.10 Hz, 1H, H3) ; 8.38 (d, $^3J_{H7-H8}$= 9.10 Hz, 1H, H8) ; 10.74 (s, CHO). ^{13}C NMR *(50 MHz, CD_3OD)* : δ (ppm) : 110.5 (s, C7) ; 111.5 (s, C1) ; 116.3 (s, C3) ; 120.0 (s, C8) ; 120.7 (s, C5) ; 126.4 (s, C10) ; 129.4 (s, C9) ; 137.1 (s, C4) ; 153.8 (s, C6) ; 162.1 (s, C2) ; 193.7 (s, CHO). MS *(DCI/CH_4)* : 189 ($M+H^+$, 100%) ; 161 ($M-C_2H_5^+$, 35%).

3.2.6.1.3 Diethyl(5-formyl-6-hydroxy-2-naphthyl)phosphate (8):

A solution of iodine (1.42 g, 5.57 mmol), triethyl phosphite (1 ml, 5.75 mmol) in 15 ml of CH_2Cl_2 was added to a cold solution (0°C) of 2,6-dihydroxy-1-naphtaldehyde **7** (0.53 g, 2.79 mmol), 0.3 ml of pyridine (3.72 mmol) in 3 ml of THF and 50 ml of CH_2Cl_2. Progress of the reaction was monitored by HPLC Reverse Phase. The mixture was stirred at 0°C for 30 min, then at room temperature overnight. Acyl acetate and water were added and the resulting organic layer was washed with water and brine, and then dried over $MgSO_4$. The solvent was evaporated under reduced pressure to give an oil which was purified by reverse chromatography (H_2O/CH_3CN: 4/6). Compound **8** was obtained as orange oil (0.28g; 31%).

^{1}H NMR (250 MHz, $CDCl_3$) *:* δ (ppm) : 1.34 (t, $^3J_{H-H}$= 7.00 Hz, 6H, CH_{3ester}) ; 4.17 (q, $^3J_{H-H}$= 7.00 Hz, 4H, CH_2-O) ; 7.10 (d, $^3J_{H7-H8}$= 9.10 Hz , 1H, H7) ; 7.45 (dd, $^3J_{H3-H4}$= 9.10 Hz, $^4J_{H3-H1}$= 2.54 Hz, 1H, H3) ;7.61 (se, 1H, H1) ; 7.86 (d, $^3J_{H8-H7}$= 9.10 Hz, 1H, H8) ;

8.27 (d, $^{3}J_{H4-H3}$= 9.10 Hz, 1H, H4) ; .10.70 (s, CHO) ; 12.99 (s, OH). ^{13}C NMR (50 MHz, $CDCl_3$) : δ (ppm) : 16.2 (d, $^{3}J_{C-P}$= 26.8 Hz, CH_{3ester}) ; 64.9 (d, $^{2}J_{C-P}$= 24.5 Hz, CH_{2ester}) ; 111.3 (s, C5) ; 118.4 (d, $^{3}J_{C-P}$= 18.75 Hz, C3) ; 120.4 (s, C7) ; 120.5 (s, C4) ; 122.7 (d, $^{3}J_{C-P}$= 20 Hz, C1) ; 128.5 (s, C10) ; 130.2 (s, C9) ; 138.4 (s, C8) ; 147.4 (d, $^{3}J_{C-P}$= 6.2 Hz, CH_2) ; 164.5 (s, C6) ; 193.1 (s, CHO). ^{31}P NMR (81 MHz, $CDCl_3$) δ (ppm) : -6.03 (s). MS (DCI/CH4) : 325 ($M+H^+$, 100%) ; 353 ($M+C_2H_5^+$, 18%). Elemental analysis - Calcd for $C_{15}H_{17}O_6P$: C, 55.56; H, 5.28. Found: C, 55.44; H, 5.41.

3.2.6.1.4 5-formyl-6-hydroxy-2-naphthyl di-sodium phosphate (9):

To a solution of compound **8** (0.16 g, 0.49 mmol) in 200 µl of CH_2Cl_2 was added 0.4 ml of silyl trimethyl bromide (3.03 mmol). Progress of the reaction was monitored by ^{31}P-NMR. After 3 h, the reaction mixture was concentrated under reduced pressure and ether/water (10/1 v/v) was added. The organic layer was washed with water and the aqueous layers were combined and neutralized to pH = 7.2 with a NaOH solution. The final compound **9** was obtained as an oil (31mg; 20%) after ion-exchange chromatography (Dowex8X200) using the eluent HCl/THF.

^{1}H NMR (200 MHz, D_2O) : δ (ppm) : 6.82 (d, $^{3}J_{H8-H7}$= 9.16 Hz, 1H, H8) ; 7.40 (dd, $^{3}J_{H3-H4}$= 9.20 Hz, $^{2}J_{H3-H1}$= 2.36 Hz 1H, H3) ; 7.48 (se, 1H, H1) ; 7.77 (d, $^{3}J_{H4-H3}$= 9.20 Hz, 1H, H4) ; 8.22 (d, $^{3}J_{H7-H8}$= 9.16 Hz, 1H, H7) ; 10.28 (s, CHO). ^{13}C NMR (50 MHz, D_2O) : δ (ppm) : 114.1 (s, C5) ; 120.1 (d, $^{3}J_{C-P}$= 4.05 Hz, C3) ; 121.7 (s, C4) ; 123.8 (s, C7) ; 126.6 (d, $^{3}J_{C-P}$= 4.35 Hz, C1) ; 130.6 (s, C9) ; 131.1 (s, C10) ; 141.4 (s, C8) ; 152.8 (d, $^{2}J_{C-P}$= 6.10 Hz, C2) ; 166.2 (s, C6) ; 197.1 (s, CHO). ^{31}P NMR (81 MHz, D_2O) : δ (ppm) : -0.13 (s).

MS (FAB) : 267 (M-H, 100%). Elemental analysis - Calcd for $C_{11}H_9O_6P.2H_2O$ (**9**, acid form): C, 44.43; H, 4.31. Found: C, 44.21; H, 4.54.

3.2.6.2 Wild-type and mutant recombinant aldolase preparations

Recombinant rabbit-muscle aldolase was overexpressed and purified as described.[4,5] Purified human liver aldolase was a gift of Dr. Tim Cox, Cambridge University, England. *Plasmodium falciparum* aldolase was a gift of Dr. Marcia Garcia, ICT-Amrad, Australia. The expression and purification of a His-tagged *L. mexicana* aldolase have been described by de Walque *et al.*[6] The gene encoding the aldolase (*ald*) from *T. brucei*[7] has been initially used for the overexpression of the protein in *Escherichia coli*. Recombinant *T. brucei* aldolase was purified by ion-exchange chromatography using an enzymatic assay for monitoring the purification[8.] However, it was expected that site-directed mutagenesis (SDM) would result in an aldolase of which the enzymatic activity was affected. Therefore, the wild-type *ald* gene was cloned in the pET15b vector (Novagen) which allows the synthesis of a His-tagged fusion protein and its purification by immobilized metal-affinity chromatography (IMAC). To this end, the *ald* gene was amplified by PCR with $Vent_R$ DNA polymerase (New England Biolabs) and oligonucleotides containing appropriate endonuclease restriction sites for cloning in pET15b. The PCR product was agarose-gel purified using a Qiaex II kit (Qiagen) and ligated into *Eco*RV-linearized plasmid pZErO-2 (Invitrogen), sequenced and then transferred to pET15b in such a way that an open-reading frame was created for a fusion protein of aldolase with an N-terminal extension of 20 amino acids including a stretch of six histidine residues. The resulting recombinant plasmid served as template for SDM and was expressed to produce the wild-type His-tagged aldolase used as reference in the enzymatic assays. Lysine residues at positions 116, 156 and 239 were substituted, one at a time, for methionine by SDM using sequential PCR steps as described by Cormack.[9]

Over-expression of His-tagged wild-type and mutated *T. brucei* aldolase was carried out in *E. coli* strain BL21(DE3)pLysS (Novagen), at 37°C in LB medium, supplemented with 100 µg/ml ampicillin and 30 µg/ml chloramphenicol. When the optical density at 600 nm reached 0.5, induction was performed by adding 1 mM isopropyl-β-D-thiogalactopyranoside. After 5 h of induction, the cultures were chilled on ice and cells were harvested by centrifugation. Pellets were resuspended in 30 ml of lysis buffer (100 mM triethanolamine (TEA) pH 7.4, 300 mM NaCl, 1 mM Tris(2-carboxyethyl)-phosphine hydrochloride (Pierce) and 2 mM imidazole, and a protease-inhibitor cocktail). Cells were disrupted by two passages through a French press (SLM Amico Inc.) and nucleic acids removed by treatment with Benzonase (Merck) and centrifugation for 15 min at 12,000 x g and 4°C. Soluble proteins were precipitated from the supernatants with 60% ammonium sulfate at 0°C. After centrifugation as above, pellets were resuspended in 10 ml of lysis buffer containing 10% glycerol and 2 mM imidazole and were applied on Talon resin (Clontech). IMAC was performed as described by the manufacturer. Elution was done with lysis buffer containing 100 mM imidazole. Purity of His-tagged proteins was checked by SDS-PAGE and activity assays[8] and recombinant proteins were stored at 4°C in presence of 80% ammonium sulfate.

3.2.6.3 Preparation of the enzyme for inhibition studies

Before use, an appropriate volume of aldolase in an ammonium sulfate suspension was taken and centrifuged 5 min at 12,000 x g. The supernatant was eliminated and the precipitate was resuspended in 250 µl of triethanolamine (TEA) buffer (100 mM TEA/HCl, pH 7.6, 50 mM NaCl). This solution was dialyzed using a Centrikon® 10 kD membrane and centrifuged at 3,500 x g for 15 min. This step was repeated 5 to 6 times. The enzyme solution was kept at 4°C. We used also another technique, in which the precipitate was solubilized after the first centrifugation step, dialysed (Spectrum®, cut of MW 12,000 – 14,000) and incubated in 500 ml of buffer during 2 h. The buffer was changed twice, after 2 and 4 h, and then left for 24 h at 4°C. The concentration of enzyme was determined spectrophotometrically at 280 nm, assuming A_{280} = 0.91 for an aldolase solution of 1 mg/ml.[10]

3.2.6.4 Activity assays

All recombinant aldolases were stored as ammonium sulfate suspensions; specific activities of trypanosomatid wild-type aldolase and rabbit muscle aldolase were 25 μmol/min.mg and 15 μmol/min.mg respectively. The wild-type and mutated forms of *T. brucei* aldolase were purified in the laboratory of P. Michels (Belgium), rabbit muscle aldolase in the laboratory of J. Sygusch (Canada). Triosephosphate isomerase (TIM) from rabbit muscle 10 mg/ml, glycerol-3-phosphate dehydrogenase (GDH) from rabbit muscle 10 mg/ml, fructose 1,6-bisphosphate (FBP) and NADH were purchased from Boehringer-Mannheim (Roche). Dihydroxyacetone phosphate (DHAP) was obtained from Sigma.

The FBP cleavage activity of aldolase was measured using a coupled assay system by following NADH oxidation at 340 nm, with detection by a SAFAS-Monaco UV mc^2 or a CARY 1 E (Varian) spectrophotometer thermostatted at 25°C.[11] Assays were initiated by the addition of substrate FBP (1 mM final concentration) to a final volume of 1 ml of solution containing aldolase in triethanolamine (TEA) buffer (100 mM TEA/HCl, pH 7.6, 50 mM NaCl), 0.42 mM NADH and coupling enzymes (10 μg/ml GDH; 1 μg/ml TIM).

3.2.6.5 Inhibition studies of compound 9 with aldolases

Aldolase (0.2 mg/ml, see Tables 1 and 2) was incubated in the presence of various concentrations of **9** (as indicated in Tables 1 and 2) in TEA buffer. Aliquots were taken after various times of incubation (5 or 15 min) and analyzed for enzymatic activity.

3.2.6.6 Residual activity in *T. brucei* aldolase upon inhibition by compound 9

T. brucei aldolase (0.2 mg/ml) was incubated in the presence of a fixed concentration of **9** (50 μM) in TEA buffer, until 10 – 20% of its activity remained. This solution was thenextensively dialyzed against TEA buffer. At different times, aliquots were analyzed for enzymatic activity. No activity was recovered after 72 h. Furthermore, high HBP concentration (1 mM) did not displace bound compound **9** as no activity was detected even after a long period of incubation. Control experiments followed an identical protocol,

but without the addition of **9**. Under these conditions, an activity loss of ~ 15 % was observed.

3.2.6.7 Interaction of compound 9 with *T. brucei* aldolase

T. brucei aldolase (0.2 mg/ml) in TEA buffer was incubated in the presence of various concentrations of **9** (0 to 20 μM). At different times, aliquots were analyzed for enzymatic activity. Loss of enzyme activity occurred according to a first-order reaction. Data analysis of the inhibition kinetics in terms of an irreversible process[12], as depicted in Figure 1, yielded a dissociation constant, K_i = 23 μM, for the rapidly formed EI complex and a first-order rate constant, k_3 = 0.39 min^{-1}, for EI* complex formation.

3.2.6.8 *T. brucei* aldolase protection by substrates and competitive inhibitors

Using the same protocol as described previously, different compounds were tested for their protection of *T. brucei* aldolase against compound **9** inhibition by adding them simultaneously with the inhibitor to the assay mixture (see Table 3). Typically, *T. brucei* aldolase (0.2 mg/ml) was incubated in the presence of a fixed concentration of **9** (100 μM) and various concentrations of substrates (DHAP: 0.25 - 10 mM; FBP: 1 or 10 mM) or competitive inhibitors (hexitol 1,6-bisphosphate : 0.1 or 1 mM; naphtyl 1,6-bisphosphate : 1 mM). Aliquots were analyzed for enzymatic activity after 5 and 15 min of incubation. In control experiments, performed without **9**, no loss of enzyme activity was detected.

3.2.6.9 Inhibition of auxiliary enzymes

A mixture of GDH (0.5 mg/ml) and TIM (0.05 mg/ml) was incubated in the presence of a fixed concentration of **9** (3 mM) in TEA buffer (pH 7.6). After 60 min, aliquots (50 μl) were analyzed for enzymatic activity in the presence of *T. brucei* aldolase (2 μg/ml), FBP (1 mM) and NADH (0.42 mM) in TEA buffer (1 ml final volume). No loss of activity was observed in these control experiments.

3.2.6.10 UV/visible difference spectroscopy

Absorbance spectra were scanned between 250 and 500 nm using a Cary 1E Varian spectrophotometer and recorded as a function of time at a constant temperature of 25 °C according to the procedure of Blonski et al.13 The same TEA buffer (pH = 7.0) as for enzymatic kinetic studies was utilized. A model compound, ε-aminocaproic acid (10 mM) which acts a lysine mimic in terms of reactivity was used as a control to investigate the reaction with 9 (50 μM) in TEA buffer pH= 7, Δt=10min. The UV/Vis difference spectrum of the resultant complex, ascribed to iminium ion formation, is shown below

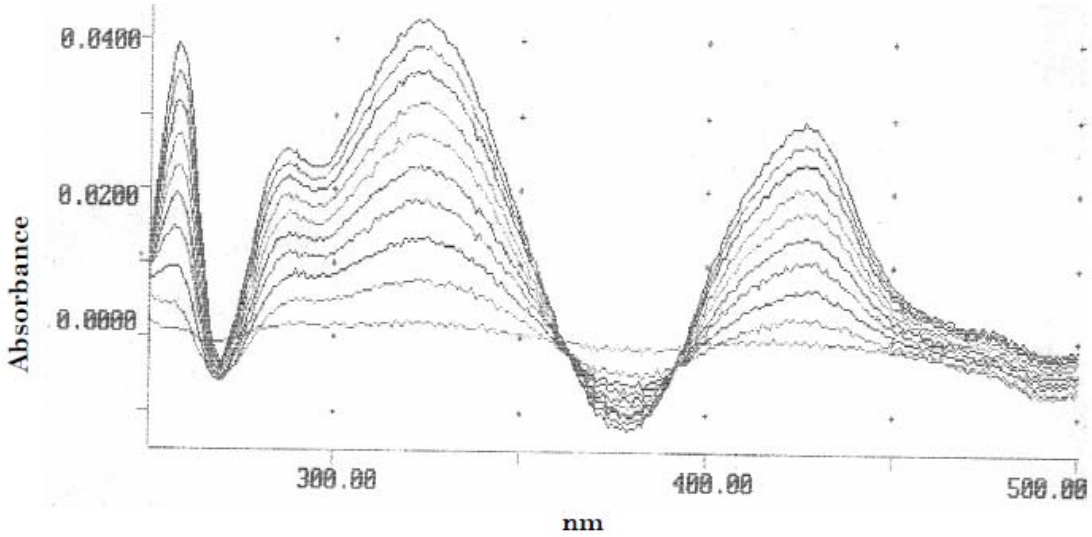

Electrospray ionization mass spectra were obtained using a TSQ700 Finnigan Mat triple quadrupole mass spectrometer in positive mode. L. mexicana aldolase (6.5 mg/ml in 10 mM triethyl ammonium acetate buffer, pH 7.0) was incubated in the presence of compound 9 (100 μM) until 60 ± 5% inactivation was attained and excess inhibitor was removed by ultra-filtration using ammonium acetate buffer (10 mM, pH 5.5). The samples were prepared at □150 pmol/μl in H_2O/methanol (1:1, v/v) with a final concentration of 1 mM ammonium acetate and 0.5% acetic acid. Samples were infused into the source of the mass spectrometer at a continuous flow rate of 4 μl/min. Protein data were acquired over a scan range of m/z 500-2000 at a scan rate of 3 s/scan with scan duration of 1 min. Several scans (□ 20) from m/z 500 to 2000 were summed to yield the final profile spectra prior to

deconvolution. The molecular mass of 9 (acid form) is 268 g/mol. Spectra were deconvoluted using the Excalibur program. The mass spectrometer was calibrated using myoglobin from horse heart (Sigma) as standard. The results are summarized in the Table below.

Compound **9**	Incubation time (min)	Complex mass m/z abundance (%)	Mass change
None	-	43162 ± 4 (100%)	-
500 µM	60	43160 ± 4 (33%) 43415 ± 4 (67%)	- 255 ± 4

3.2.6.11 Molecular modeling

To examine the selective inhibition at the molecular level**,** compound **9** was modeled into the active site of *T. brucei* and rabbit muscle aldolase. Inhibitor docking was initially performed on a Silicon Graphics Indigo workstation using INSIGHT II version 97.0 (BioSym/MSI). Energy minimization using GROMACS[16] and the all-atom force field GROMOS96 for calculation of the potential interaction energy was then performed to optimize binding interaction of the Michaelis complex formed with compound **9**. The crystallographic structures used for the modeling were taken from the Protein Data Base (PDB): rabbit muscle aldolase in complex with DHAP - entry 1ADO and unbound *T. brucei* aldolase – entry 1F2J. The conformation of a DHAP bound subunit of the tetrameric aldolase-DHAP complex[14] was used as template for inhibitor modeling and energy minimization. Docking of compound **9** in the active site of rabbit muscle and parasite aldolase wascarbonyl. In the case of *T. brucei* aldolase for which only the unbound

structure was available, docking entailed repositioning of the Arg313 side chain from its extended conformation in the native state to a curled configuration as observed in the rabbit muscle aldolase-DHAP complex in order to optimally interact with the phosphate oxyanion. No other positional changes were made in the *T. brucei* isozyme with respect to the rabbit muscle aldolase. Close contacts if any were relieved by 10-25 rounds of steepest energy minimization, water molecules solvating the subunit in the crystal structure were added and 300-500 cycles of conjugated gradient energy minimization were performed while keeping Catom positions constrained to the native structure. An additional 1500 cycles of conjugated gradient energy minimization were then carried out with no positional constraints of any kind imposed on the aldolase subunit. The protocol yielded RMS values for energy derivatives as a function of the Cposition that were less than 1.6 Å with respect to the crystallographic coordinates of the subunit. performed based on a protocol previously described[15]. Briefly, compound **9** was docked in the active site by first superimposing its phosphate onto the equivalent DHAP phosphate-binding site in a manner that preserves the hydrogen-bonding pattern made in the rabbit muscle enzyme Michaelis complex with DHAP. The compound **9** aldehyde function was then aligned such that it would be capable of hydrogen bonding with either Lys107 (muscle aldolase) or Lys116 (parasite aldolase) by adjusting torsion angles about the P-O ester bond, $\xi_{1,}$ and ester-oxygen C_6 carbon bond, ξ_2. The C_7 carbonyl was chosen oriented *cis* with respect to the C_1OH maximizing its hydrogen bonding interaction with the $C_{7\,\alpha\,\alpha}$

Molecular dynamics, using GROMACS, was then undertaken to study the reactivity of the Michaelis complex formed with compound **9** in rabbit muscle and *T. brucei* aldolase. Simulations of 5 ns duration were conducted for each modeled structure. Atomic coordinates generated by the dynamical simulations were sampled at a frequency of 1 ps. The atomic coordinate frames and corresponding potential energies were then used to calculate appropriate model conformational statistics. Geometry conducive for incipient formation of the carbinolamine precursor was used to filter configurations generated in the simulations. Candidate geometry competent for attack was analyzed whenever the attacking

nucleophile, Lys-116/107 Nz atom, was less than the van der Waals distance from the electrophilic aldehyde C_{11} carbon. The angle of attack was calculated as the direction defined by the Lys-116/107 Nz atom and compound **9** C_7 carbon and the normal to the hybridization plane containing the aldehyde C_7 carbon. Of the frames competent for nucleophilic attack with *T. brucei* aldolase, these corresponded to an average interatomic distance between the electrophilic C_7 carbon of compound **9** and Lys116 Nz atom of 3.41Å (± 0.12) and had an angle of attack that deviated slightly from perpendicularity by 29.5 ° (± 7.4). Frames generated in the first 300ps of each simulation were excluded from the analysis to minimize modeling bias with respect to starting geometry.

Control simulations comparing rms positional deviation of a 1 ns simulation using a hydrated unbound *T. brucei* aldolase subunit with that of the hydrated tetramer did not show significant positional differences justifying use of a single subunit for our analysis and considerably reducing computational overhead. A similar result was found previously for the rabbit muscle enzyme[15].

3.2.6.12 References of SI

1. Ginsburg, A. and Mehler, A. H. (1966) Specific anion binding to fructose bisphosphate aldolase from rabbit muscle. Biochemistry *5*, 2623-2634.

2. Shoesmith, J. B. and Aldane, J. (1923) Condensation of diphenyl formamidine with phenol. Part I, a new synthesis of β-resorcy-aldehyde. J. Chem. Soc. *123*, 2704-20707.

3. Shoesmith, J. B. and Aldane, J. (1924) Condensation of diphenyl formamidine with phenol. Part II, the general nature of the reaction. J. Chem. Soc. *125*, 2405-2407.

4. Morris, A. J. and Tolan, D. R. (1993) Site-directed mutagenesis identifies aspartate 33 as a previously unidentified critical residue in the catalytic mechanism of rabbit aldolase A, J. Biol. Chem. *268*, 1095-1100.

5. Berthiaume, L., Tolan, D. R. and Sygusch, J. (1993) Differential usage of the carboxyl-terminal region among aldolase isozymes, J. Biol. Chem. *268*, 10826-10835.

6. De Walque, S., Opperdoes, F.R. and Michels, P.A.M. (1999) Cloning and characterization of *Leishmania mexicana* fructose-1,6-bisphosphate aldolase. Mol. Biochem. Parasitol. *103*, 279-283.

7. Marchand, M., Poliszczak, A., Gibson, W.C., Wierenga, R.K., Opperdoes, F.R. and Michels, P.A.M. (1988). Characterization of the genes for fructose-bisphosphate aldolase in *Trypanosoma brucei*. Mol. Biochem. Parasitol. *29*, 65-75.

8. Chevalier, N., Callens, M. and Michels, P.A.M. (1995). High-level expression of *Trypanosoma brucei* fructose-1,6-bisphosphate aldolase in *Escherichia coli* and purification of the enzyme. Protein Expr. Purif. *6*, 39-44.

9. Cormack, B. (1995). Introduction of point mutations by PCR, p.8-17. *In* Short Protocols in Molecular Biology, 3rd edition (F. Ausubel *et al*., Eds). John Wiley & Sons Inc., New-York.

10. Baranowski, T. and Niederland, T.R. (1949) Aldolase activity of myogen A. J.Biol. Chem. *180*, 543-551.

11. Racker, E. (1949) Spectrophotometric measurement of hexokinase and phosphohexokinase activity. J. Biol. Chem. *167*, 843-854.

12. Meloche, H. P. (1967) Bromopyruvate inactivation of 2-keto-3-deoxy-6-phosphogluconic aldolase. I. Kinetic evidence for active site specificity. Biochemistry *6*, 2273-2280.

13. Blonski, C., Moissac, D., Périé, J. and Sygusch, J. (1997) Inhibition of rabbit muscle aldolase by phosphorylated aromatic compounds. Biochem. J. *323*, 71-77.

14. Blom, N. and Sygusch, J. (1997) Product binding and role of the C-terminal region in class I D-fructose-1,6-bisphosphate aldolase. Nature Struct. Biol. *4*, 36-39.

15. Dax, C., Coincon, M., Sygusch, J. and Blonski, C. (2005) Hydroxynaphthaldehyde phosphate derivatives as potent covalent Schiff base inhibitors of fructose-1,6-bisphosphate aldolase. Biochemistry, *44*, 5430-43.

16. Berendsen, H. J. C., van der Spoel, D. and van Drunen, R. (1995) GROMACS: A message-passing parallel molecular dynamics implementation. Phys. Commun. *91*, 43-56.

3.3 Application aux FBPA de classe II : Des résultats préliminaires encourageants

3.3.1 Description de notre système

C'est principalement la dynamique de la boucle α7-β5 qui nous intéresse. Cette boucle diffère beaucoup entre les classes IIA et les classes IIB, aussi nous avons choisi de simuler la FBPA d'*Escherichia coli* ainsi que celle d'*Helicobacter pylori*.

Le site actif étant constitué de résidus appartenant aux deux sous-unités, il est nécessaire de simuler le dimère complet. Nous avons généré la conformation de la boucle manquante en utilisant une « routine » du logiciel de modélisation par homologie MODELLER (Eswar et al., 2007). 200 boucles furent générées pour chaque sous-unité. Celle possédant l'aire d'accessibilité au solvant la plus importante a été conservée. Ceci nous a permis d'obtenir un modèle non biaisé et dont la boucle est relativement éloignée du site actif. Les fichiers de topologies pour le DHAP ont été générés de la même façon que ceux des inhibiteurs présentés précédemment (Dax et al., 2005; Dax et al., 2006). Le protocole de « solvatation » et d'équilibration est aussi identique à celui testé chez les classes I. La taille du système est néanmoins bien plus importante, due à l'utilisation de deux sous-unités. Il est constitué d'environ 160 000 atomes, appartenent principalement à des molécules d'eau. La coordination du zinc a été modélisée sur la base du protocole publié par Bianchini & al. (Bianchini et al., 2006)

Pour de tels systèmes, nos simulations ont demandé entre 30 et 45 heures de calcul par nanoseconde simulée en utilisant 16 processeurs sur les serveurs ALTIX du RQCHP (http://rqchp.ca). Nos tests ont demandé plus de 250 nanosecondes de simulations afin que le zinc et le substrat soient modélisés de manière convenable.

3.3.2 Choix des simulations

Pour chaque homologue (ecFBPA et hpFBPA), nous avons lancé une simulation de:

1. L'apoenzyme (coordonnés provenant de la structure cristalline sans ligand PDB ID : 3C4U, mais sans le zinc)
2. La protéine libre (coordonnés provenant de la structure cristalline sans ligand) *
3. La protéine libre avec phosphate au site de liaison du DHAP *
4. La protéine libre avec DHAP *
5. La protéine avec DHAP (coordonnés provenant de la structure cristalline en complexe avec le DHAP) *

Chaque simulation a une durée minimum de 5ns et celles des complexes avec le DHAP durent plus de 10ns. Les simulations sans zinc servent à tester son importance pour la stabilité de notre protéine. Celle de la protéine libre nous permet d'évaluer la capacité intrinsèque de la boucle à se replier vers la protéine. Les simulations de la protéine libre avec DHAP ou phosphate ont pour but de reproduire la migration du zinc suite à la liaison d'un ligand. Enfin nous voulions voir si le résidu Glu182/Glu142 (ecFBPA/hpFBPA) pouvaient contacter le DHAP en simulant la conformation du complexe cristallin DHAP-FBPA.

Les simulations marquées d'un astérisque ont aussi été lancées en omettant la contrainte de distance entre le zinc et l'histidine His226/His180 (ecFBPA/hpFBPA) afin de rendre compte de la flexibilité de sa chaine latérale observée dans nos structures.

3.3.3 Premières observations

Toutes nos simulations se comportent convenablement si l'on s'intéresse à la stabilité et la compacité de la protéine. De même, le comportement des divers termes thermodynamiques et énergétiques témoigne de l'utilisation d'un protocole adéquat.

Par contre, la migration du zinc et les changements conformationnels qui y sont liés ne sont jamais observés. L'utilisation des contraintes de distance et d'angles qui servent à

coordonner le zinc semble le figer dans une seule position, même si His226/His180 est libérée. Les boucles ont tout de même tendance à se refermer vers la protéine puis à ramper sur la surface en utilisant principalement des interactions de type pont-salins. Cette observation demande une validation faisant appel à une analyse énergétique de ces contacts que nous implémentons actuellement.

Ce sont les simulations des complexes DHAP-FBPA qui se sont révélées les plus surprenantes et leurs faits marquants sont exposés dans la suite de ce chapitre.

3.3.4 Reproduction d'une géométrie propice à l'abstraction du proton par Glu182 chez ecFBPA

La recherche d'une distance maximale de 3.8 Å entre les groupements chargés de la boucle et le carbone C3 du DHAP a permis d'isoler 173 conformations sur les 10342 générées au cours de la simulation. Nous avons ainsi constaté que lors de la simulation la boucle se déplace vers le site actif et positionne Glu182 dans une géométrie propice à l'abstraction du proton (figure 3-13). En superposant ces conformations sur la structure cristallographique du complexe PGH-ecFBPA de Hall *& al*. (Hall et al., 1999), on peut voir que la boucle suit à peu près le même chemin. Ces auteurs ont cristallisé l'enzyme en utilisant des conditions de haute concentration de zinc (5 mM) (Naismith et al., 1992), ceci a permis à un ion métallique de se fixer à un site non spécifique. C'est probablement l'interaction de cet ion métallique avec l'Asp181 qui recrute la boucle dans cette conformation.

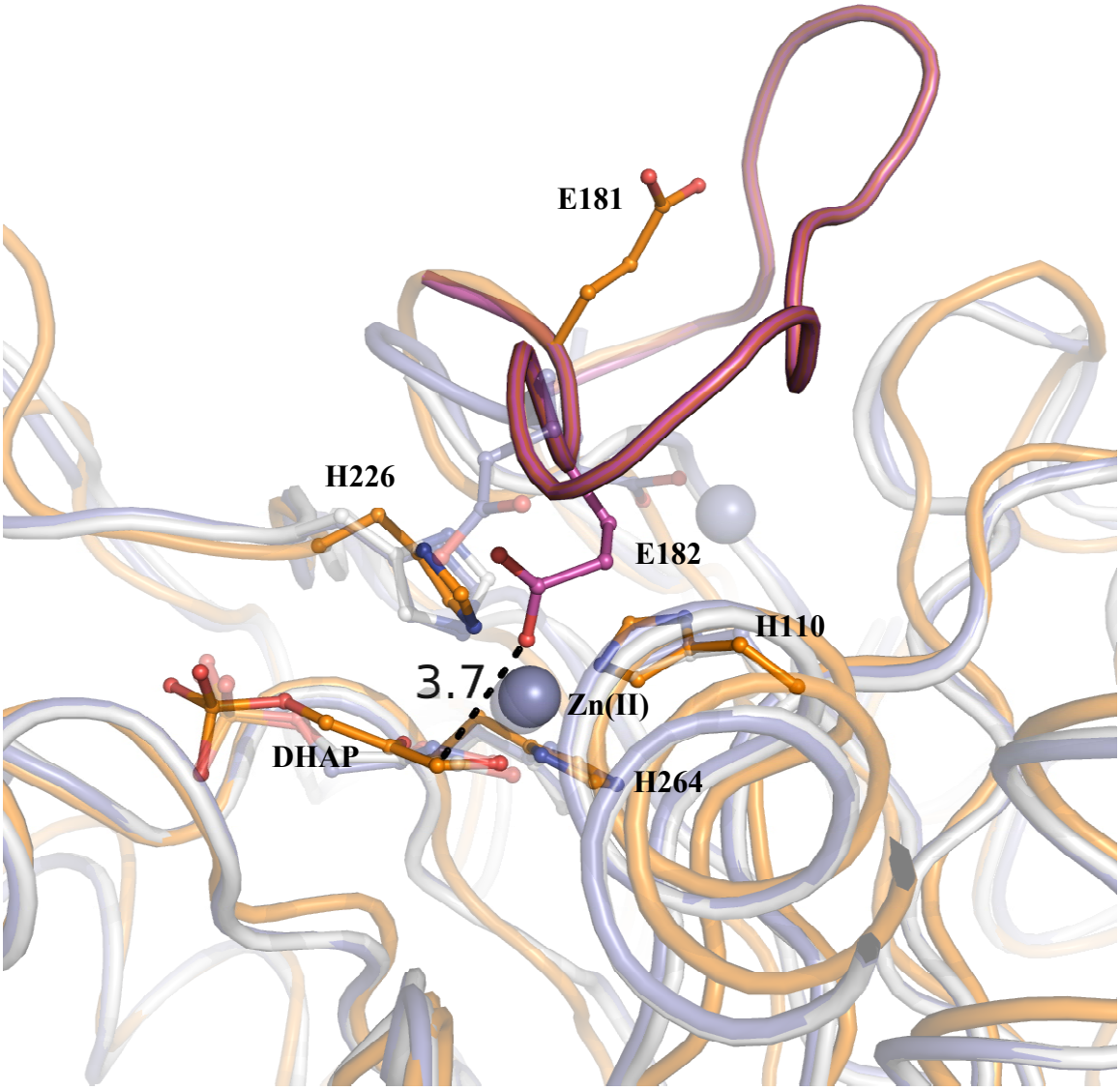

Figure 3-13. Géométrie propice à l'abstraction du proton pro-(S) du carbone 3 de DHAP tirée de la simulation du complexe DHAP-FBPA d'*Escherischia coli.*

Les structures cristallographiques du complexe DHAP-ecFBPA et PGH-ecFBPA (PDB: 1B57) sont respectivement représentées en blanc et en bleu. Leur superposition témoigne de la conservation de l'intégrité structurale de l'enzyme au cours de la dynamique. La conformation issue de la simulation est colorée en orange et sa boucle α7-β5 en violet.

Ce résultat demande la réalisation d'un duplicata (même simulation lancée avec une nouvelle génération de vitesses aléatoires).

3.3.5 Identification d'un autre résidu chez hpFBPA

Chez *Helicobacter pylori*, la recherche d'une telle géométrie a échoué. Nous avons alors cherché à savoir si cette interaction pouvait se faire via une molécule d'eau. C'est le résidu Glu149 et non Glu142 qui a été identifié par cette approche (voir figure 3-14).

Ceci nous a tout d'abord fait douter de la qualité et de la validité de nos simulations car Glu142 est bien conservée chez les FBPA de classe II et l'identification de Glu182 comme étant le résidu responsable de l'abstraction chez ecFBPA est indiscutable (Zgiby et al., 2002).

Figure 3-14. Alignement des séquences de la boucle α7-β5 entre ecFBPA et hpFBPA

Nous avons donc produit et caractérisé cinétiquement les deux mutants E142A et E149A dans le but de valider cette observation.

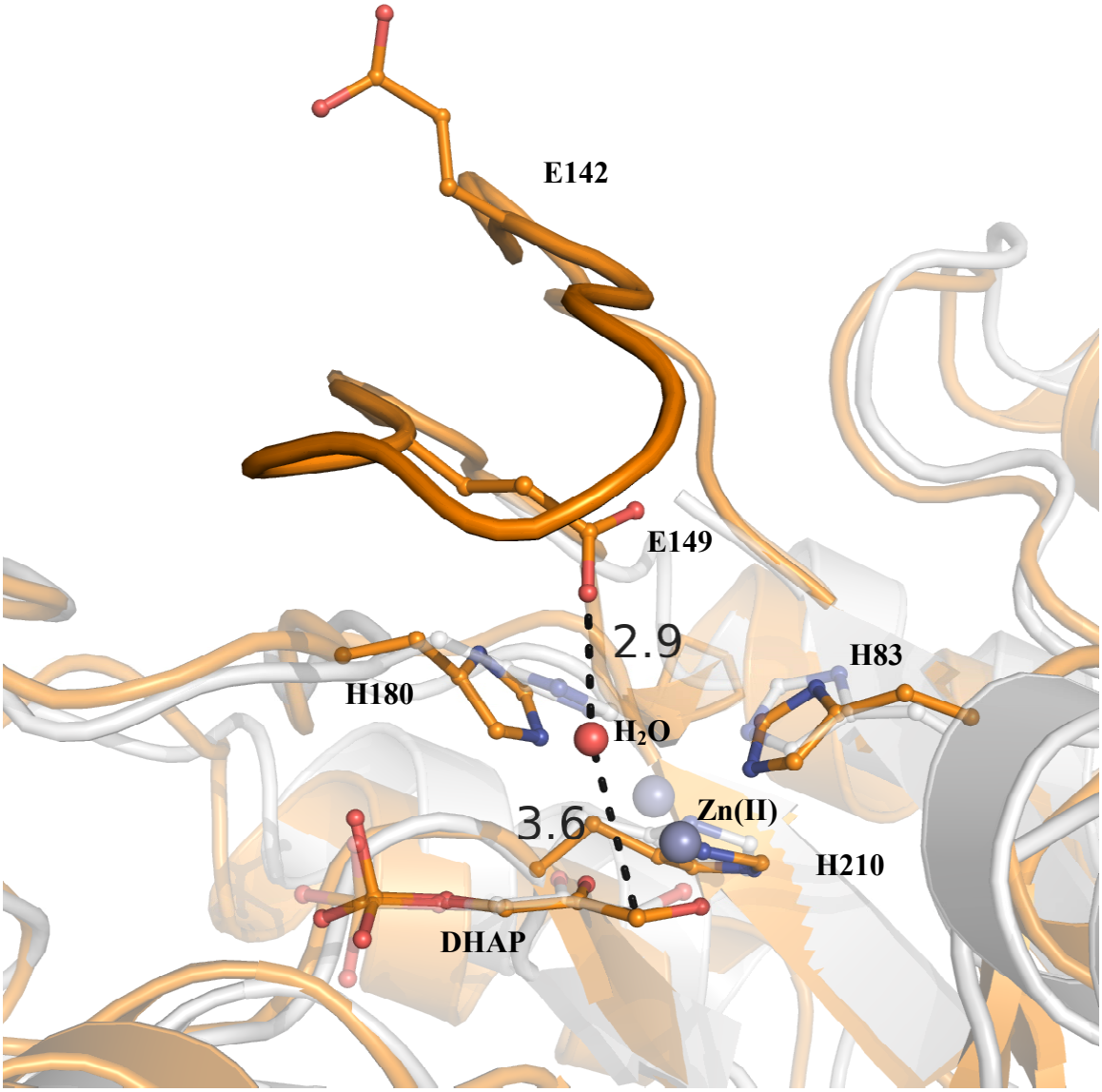

Figure 3-15. Géométrie propice à l'abstraction du proton pro-(S) du carbone 3 de DHAP tirée de la simulation du complexe DHAP-FBPA d'*Helicobacter pylori.*

La structure cristallographique du complexe DHAP-hpFBPA est représentée en blanc. La conformation issue de la simulation est colorée en orange.

Tableau 3-7. Paramètres cinétiques des mutants E149A et E142A chez hpFBPA

	k_{cat} (s^{-1})				K_m (µM)			
	0 % D_2O		100 % D_2O		0 % D_2O		100 % D_2O	
		St.error		St.error		St.error		St.error
WT	**2,15**	0,02	**1,75**	0,02	**14,1**	0,8	**15,1**	**0,9**
E149A	**0,0015**	0,0001	**0,0022**	0,0001	**-**	-	**-**	-
E142A	**0,21**	0,004	**0,10**	0,006	**630**	59	**238**	**130**

La perte d'activité due à la mutation E149A est bien plus importante que celle liée à la mutation de E142 et montre l'importance de ce résidu. Nous voulons aussi tester l'existence d'un effet isotopique du solvant sur la vitesse de la réaction. Si effectivement l'abstraction ce fait via une molécule d'eau, cet effet pourrait être moindre dans le cas du mutant E149A que dans celui de la protéine sauvage (WT pour « wild-type ») ou de E142A. Des difficultés d'ordre technique probablement liées à la faible activité du mutant E149A ne nous ont pas permis de déterminer sa constante de Michaelis de manière certaine et nous limite actuellement dans notre interprétation.

Nous allons générer d'autres mutations pour ces résidus mais aussi pour des résidus voisins dans la boucle et reproduire nos essais enzymatiques afin de consolider notre approche. Des études par marquage isotopique du DHAP seront aussi entreprises. Et permettront de nous assurer de l'implication de chacun des résidus dans l'échange stéréospécifique du proton pro-(S) en C3 du DHAP (St-Jean and Sygusch, 2007). De plus, la réalisation d'un duplicata de notre simulation est encore nécessaire.

Néanmoins, le fait d'avoir identifié un résidu de la boucle qui est non conservé mais dont la mutation a un effet important sur la vitesse de la catalyse est déjà un résultat en soi.

CHAPITRE IV

Développement d'antimicrobiens

"J'entends et j'oublie,
je vois et je me souviens,
je fais et je comprends."
Confucius.

4 Développement d'antimicrobiens

Cette partie de la thèse repose sur des travaux collaboratifs avec le groupe de chimie du professeur Michel Therisod et le groupe de microbiologie du docteur Mary Jackson.

Initialement, c'est l'obtention de nouveaux analogues d'état de transition, ou d'intermédiaires réactionnels, afin d'approfondir nos études du mécanisme catalytique qui nous a poussé à développer ces collaborations. Mais petit à petit, la perspective applicative de cette recherche s'est révélée stimulante et enrichissante. Le développement rationnel de nouvelles drogues demande à la fois rigueur et imagination, et permet l'utilisation de techniques originales.

Dans le premier article présenté (Fonvielle et al., 2008), mon travail a consisté à fournir une base structurale pour permettre de comprendre le mode de liaison d'un nouvel inhibiteur, le N-(3-Hydroxypropyl)-glycolohydroxamic acid bisphosphate (TF). Cet analogue du FBP basé sur le PGH, a été cristallisé en complexe avec hpFBPA. Afin de pouvoir comprendre où réside son originalité, j'ai aussi obtenu la structure du complexe PGH-hpFBPA pour les comparer. Enfin, j'ai également déposé les coordonnées de la structure non liée afin de présenter les changements conformationnels induits par la liaison des ligands.

Un second article lui fait directement suite (Coincon et al., *In press*). On y présente les inhibiteurs obtenus par optimisation du TF. En me basant sur plusieurs complexes obtenus chez *Helicobacter pylori* et sur des approches de modélisation, j'ai décrit et exliqué les différences obtenues entre les inhibiteurs. Mais surtout, nous avons mis en évidence des réponses différentes pour un même inhibiteur entre diverses FBPA.

4.1 Synthesis and Biochemical Evaluation of Selective Inhibitors of Class II Fructose Bisphosphate Aldolases: Towards New Synthetic Antibiotics

Matthieu Fonvielle Dr., Mathieu Coinçon, Racha Daher, Nicolas Desbenoit, Katarzyna Kosieradzka, Nathalie Barilone, Brigitte Gicquel Dr., Jurgen Sygusch Prof., Mary Jackson Dr., Michel Therisod Prof.

Groupe LCBB–ICMMO, UMR 8182, Université Paris-Sud, 91405 Orsay (France), Fax: (+33) 1-6915-7281; Biochimie, Université de Montréal, CO 6128, Stn centre-ville, Montréal, PQ H3C 3J7 (Canada); Unité de Génétique Mycobactérienne, Institut Pasteur, 75724 Paris (France)

Chemistry – A European Journal **2008,** 14 (28)*,* 8521-8529

4.1.1 Abstract

We report the synthesis and biochemical evaluation of selective inhibitors of class II (zinc-dependent) fructose bisphosphate aldolases. The most active compound is a simplified analogue of fructose bisphosphate, bearing a well-positioned metal chelating group. It is a powerful and highly selective competitive inhibitor of isolated class II aldolases. We report crystallographic studies of this inhibitor bound in the active site of the *Helicobacter pylori* enzyme. The compound also shows activity against *Mycobacterium tuberculosis* isolates.

4.1.2 Introduction

Bacterial infections, including nosocomial diseases contracted in hospital from antibiotic-resistant strains of pathogenic bacteria, are a public health problem of major concern. Tuberculosis (TB) is one of the most common infectious diseases known to man. The increasing occurrence of multiple-drug resistant TB, even in developed countries, is also alarming because there are only a few effective drugs available, and infection with drug-resistant *Mycobacterium tuberculosis* (*M. tb*) could give rise to a potentially untreatable form of disease. It must be noted that there have been no new major anti-TB drugs introduced into widespread use since rifampicin in the 1960s. *Helicobacter pylori* is another very widespread bacterium, responsible for most gastric ulcers and the sole known microorganism directly involved in the development of cancer.[1]

There is clearly an urgent need for new drugs with bactericidal mechanisms different from those of currently available agents.[2] This implies identification of new metabolic targets, specific to microbes, as likely sites of action for rationally designed drugs. The search for new therapeutic targets resulted in our interest in ATP synthesis from glucose in microbial pathogens, and more specifically in fructose-1,6-bisphosphate aldolase (Fba; E.C. 4.1.2.13).

Fba is an enzyme involved in glycolysis, in which it catalyses the retro-ketolic cleavage of fructose-1,6-bisphosphate (FBP) to yield dihydroxyacetone phosphate (DHAP) and glyceraldehyde-3-phosphate (G3P), and it also plays a role in gluconeogenesis and the Calvin cycle, in which it catalyses the condensation of DHAP with G3P.

Selective inhibition of microbial Fba would be expected to disrupt glycolysis, thereby affecting a major metabolic pathway and hindering survival and persistence of pathogens within their human host.3 Although ubiquitous in living organisms, Fbas can be divided into two classes that differ in their structures and catalytic mechanisms. Class I Fbas are found in mammals and higher plants and form Schiff-base intermediates between the carbonyl substrates (FBP or DHAP) and lysine residues in their active sites. Class II Fbas, in contrast, require divalent metal ions (usually zinc or cobalt) to polarize the carbonyl groups of the substrates (FBP or DHAP) and to stabilize the enediolate intermediates during catalysis (Figure 1). They are found mainly in micro-organisms such as bacteria, yeasts, micro-algae and protozoa (occasionally in combination with class I enzymes).1

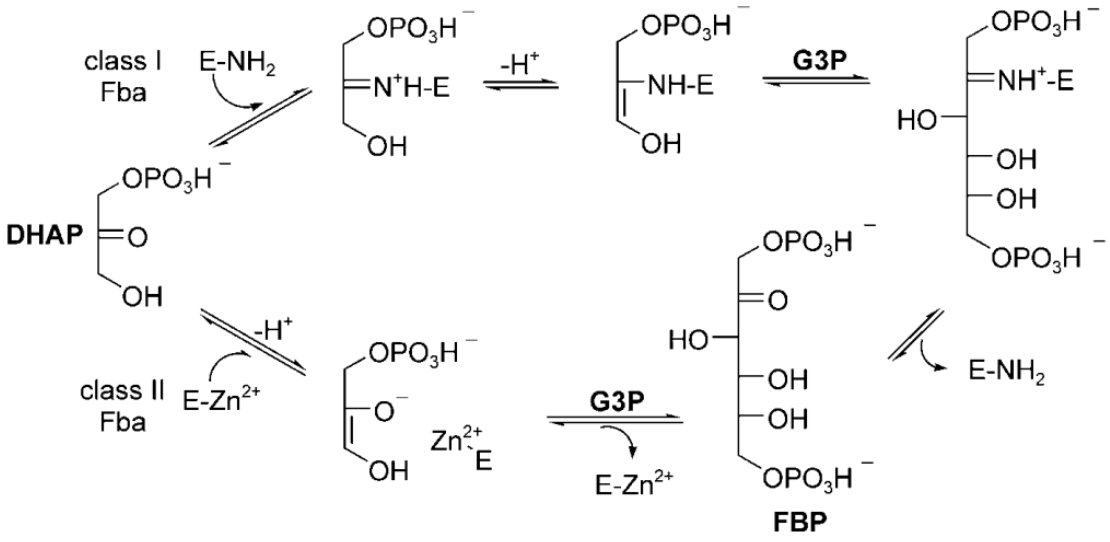

Figure 4-1. Mechanisms of class I (e.g., human) and class II (e.g., bacterial) FBP aldolases.

Because of their occurrence in many pathogenic bacteria (*M. tb*, *Pseudomonas aeruginosa*, *Burkholderia cepacia*, *H. pylori*, *Yersinia pestis*, *Clostridium difficile*), yeasts (*Candida albicans*) and parasites (*Giardia lamblia*) and their absence in animals, it has been suggested that class II Fbas may serve as drug targets.[4] This assumption was further supported by the inability to knock out the class II FBP aldolase genes of *E. coli* and *Streptomyces*.[5, 6] Also, the conditional loss of class II aldolase activity in temperature-sensitive mutants of *E. coli*harbouring point mutations in the class II FBP aldolase gene (*fda*) was found to result in loss of viability attributable to inhibition of rRNA synthesis.[7, 8]*M. tb*, like *E. coli*, is distinctive in that it possesses both a class I and a class II FBP aldolase.[9, 10] A recombinant form of the class II *M. tb* Fba protein was recently produced in *E. coli*.[11] However, hypoxic conditions, generally believed to be determinant in establishment of a latent infection by *M. tb*, have been shown to induce both increased levels and increased activity of the class II Fba.[9, 12]The apparent essentiality of class II Fbas in various micro-organisms and the likely importance of these enzymes during latent infection thus make Fbas an attractive and specific target for the development of novel anti-TB drugs.

Surprisingly, while dozens of class I Fba inhibitors have been reported,[13] only one potent inhibitor of class II enzymes was known when we started this work. Phosphoglycolohydroxamate (PGH; Figure 2) was first prepared independently by two groups in 1973.[4, 14] It is a very powerful inhibitor of the *E. coli* class II Fba (K_i≈10–50 nM). However, PGH is poorly stable in water, releasing (toxic) hydroxylamine through hydrolysis within a few hours. It has limited selectivity for class II Fbas over class I Fbas, and is a powerful inhibitor of several other enzymes. PGH has been shown to act both as a stable analogue of the high-energy intermediate of the reaction (Figure 2) and as a strong chelator of Zn^{2+}. The report of structural data on PGH-fuculose phosphate aldolase complexes[15] was a major breakthrough for understanding of the role of PGH as an inhibitor of metalloenzymes. [2]

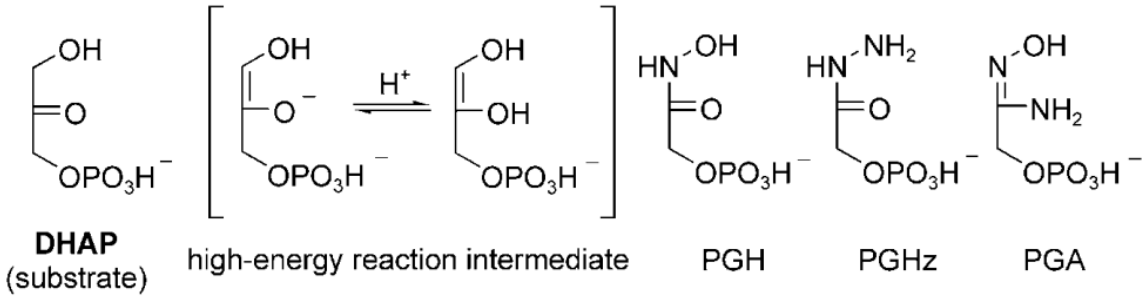

Figure 4-2. Substrate, reaction intermediate and inhibitors of class II Fbas

We first reasoned that through changing the hydroxamate chelating group for other functions we might be able to retain strong inhibition while at the same time increasing selectivity and resistance to hydrolysis. This goal was only partly achieved with PGHz (phosphoglycolohydrazide) and PGA (phosphoglycoloamidoxime; Figure 2). The selectivities of both compounds for class II aldolases were increased and they were much more stable in water, but their K_i values were much higher than that of PGH (Table 1).16

Inhibitor	K_i [μM] class I Fba	K_i [μM] class II Fba	Selectivity[b]
PGH[a]	2	0.05	273
PGHz	370	0.34	8900
PGA	>1000	2.3	3560

[a] Data from ref. [4]. [b] $(K_M/K_{iclass\ II})/(K_M/K_{iclass\ I})$. K_M class I (rabbit muscle) = 55 μM; K_M class II (*S cerevisiae*) = 450 μM.

Table 4-1. Activities of DHAP analogues as selective inhibitors of class II Fbas.

PGHz and PGA probably behaved as analogues of DHAP rather than as analogues of a high-energy intermediate. PGH was unambiguously shown to be present in its *s-Z* conformation within the active sites of several enzymes (Fbas from *E. coli* and *H. pylori*,17–19fuculose bisphosphate aldolase from *E. coli*,15 methylglyoxal synthase20 and triose phosphate isomerase21). Similarly, PGHz in complexation with *H. pylori* Fba chelates the Zn^{2+} ion in the *s-Z* conformation (M. Coinçon, J. Sygusch, unpublished results). Although we have no structural data on the structure of PGA in the active site of Fba yet, the *Z* configuration is very likely.

4.1.3 Results and Discussion

4.1.3.1 Chemistry

We therefore decided to design and synthesize analogues of the substrate of the forward reaction: FBP. Previous studies on class I Fbas had indicated that very simple structures can be potent inhibitors, provided that two phosphate groups, separated by an appropriate distance, are present.13 The selectivity for class II Fbas would be induced by the presence, at the appropriate position, of a function capable of chelating the divalent Zn^{2+} ion in the active site. Taking into consideration the good inhibitory properties of PGH and PGHz,16 we chose an N-substituted hydroxamate and an N-substituted hydrazide as basic structures. We further decided to omit the two secondary hydroxyl groups present in FBP, leading as a first step to the simplified analogues **1** and **2** (Figure 3).

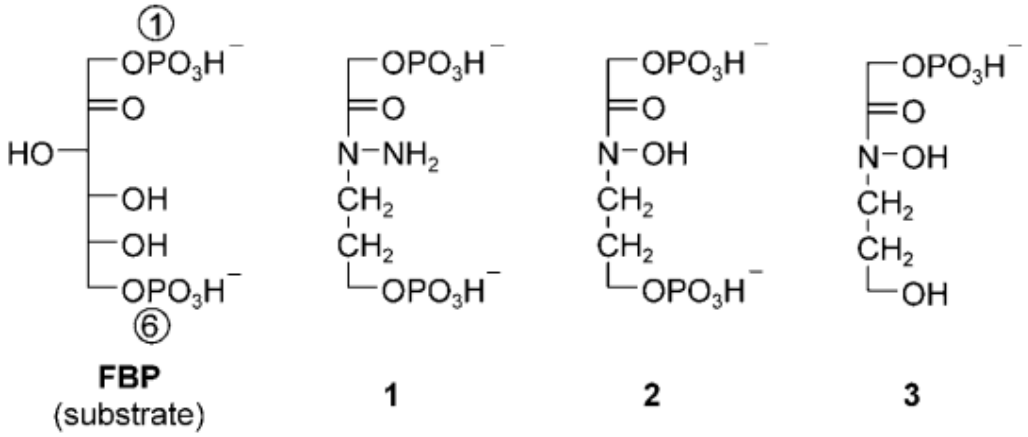

Figure 4-3. Substrate analogues designed as selective inhibitors of class II Fbas (with labelling of phosphates 1 and 6 on FBP).

Even if active in vitro, these bisphosphorylated compounds would be very unlikely readily to undergo passive diffusion across cellular membranes. The removal of one phosphoryl group could, however, favour permeation. The phosphoryl group at the 1-position of FBP has been reported to be essential for recognition by Fbas, while the one at the 6-position is not. Compound **3** can thus be considered a simplified analogue of fructose-1-phosphate, which is a rather weak inhibitor of class I Fbas, with K_i >2 mM.[13] Syntheses of these three products are shown in Scheme 1.

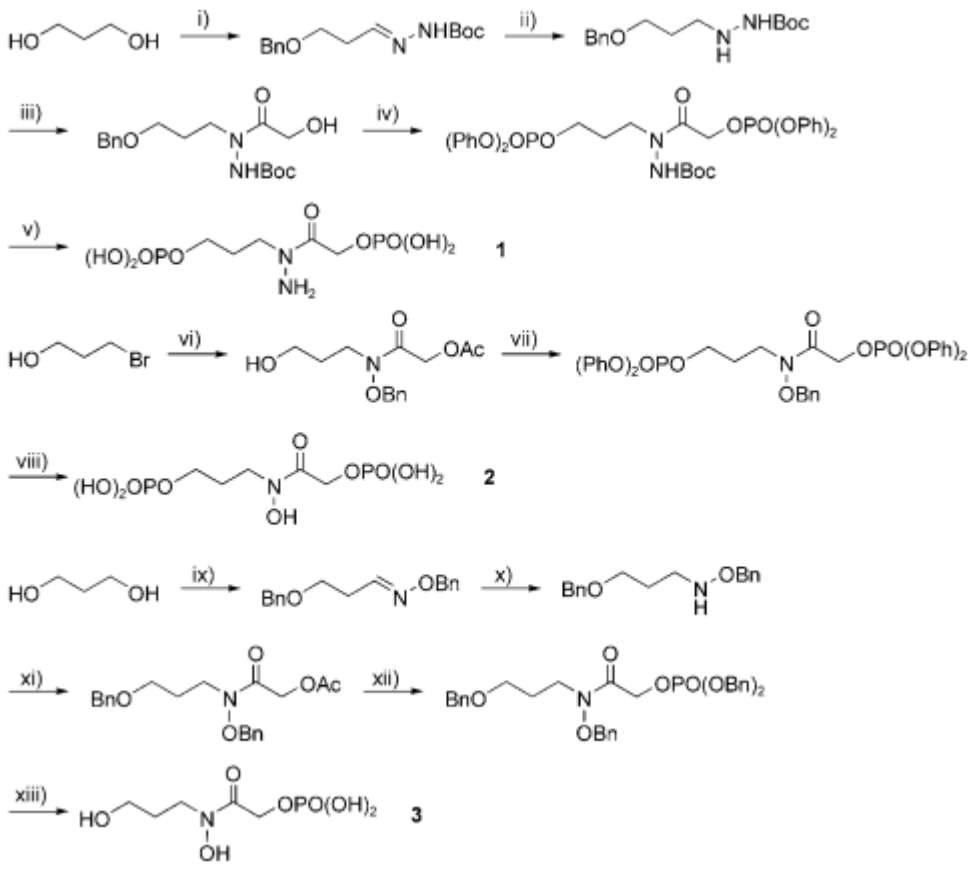

Scheme 4-1. Synthesis of hydrazide 1 and of hydroxamates 2 and 3.

Reagents and conditions: i) a) NaH, BnBr (0.2 equiv), 75 %; b) PCC/CH_2Cl_2, 47 %; c) $BocNHNH_2$/THF, 68 %. ii) DIBAH/toluene, 62 %. iii) a) $ClCOCH_2OAc$/THF/pyridine, 76 %; b) NEt_3/MeOH/H_2O 2:8:1, 100 %. iv) a) $ClPO(OPh)_2$/pyridine, 82 %; b) H_2/Pd-C, 96 %; c) $ClPO(OPh)_2$/pyridine, 81 %. v) a) H_2/PtO_2, 83 %; b) H_2O/TFA 2:1, 100 %. vi) a) $BnONH_2$/EtOH reflux, 63 %; b) $ClCOCH_2OAc$/MeOH/NEt_3, 70 %. vii) a) $ClPO(OPh)_2$/pyridine, 81 %; b) NEt_3/MeOH/H_2O 2:8:1, 100 %; c) $ClPO(OPh)_2$/pyridine, 52 %. viii) a) H_2/Pd-C, 98 %; b) H_2/PtO_2, 98 %. ix) a) NaH, BnBr (0.2 equiv), 67 %; b) PCC/CH_2Cl_2, 88 %. c) $BnONH_2$, EtOH/pyridine 80 °C, 24 h. x) $NaBH_3CN$, EtOH/AcOH 1:1, RT, 4 h, 61 % from ix. xi) $ClCOCH_2OAc$/THF/pyridine, 90 %. xii) a) NEt_3/MeOH/H_2O 2:8:1, 68 %; b) $P(OBn)_2N$*i*Pr/imidazole/triazole/AcCN, 24 h RT; c) *t*BuOOH, 77 % from xi. xiii) H_2/Pd-C, 100 %..

4.1.3.2 Biochemical studies.

All three compounds were tested as inhibitors of class I (from rabbit muscle) and class II (from *Saccharomyces cerevisiae*, *H. pylori* and *Mycobacterium bovis* BCG) aldolases.

Fba from *H. pylori* was a recombinant form produced in *E. coli*. The activities of the *M. bovis* BCG (Pasteur strain; an attenuated strain of *M. bovis* used for vaccination against tuberculosis) and yeast enzymes were monitored in crude or partially purified cell-free extracts obtained by breaking fresh cells in a French press. The primary sequence of the *M. bovis* BCG enzyme is 100 % identical to that of the pathogenic species: *M. tuberculosis* H37Rv. The compounds behaved as purely competitive inhibitors of all tested enzymes. Results are shown in Table 2.

Inhibitor	Class I Fba	Class II Fba		
	Rabbit muscle	*S. cerevisiae*	*H. pylori*	*M. bovis*
		K_i [μM] (selectivity)[a]		
1	524	49 (90)	21 (23)	3.1[b] (180)
2	264	0.025[b] (86500)	0.013 (18500)	0.013 (22200)
3	2500[b]	1.6 (12800)	4.7[b] (480)	0.17 (16000)

[a] $(K_M/K_{iclass\ II})/(K_M/K_{iclass\ I})$. [b] Estimated from IC_{50} value. $K_{M\ rabbit\ muscle}$ = 55 μM; $K_{M\ S.\ cerevisiae}$ = 450 μM; $K_{M\ H.\ pylori}$ = 50 μM; $K_{M\ M.\ bovis}$ = 60 μM.

Table 4-2. In vitro inhibition of various class I and class II Fbas by FBP analogues.

The hydrazide **1** acted as a modest inhibitor, both in terms of K_i and in terms of selectivity. In contrast, the hydroxamate **2** was very active, with a K_i comparable to that of PGH but a greatly increased selectivity for class II Fbas. The important difference between compounds **1** and**2** can be explained in part by the different affinities of a hydrazide and a hydroxamate for Zn^{2+}. Also, the ^{1}H NMR spectrum of **1** as a cyclohexylammonium salt

indicates the presence of three cyclohexylamines (see Experimental Section), which means that one acidity of a phosphate is neutralized by the NH_2 of the neighbouring hydrazide (pK_a values of normal hydrazides are usually close to 7). Should this amphoteric form exist within the active site of the enzyme, it could lower the affinity of the hydrazide function for the zinc ion. As would be expected for N-alkylated hydroxamic acids, **2** and **3** were also much more stable in water than PGH (as verified by NMR of the product dissolved in D_2O). The higher K_i value of **3** confirmed that a phosphoryl group at the 6-position is an important, although non-essential, element of class II enzyme inhibitors. Against the *M. bovis* BCG enzyme, **3** was "only" ten times less active than **2**, a particularly encouraging result for an analogue of fructose-1-phosphate. We believe that compound **3** might represent an interesting basis lead compound for the further synthesis of improved monophosphorylated compounds and lipophilic prodrugs.

4.1.3.3 Biological studies—growth inhibition of cultivated bacteria

Minimal inhibitory concentration values of compound **2** against *M. tb* H37Rv were determined in 7H9-ADC broth at 37 °C by the colorimetric resazurin microtiter assay described by Martin and collaborators.[22] The bacteria were grown aerobically under conditions compatible with class II Fba expression[9] and similar to those used for the preparation of the *M. bovis* BCG extracts (see above). Compound **2** inhibited the growth of *M. tb* H37Rv at a concentration of 1 mM. Although modest, this result was unexpected in view of the high polarity of compound **2** at physiological pH. The presence of the class I aldolase (not verified) might in part have offset the effect of **2**. We have no evidence yet that growth inhibition of cultivated *M. tuberculosis* by **2** correlates with inhibitory properties observed in vitro. If it is assumed, however, that this product kills *M. tb* through the inhibition of Fba, this effect could also be accounted for by an extra-cytosolic location of the enzyme.[12] We are now investigating the question of the permeation of compound **2** into *M. tb* cells (active transport or passive diffusion) and whether the inhibition of mycobacterial growth results directly from the effect of this compound on the *M. tb* class II

Fba. Experiments to measure the MIC of **2** against *M. tb* grown under anaerobic conditions—under which substrate-level phosphorylation-dependent (and thus Fba-dependent) synthesis of ATP would be expected to prevail—are also underway.

4.1.3.4 Crystallographic studies

To examine the high affinity and selectivity of **2** for class II aldolases, crystallographic structures of Fba from *H. pylori* alone and bound with compound **2** were solved to 1.8 and 2.3 Å resolutions, respectively. Crystals of *H. pylori* Fba used for the studies were grown by vapour diffusion from a protein solution (10 mg mL^{-1}) diluted with an equal volume of precipitant buffer [PEG 1000 (12 %), PEG 8000 (12 %), calcium acetate (0.2 M) and Tris/HOAc (pH 8, 50 mM)] equilibrated against a reservoir of the same buffer. The *H. pylori* Fba structure was solved by molecular replacement with use of *Thermus aquaticus* Fba as search model. The refined native structure was then used as search model to determine the structure of *H. pylori* Fba bound with **2** by molecular replacement.

Superposition of native Fba with bound Fba (RMSD 0.48 Å based on all Cα atoms) revealed several significant localized conformational changes (Figure 4).

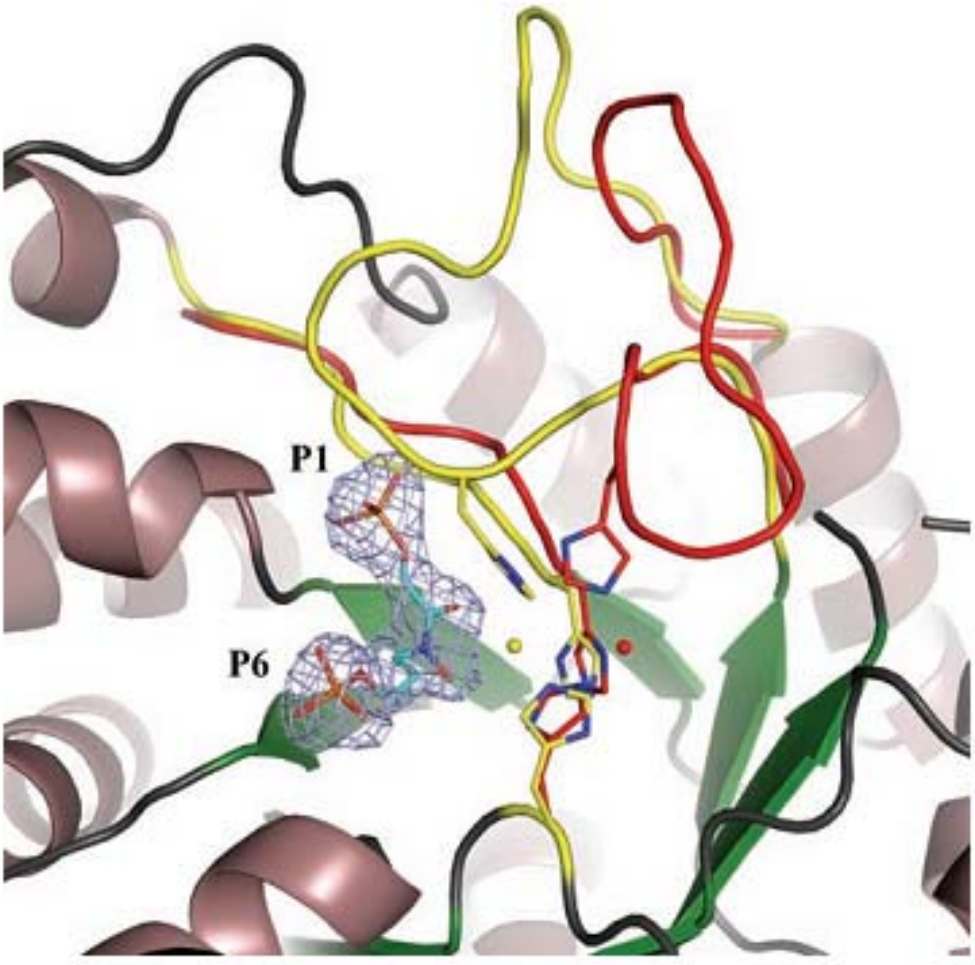

Figure 4-4. Difference electron density (F0−FC) annealed omit map showing fit of compound 2 bound in the active site of *H. pylori* Fba.

Conformational changes induced upon binding of 2 are also highlighted. Loops and catalytic zinc ion that undergo positional changes are shown in red for the native Fba structure and in yellow for the bound Fba structure. P1 and P6 phosphoryls are identified. Figure and superposition were prepared with the program PyMOL.[23]

A loop (residues 177–191) in native Fba undergoes a 16 Å displacement (calculated from Cα atoms) upon binding of **2**, allowing Gly181 and Lys184 to interact with the P_1 phosphoryl group. The same loop also repositions His180, which binds the catalytic zinc ion. A second, adjacent loop (residues 210–214) adjusts by 1.7 Å, enabling Ser213 also to bind the P_1 phosphoryl group. Concomitantly with this movement, the catalytic zinc ion is displaced by 3.7 Å from its buried position in the native structure towards the active site surface, chelating the C=O and N—O oxygens of **2** while maintaining its interaction with the chelating His residues of the active site. Interactions between **2** and neighbouring residues in the *H. pylori* Fba active site are summarized in Figure 5.

The structural data obtained with **2** in *H. pylori* Fba indicate, consistently with data previously reported for PGH bound in *E. coli* Fba,[17, 18]that the interaction with the hydroxamate-based inhibitor results in a loosely coordinated trigonal bipyramid geometry around the catalytic Zn^{2+} ion (Figure 6). The conformational change stabilized by attachment of the P_1 phosphoryl results in tighter oxyanion binding (seven interactions; Figure 5) in relation to the interactions stabilizing attachment with the P_6 phosphoryl (three interactions; Figure 5) and corroborates P_1 phosphoryl as essential for active site binding. The hydroxamate moiety atoms C2, O2, N3 and O3 in compound **2** are coplanar (dihedral angle <1°) and in the s-*Z* conformation (Figure 6 A), mimicking an enediolate transition-state analogue, which would favour a potent K_i value. Because the catalytic Zn^{2+} ion is significantly out of the plane containing the putative enediolate, however, optimal chelation is unlikely. The same hydroxamate atoms in active site complexes formed by PGH bound with *E. coli*[17, 18] and *H. pylori* Fba,[19]although not coplanar (dihedral angle ≈45°), do chelate the catalytic Zn^{2+} ion in an approximately s-*Z* conformation (Figure 6 B). Further synthetic exploration of simplified substrate analogues using the PGH scaffold that optimizes Zn^{2+} ion chelation while ensuring hydroxamate coplanarity should afford compounds with more potent K_i values.

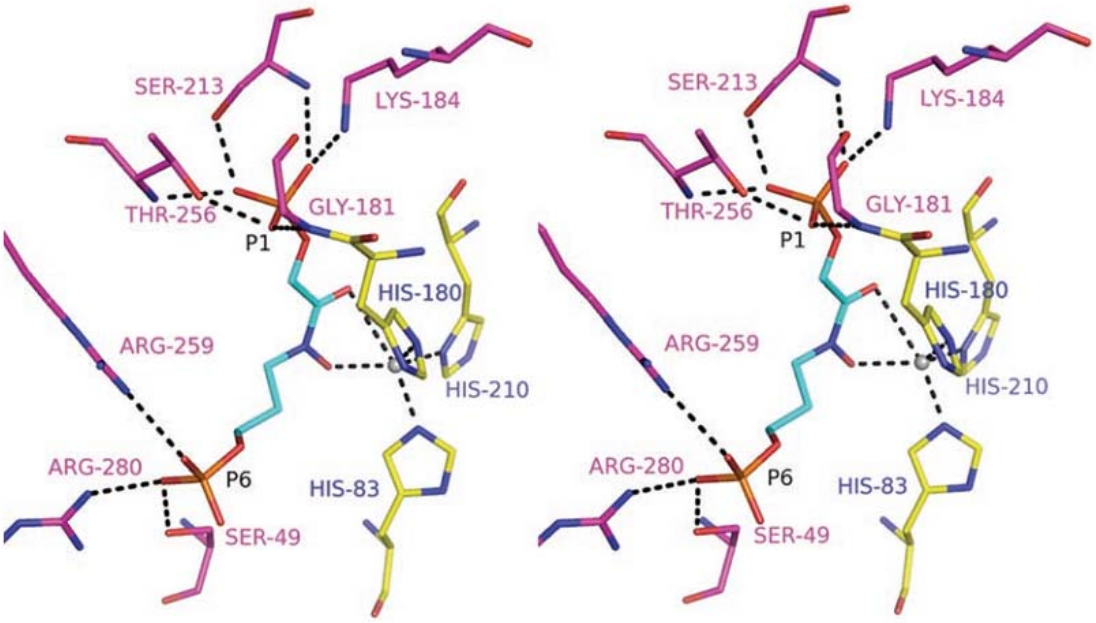

Figure 4-5. Interactions of inhibitor 2 with proximal residues in the *H. pylori* Fba active site

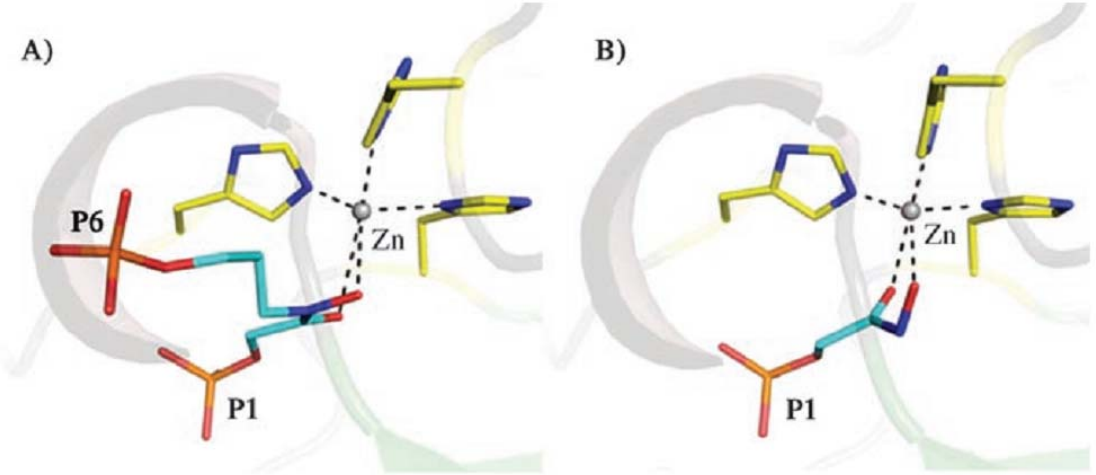

Figure 4-6. Coordination of catalytic Zn^{2+} ion in *H. pylori* Fba structure.

Binding of A) compound 2, and B) PGH. View was obtained by first overlaying bound structures.

Compound **2** differs from the aldolase substrate and class I aldolase inhibitor hexitol-bisphosphate (K_i ≈0.5 μM)17 in the absence of hydroxyl moieties at its C_4 and C_5 atoms. In class I aldolases, both C_4 and C_5 hydroxyls participate directly and indirectly in hydrogen-bonding interactions with active site residues.25 We postulate that **2**, because it lacks hydroxyl moieties at positions C_4 and C_5, is less able to participate in hydrogen bonding interactions with active site residues of class I aldolases and that this, together with the apparent coplanarity of the hydroxamate moiety atoms in **2**—that would further hinder optimal fit into the class I aldolase active site—forms a basis for the high selectivity of **2** for class II aldolases.

Although our initial goal was the synthesis of simplified analogues of the substrate FBP, the potent K_i value of compound **2** and the planarity of its hydroxamate moiety suggests that it behaves more like a transition-state analogue. One reasonable hypothesis is that the planar geometry enables internal electronic delocalization of the hydroxamic acid function in **2** that mimics in part the movement of electrons during the retro-ketolic cleavage of FBP (Figure 7).

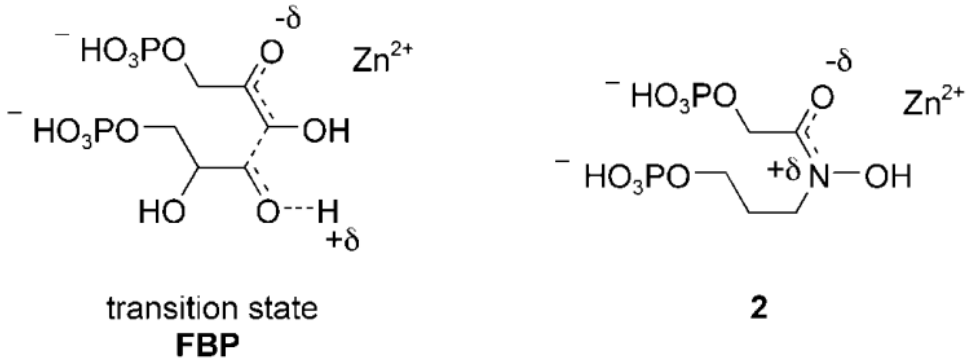

Figure 4-7. Presumed transition state of the retro-ketolic cleavage of FBP and mesomeric structure of compound 2.

4.1.4 Conclusion

Taking advantage of previous results on analogues of DHAP as inhibitors of Fba, we have prepared several analogues of FBP. We introduced a well-positioned chelating function in the hope of making these inhibitors selective for class II (zinc-dependent) Fbas. Compound **2** gave the best results, with low K_i values (10–20 nM) and good selectivity for class II over class I (more than 20 000). The inhibition results, however, with K_M/K_i >2000, indicate that **2** is not only a simple substrate analogue, but probably acts as a transition-state analogue. This inhibitor was co-crystallized with *H. pylori* Fba (representative of class II Fbas). The resolved structure of the complex unambiguously indicates that the inhibitor is linked to the active site around the catalytic zinc ion. Compound **2** is weakly active against cultivated *M. tuberculosis* (MIC 1 mM). The discrepancy between in vitro inhibition tests and biological assays can be partly explained by the high polarity of **2**, bearing four negative charges at physiological pH, and thus unlikely to cross biological membranes by simple diffusion. Compound **3**, in which the non-essential phosphoryl group is missing, is "only" ten times less efficient than **2** in inhibition tests. It could be a lead compound for further synthesis of lipophilic derivatives acting as prodrugs.

4.1.5 Experimental section

4.1.5.1 Chemical syntheses

N-(3-Hydroxypropyl)-glycolohydrazide-bisphosphate (compound 1)

Compound 1 a: NaH (8 g) was added in portions to propane-1,3-diol (60 g, 0.79 mol) dissolved in anhydrous DMF (350 mL), followed by drop-by-drop addition of benzyl bromide (34.2 g, 0.2 mol). After 12 h at RT with stirring, the solvent was evaporated, the residue was dissolved in Et_2O, and the organic phase was washed with water, dried and concentrated. The product was purified by flash chromatography (Et_2O/pentane 1:1) to give

1 a (25 g, 75 %). ^{1}H NMR (250 MHz, $CDCl_3$): δ=7.36 (m, 5 H), 4.55 (s, 2 H), 3.80 (dt, *J*=11 Hz, 6 Hz, 2H), 3.68 (t, *J*=6 Hz, 2 H), 1.89 ppm (q, *J*=6 Hz, 2 H).

Compound 1 b: PCC (19.4 g, 90.2 mmol) was suspended in anhydrous dichloromethane (250 mL) with vigorous stirring. Compound **1 a**(10 g) was added dropwise, and the mixture was stirred overnight at RT. The black mixture was then filtered on a column of silica gel (200 mL), washed through with dichloromethane. After evaporation, the crude product was purified by flash chromatography (Et_2O/pentane 1:1) to give **1 b** (4.61 g, 47 %). ^{1}H NMR (250 MHz, $CDCl_3$): δ=9.78 (s, 1 H), 7.36 (m, 5 H), 4.55 (s, 2 H), 3.82 (t, *J*=6 Hz, 2 H), 2.68 ppm (t, *J*=7 Hz, 2 H); ^{13}C NMR (62.9 MHz, $CDCl_3$): δ=201.15, 137.99, 128.47, 127.79, 127.72, 73.21, 63.89, 43.87 ppm.

Compound 1 c: Boc-hydrazine (1.74 g, 13.2 mmol) was added to compound **1 b** (2.18 g, 13.45 mmol) in THF (25 mL). The mixture was stirred overnight at RT and was then concentrated. The residue was recrystallized from anhydrous pentane, giving **1 c** (2.5 g, 68 %). ^{1}H NMR (250 MHz, $CDCl_3$): δ=7.31 (m, 5 H), 7.25 (t, *J*=5 Hz, 1 H), 4.51 (s, 2 H), 3.67 (t, *J*=6 Hz, 2 H), 2.60 (q, *J*=6 Hz, 2 H), 1.48 ppm (s, 9 H);^{13}C NMR (62.9 MHz, $CDCl_3$): δ=152.58, 144.64, 134.07, 129.74, 128.54, 128.41, 127.69, 127.16, 81.02, 73.00, 67.59, 32.76, 28.00 ppm; HR-MS (ESI): *m*/*z*: calcd for $C_{15}H_{22}N_2O_3$ [M+Na^+]: 301.1523; found: 301.1524.

Compound 1 d: DIBAL-H (20 % in toluene, 45 mL, 55 mmol) was added dropwise under Ar at 0 °C over 1 h to **1 c** (5 g, 18.3 mmol) in toluene (100 mL). After the system had been kept for 5 h at RT, NaOH solution (1 M, 100 mL) was added slowly (exothermic reaction). After evaporation of the toluene, the remaining aqueous phase was extracted with dichloromethane. The organic phase was then washed successively with NaOH (1 M) and brine. Compound **1 d** was purified by flash chromatography (pentane/ethyl acetate/NEt_3 30:70:0.1, 3.18 g, 62 %). ^{1}H NMR (250 MHz, $CDCl_3$): δ=7.32 (m, 5 H), 6.3 (br s, 1 H), 4.52 (s, 2 H), 3.56 (t, *J*=6 Hz, 2 H), 2.96 (t, *J*=6 Hz, 2 H), 1.79 (quint,*J*=6 Hz, 2 H), 1.47 ppm (s, 9 H); ^{13}C NMR (62.9 MHz, $CDCl_3$): δ=156.67, 138.38, 128.27, 127.55, 127.44, 80.24,

72.88, 68.47, 49.41, 28.29, 28.04 ppm; HR-MS (ESI): *m*/*z*: calcd for $C_{15}H_{24}N_2O_3$ [*M*+Na^+]: 303.1679; found: 303.1681.

Compound 1 e: Pyridine (1.19 mL, 15.7 mmol) was added to **1 d** (3.18 g, 11.34 mmol) in anhydrous THF (50 mL), followed dropwise by acetoxyacetyl chloride (2.15 g, 15.7 mL) in THF (25 mL). After the system had been kept for 3 h at RT, water (20 mL) and dichloromethane (100 mL) were added, and the organic phase was washed with water and brine, dried over sodium sulfate and concentrated. Compound **1 e** was obtained after flash chromatography (pentane/Et_2O/Et_3N 1:1:0.01, 3.38 g, 76 %). ^{1}H NMR (250 MHz, $CDCl_3$): δ=7.40 (m, 5 H), 4.85 (m, 2 H), 4.57 (s, 2 H), 4.26 (m, 1 H), 3.61 (m, 2 H), 3.19 (m, 1 H), 2.24 (s, 3 H), 1.93 (m, 2 H), 1.54 ppm (s, 9 H); ^{13}C NMR (62.9 MHz, $CDCl_3$):δ=170.39, 168.87, 154.22, 137.64, 128.23, 127.23, 81.90, 72.97, 68.35, 61.10, 46.02, 27.88, 26.64, 20.39 ppm; HR-MS (ESI): *m*/*z*: calcd for $C_{19}H_{28}N_2O_6$ [*M*+Na^+]: 403.1840; found: 403.1850.

Compound 1 f: Compound **1 e** (3.38 g, 8.87 mmol) was stirred overnight at RT in a methanol/Et_3N/water mixture (8:2:1). After concentration,**1 f** was obtained (3 g, 100 %). ^{1}H NMR (250 MHz, $CDCl_3$): δ=7.25 (m, 5 H), 4.45 (s, 2 H), 4.11 (m, 2 H), 4.06 (br s, 2 H), 3.61 (t, *J*=7 Hz, 2 H), 3.19 (m, 1 H), 1.93 (quint, *J*=7 Hz, 2 H), 1.45 ppm (s, 9 H); ^{13}C NMR (62.9 MHz, $CDCl_3$): δ=174.39, 154.16, 137.48, 128.15, 127.23, 81.75, 72.91, 68.15, 59.65, 46.02, 27.88, 26.59 ppm; HR-MS (ESI): *m*/*z*: calcd for $C_{17}H_{26}N_2O_5$ [*M*+Na^+]: 361.1734; found: 361.1738.

Compound 1 g: Compound **1 f** (3 g, 8.87 mmol) was dissolved in anhydrous pyridine (100 mL). Diphenylphosphoroyl chloride (2.8 mL, 35.5 mmol) and DMAP (0.1 mmol) were added at once. The solution was stirred overnight at RT. Water was added, and after 10 min the reaction mixture was concentrated. Water and dichloromethane were added to the residue. The organic phase was washed with water, dried and concentrated. Compound **1 f** was obtained after flash chromatography (AcOEt, 4.16 g, 82 %). ^{1}H NMR (250 MHz,$CDCl_3$): δ=7.32 (m, 15 H), 4.77 (m, 1 H), 4.95 (s, 1 H), 4.49 (s, 2 H), 4.16 (m, 1 H), 3.36 (t, *J*=6 Hz, 2 H), 3.23 (m, 1 H), 1.87 (dquint, *J*=6 Hz, 2 H), 1.47 ppm (s, 9 H); ^{13}C NMR (62.9 MHz, $CDCl_3$): δ=167.00, 168.90, 154.26, 150.27, 15.,25, 137.54, 129.5,

128.35, 127.69, 125.25, 120.08, 82.18, 73.15, 68.52, 65.42, 46.15, 27.96, 26.74 ppm; ^{31}P NMR (101.3 MHz, $CDCl_3$): δ=−11.70 ppm; HR-MS (ESI): *m*/*z*: calcd for $C_{29}H_{35}N_2O_8P$ [*M*+Na^+]: 593.2023; found: 593.2037.

Compound 1 h: Compound **1 g** (4.16 g, 7.29 mmol) was dissolved in ethanol (50 mL). Pd/C (10 %, 425 mg) was added, and the suspension was stirred overnight under dihydrogen (4 bar). The catalyst was filtered, and the solution was concentrated to give **1 h** (3.38 g, 96 %). ^{1}H NMR (250 MHz, $CDCl_3$): δ=8.07 (br s, 1 H), 7.30 (m, 10 H), 5.05 (m, H), 4.76 (m, 1 H), 3.99 (m, 1 H), 3.59 (m, 2 H), 3.28 (m, 1 H), 1.71 (m, 2 H), 1.45 ppm (s, 9 H); ^{13}C NMR (62.9 MHz, $CDCl_3$): δ=168.85, 168.76, 129.65, 125.42, 120.08, 82.18, 65.58, 59.58, 45.92, 28.91, 28.00 ppm; ^{31}P NMR (101.3 MHz, $CDCl_3$): δ=−11.72 ppm; HR-MS (ESI): *m*/*z*: calcd for $C_{22}H_{29}N_2O_8P$ [*M*+Na^+]: 503.1554; found: 503.1561.

Compound 1 i: Compound **1 h** was phosphorylated with diphenylphosphoroyl chloride as described for **1 g**. Yield 2.99 g (81 %); ^{1}H NMR (250 MHz, $CDCl_3$): δ=8.21 (br s, 1 H), 7.24 (m, 20 H), 5.28 (m, 1 H), 5.03 (m, 1 H), 4.31 (m, 1 H), 3.88 (m, 2 H), 3.88 (m, 1 H), 3.40 (m, 1 H), 2.01 (m, 2 H), 1.48 ppm (s, 9 H); ^{13}C NMR (62.9 MHz, $CDCl_3$): δ=168.3, 154.3, 150.2, 129.70, 125.3, 119.9, 81.9, 66.7, 65.4, 45.5, 27.9, 27.2 ppm; ^{31}P NMR (101.3 MHz, $CDCl_3$): δ=−11.76, −11.66 ppm; HR-MS (ESI): *m*/*z*: calcd for $C_{34}H_{38}N_2O_{10}P_2$ [*M*+Na^+]: 735.1843; found: 735.1847.

***N*-(3-Hydroxypropyl)-glycolohydrazide bisphosphate (compound 1) (tris-cyclohexylammonium salt)**: Compound **1 i** (1.87 g, 2.63 mmol) was dissolved in ethanol (20 mL). PtO_2 (200 mg) was added, and the suspension was treated under dihydrogen (40 bar) overnight with vigorous stirring. After filtration and evaporation, solid **1 j** (977 mg, 83 %) was recovered. The product was dissolved in a H_2O/CF_3COOH mixture (2:1, 10 mL), and the solution was kept for 12 h at RT. After evaporation, the residue was dissolved in aqueous cyclohexylamine (1 M), concentrated and recrystallized from EtOH. Yield 0.9 g (49 %); ^{1}H NMR (250 MHz, D_2O): δ=4.49 (d, $J_{H,P}$=6 Hz, 2 H; -CO-*CH_2*-OPO_3H^-), 3.62 (dt, $J_{H,P}$=6 Hz, $J_{H,H}$=7 Hz, 2 H; $^{2-}O_3PO$-*CH_2*-CH_2-), 3.40 (t, *J*=7 Hz, 2 H; -CH_2-*CH_2*-N), 1.74 ppm (m, 2 H; -CH_2-*CH_2*-CH_2-) [CHA+: 2.90 (m, 3 H), 1.40–1.80 (m, 15 H), 0.95–1.19 (m,

15 H)]; ^{13}C NMR (62.9 MHz, D_2O): δ=174.20, 174.09, 63.41, 48.36, 27.90, 27.82 ppm [CHA: 51.18, 31.34, 25.20, 24.7 ppm]; ^{31}P NMR (101.3 MHz, D_2O): δ=− 0.46 (s, 1 P), −0.17 ppm (s, 1 P); HR-MS (ESI, negative): *m*/*z*: calcd for $C_5H_{13}N_2O_9P_2^-$: 307.01018; found: 307.01021.

***N*-(3-Hydroxypropyl)-glycolohydroxamic acid bisphosphate (compound 2)**

Compound 2 a: *O*-Benzylhydroxylamine (4.63 g, 37 mmol) was added to 3-bromopropanol (2.72 g, 18 mmol) in anhydrous ethanol (30 mL), and the mixture was heated at reflux for 45 h. After complete concentration of the mixture, ethyl acetate (200 mL) was added, and the precipitated *O*-benzylhydroxylamine hydrobromide was removed by filtration. After repeated concentration of the mixture, the oily residue was redissolved in Et_2O. This organic solution was washed with potassium hydrogencarbonate (1 M), dried and concentrated. The product was purified by flash chromatography (Et_2O/NEt_3 100:0.1). Yield 2.04 g (63 %); ^{1}H NMR (250 MHz, $CDCl_3$): δ=7.33 (m, 5 H), 5.62 (br s, 1 H), 4.73 (s, 2 H), 3.74 (t, *J*=7 Hz, 2 H), 3.18 (t, *J*=7 Hz, 2 H), 2.85 (br s, 1 H), 1.76 ppm (quint, *J*=7 Hz, 2 H); ^{13}C NMR (62.9 MHz, $CDCl_3$):δ=135.3, 128.5, 128.1, 76.3, 62.6, 51.0, 29.6, 25.20 ppm; HR-MS (ESI): *m*/*z*: calcd for $C_{10}H_{15}NO_2$ [*M*+Na^+]: 204.0995; found: 204.0996.

Compound 2 b: Compound **2 a** (0.839 g, 4.64 mmol) and triethylamine (0.563 g, 5.6 mmol) were dissolved in methanol (10 mL) at 0 °C. Acetoxyacetyl chloride (0.76 g, 5.57 mmol) in anhydrous Et_2O was added dropwise to this solution. The reaction mixture was stirred for 15 min at RT and was then diluted with Et_2O and treated with water (30 mL). The organic phase was washed with water, dried and concentrated. The product was purified by flash chromatography (Et_2O/NEt_3 100:0.1) to yield **2 b** (0.914 g, 70 %). ^{1}H NMR (250 MHz, $CDCl_3$): δ=7.4 (m, 5 H), 4.89 (s, 2 H), 4.73 (s, 2 H), 3.83 (t, *J*=7 Hz, 2 H), 3.58 (t, *J*=7 Hz, 2 H), 2.15 (s, 3 H), 1.83 ppm (quint, *J*=7 Hz, 2 H);^{13}C NMR (62.9 MHz, $CDCl_3$): δ=170.36, 168.88, 133.55, 129.01, 128.54, 76.23, 60.81, 58.39, 42.22, 29.18, 20.21 ppm; HR-MS (ESI): *m*/*z*: calcd for $C_{14}H_{19}NO_5$ [*M*+Na^+]: 304.1155; found: 304.1156.

Compound 2 c: Compound **2 b** (1.38 g, 4.9 mmol) was phosphorylated with diphenylphosphoroyl chloride as described for **1 f**. Yield 2.05 g (81 %); ^{1}H NMR (250

MHz, $CDCl_3$): δ=7.15–7.4 (m, 15 H), 4.87 (s, 2 H), 4.69 (s, 2 H), 4.31 (dt, *J*=12, 7 Hz, 2 H), 3.73 (t, *J*=7 Hz, 2 H), 2.15 (s, 3 H), 2.06 ppm (quint, *J*=7 Hz, 2 H); ^{13}C NMR (62.9 MHz, $CDCl_3$): δ=170.4, 168.6, 150.3, 150.2, 133.6, 129.0, 129.2, 129.1, 128.7, 125.2, 119.9, 119.8, 76.5, 66.7, 66.6, 61.1, 42.4, 27.5, 27.4, 20.4 ppm; ^{31}P NMR (101.3 MHz, $CDCl_3$): δ=−12 ppm; HR-MS (ESI): *m*/*z*: calcd for $C_{28}H_{28}NO_8P$ [*M*+Na^+]: 536.1445; found: 536.1452.

Compound 2 d: Compound **2 c** (2.2 g, 4.2 mmol) was deprotected as described for **1 e**. Yield 2 g (100 %); ^{1}H NMR (250 MHz, $CDCl_3$):δ=7.15–7.4 (m, 15 H), 4.73 (s, 2 H), 4.30 (dt, *J*=12, 7 Hz, 2 H), 4.21 (s, 2 H), 3.75 (t, *J*=7 Hz, 2 H), 2.04 ppm (quint, *J*=7 Hz, 2 H); ^{13}C NMR (62.9 MHz, $CDCl_3$): δ=173.66, 150.24, 150.13, 133.46, 129.61, 129.08, 128.58, 125.23, 119.81, 119.75, 76.41, 66.51, 66.43, 59.97, 42.45, 27.46, 27.36 ppm; ^{31}P NMR (101.3 MHz, $CDCl_3$): δ=−11.98 ppm; HR-MS (ESI): *m*/*z*: calcd for $C_{24}H_{26}NO_7P$ [*M*+Na^+]: 494.1339; found: 494.1347.

Compound 2 e: Compound **2 d** (2 g, 4.24 mmol) was phosphorylated as described for **1 f**. Yield 1.56 g (52 %); ^{1}H NMR (250 MHz, $CDCl_3$):δ=7.15–7.4 (m, 25 H), 4.83 (d, *J*=11 Hz, 2 H), 4.76 (s, 2 H), 4.33 (dt, *J*=7.5, 7 Hz, 2 H), 3.77 (t, *J*=7 Hz, 2 H), 2.10 ppm (quint, *J*=7 Hz, 2H);^{13}C NMR (250 MHz, $CDCl_3$): δ=167.91, 150.54, 150.42, 133.58, 129.91, 129.82, 129.44, 128.95, 125.51, 120.30, 120.23, 120.13, 76.71, 66.85, 66.77, 65.41, 42.68, 27.74, 27.65 ppm; ^{31}P NMR (101.3 MHz, $CDCl_3$): δ=−11.98, −11.53 ppm; HR-MS (ESI): *m*/*z*: calcd for $C_{36}H_{35}NO_{10}P_2$ [*M*+Na^+]: 726.1628; found: 726.1628.

Compound 2 f: Compound **2 e** (0.945 g, 1.34 mmol) was dissolved in ethanol (20 mL). Pd-C (10 %, 100 mg) was added, and the suspension was vigorously stirred under dihydrogen overnight. After filtration and evaporation, **2 f** (0.805 g, 98 %) was recovered. ^{1}H NMR (250 MHz, $CDCl_3$): δ=7.15–7.4 (m, 20 H), 4.97 (d, *J*=11 Hz, 2 H), 4.33 (dt, *J*=6 Hz, 2 H), 3.67 (t, *J*=6 Hz, 2 H), 2.10 ppm (quint, *J*=6 Hz, 2 H);^{13}C NMR (62.9 MHz, $CDCl_3$): δ=167.39, 167.28, 150.38, 150.29, 150.20, 129.85, 129.75, 125.57, 120.19, 120.13, 12.01, 119.95, 67.04, 66.37, 65.71, 65.65, 45.09, 27.42, 27.34 ppm; ^{31}P NMR (101.3 MHz,

$CDCl_3$): δ=−11.26, −11.64 ppm; HR-MS (ESI): *m*/*z*: calcd for $C_{29}H_{29}N_2O_{10}P_2$ [M+Na^+]: 636.1159; found: 636.1171.

***N*-(3-Hydroxypropyl)-glycolohydroxamic acid bisphosphate (compound 2) tetrakis-cyclohexylammonium salt**: Compound **2 g** (0.805 g, 1.31 mmol) was dephenylated as described for **1 i**. The residue was dissolved in ethanol (20 mL), and an excess of cyclohexylamine was added. The solution was evaporated to afford a white powder, which was recrystallized from ethanol. Yield 0.32 g (34 %); ^{1}H NMR (250 MHz, D_2O): δ=430 (d, $J_{H,P}$=6 Hz, 2 H; -CO-CH_2-OPO_3^{2-}), 3.54 (dt, $J_{H,P}$=$J_{H,H}$=6 Hz, 2 H; $^{2-}O_3PO$-CH_2-CH_2-), 3.45 (t, J=7 Hz, 2 H; -CH_2-CH_2-N), 1.66 ppm (quint, J=7 Hz, 2 H; -CH_2-CH_2-CH_2) [CHA+: 2.85 (m, 4 H), 1.25–1.80 (m, 20 H), 0.80–1.25 (m, 20 H)]; ^{13}C NMR (62.9 MHz, D_2O): δ=172.13, 62.30, 62.24, 62.08, 50.92, 47.00, 31.04, 28.13, 28.04, 24.99, 24.49 ppm; ^{31}P NMR (101.3 MHz, D_2O): δ=3.52, 3.65 ppm; HR-MS (ESI, negative): *m*/*z*: calcd for $C_5H_{12}NO_{10}P_2^-$: 307.99420; found: 307.99427

***N*-(3-Hydroxypropyl)-phosphoglycolohydroxamic acid (compound 3)**

Compound 3 a: BnBr (0.1 mol, 17 g) was added dropwise over 20 minutes to a solution of propane-1,3-diol (0.3 mol, 21.67 mL) in anhydrous DMF (100 mL). After cooling of the mixture in an ice-bath, NaH (60 %, 3 g, 0.125 mol) was added in portions. This mixture was stirred under argon overnight at RT. The solvent was concentrated under reduced pressure. Water (75 mL) was added, and the water phase was extracted with CH_2Cl_2 (2×75 mL). The combined organic phases were dried with Na_2SO_4 and concentrated under reduced pressure. The product was an oil (0.067 mol, 11.24 g, 67 %). R_f=0.18 (pentane/Et_2O 8:2). ^{1}H NMR (250 MHz, $CDCl_3$): δ=7.3–7.4 (m, 5 H), 4.54 (s, 2 H), 3.76 (m, 2 H), 3.64–3.67 (t, J=6 Hz, 2 H), 1.9 ppm (quint, J=5.8 Hz, 2 H); ^{13}C NMR (62.9 MHz, $CDCl_3$): δ=138.2, 128.5, 127.7, 127.6, 32.31 73.2, 68.84, 61.09 ppm.

Compound 3 b: PCC (0.036 mol, 7.74 g), 3-benzyloxypropan-1-ol (**3 a**, 0.018 mol, 3 g) and powdered molecular sieves were added to dry CH_2Cl_2 (72 mL). This mixture was stirred under argon for 2.5 h. Et_2O (500 mL) was then added to the reaction mixture, which was filtered through a short column of silica gel. The solvent was evaporated under reduced

pressure. The product was an oil (0.0157 mol, 2.584 g, 88 %). R_f=0.77 (pentane/ethyl acetate 8:2). ^{1}H NMR (250 MHz, $CDCl_3$): δ=9.81 (t, J=2 Hz, 1 H), 7.4 (m, 5 H), 4.57 (s, 2 H), 3.84 (t, J=6 Hz, 2 H), 2.72 ppm (dt, J=6, 2 Hz, 2 H); ^{13}C NMR (62.9 MHz, $CDCl_3$): δ=201.3, 137.9, 128.5, 127.7, 127.6, 73.27, 63.9, 43.9 ppm.

Compound 3 c: 3-Benzyloxypropionaldehyde (**3 b**, 0.0157 mol, 2.57 g) was dissolved in methanol (78.5 mL). *O*-Benzylhydroxylamine (0.024 mol, 2.89 g) and pyridine (0.145 mol, 11.72 mL) were added. The mixture was stirred at reflux at 65 °C for 3.5 h and concentrated under reduced pressure. The resultant product was dissolved in CH_2Cl_2 (50 mL), washed with water (3×50 mL), dried with Na_2SO_4 and concentrated under reduced pressure. The product was an oily mixture of two *Z*/*E* stereoisomers (together with remaining benzylhydroxylamaine). Yield 4.211 g, R_{f1}=0.94, R_{f2}=0.88 (pentane/ethyl acetate 8:2). ^{1}H NMR (250 MHz, $CDCl_3$): δ=7.4 (m, 10 H), 6.9 and 7.5 (t, J=5.5 Hz, 1 H), 5.14 and 5.19 (s, 2 H), 4.76 (s, 2 H), 3.65 and 3.68 (t, J=6.5 Hz, 2 H), 2.56 and 2.75 ppm (q, J=6.5 Hz, 2 H); ^{13}C NMR (62.9 MHz, $CDCl_3$): δ=149.0, 137.75, 137.5, 128.5, 128.3, 128.0, 127.9, 127.7, 127.1, 75.9, 75.7, 66.7, 30.4 ppm.

Compound 3 d: Sodium cyanoborohydride (0.0188 mol, 1.18 g) was added in portions, with cooling in an ice-bath, to **3 c** (0.0157 mol, 4.211 g) dissolved in a mixture of ethanol and acetic acid (1:1, 25 mL). This was stirred at RT for 7.5 h. The solvent was then evaporated under reduced pressure, and the resultant product was made alkaline (pH 8.00) with saturated $NaHCO_3$. The mixture was extracted with CH_2Cl_2 (3×150 mL), washed with water (150 mL) and sat. NaCl (150 mL), dried with Na_2SO_4 and concentrated under reduced pressure. The product was purified by column chromatography (pentane/AcOEt 9:1). Yield 2.61 g (61 % from **3 b**). R_f=0.1 (pentane/Et_2O 9:1); ^{1}H NMR (250 MHz, $CDCl_3$): δ=7.4 (m, 10 H), 4.76 (s, 2 H), 4.55 (s, 2 H), 3.6 (t, J=6.5 Hz, 2 H), 3.12 (t, J=6.5 Hz, 2 H), 1.9 ppm (quint, J=6.5 Hz, 2 H); ^{13}C NMR (62.9 MHz, $CDCl_3$): δ=138.55, 138.1, 128.55, 128.45, 128.08, 127.85, 127.7, 76.2, 73.0, 68.65, 49.65, 27.6 ppm.

Compound 3 e: Compound **3 d** (6.47 mmol, 1.754 g), triethylamine (9.7 mmol, 1.36 mL) and acetoxyacetyl chloride (7.764 mmol, 0.83 mL) were dissolved in dry CH_2Cl_2

(10 mL). This mixture was stirred at RT for 20 minutes. The organic phase was washed with water (3×10 mL), dried with Na_2SO_4 and concentrated under reduced pressure. The product was an oil (2.167 g, 90 %). R_f=0.49 (pentane/ethyl acetate 6:4);^{1}H NMR (250 MHz, $CDCl_3$): δ=7.4 (m, 10 H), 4.88 (s, 2 H), 4.75 (s, 2 H), 4.5 (s, 2 H), 3.8 (br t, *J*=6.5 Hz, 2 H), 3.55 (t, *J*=6.5 Hz, 2 H), 2.2 (s, 3 H), 2.0 ppm (quint, *J*=6.5 Hz, 2 H); ^{13}C NMR (62.9 MHz, $CDCl_3$): δ=170.7, 168.5, 138.4, 134.0, 129.3, 129.2, 128.9, 128.4, 127.74, 127.6, 76.5, 73.0, 67.5, 61.4, 43.45, 27.12, 20.7 ppm.

Compound 3 f: Compound **3 e** was dissolved in a methanol/triethylamine/water mixture (8:2:1, 44 mL). This was stirred at RT for 18 h. After complete evaporation, the product was purified by flash chromatography (pentane/AcOEt 6:4). The product was an oil (1.305 g, 68 %).R_f=0.38 (pentane/ethyl acetate 7:3); ^{1}H NMR (250 MHz, $CDCl_3$): δ=7.4 (m, 10 H), 4.82 (s, 2 H), 4.52 (s, 2 H), 4.25 (s, 2 H), 3.85 (m, 2 H), 3.55 (t, *J*=6 Hz, 2 H), 3.23 (br s, 1 H), 2.0 ppm (quint, *J*=6 Hz, 2 H); ^{13}C NMR (62.9 MHz, $CDCl_3$): δ=173.75, 138.3, 133.95, 129.35, 128.9, 128.5, 127.8, 76.6, 73.1, 67.45, 60.25, 43.7, 27.14 ppm.

Compound 3 g: A mixture of **3 f** (3.96 mmol, 1.305 g), dibenzyl *N*,*N*-diisopropylphosphoramidite (7.923 mmol, 2.73 g), imidazole (11.88 mmol, 0.808 g) and 1,2,4-triazole (7.92 mmol, 0.55 g) was dissolved in dry acetonitrile (27 mL). This system was stirred at RT under argon for 27 h. *t*BuOOH (7.92 mmol, 1.08 mL, 7.3 M) and CH_2Cl_2 (30 mL) were then added. This mixture was stirred for 2 h at RT. An aqueous solution of sodium thiosulfate (1 M, 75 mL) and CH_2Cl_2 (30 mL) were added. The aqueous phase was extracted with CH_2Cl_2 (3×100 mL). The collected organic phases were washed with sat. Na_2CO_3 (200 mL), dried with Na_2SO_4, concentrated under reduced pressure and purified by flash chromatography (pentane/AcOEt). The product was an oil (1.794 g, 77 %). R_f=0.67 (pentane/ethyl acetate 1:1); ^{1}H NMR (250 MHz, $CDCl_3$): δ=7.4 (m, 20 H), 5.2 (m, 4 H), 4.78 (s, 2 H), 4.7 (d, *J*=11.25 Hz, 2 H), 4.5 (s, 2 H), 3.8 (br t, *J*=8.7 Hz, 2 H), 3.5 (t, *J*=8.7 Hz, 2 H), 2.0 ppm (quint, *J*=8.75 Hz, 2 H); ^{13}C NMR (62.9 MHz, $CDCl_3$): δ=168.5, 138.4, 135.9, 133.9, 129.3, 128.9, 128.6, 128.5, 128.4, 128.0, 127.7, 127.6, 76.5, 73.0, 69.6, 67.5, 64.4, 43.5, 27 ppm; ^{31}P NMR (101.3 MHz, $CDCl_3$): δ=0.8 ppm.

***N*-(3-Hydroxypropyl)-phosphoglycolohydroxamic acid (compound 3) bis-cyclohexylammonium salt**: A mixture of **3 g** (1.5 mmol, 0.9 g), Na_2CO_3 (1.5 mmol, 0.15 g) and Pd/C (170 mg) in water/ethanol (1:1, 40 mL) was stirred under hydrogen (3 bar) for 36 h. It was then filtered through celite and concentrated under reduced pressure. The product, dissolved in water, was then filtered through a Dowex-50 column (cyclohexylammonium form), and the eluate was concentrated under reduced pressure to give the crystalline product (0.566 g, 86 %). ^{1}H NMR (250 MHz, D_2O): δ=4.4 (d, $J_{H,P}$=5.75 Hz, 2 H; CO-CH_2-OPO_3^{2-}), 3.55 (t, J=6.5 Hz, 2 H; -CH_2-OH), 3.5 (t, J=6.5 Hz, 2 H; -CH_2-N-), 1.9 ppm (quint, J=6.5 Hz, 2 H; -CH_2-CH_2-CH_2-) [CHA+: 3.0 (m, 2 H), 1–2 (m, 22H)]; ^{13}C NMR (62.9 MHz, D_2O): δ=171.7, 63.3, 61.6, 58.8, 50.2, 45.3, 30.3, 28.4, 24.2, 23.8 ppm; ^{31}P NMR (101.3 MHz, D_2O): δ=3.6 ppm; HR-MS (ESI, negative): m/z: calcd for $C_5H_{11}NO_7P^-$ $[M-H]^+$: 228.0273; found: 228.0272.

Compound 3 is apparently subject to the following rearrangement in acidic medium:

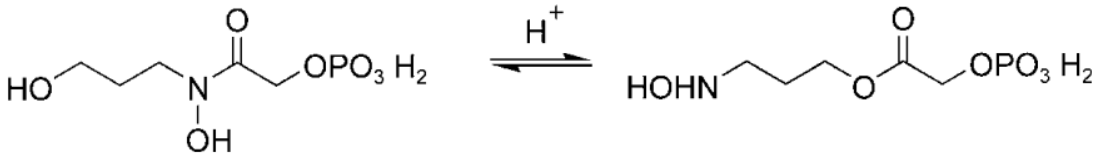

4.1.5.2 Biochemistry

4.1.5.2.1 Biochemical evaluation of inhibitors 1–3

4.1.5.2.1.1 Enzymes

Rabbit muscle Fba was a commercial preparation, available from Sigma or Fluka.

H. pylori Fba was a recombinant enzyme expressed in *E. coli* strain JM109. Yeast Fba was isolated from *S. cerevisiae*. Cells were disrupted in a French press (110 psi). The enzyme was partly purified by precipitation with ammonium sulfate.[38]

M. bovis Fba was isolated from cultivated cells by disruption in a French press. Crude extracts were used.

4.1.5.2.1.2 Solutions

Glycylglycine buffer (0.1 M, pH 7.4, with 0.2 M potassium acetate for class II aldolases).

NADH 1.41 mM in buffer.

Fructose bisphosphate 2 mM in buffer.

Glycerophosphate dehydrogenase (GPDH, 274 U mL^{-1}).

4.1.5.2.1.3 Enzymatic test

Fructose bisphosphate and inhibitor at the convenient concentration, NADH (0.12 mM), GPDH (11 U) and aldolase (4 mU) were placed in a cuvette to give a final volume of 1.2 mL. The decrease in absorbance of NADH at 340 nm was monitored on a spectrophotometer over 1–2 min.

4.1.5.2.2 Purification and recrystallization of H. pylori Fba

Plasmid pKK223-3 coding for *H. pylori* Fba was transformed and over-expressed in *E. coli* strain JM109. Recombinant *H. pylori* Fba was purified by a combination of anion exchange (DEAE), hydrophobic exchange chromatography (Phenyl-Sepharose) and size exclusion chromatography.26 Aldolase concentration was determined by use of BCA Protein Assay Reagent (Pierce) with bovine serum albumin serving as standard. Enzymatic activity was monitored by spectrophotometry with use of a coupled assay and monitoring of NADH oxidation at 340 nm. The purified protein was stored at 4 °C in 85 % saturated ammonium sulfate solution (25 mM Tris·HCl, pH 8).

H. pylori aldolase crystals were grown by vapour diffusion from a mixture (1:1) of protein solution (10 mg mL^{-1} initial protein concentration made up in 25 mM Tris·HCl pH 7.0) and precipitant buffer [PEG 1000 (12 %), PEG 8000 (12 %), calcium acetate (0.2 M)

and Tris/HOAc (pH 8, 50 mM)]; 4 μ drops were equilibrated at 23 °C against 1 mL reservoirs of precipitant solution. Crystals grew over two weeks.

4.1.5.2.3 Data collection and processing

Aldolase crystals were soaked in compound **2** buffer [mother liquor plus compound **2** (10 mM)] or in PGH buffer [mother liquor plus PGH (10 mM)]. Prior to data collection, crystals were cryoprotected by transfer through a cryobuffer solution [compound **2** or PGH buffer plus glycerol (10 %)] and immediately flash frozen in a stream of gaseous N_2 cooled to 100 K. Diffraction data were collected from single crystals at beamlines X8C and X29 of the National Synchrotron Light Source (Brookhaven National Laboratory, Upton, USA). As control, a native data set was also collected with use of beamline X8C. A fluorescence energy scan, collected at beamline X8C by energy scanning about the Zn Kα edge (1.2818 Å), demonstrated that the *H. pylori* Fba crystals contained zinc, although no exogenous zinc had been added during purification or recrystallization of the protein. All data sets were processed by use of HKL2000[27], and the results are summarized in Table I in the Supporting Information

4.1.5.2.4 Structure solution and refinement

A model structure of *H. pylori* aldolase was generated by feeding to the molecular replacement (MR) program AMORE[28] 20 comparative homology models obtained with the program MODELLER[29] with use of the structure of class II *T. aquaticus* aldolase[30] as template (PDB code 1RVG). The best solution was used as starting point for refinement. The native structure was solved by iterative rounds of refinement (simulated annealing and minimization) with CNS[31] and model building.[32] Initial phases used for model building of liganded structures were obtained by using the refined native structure as template for input into the program Phenix autoMR/autoBuild.[33] The native and PGH structures belong to the monoclinic space group $P2_1$ and each have one aldolase homodimer in the asymmetric unit. The structure in complexation with compound **2** belongs to space group *P*1 and also has one aldolase homodimer in the asymmetric unit. All reflections with I/σ(I) >1 were used in

refinement; however, electron density maps were calculated to the resolution shown in Table I in the Supporting Information and corresponded to completeness of greater than 70 % in the highest-resolution shell. The liganded structures were subjected to iterative rounds of refinement Phenix and model building with Coot[34] and PyMol.[23] The Molprobity server[35] and the Coot validating tools were used to optimize the structures during the refinement. Water molecules were added automatically by CNS or Phenix in the initial rounds and manually near the end of refinement. Loop regions (residues 139–153) in each subunit were associated with regions of weak electron density.

Ligand modelling was based on interpretation of electron density shapes of $2F_o-F_c$ and F_o-F_c annealed omit maps and use of the phenix.elbow command for generation of topology and parameters. Binding by compound **2** and PGH were readily discernable and were associated with clearly defined electron densities in the active site. Difference electron density (F_o-F_c) annealed omit maps calculated in the final round of refinement confirmed identical binding of ligands in both subunits. Final model statistics, calculated with CNS and PROCHECK,[36] are shown in Table I in the Supporting Information. The coordinates and structure factors of *H. pylori* aldolase, as well as those of the native enzyme in complexation with PGH and with compound **2**, have been deposited with the Protein Data Bank (PDB entry codes 3C4U, 3C52 and 3C56, respectively).[37] The final structure models of native aldolase, compound **2** and PGH enzymatic complexes have R_{cryst} (R_{free}) values of 0.185 (0.207), 0.172 (0.208) and 0.204 (0.249), respectively. The corresponding Luzzati atomic coordinate errors were estimated at 0.20, 0.23 and 0.28 Å, respectively. Ramachandran analysis with PROCHECK placed at least 90 % of non-glycine and non-proline residues of the four structures in the most favourable region and with the remainder found in allowed regions, attesting to good model geometry in the structures.

4.1.5.2.5 Comparisons

Superpositions were performed with the program PyMOL with use of C_α atom coordinates of identical regions of amino acid sequences. Root mean square (rms) deviations based on superposition of equivalent C_α atoms are reported. The dihedral angles

for the hydroxamate moieties in compound **2** and PGH are the angles between the planes defined by atoms C2, N3 and O2 and by atoms C2, N3 and O3. A dihedral angle of 0° indicates coplanarity and has atoms O2 and O3 positioned *cis* to each other and coplanar with atoms C2 and N3

4.1.5.2.6 Biology

4.1.5.2.6.1 Growth inhibition of cultivated bacteria

Minimal inhibitory concentration values of compound **2** against *M. tb* H37Rv were determined in 7H9-ADC broth at 37 °C by the colorimetric resazurin microtiter assay described by Martin and collaborators.22 The bacteria were grown aerobically under conditions compatible with class II Fba expression9 and similar to those used for the preparation of the *M. bovis* BCG extracts.

4.1.6 Acknowledgements

This work was supported by a scholarship to R.D. from the Region Ile de France. K.K. was on leave from Politechnika Warszawska in an Erasmus EC program. J.S. was supported by the Natural Science and Engineering Research Council (Canada) and the Canadian Institutes for Health Research, and work was carried out in part at the National Synchrotron Light Source, Brookhaven National Laboratory, which is supported by the United States Department of Energy, Division of Materials Sciences and Division of Chemical Sciences under contract DE-AC02-98CH10886.

4.1.7 Supporting Information

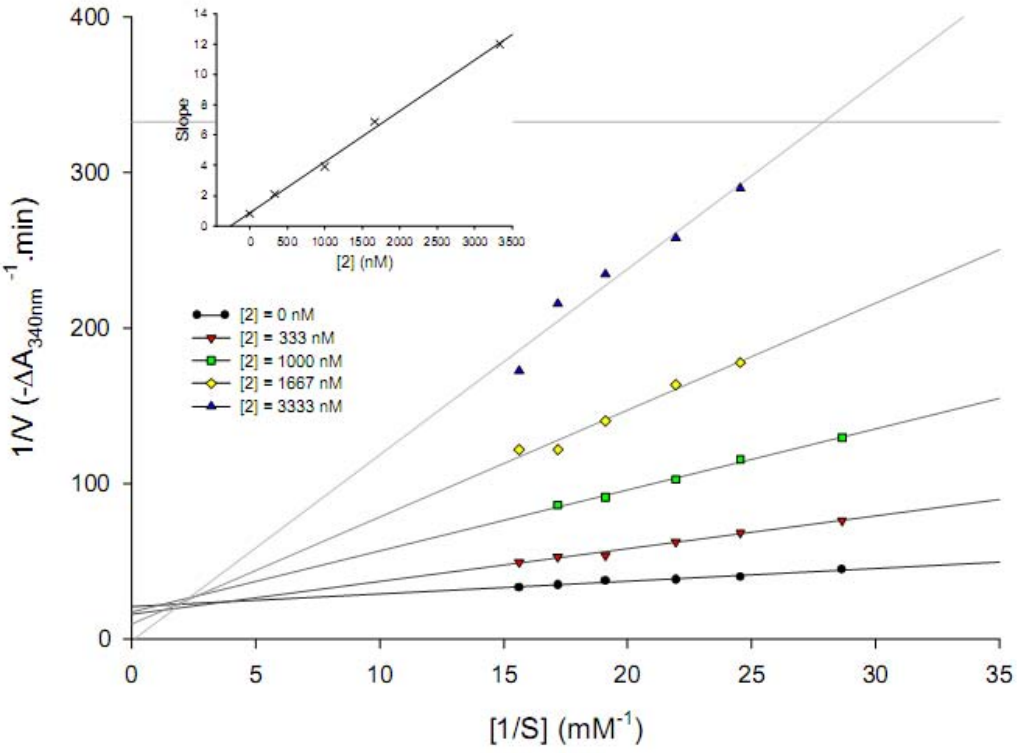

Figure 4-8. Inhibition of rabbit muscle Fba by compound 2

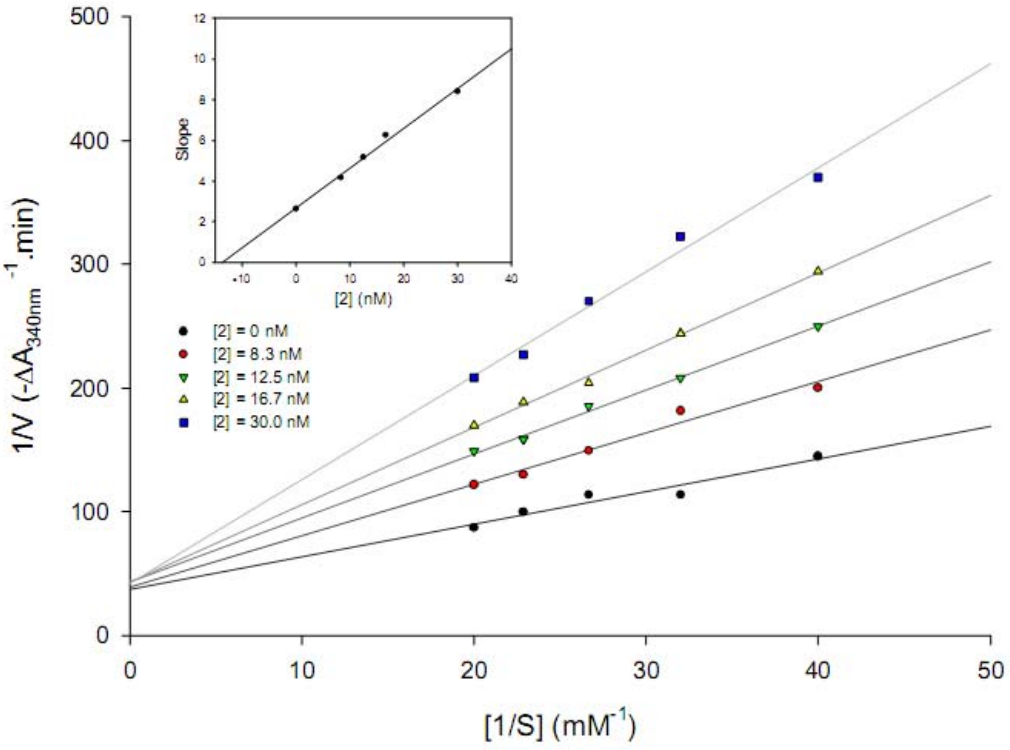

Figure 4-9. Inhibition of *M. bovis* Fba by compound 2

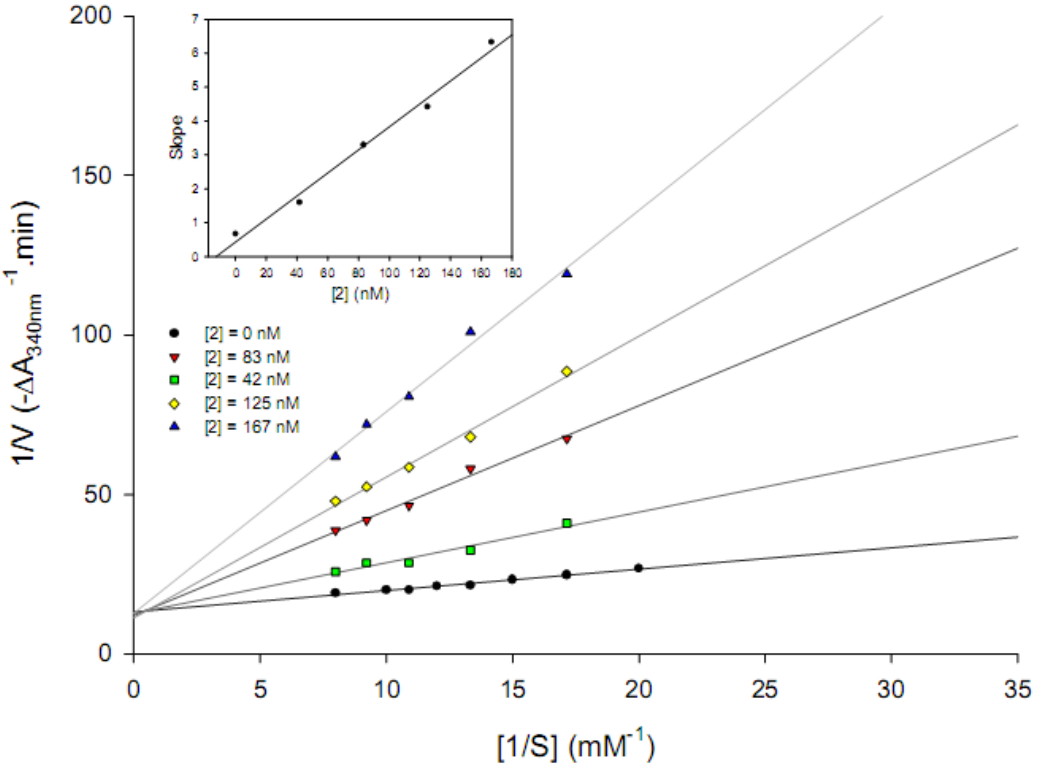

Figure 4-10. Inhibition of *H. pylori* Fba by compound 2

	Native	PGHPP	PGH
Data collection			
Resolution (Å)	30-1.83 (1.89-1.83)*	29 -2.31 (2.38 -2.31)*	32-2.3 (2.38-2.3)*
Wavelength (Å)	1.0	1.1	1.1
Reflections			
Observed	626119	526576	901728
Unique	47884	21015	24022
Completeness (%)	99.6(99.3)	93.49 (74.5)	97.0 (86.3)
Average I/σ(I)	19.5 (6.32)	8.8 (2.7)	12.9 (7)
R_{sym}†	0.101 (0.287)	0.070 (0.233)	0.072 (0.141)
Space group	$P2_1$	P1	$P2_1$
Unit cell parameters			
a (Å), b (Å), c (Å), a(°), β (°), γ(°)	39.02, 82.56, 91.27 90, 99.7, 90	39.2, 62.0, 65.6, 82.9, 79.8, 71.0	39.2, 85.4, 90.8 90, 100.2, 90
Refinement			
Number of atoms			
Protein	4520	4567	4566
Water	933	593	631
Hetero	4	38	26
σ cutoff; I /σ(I) >	1	1	1
R_{cryst} (%)‡	18.5	17.2	20.4
R_{free} (%)§	20.7	20.8	24.9
rms deviation			
Bond length (Å)	0.004	0.005	0.009
Bond angle (°)	0.573	0.618	1.134
< B > (Å²)	17.9	28.8	34.7
Ramachandran analysis¶ (%)			
Most favourable	92.5	91.3	91.5
Allowed	7.5	8.7	8.5
Generously allowed	0	0	0
Luzzati plot (Å)	0.20	0.23	0.28

*All values in parentheses are given for the highest resolution shell

†$R_{sym} = \Sigma_{hkl} \Sigma_i |I_i(hkl) - I_i(hkl)| / \Sigma_{hkl} \Sigma_i I_i(hkl)$ with *i* running over number of independent observations of reflection hkl.

‡$R_{cryst} = \Sigma_{hkl} ||I_o(hkl)| - |I_c(hkl)|| / \Sigma_{hkl} |I_o(hkl)|$.

§$R_{free} = \Sigma_{hkl \in T} || I_o(hkl) - |I_c(hkl)|| / \Sigma_{hkl \in T} |I_o(hkl)|$, where T is a test data set randomly selected from the observed reflections prior to refinement. Test data set was not used throughout refinement and contained 7%, 6%, and 9% of the total unique reflections for native, **2**, and PGH, respectively.

¶Analyzed by PROCHECK.

Table 4-3. Data collection and refinement statistics.

4.2 Rational design, synthesis and evaluation of new selective inhibitors of microbial class II (zinc dependent) fructose bis-phosphate aldolases.

Mathieu Coinçon†, Racha Daher†, Matthieu Fonvielle, Petra M. Gest, Marcelo E. GuerinMary Jackson, Jurgen Sygusch and Michel Therisod

† *These authors contributed equally to this work*

ECBB, ICMMO, Univ Paris-Sud, UMR 8182, F-91405 Orsay, France. Department of Microbiology, Immunology and Pathology, Mycobacteria Research Laboratories, Colorado State University, Fort Collins, CO 80523-1682 (USA). Biochimie, Université de Montréal, CP 6128, Stn Centre-Ville Montréal, PQ H3C 3J7 (Canada).

Accepted 13th September 2010 for publication in *J. Med. Chem.*

4.2.1 Abstract

We report the synthesis and biochemical evaluation of several selective inhibitors of class II (zinc dependent) fructose bis-phosphate aldolases (Fba). The products were designed as transition-state analogues of the catalyzed reaction, structurally related to the substrate fructose bis-phosphate (or sedoheptulose bis-phosphate) and based on an N-substituted hydroxamic acid, a chelator of the zinc ion present in active site. The compounds synthesized were tested on class II Fbas from various pathogenic microorganisms and, by comparison, on a mammalian class I Fba. The best inhibitor shows K_i against class II Fbas from various pathogens in the nM range, with very high selectivity (up to 10^5). Structural analyses of inhibitors in complex with aldolases rationalize and corroborate the enzymatic kinetics results. These inhibitors represent lead compounds for the preparation of new synthetic antibiotics, notably for tuberculosis prophylaxis.

KEYWORDS Fructose bisphosphate aldolase; Selective inhibitors; Hydroxamates; *Candida albicans*; *Helicobacter pylori., Mycobacterium tuberculosis; Yersinia pestis*; antibiotics.

BRIEFS (WORD Style “BH_Briefs”). Selective inhibitors of microbial fructose bisphosphate aldolases were efficiently bound into the active site of this enzyme present in several pathogenic species.

4.2.2 Introduction

The resistance of pathogenic microorganisms to current antibiotics is a public health problem of major concern.[1] Factors contributing to this phenomenon are the emergence of resistant bacteria due to massive usage of antibiotics in human and veterinary medicine, and the diffusion of the resistant bacteria in various ecosystems. The main consequences are: 1- An increase of nosocomial diseases contracted in hospitals : 5% of all hospitalized patients, at an annual cost exceeding 2 billion dollars per year resulting from infection by opportunistic pathogens such as *Pseudomonas aeruginosa*, *Candida albicans, Clostridium difficile*.[2] 2- A re-emergence of historic diseases such as tuberculosis (caused by

Mycobacterium tuberculosis) and plague (infection by *Yersinia pestis*).[3] 3- A new threat of bioterrorism[4] that could make use of infectious agents such as *Bacillus anthracis* (anthrax), *C. botulicum* (producing the botulic toxin), *Francisella tularensis* (agent of tularemia), *Coxiella burnetii* (Q fever), *Richetsia prowasek* (typhus). Efficacious treatment of emerging antibiotic-resistant bacterial diseases thus requires alternatives to current antibiotic therapy. There is therefore a need to identify new microbial targets.

Because of their occurrence in many pathogenic microbes (bacteria, yeasts, parasites) and their absence in animals, class II fructose bis-phosphate aldolases (Fbas)[a] could be such promising new targets.

Aldolases (E.C. 4.1.2.13) are essential enzymes used in glycolysis, where they catalyze cleavage of fructose 1,6-bisphosphate (FBP) to yield dihydroxyacetone phosphate (DHAP) and glyceraldehyde-3-phosphate (G3P), and in gluconeogenesis and the Calvin cycle, where they catalyze the opposite reaction of triose-P condensation. These enzymes occur in two distinct classes. Class I Fbas, which are present in higher organisms (plants and animals) and some prokaryotes, form a Schiff-base intermediate between the keto substrate (FBP or DHAP) and a lysine residue of the active site. Class II Fbas in contrast, require a divalent metal ion (usually zinc or cobalt ion) to polarize the keto carbonyl group of the substrate (FBP or DHAP) and to stabilize the enediolate intermediate formed during catalysis (Figure 11). They are found exclusively in lower organisms such as yeasts, micro-algae, protozoa, and bacteria, which include most pathogenic microorganisms mentioned above.

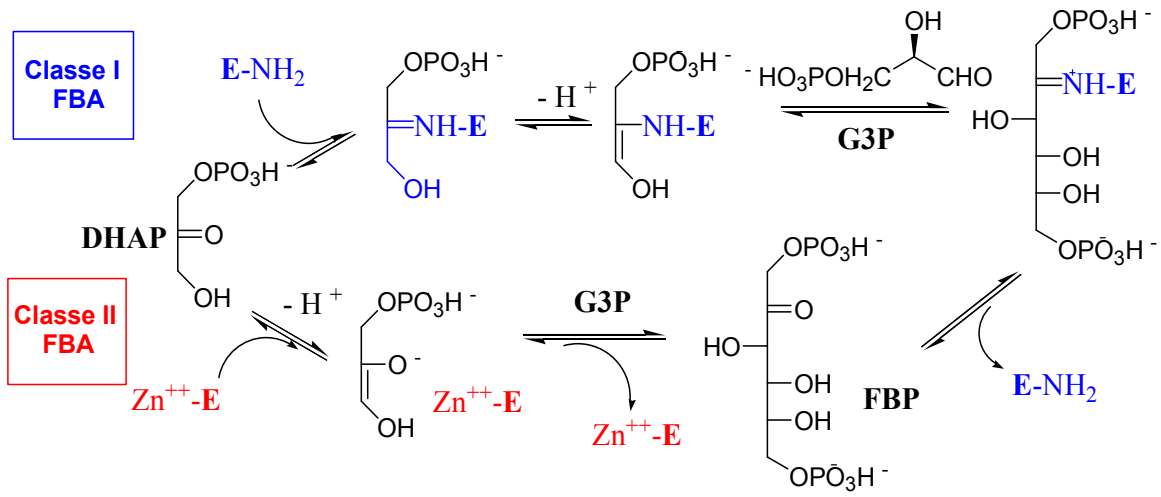

Figure 4-11. Mechanisms of class I (eg. human) and class II (eg. bacterial) Fbas

Of the Fba inhibitors that have been prepared, the very large majority display poor selectivity for class II versus class I Fbas and act as substrate analogues.[5] One notable exception is phospho-glycolohydroxamic acid (PGH),[6] considered to be either an analogue of the substrate DHAP or that of a high energy reaction intermediate (figure 12). This compound has however only a hundred-fold selectivity for class II Fbas and has severe drawbacks that limit its potential use *in vivo*: 1) It is spontaneously hydrolyzed, releasing (toxic) hydroxylamine; 2) It is a powerful inhibitor of several other enzymes present both in mammals and microorganisms.

Other DHAP analogues have been reported with better selectivities (300 - 1000) but with lower potency.[7]

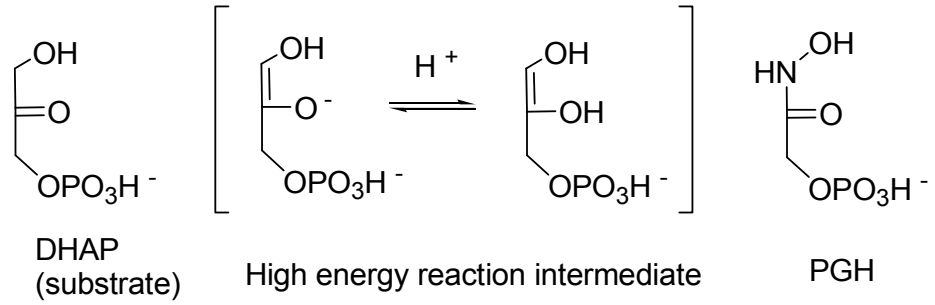

Figure 4-12. Structures of phosphoglycolo hydroxamic acid (PGH), DHAP (Fba substrate) and the high energy intermediate formed by deprotonation of DHAP.

We thus explored the use of compounds that are transition-state (TS) or high-energy intermediate analogues, whose structures are related to the substrate FBP, to improve inhibitory performances and selectivity.

4.2.3 Results and discussion

4.2.3.1 Design of inhibitors

We previously reported on the preparation and evaluation of N-(3-hydroxypropyl)-phospho-glycolohydroxamic acid bis-phosphate (**1'**) (figure 3), a compound designed as an analogue of the natural substrate, FBP. **1'** gave encouraging results both in terms of inhibitory power (K_i < 20 nM) and selectivity for the class II Fbas (> 20 000).[8] This competitive inhibitor was shown by crystallographic analysis to bind within the active site of *H. pylori* Fba, a representative class II aldolase.

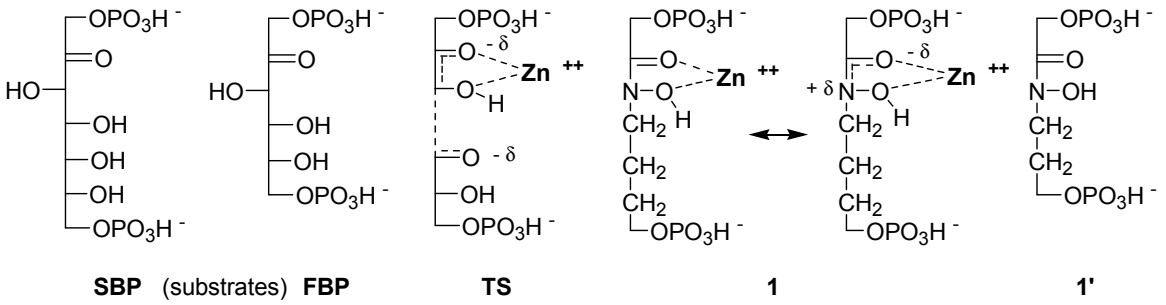

Figure 4-13. Fischer representations of sedoheptulose bis-phosphate, fructose bis-phosphate (SBP, FBP: substrates of Fba), of the transition-state of the reaction catalyzed by a class II Fba (TS) and of the designed inhibitor **1** (and its mesomeric hybrid structure).

On this basis, we decided to prepare N-(4-hydroxybutyl)-phospho-glycolohydroxamic acid bis-phosphate (**1)**, shown in figure 13, with the following rationale for the design of a true selective transition-state analogue inhibitor:

- A well positioned hydroxamic acid function, responsible for the chelation of the transition metal zinc ion present at the active site of class II Fbas. The electronic delocalization in this functional group is intended to mimic the electronic density in the transition-state of the retro-aldol cleavage of FBP

- Two phosphate groups separated by an additional methylene group compared to **1'** to mimic sedoheptulose-1,7-bisphosphate (SBP), which is also a substrate for class II aldolases. K_M values for these two substrates are different and in algal and cyanobacterial class II Fba, sedoheptulose-1,7-bisphosphate exhibits significantly tighter binding compared to FBP.[9] In addition, an increased distance between the two phosphate groups compared to FBP would more likely mimic the distance found in the transition state of the reaction.

- Furthermore *N*-alkylated hydroxamic acids are considerably more resistant to hydrolysis than the primary hydroxamate found in PGH.

The proposed analogue differs from the natural substrate FBP (SBP) in that the C4, C5 (C6) hydroxyl groups are absent. Consequently, from a synthetic standpoint, the analogue does not possess asymmetric centers, which considerably simplifies its synthesis.

The designed structure of the inhibitor **1** makes it a very polar compound rendering passive transport across the cytoplasmic membranes of pathogenic bacteria or yeasts problematic. We therefore chose to study the inhibitory properties of mono-phosphorylated derivatives of **1** or a lipophilic ester in place of the P7 phosphate. If sufficiently active *in vitro*, N-(4-hydroxybutyl)-phospho-glycolohydroxamic acid mono-phosphate (**2)**, its hexanoyl ester (**3)** and its lauroyl ester (**4)** (Figure 14) could then act as lead compounds for the further synthesis of non-polar prodrugs.[10]

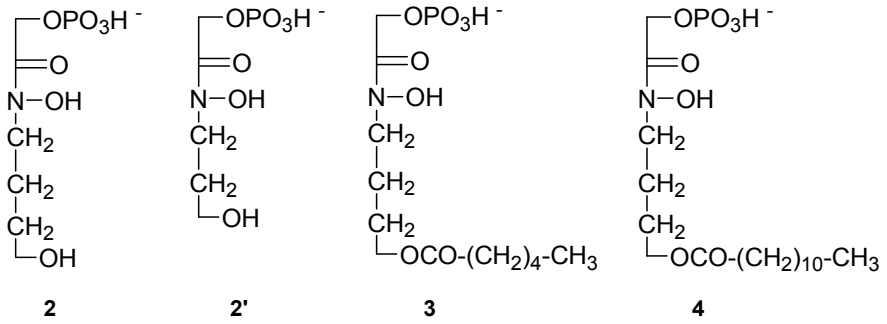

Figure 4-14. Mono-phosphorylated derivatives of **1**.

(Compound **2'** is the monophosphorylated derivative of **1'**. Both compounds were previously described[8]).

4.2.3.2 Syntheses

The four new compounds were synthesized according to Schemes 2 and 3.

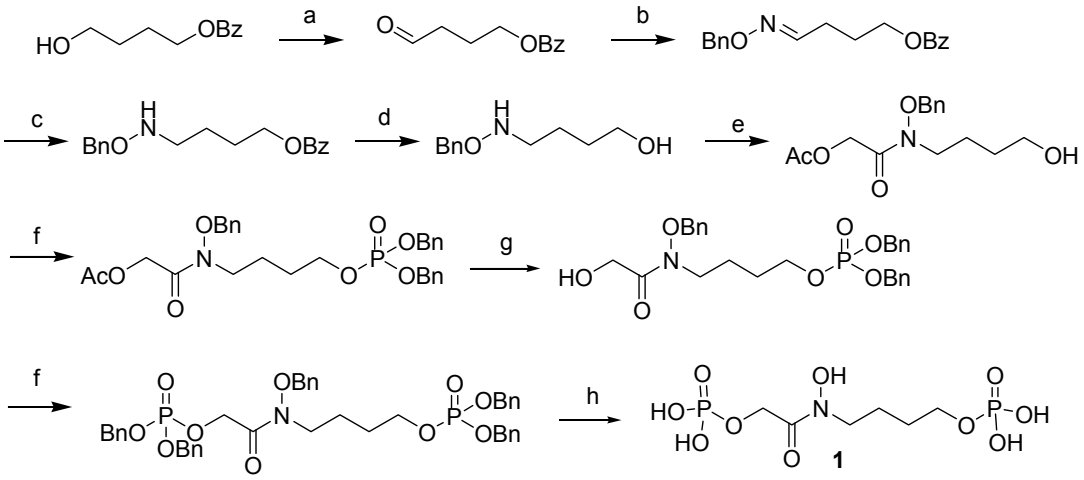

Scheme 4-2. Synthesis of inhibitor **1**

a) PCC b) $BnONH_2$ c) $NaBH_3CN$ d) MeONa e) $AcOCH_2COCl$ f) $^{i}PrNP(OBn)_2$, then $^{t}BuOOH$ g) NEt_3 / MeOH h) $^{i}PrNP(OBn)_2$, then $^{t}BuOOH$ i) H_2 / Pd

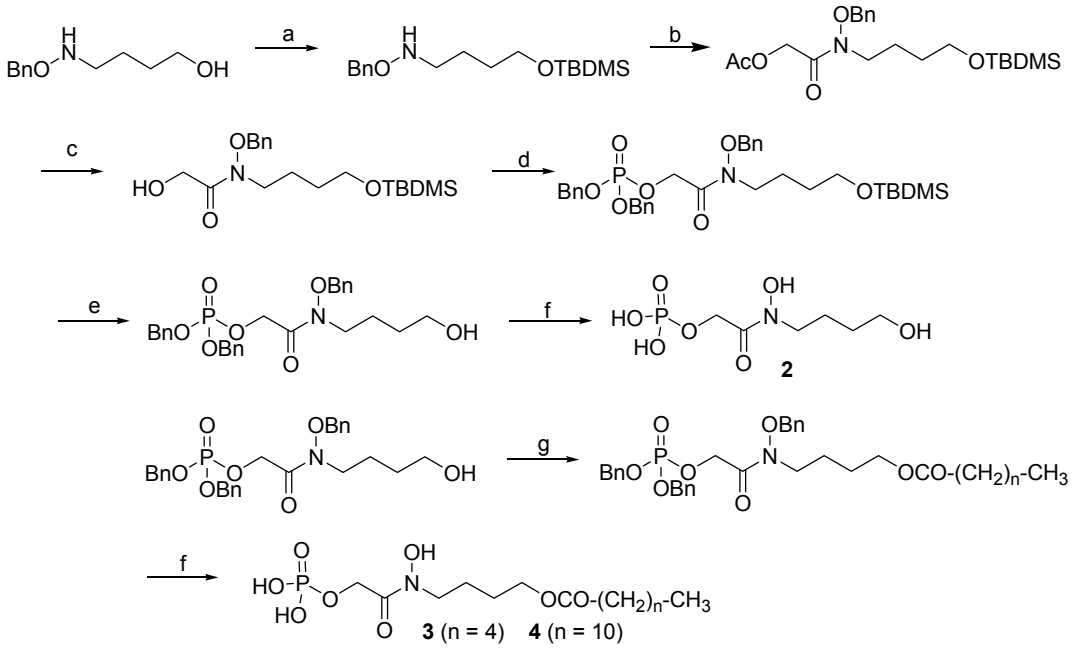

Scheme 4-3. Synthesis of inhibitors **2**, **3**, **4**

a) TBDMS-Cl b) $AcOCH_2COCl$ c) NEt_3 / MeOH d) $^{i}PrNP(OBn)_2$, then $^{t}BuOOH$ e) Bu_4NF f) H_2 / Pd-C g) Hexanoyl or lauroyl chloride.

4.2.3.3 Biochemical evaluation

The four compounds were tested *in vitro* as inhibitors of class II Fbas from various pathogenic species, using an inhibition assay previously reported.[8] For comparison and determination of selectivity, the compounds were also tested against a representative of mammalian class I Fba, isozyme A from rabbit muscle.

We first determined whether the microbial Fbas under study were indeed class II enzymes by conducting the enzymatic test in presence of 10 mM EDTA. Under these conditions, the four enzymes chosen were inhibited at more than 80%. By comparison, the rabbit enzyme (class I) in the same conditions retained full activity.

The analysis of the inhibition kinetics of these enzymes in presence of compounds **1 - 4** are reported in Table 4.

Compound	*Class I Fba*	*Class II Fbas*			
	Rabbit muscle	*H. pylori*	*C. albicans*	*M. tuberculosis*	*Y. pestis*
		K_M or K_i (μM) / (Selectivity)[a]			
FBP (substrate)	15	17	85	21	55
1	57.5 [b]	0.07 [b] *(935)*	0.003 *($1.1x10^5$)*	0.0016 [b] *($5x10^4$)*	0.018 [b] *($1.2x10^4$)*
2	400 [b]	5.5 [b] *(82)*	0.30 *($7.5x10^3$)*	0.185 [b] *($3x10^3$)*	0.195 [b] *($7.25x10^3$)*
3	850	1 [b] *(950)*	0.28 *($1.7x10^4$)*	0.12 [b] *($9.7x10^3$)*	0.195 [b] *($1.6x10^4$)*
4	67	4 [b] *(19)*	0.8 *(475)*	0.31 [b] *(305)*	0.234 [b] *(10^3)*
1'[8]	*264* [b]	0.013 *($2.3x10^4$)*	*0.2* *($7.5x10^3$)*[b]	*0.013* *($2.8x10^4$)*	-
2' [8]	*2500*	*4.7* *(600)*	*0.416* *($3.4x10^4$)*	*0.17* *($2x10^4$)*	-

Table 4-4. *In vitro* biochemical evaluation of inhibitors

[a] Expressed as $(K_M/K_{i\ class\ II}) / (K_M/K_{i\ class\ I})$; [b] calculated from IC_{50} values estimated with $[S] = K_M$.

All four compounds tested show inhibitory activity and selectivity towards class II aldolases. As expected, compound **1** is by far the best inhibitor, with IC_{50} values in the nanomolar range with Fbas from *M. tuberculosis* and *C. albicans*, and selectivities of up to 10^5. A ten-fold lower result was obtained with the enzyme from *Y. pestis.* A still less potent inhibition was observed on *H. pylori* Fba, with K_i and selectivity of 70 nM and 935 respectively. These variations were unexpected in view of the high similarity among the reported structures of class II Fbas.[8,11-13] Interestingly, compounds **2** – **4,** lacking one phosphate group retain selectivity (up to 10^4) and good inhibitory power (largely sub-micromolar), on three out of the four tested enzymes. The presence of a fatty ester on **3** and **4** does not change significantly K_i values, indicating that the compounds can be accommodated in the active site of class II Fbas. Thus, compounds **2 - 4** can be leads for the further synthesis of lipophilic prodrugs, more likely to cross biological membranes.[10] The best inhibitions were obtained on the *C. albicans* Fba. Consequently, this enzyme, considered as representative of the class II Fbas, was chosen for the determination of the type of inhibition. On this enzyme, all four inhibitors **1 - 4** displayed competitive inhibition (see supplementary information). The K_M / K_i value of up to 28 000 obtained with **1** on *C. albicans* Fba is indicative of a transition-state analogue inhibitor rather than a simple substrate analogue.[14,15]

4.2.3.4 **Crystallographic results**

The crystallographic structures of Fba from *H. pylori* bound with compound **1** and **2** were solved to 1.85Å and 1.8Å resolution, respectively, in order to investigate the significant differences in affinity by compounds **1** and **2** among the class II aldolases shown in table 4. Crystals of *H. pylori* Fba were grown by vapour diffusion as described previously[8]. *H. pylori* Fba structures in complex with **1** and **2** were solved by molecular replacement using *H. pylori* Fba complexed with **1'** (PDB ID 3C56)[8] as search model and the structures corresponding to the best solution were refined and analyzed.

The compounds **1** and **2** bind in the active site of *H. pylori* Fba, consistent with their role as competitive inhibitors. The modes of active site binding for compounds **1** and **2** are shown in figure 15A and 15B, respectively.

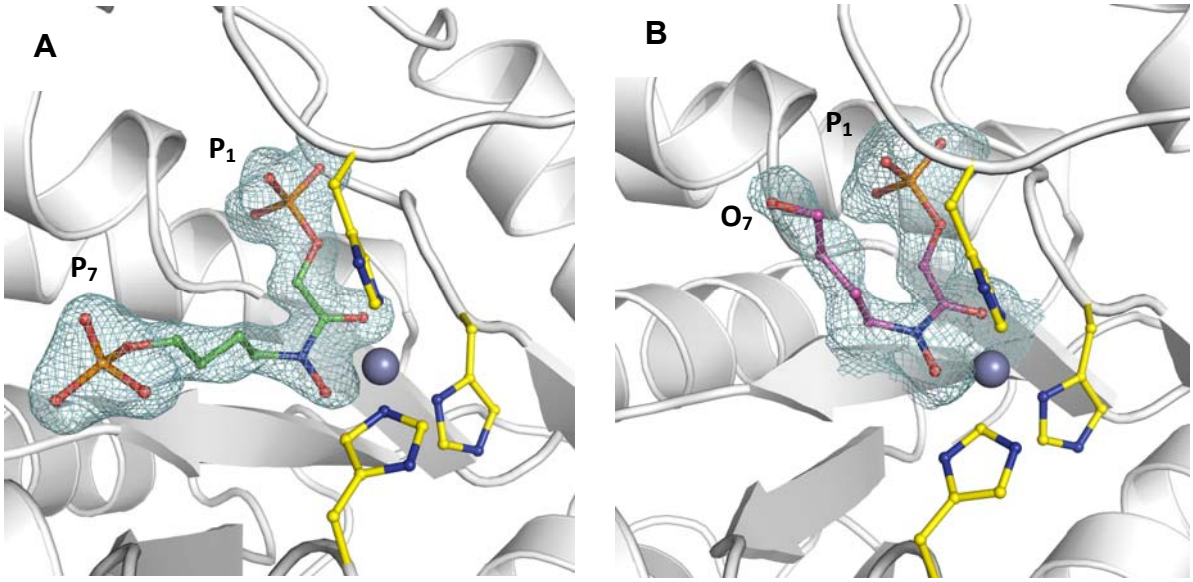

Figure 4-15. Difference electron density (F_0-F_C) simulated annealed omit map showing fit to the electron density map by compounds **1** and **2** that are bound in the active site of *H. pylori* Fba.

Binding by compound **1** is shown in panel **A** while that for compound **2** is shown in panel **B**. P_1 and P_7 phosphates of **1** as well as O_7 atom of **2** are identified. Side chains for the histidine residues chelating the catalytic zinc ion are also depicted. Figure drawing and superposition were prepared using the program PyMOL.[16] The catalytic zinc ion is shown as a grey sphere in all figures. The electron densities shown were contoured at 3.5σ.

The structural data obtained with **1** in *H. pylori* Fba reflects binding properties indicating that the interaction by the hydroxamate based inhibitor results in a loosely coordinated trigonal bi-pyramid geometry around the catalytic Zn^{++} ion. Differences in the bound configurations of **1** and **2** are conditioned by the presence or absence of the P7-

phosphate. In compound **1** bearing the P7-phosphate, the bound geometry is coincident with **1'** bound in *H. pylori* Fba previously reported[8], and shown in figure 16.

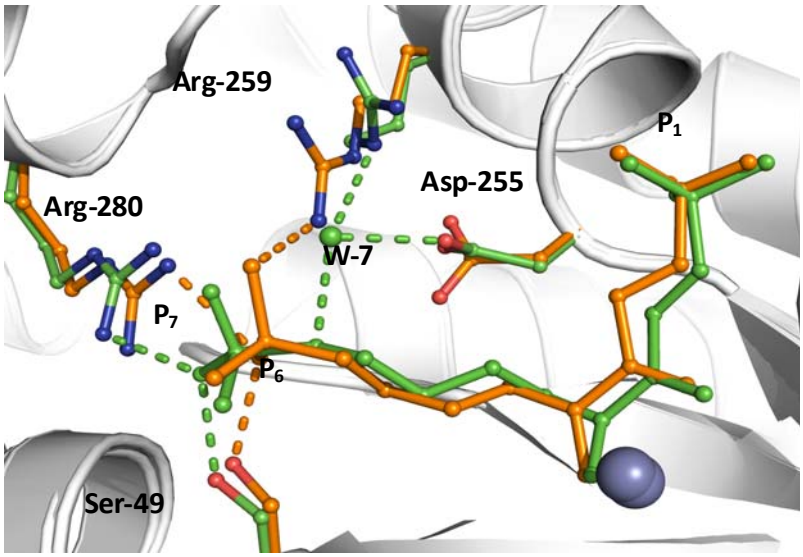

Figure 4-16. Differences in binding modes between compounds **1'** (orange) and **1** (green) in *H. pylori* Fba.

The P6 – phosphate in **1'** participates in electrostatic interactions with Arg-259 and Arg-280 and one hydrogen bond with Ser-49. In **1**, the P7-phosphate loses its charged interaction with Arg-259, replaced by a hydrogen bond with W-7.

Although, the binding sites for the P7-phosphate of **1** and the P6-phosphate of **1'** overlap substantially, there is a notable difference regarding oxyanion binding. In compound **1**, the P7-oxyanion looses an electrostatic interaction made by the P6-oxyanion of compound **1'** with Arg-259**.** The longer alkyl carbon chain in **1** repositions the P7-oxyanion in the active site abrogating the electrostatic interaction and is replaced by a hydrogen bond between the P7-phosphate ester oxygen and W-7. The weaker strength of the hydrogen bond relative to the electrostatic interaction diminishes active site affinity by **1** compared to **1'** and is consistent with 5 fold greater K_i value for **1** than that reported for **1'**[8], also shown in Table 4.

Compound **2** due to the absence of a P7-phosphate adopts an alternate configuration with atoms C4, C5, C6, and O7 pointing out of the active site. Electron density delineating the configuration of compound **2** in each asymmetric unit cell was well defined for 4 of the 8 protomers and was characterized by O7 interacting solely with water molecules. A representative fit by compound **2** to the electron density in these asymmetric unit cells is shown in Figure 5b. In the remaining asymmetric unit cells, carbon atoms C4 – C7 and O7 of compound **2** were fitted to progressively weaker electron density that corresponded to a slightly different traces for these atoms. In this secondary configuration, O7 interacted with its phosphate oxyanion. Superimposition of compound **2** from all asymmetric subunits indicated considerable configurational heterogeneity, notably for the positions of the terminal C7 and O7 atoms (RMSD for C7 and O7 were 0.82 Å and 1.01 Å, respectively). The absence of the P7-phosphate moiety in **2** decreases affinity by nearly two orders of magnitude shown from table 1 and reflects a similar loss in binding affinity by compound **2'** (the monophosphorylated form of **1'** lacking the P6-phosphate) compared to **1'**, shown in Table 1. In the bound configuration, the hydroxamate moiety of **2** coordinates the Zn ion in a coplanar geometry mimicking an enediolate transition-state that could partially compensate for the loss in binding affinity by **2** due to the absence of the P7-phosphate.

Superposition of native Fba with each bound Fba (RMSD < 0.5 Å, based on all Cα atoms) indicates the same localized conformational changes induced upon binding, reported previously,[8] allowing efficient interaction with the P_1 phosphate of each compound. Concomitantly with this conformational movement, the catalytic zinc ion displaces by 3.7 Å from its buried position in the native structure towards the active site surface, chelating C=O and N-O oxygens of **1** and **2**, while maintaining its interaction with the chelating His residues of the active site. The identical conformational responses to compounds **1** and **2** binding (also previously observed with **1'**) indicate that the differential interaction by the alkyl fraction of these compounds with the active site modulates their binding affinity rather than differential conformational responses by *H. pylori* Fba to binding by compounds **1** and **2**.

M. tuberculosis aldolase in complex with FBP (PDB ID: 3ELF)[17] was next used as a surrogate template to model interactions made by *M. tuberculosis* aldolase with compounds **1'**, **1**, and **2**. Modeling consisted of superimposing the structures of *H. pylori* aldolase in complex with compounds **1'**, **1**, and **2** onto the structure of *M. tuberculosis* aldolase in complex with FBP using the Align function in the program PyMOL (RMSD < 1Å based on 175 superimposed Cα atoms). The superimposition coincided FBP phosphate oxyanions with those of the **1'** analogue and closely aligned the positions of the homologous backbone carbons of **1'** with those of FBP (Figure 18 - supplemental information). The match of FBP with the positions of **1'** corroborates use of the structure of *M. tuberculosis* aldolase in complex with FBP as a good surrogate template to probe the response of *M. tuberculosis* aldolase to active site ligand binding events.

The superimposition highlighted active site differences that rationalized trends in binding affinity between the two Fbas. A significant difference is the electrostatic interaction made in *H. pylori* Fba between the **1'** P6-oxyanion and an arginine, Arg-259, which does not have a homologue in *M. tuberculosis* Fba. Instead, in *M. tuberculosis* Fba, the P6-oxyanion electrostatic interaction is replaced by hydrogen bond to a water molecule W-463 that maximizes its hydrogen bonding interaction with three additional active site residues, Lys-308, Asp-276, and Gln-280, shown in Figure 17a. The hydrogen bond interaction is complemented by an additional electrostatic interaction, albeit weaker between the P6-oxyanion and Arg-314 (3.1Å). Identical K_i values for **1'** in both Fbas and also very similar K_M values, according to table 4, suggests that these two interactions in *M. tuberculosis* Fba compensate for the loss of the strong electrostatic interaction made in *H. pylori* Fba.

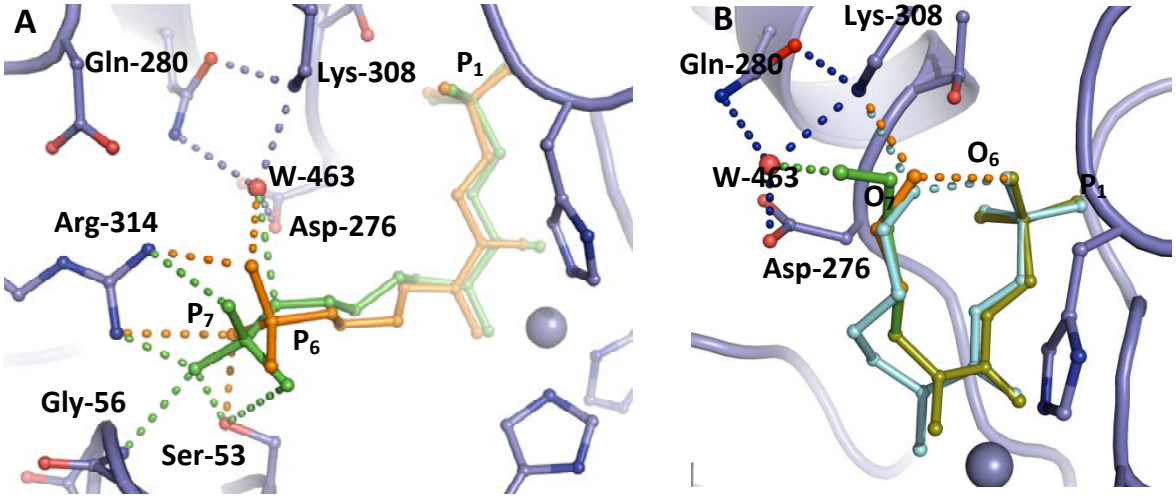

Figure 4-17. Modeling of compounds **1'**, **1**, **2** and **2'** into active site of *M. tuberculosis* Fba active site.

Interactions made by **1'**, **1**, **2** and **2'** with active site residues other than with their alkyl fractions are identical among the two Fbas. Panel **A** shows the interactions made by the P6-phosphate of **1'** (orange) and the P7-phosphate of **1** (green) while panel **B** shows the interactions made by the O6 atom in **2'** (monophosphorylated form of **1'** without the P6-phosphate) (orange) and O7 atom in **2** (green). Panel **B** also shows the interactions made by O7 in a representative secondary configuration (cyan) fitted for compound **2**. Water molecule W-463 positioned through hydrogen bonding with Asp-276, Gln-280 and Lys-308 is shown in orange. View was obtained by overlaying structures of *H. pylori* Fba bound by **1'** and *M. tuberculosis* Fba bound with FBP.

The interaction of **1** with *M. tuberculosis* Fba, as shown in Figure 17a, results in formation of an additional H-bond between the P7-oxyanion and a backbone amide of Gly-56 that does not occur in *H. pylori* Fba. In *H. pylori* aldolase, the homologous residue, Ala-52, points its methyl group towards the P7-oxyanion, precluding additional hydrogen bonding, and corroborating the greater affinity (estimated through the inhibitory activity)

by **1** for *M. tuberculosis* Fba compared to **1',** shown in Table 4. This difference in active site residues, Ala-52 in *H. pylori* Fba versus Gly-56 in *M. tuberculosis* Fba, rationalizes the inverse trend in binding affinity for **1** between these two class II Fbas.

Figure 17b shows the results of the modeling of **2** into the active site of *M. tuberculosis* aldolase (PDB ID: 3elf). In contrast to *H. pylori* Fba, where O7 in **2** does not interact with active site residues, superimposition of **2** onto *M. tuberculosis* Fba indicates additional stabilization of binding by compound **2**. Although direct superimposition of compound 2, as shown in Figure 15b, introduces an apparent steric conflict between Lys-308 Cα and O7 atom of **2**, the steric clash can be relieved by slight displacement of the terminal alkyl chain in **2** (0.6Å) that is comparable in magnitude to the RMSD value of the configurational heterogeneity observed for atoms C7 and O7. In this unencumbered configuration, O7 of **2** is able to hydrogen bond with water molecule Wat-463 that enhances its interaction with the active site in *M. tuberculosis* aldolase. In its secondary configuration, superposition enables compound **2** to interact with Lys-308 while maintaining its interaction with its own oxyanion. Compound **2'** lacking the P6-phosphate in **1'** can be modeled bound isostructurally with **2** as shown in Figure 5b, and allowing its O6 atom to form a hydrogen bond with Lys-308 as well as with its own oxyanion, shown in orange in figure 17b. The additional hydrogen bond made by compounds, **2** and **2'**, in *M. tuberculosis* Fba are consistent with their greater active site binding affinity in *M. tuberculosis* Fba compared to *H. pylori* Fba, shown in Table 4.

Multiple alignment of class II Fba (Figure 19 - supplemental information) supports greater active site similarity between the Fba enzymes of C. albicans / Y. pestis and *M. tuberculosis* than with the *H. pylori* Fba. Active site residues that contact compounds **1'**, **1** and **2** in *M. tuberculosis* Fba are conserved in C. albicans and Y. pestis Fba including the residues homologous to Gly-56 and Gln-280. Indeed, compounds **1** and **2** exhibit tighter inhibitions of C. albicans and Y. pestis Fbas similar to *M. tuberculosis* Fba, as seen in Table 1, compared to *H. pylori* Fba. These two residues rationalize the differential response to active site binding by compounds **1'**, **1** and **2** within class II Fbas. The modification of

compound **2** by the addition of lipophilic esters does not significantly impact binding affinity for compounds **3** and **4** for all class II Fbas, shown in Table 4, and would indicate that lipophilic esters do not interact with active residues and likely point towards the bulk solution.

Compound 1 differs from aldolase substrate sedoheptulose-1,7-bisphosphate in the absence of hydroxyl moieties at C4, C5, and C6 atoms. In class I aldolase, KM values determined with sedoheptulose-1,7-bisphosphate are comparable with those determined for FBP9. We postulate that **1**, in lacking hydroxyl moieties at atom positions C4, C5 and C6 reduces its ability to participate in hydrogen bonding interactions with active site residues of class I aldolase and together with the apparent coplanarity of hydroxamate moiety atoms in 1 would further hinder optimal fit into class I aldolase active site and forms an additional basis for high selectivity of **1** for class II aldolases. Future design would exploit stereochemical differences introduced at C4, C5, and/or C6 atoms with respect to FBP and sedoheptulose-1,7-bisphosphate substrates in order to enhance inhibitor potency.

4.2.3.5 Antibacterial evaluation

Compounds **1-4** were assayed by standard procedures18, 19 for inhibition of growth of cultivated microorganisms: *M. tuberculosis*, *C. albicans*, *Y. pestis*. No inhibition was observed at concentrations up to 1 mM.

4.2.4 Conclusion

We have prepared and evaluated the most powerful and selective inhibitor of class II Fba reported so far. Non-phosphorylated derivatives of this compound, although less potent, may serve as lead candidates for the synthesis of prodrugs to be tested on cultivated pathogenic species. The detailed structural analysis, in full accordance with the kinetics data, indicates that the design of potent hydroxamate based inhibitors for class II Fbas is conditioned by the absence or presence of specific non-homologous active site residues. These differences can be exploited in the design of more potent and selective inhibitors for therapeutic gain. No inhibition of growth of cultivated pathogens however was observed so

far with compounds **1 – 4**, most probably as a consequence of the presence of phosphate groups. We propose to synthesize lipophilic prodrugs of the best inhibitors bearing phosphomimetic groups.

4.2.5 Methods

4.2.5.1 Enzymes

The four class II Fbas were purified recombinant enzymes, expressed in *E. coli*. Class I Fba from rabbit muscle was purchased from Sigma.

Enzymatic test

Fructose bisphosphate and inhibitor, made up at the appropriate concentration in a glycyl-glycine buffer (0.1 M pH 7.4, 0.2 M in AcOK), NADH (0.12 mM), glycerophosphate dehydrogenase (11 U), triose-phosphate isomerase (3 U) and aldolase (4 mU) were placed in a cuvette to give a final volume of 1.2 mL. The decrease in absorbance of NADH at 340 nm was monitored on a spectrophotometer over 1–2 min.

4.2.5.2 Chemical syntheses

The complete procedure is given in the Supplementary Information File. The determination of purity of the four synthesized compounds was performed with a Perkin-Elmer HPLC system using a Hypersil ODS C18 analytical column (250 x 4.6 mm) and a linear gradient solvent system: 0.1 M triethylammonium acetate buffer: CH_3CN in ratios from 95/5 to 40/60 for 20 min with flow rate 1mL/min. Peaks were detected by UV absorption using a diode array detector. Retention times, min (purity): **1:** 4.5 min (95%); **2:** 6.8 (96%); **3:** 8.7 (96%); **4:** 10.2 (95%).

Selected analytical data for compounds **1 - 4**:

1 (disodium salt) : ^{1}H NMR (250 MHz, D_2O): δ 4.5 (d, *J* = 6.5 Hz, 2H) 3.7 (q, *J* = 6.25 Hz, 2H) 3.5 (t, *J* = 6.25 Hz, 2H) 1.56 - 1.44 (m, 2H), 1.62 - 1.56 (m, 2H). ^{13}C NMR (62.5 MHz, BB, D_2O): δ 171.0, 170.86, 65.0, 64.92, 61.8, 47.88, 27.0, 26.89, 22.11. ^{31}P NMR (101.25 MHz, BB, D_2O): δ 1.85, 0.95.

HR-MS (ESI negative): *m/z* 322.0088 (calcd for $C_6H_{14}NO_{10}P_2$: 322.0093).

2 (monosodium salt) : ^{1}H NMR (250 MHz, D_2O): δ 4.49 (d, *J* = 6.25 Hz, 2H) 3.52 (t, *J* = 6.5 Hz, 2H) 3.48 (t, *J* = 6.5 Hz, 2H) 1.52 (p, *J* = 6.5 Hz, 2H) 1.42 (t, *J* = 6.5 Hz, 2H). ^{13}C NMR (62.5 MHz, BB, D_2O): δ 171, 61.63, 61.18, 47.90, 28.29, 22.18. ^{31}P NMR (101.25 MHz, BB, D_2O): δ 2.47.

HR-MS (ESI negative): *m/z* 242.0429 (calcd for $C_7H_{13}NO_7P$: 242.0430).

3 (monosodium salt) : ^{1}H NMR (250 MHz, D_2O): δ 4.5 (d, *J* = 5.7 Hz, 2H) 4.05 (t, *J* = 5.85 Hz, 2H) 3.55 (t, *J* = 5.8 Hz, 2H) 2.29 (t, *J* = 7.5 Hz, 2H) 1.66 – 1.4 (m, 6H) 1.30 – 1.10 (m, 4H) 0.77 (t, *J* = 6.9 Hz, 3H). ^{13}C NMR (62.5 MHz, BB, D_2O): δ 177.56, 64.82, 61.51, 47.81, 34.02, 30.54, 25.02, 24.13, 22.46, 21.64, 13.21. ^{31}P NMR (101.25 MHz, BB, D_2O): δ 3.72.

HR-MS (ESI negative): *m/z* 340.1163 (calcd for $C_{12}H_{23}NO_8P$: 340.1161).

4 (monosodium salt) : ^{1}H NMR (250 MHz, D_2O): δ 4.51 (d, *J* = 4.0 Hz, 2H) 4.07 – 3.93 (m, 2H) 3.58 – 3.45 (m, 2H) 2.2 (t, *J* = 6Hz, 2H) 1.66 -1.42 (m, 6H) 1.29 – 1.05 (m, 16H), 0.75 (t, *J* = 6 Hz, 3H). ^{13}C NMR (62.5 MHz, BB, D_2O): δ 174.6, 64.37, 61.63, 34.11, 32.0, 29.85 – 29.3, 25.36, 24.86, 22.66, 22.53, 13.85. ^{31}P NMR (101.25 MHz, BB, D_2O): δ 3.78.

HR-MS (ESI negative): *m/z* 424.2113 (calcd for $C_{18}H_{35}NO_8P$: 424.2100).

4.2.6 Acknowledgments

We are very grateful to Dr Jean-Michel Bruneau (NOVEXEL, Romainville, France) for the kind supply of recombinant Fba from *C. albicans*. JS was supported by funding from Natural Sciences and Engineering Research Council (Canada) and Canadian Institutes for Health Research. RD was supported by a scholarship from the Region Ile de France. MJ is supported by the National Institute of Allergy and Infectious Diseases (NIAID), National Institutes of Health (NIH) grant AI078126 and the National Institute of Neurological Disorders and Stroke (NINDS), NIH grant NS066438.

4.2.7 References

(1) Soulsby, E.J. Resistance to antimicrobials in humans and animals. *Br.Med. J. (Clin. Res. Ed.)* **2005**, *331*, 1219-1220.

(2) Mc Fee, R.B. Nosocomial or hospital-acquired infections: an overview *Disease-A-Month* **2009**, *55*, 422-438.

(3) a) Maartens, G.; Wilkinson, R.J. Tuberculosis, *Lancet* **2007**, *370*, 2030-2043. b) Prentice, M.B.; Rahalison, M. Plague, *Lancet* **2007**, *369*, 1196-1207.

(4) World, M.J. Bioterrorism. The need to be prepared, *Clin. Med.* **2004**, *4*, 161-164.

(5) Gefflaut, T.; Blonski, C.; Perie, J.; Willson, M. Class I aldolases: Substrate specificity, mechanism, inhibitors and structural aspects. *Prog. Biophys. Mol.Biol.* **1995**, *63*, 301-340.

(6) Collins, K. D. An activated intermediate analogue. The use of phosphoglycolohydroxamate as a stable analogue of a transiently occurring dihydroxyacetone phosphate-derived enolate in enzymatic catalysis *J. Biol. Chem.* **1974**, *249*, 136-142.

(7) Fonvielle, M.; Weber, P.; Dabkowska, K.; Therisod, M. New highly selective inhibitors of class II fructose-1,6-bisphosphate aldolases. *Bioorg. Med.Chem. Lett.* **2004**, *14*, 2923-2926.

(8) Fonvielle, M.; Coinçon, M.; Daher, R.; Desbenoit, N.; Kosieradzka, K; Barilone, N.; Gicquel, B.; Sygusch, J.; Jackson, M.; Therisod, M. Synthesis and biochemical evaluation of selective inhibitors of class II fructose bis-phosphate aldolases: towards new synthetic antibiotics *Chem. Eur. J.* **2008**, *14*, 8521-8529.

(9) a) Flechner, A.; Gross, W.; Martin, W.F.; Schannenberger, C. Chloroplast class I and class II aldolases are bifunctional for fructose-1,6-biphosphate and sedoheptulose-1,7-biphosphate cleavage in the Calvin cycle. *FEBS lett.* **1999**, *447*, 200-202. b) Nakahara, K.; Yamamoto, H.; Miyake, C.; Yokota, A. Purification and characterization of class-I and class-II fructose-1,6-bisphosphate aldolases from the

cyanobacterium *Synechocystis sp*. PCC 6803. *Plant Cell. Physiol.* **2003**, *44*, 326-333. c) Erales, J; Avilan, L; Lebreton, S; Gontero, B. Exploring CP12 binding proteins revealed aldolase as a new partner for the phosphoribulokinase/glyceraldehyde 3-phosphate dehydrogenase/CP12 complex - purification and kinetic characterization of this enzyme from *Chlamydomonas reinhardtii*. *FEBS J.* **2008**, *275*, 1248-1259.

(10) Schultz, C. Prodrugs of biologically active phosphate esters. *Bioorg. Med. Chem.* **2003**, *11*, 885-898.

(11) Hall, D.R.; Leonard, G.A.; Reed, C.D.; Watt, C.L.; Berry, A.; Hunter, W.N. The crystal structure of Escherichia coli class II fructose-1,6-bisphosphate aldolase in complex with phosphoglycolohydroxamate reveals details of mechanism and specificity. *J. Mol. Biol.* **1999**, *287*, 383-394.

(12) Galkin, A.; Kulakova, L.; Melamud, E.; Li, L.; Wu, C.; Mariano, P.; Dunaway-Mariano, D.; Nash, T.E.; Herzberg, O. Characterization, kinetics, and crystal structures of fructose-1,6-bisphosphate aldolase from the human parasite, *Giardia lamblia*. *J. Biol. Chem*. **2007**, *282*, 4859-4867.

(13) Izard,T; Sygusch, J. Induced fit movements and metal cofactor selectivity of class II aldolases: structure of *Thermus aquaticus* fructose-1,6-bisphosphate aldolase. *J. Biol. Chem*. **2004**, *279*, 11825-11833.

(14) Kurz, J.L. Transition state characterization for catalyzed reactions. *J. Am. Chem. Soc.* **1963**, *85*, 987-991.

(15) Wolfenden, R. Transition state analogues for enzyme catalysis. *Nature* **1969**, *223*, 704-705.

(16) DeLano, W.L. (2004) The PyMOL Molecular Graphics System, DeLano Scientific LLC, San Carlos, CA

(17) Pegan, S.D.; Rukseree, K.; Franzblau, S.G.; Mesecar, A.D. Structural basis for catalysis of a tetrameric class II fructose 1,6-bisphosphate aldolase from *Mycobacterium tuberculosis. J. Mol. Biol.* **2009**, *386*, 1038-1053.

(18) Bai, N.J.; Pai, M.R.; Murthy, P.S.; Venkitasubramanian, T.A. Effect of oxygen tension on the aldolases of *Mycobacterium tuberculosis*. *FEBS Lett.* **1974**, *45*, 68 – 70.

(19) Martin, A.; Camacho, M.; Portaels, F.; Palomino, J.-C. Rezazurin microtiter assay plate testing of *Mycobacterium tuberculosis* susceptibilities to second-line drugs : rapid, simple and inexpensive method. *Antimicrob.Agents Chemother.* **2003**, *47*, 3616 –3619.

4.2.8 Supporting Information

4.2.8.1 Chemistry

All reactions were performed in open flasks, unless otherwise stated. Solvents used were dry solvents. Dichloromethane and acetonitrile were distilled over CaH_2; tetrahydrofuran, toluene, diethylether were distilled over sodium chips using benzophenone as indicator of dryness; dimethyl formamide was distilled at reduced pressure over anhydrous BaO. All other solvents were used as purchased. Commercial reagents were used as purchased without any further purification. Organic solutions were concentrated under reduced pressure on a Büchi rotary evaporator. Chromatographic purification of products was carried out using SDS silica gel (35 – 70 μm). Thin layer chromatography was carried out using Merck Kieselgel 60 F_{254} (230-400 mesh) fluorescent treated silica which were visualized under UV light (240 nm) or by staining with aqueous basic potassium permanganate solutions. NMR spectra were recorded in deuterated solvents on Bruker spectrometers, with residual protic solvent as the internal standard. ^{13}C and ^{31}P NMR spectra were recorded under broad-band irradiation of the protons. Interpretation of the spectra was made possible by use of 2D (proton-proton and proton-carbon) and DEPT experiments.

4.2.8.2 **Biochemistry**

4.2.8.2.1 Enzymes:

Glycerophosphate dehydrogenase from rabbit muscle (GPDH, 274 $U.mL^{-1}$), triose-phosphate isomerase from rabbit muscle (TIM, 32,000 $U.mL^{-1}$), rabbit muscle Fba ($8U.mg^{-1}$) were commercial preparations, available from Sigma or Fluka. Microbial Fbas were recombinant enzymes expressed in *E. coli*.

fba from *Yersinia pestis* was PCR-amplified from *Y. pestis* A1122 genomic DNA using primers fba_NdeI_fwd (5'-gggaattccatatgtctaaaatttttgatttcgtaaaacc-3') and fba_BamHI_rev (5'-cgcggatcctcacagtacgtcgatggcgttcag-3') and Phusion DNA Polymerase

(New England Biolabs), and the PCR product was ligated into the NdeI and BamHI restriction sites of the expression vector pET29a (Novagen). *E. coli* strain BL21(DE3) cells (Novagen) were transformed with this construct and the Fba protein produced with this system (which carries no C-ter or N-ter tag) was then purified to near homogeneity from *E. coli* sonicates using a combination of ammonium sulfate fractionation and anion exchange, hydrophobic interaction and size exclusion chromatography. The production and purification of an untagged form of the *M. tuberculosis* Fba protein will be reported elsewhere.

fba: Plasmid pKK223-3 coding for *H. pylori* Fba was transformed and overexpressed in *E. coli* strain JM109. Recombinant *H. pylori* Fba was purified by a combination of anion exchange (DEAE), hydrophobic exchange chromatography (Phenyl-Sepharose) and size exclusion chromatography (^{i}). Aldolase concentration was determined by BCA Protein Assay Reagent (Pierce) with bovine serum albumin serving as standard.

Candida albicans Fba was kindly provided by Dr Jean-Michel Bruneau, NOVEXEL, Romainville (France).

4.2.8.2.2 Solutions:

Glycylglycine buffer (0.1 M, pH 7.4, with 0.2 M potassium acetate for activity assay of class II aldolases). NADH 1.41 mM and fructose bisphosphate 2 mM separately made up in assay buffer.

4.2.8.2.3 Enzymatic assays:

Fructose bisphosphate and inhibitor at the appropriate concentration, NADH (0.12 mM), GPDH (11 U) TIM (4 U) and aldolase (4 mU) were placed in a cuvette to give a final volume of 1.2 mL. The decrease in absorbance of NADH at 340 nm was monitored on a spectrophotometer over 5 min.

For determination of IC_{50} values, the substrate (FBP) was used at a concentration equal to the determined K_M of the enzyme (see table 4 of the manuscript).

4.2.8.3 Chemical syntheses

4.2.8.3.1 Synthesis of compound 1

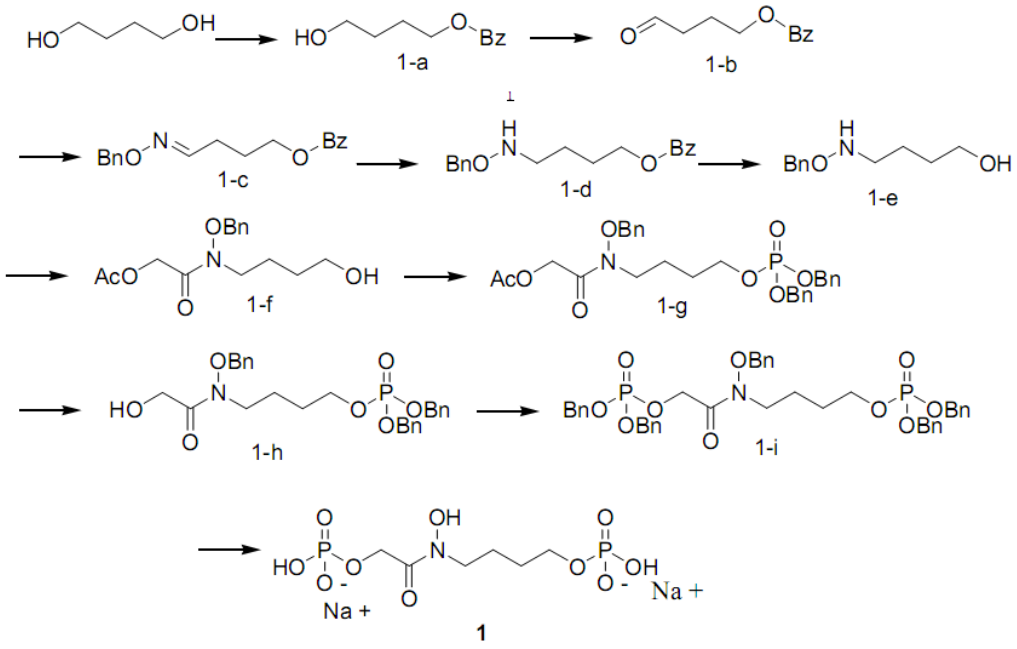

1-a:

1,4-butanediol (0.5 mol, 44.3 mL) was dissolved in anhydrous pyridine under an Ar atmosphere. Benzoyl chloride (0.1 mol, 11.6 mL) was added dropwise. The mixture was further stirred at RT during 2 hours and then the solvent evaporated. The residue was redisolved in 60 mL of dichloromethane, and the solution washed three times with 60 mL of water. After drying and evaporation, the product was purified by flash-chromatography (pentane / AcOEt 6:4); 12 g, 62%.

^{1}H NMR (250 MHz, $CDCl_3$): δ 8.02 - 7.38(m, 5H) 4.33 (t, J = 6.45 Hz, 2H) 3.68 (t , J = 6..45 Hz, 2H) 1.86 - 1.8 (m, 2H) 1.73 - 1.68 (m, 2H). ^{13}C NMR (62.5 MHz, BB, $CDCl_3$): δ 166.79, 132.94, 130.28, 129.52, 128.36, 64.87, 62.1, 29.15, 25.24 ppm.

1-b:

PCC (51 mmol, 11 g) was suspended in dichlorométhane (105 mL) together with 1g powdered activated molecular sieves and vigorously stirred. Compound 1-a (26 mol, 5 g) was added at once and the mixture was stirred at RT for 3 h. The very black mixture was poured into ether (800 mL). The supernatant was directly filtered on a silicagel column (20 g), and the column washed with dichloromethane. 1-b was obtained after evaporation of the solvent a nd used without further purification. 4.3 g, 87%.

^{1}H NMR (250 MHz, $CDCl_3$): δ 9.77 (s, 1H) 7.99 - 7.38 (m, 5H) 4.31 (t, *J* = 6.33 Hz, 2H) 2.59 (t, *J*= 6.43 Hz) 2.06 (p, *J*= 6.75 Hz, 2H). ^{13}C NMR (62.5 MHz, BB, $CDCl_3$): δ 201.36, 166.42, 133.04, 130.03, 129.52, 128.4, 63.95, 40.48, 21.42 ppm.

1-c

Compound 1-b (15.6 mmol, 3 g) and O-benzylhydroxylamine (23.5 mmol, 2.9 g were dissolved in a 1:6.5 mixture of pyridine and methanol. The solution was heated under reflux overnight. After evaporation, the product (mixture of Z / E isomers) was purified by flash-chromatography (pentane/ Et_2O 8:2). 3.3 g, 71%.

Z isomer:

^{1}H NMR (250 MHz, $CDCl_3$): δ 8.08 - 7.3 (m, 12H) 6.81 (t, *J*= 5.5 Hz, 2H) 5.2 (s, 2H) 4.38 (t, *J* = 6.4 Hz, 2H) 2.59 (q, *J* = 6.85 Hz , 2H) 2 (p, *J* = 6.9 Hz, 2H). ^{13}C NMR (62.5 MHz, BB, $CDCl_3$): δ 166.49, 150.94, 138, 132.98, 130.3, 129.63, 128.43, 127.98, 127.82, 75.89, 64.32, 25.6, 22.89 ppm.

E isomer:

^{1}H NMR (250 MHz, $CDCl_3$): δ 8.09 - 7.38(m, 10H) 5.11 (s, 2H) 4.39 (t, *J* = 6.35 Hz, 2H) 2.41 (q, *J* =6.85 Hz, 2H) 2.02 (p, *J* =6.9 Hz, 2H). ^{13}C NMR (62.5 MHz, BB, $CDCl_3$): δ 166.48, 150.08, 137.7, 132.98, 130.3, 129.64, 128.43, 128.3, 127.89, 75.7, 64.1, 26.55, 25.85 ppm.

1-d

Compound 1-c (mixture of E / Z isomers, 9.34 mmol, 2.8g) was dissolved in a 1 :1 mixture of acetic acid and methanol (15 mL) at 0°C. Sodium cyanoborohydride (11.2 mmol, 0.7 g) was added by portions. The mixture was then stirred at RT for 5 h. After evaporation, the product was redissolved in saturated sodium hydrogenocarbonate and extracted with 3 x 25 mL dichloromethane. The organic phase was washed by water, brine, dried, evaporated and the product purified by flash chromatography (pentane/ ether/ triethylamine 70:30:0.01. 2.3 g, 79%.

^{1}H NMR (250 MHz, $CDCl_3$): δ 8.08 - 7.3 (m, 10H) 4.75 (s, 2H) 4.36 (t, *J*= 6.25 Hz, 2H) 3.04 (t, *J*= 6.9 Hz, 2H) 1.88 - 1.8(m, 2H) 1.75 - 1.69 (m, 2H). ^{13}C NMR (62.5 MHz, BB, $CDCl_3$): δ 166.67, 137.95, 132.93, 130.41, 129.59, 128.43, 127.88, 76.36, 64.87, 51.72, 26.49, 24.13 ppm.

1-e

Compound 1-d (6.94 mmol, 2.1 g) was dissolved in 1M sodium methanolate in methanol and the mixture was left 2h at RT. The solution was diluted with dichloromethane, washed with water, dried and evaporated. 1-e was used without further purification. 1.18g, 87%).

^{1}H NMR (250 MHz, $CDCl_3$): δ 7.46 - 7.28 (m, 5H) 4.74 (s, 2H) 3.6 (t, *J*= 6 Hz, 2H) 2.97 (t, *J*= 6.5 Hz, 2H) 1.71 - 1.53 (m, 4H). ^{13}C NMR (62.5 MHz, BB, $CDCl_3$): δ 137.61, 128.48, 127.98, 76.14, 62.46, 51.81, 30.89, 24.35 ppm

1-f

To 1-e (6.04 mmol, 1.18 g) and triethylamine (7.25 mmol, 0.733 g) dissolved in methanol at 0°C (15 mL) was added dropwise under vigorous stiring a solution of acetoxyacetyl chloride (7.24 mmol, 0.989 g) in anhydrous ether. The mixture was left 30 min at RT, then it was diluted with ether (20 mL). This solution was washed three times with water, dried and evaporated. 1.75 g, 98%.

^{1}H NMR (250 MHz, $CDCl_3$): δ 7.44 - 7.32 (m, 5H) 4.85 (s, 2H) 4.71 (s, 2H) 3.68 (t, *J*= 7 Hz, 2H) 3.6 (t, *J*= 6.4 Hz, 2H) 2.13 (s, 3H) 1.72 (p, *J* =7.3 Hz, 2H) 1.54 (p, *J* =7 Hz,

2H). ^{13}C NMR (62.5 MHz, BB, $CDCl_3$): δ 170.71, 168.53, 134.02, 129.25, 128.84, 76.59, 62.03, 61.32, 45.61, 29.49, 23.23, 20.57 ppm.

1-g

To a mixture of compound 1-f (5.84 mmol, 1.73 g) and dibenzyl-diisopropylphosphoramidite (11.7 mmol, 4.04 g) thoroughly dried under vacuum were added triazole (17.5 mmol, 1.21 g), imidazole (11.7 mmol, 0.796 g) and acetonitrile (50 mL). The mixture was stirred overnight at RT, then ^{t}butylhydroperoxide (11 .7 mmol, aqueous solution) was added. After a further 3 h, the mixture was diluted with dichloromethane (25 mL) and washed with 1M aqueous sodium thiosulfate. This solution was reextracted three times with DCM.. The organic phase was washed with saturated sodium bicarbonate, dried and evaporated. 1-g was purified by flash chromatography (pentane/ AcOEt 6:4. 2.24 g, 69%.

^{1}H NMR (250 MHz, $CDCl_3$): δ 7.49 - 7.29 (m, 15H) 5.05 (d, *J* =8.3 Hz, 4H) 4.83 (s, 2H) 4.73(s, 2H) 4.01 (q, *J* = 6.25 Hz, 2H) 3.65 (t, *J*= 6.4 Hz, 2H) 2.16 (s, 3H) 1.79 - 1.53 (m, 4H). ^{13}C NMR (62.5 MHz, BB, $CDCl_3$): δ 170.61, 168.5, 135.97, 135.86, 133.96, 129.3, 128.9, 128.61, 127.98, 76.7, 69.23, 69.21, 67.26, 67.17, 61.32, 45.14, 27.35, 27.24, 22.84, 20.64 ppm. ^{31}P NMR (101.25 MHz, BB, $CDCl_3$): δ - 0.835 ppm.

1-h

1-g (3.8 mmol, 2.11 g) was dissolved in 20 mL of a mixture of methanol/triethylamine/water 8:2:1 and kept overnight at RT. 1-h was obtained after evaporation of this mixture. 1.89g, 100%.

^{1}H NMR (250 MHz, $CDCl_3$): δ 7.56 - 7.18 (m, 15H) 5.03 (d, *J* =8.3 Hz, 4H) 4.75 (s, 2H) 4.21 (s, 2H) 3.98 (q, *J* = 6.2 Hz, 2H) 3.66 (t, *J*= 5.75 Hz, 2H) 1.66 - 1.59 (m, 4H). ^{13}C NMR (62.5 MHz, BB, $CDCl_3$): δ 173.71, 135.89, 135.81, 133.96, 129.3, 128.9, 128.86, 127.96, 76.7, 69.31, 69.24, 67.17, 67.09, 60.15, 45.45, 27.34, 27.24, 22.84 ppm. ^{31}P NMR (101.25 MHz, BB, $CDCl_3$): δ - 0.84 ppm.

1-i

The second hydroxyl group was phosphorylated as described above for 1-g. 2.9 g, 98%.

^{1}H NMR (250 MHz, $CDCl_3$): δ 7.56 - 7.16 (m, 25H) 5.15 (d, *J* =7.89 Hz, 4H) 5.05 (d, *J* =8.3 Hz, 4H) 4.74 (s, 2H) 4.68 (d, *J*= 11.25 Hz, 2H) 4 (q, *J* =5.9 Hz, 2H) 3.64 (t, *J*= 6.5 Hz, 2H) 1.78 - 1.5 (m, 4H). ^{13}C NMR (62.5 MHz, BB, $CDCl_3$): δ 168.51, 168.46, 135.92, 135.82, 133.79, 129.26, 129.11, 128.9, 128.58, 128.35, 128.22, 128.04, 127.36, 76.7, 69.64, 69.55, 67.24, 67.14, 64.28, 64.22, 45.25, 27.37, 27.26, 22.82 ppm. ^{31}P NMR (101.25 MHz, BB, $CDCl_3$): δ - 0.83 ppm.

N-(4-hydroxybutyl)-glycolohydroxamic acid bis-phosphate (1) (disodium salt)

1-i (0.84 mmol, 0.65 g) and sodium hydrogenocarbonate (1.68 mmol, 0.141 g) were dissolved in a 3:1 mixture of ethanol and water (20 mL). 10%-Pd/C (0.065 g) was added, and the mixture was kept under hydrogen (4 bar) with a vigorous stirring overnight. After filtration and evaporation, the bis-sodium salt of 1 was obtained as a white hygroscopic powder. 0.361 g, 100%.

^{1}H NMR (250 MHz, D_2O): δ 4.5 (d, *J* = 6.5 Hz, 2H) 3.7 (q, *J* = 6.25 Hz, 2H) 3.5 (t, *J* = 6.25 Hz, 2H) 1.56 - 1.44 (m, 2H), 1.62 - 1.56 (m, 2H). ^{13}C NMR (62.5 MHz, BB, D_2O): δ 171.0, 170.86, 65.0, 64.92, 61.8, 47.88, 27.0, 26.89, 22.11. ^{31}P NMR (101.25 MHz, BB, D_2O): δ 1.85, 0.95.

HR-MS (ESI negative): *m/z* 322.0088 (calcd for $C_6H_{14}NO_{10}P_2$: 322.0093).

4.2.8.3.2 Syntheses of compounds 2, 3, 4.

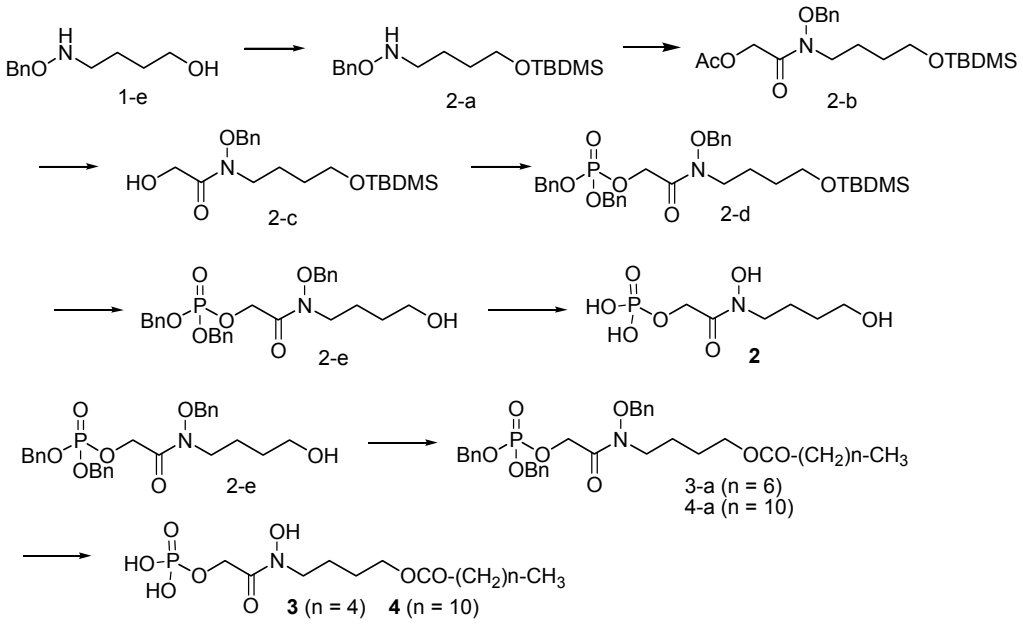

2-a

Intermediate 1-g from the previous synthesis (9.12 mmol, 1.8 g), ^{t}butyl-diméthylsilyl chloride (9.12 mmol, 1.5 g) and imidazole (36.5 mmol, 2.5 g) were dissolved in anhydrous DMF, and the mixture was stirred at RT overnight. The solvent was evaporated and replaced by DCM. This solution was washed three times with water, dried and evaporated to yield 2-a. 2.42 g, 86%.

^{1}H NMR (250 MHz, $CDCl_3$): δ 7.47 – 7.29 (m, 5H) 4.75 (s, 2H) 3.66 (t, *J* =6 Hz, 2H) 2.99 (t, *J* =6.1 Hz, 2H) 1.77 – 1.55 (m, 4H) 0.95 (s, 9H) 0.1 (s, 6H). ^{13}C NMR (62.5 MHz, BB, $CDCl_3$): δ 138.11, 128.39, 127.77, 76.25, 63.14, 52.031, 30.87, 26.05, 23.83, 18.4, -5.2 ppm.

2-b

Compound 2-a (5.mmol, 1.54 g) was acylated by the method used for preparation of 1-f. 2.02 g, 99%.

^{1}H NMR (250 MHz, $CDCl_3$): δ 7.42 – 7.29 (m, 5H) 4.86 (s, 2H) 4.72 (s, 2H) 3.67 (t, *J* = 7 Hz, 2H) 3.6 (t, *J* = 6.2 Hz, 2H) 2.13 (s, 3H) 1.72 (p, *J* = 7.4 Hz, 2H) 1.5 (p, *J* =6.85 Hz, 2H) 0.88 (s, 9H) 0.03 (s, 6H). ^{13}C NMR (62.5 MHz, BB, $CDCl_3$): δ 170.58, 168.334, 134.11, 129.2, 129.15, 128.81, 76.55, 62.5, 61.34, 45.79, 29.84, 25.96, 23.3, 20.6, 18.3, -5.3 ppm.

2-c

Compound 2-b (6.5 mmol, 2.65 g) was deacetylated by the method described for preparation of 1-h.. 2.3 g, 97%.

^{1}H NMR (250 MHz, $CDCl_3$): δ 7.44 – 7.3 (m, 5H) 4.79 (s, 2H) 4.23 (s, 2H) 3.72 (t, *J* = 4.5 Hz, 2H) 3.62 (t, *J* = 6.3 Hz, 2H) 1.74 (p, *J* = 7.35 Hz, 2H) 1.51 (p, *J* = 7 Hz, 2H) 0.9 (s, 9H) 0.04 (s, 6H). ^{13}C NMR (62.5 MHz, BB, $CDCl_3$): δ 173.59, 133.96, 129.22, 128.82, 128.71, 76.59, 62.47, 60.16, 46, 29.83, 25.96, 23.33, 18.31, -5.29 ppm

2-d

Compound 2-c (6.64 mmol, 2.4 g) was phosphorylated by the same method used for preparation of 1-g and 1-i. 3.03g, 75%.

^{1}H NMR (250 MHz, $CDCl_3$): δ 7.56 – 7.16 (m, 15H) 5.2 (d, *J* = 7.8 Hz, 4H) 4.8 (s, 2H) 4.76 (d, *J* = 11.3 Hz, 2H) 3.74 (t, *J* = 7 Hz, 2H) 3.68 (t, *J* = 6.2 Hz, 2H) 1.79 (p, *J* = 7.3 Hz, 2H) 1.58 (p, *J* = 6.8 Hz, 2H) 0.98 (s, 9H) 0.13 (s, 6H). ^{13}C NMR (62.5 MHz, BB, $CDCl_3$): δ 168.38, 133.97, 129.23, 128.84, 127.48, 76.56, 69.66, 69.57, 64.37, 64.3, 62.57, 46.2, 29.92, 26.04, 23.35, 18.38, -5.21 ppm. ^{31}P NMR (101.25 MHz, BB, $CDCl_3$): δ - 0.79 ppm.

2-e

Compound 2-d (4.2 mmol, 2.55 g) was desilylated by treatment for 1 h with tetrabutylammonium fluoride (5 mmol, 1.6 g) and acetic acid (8.35 mmol, 0.5 g) in wet THF (42 mL) at 0°C. After evaporation, the product was purified by column chromatography (pet. Ether/ AcOEt/ triethylamine 40:60:0.01). 1.3 g, 60.5%.

^{1}H NMR (250 MHz, $CDCl_3$): δ 7.54 – 7.14 (m, 15H) 5.14 (d, *J* = 7.8 Hz, 4H) 4.76 (s, 2H) 4.66 (d, *J* = 11.7 Hz, 2H) 3.7 (t, *J* = 6.9 Hz, 2H) 3.63 (t, *J* = 6.4 Hz, 2H) 1.74 (p, *J* = 7.2 Hz, 2H) 1.56 (p, *J* = 7 Hz, 2H). ^{13}C NMR (62.5 MHz, BB, $CDCl_3$): δ 168.65, 135.9, 135.81, 133.89, 129.26, 128.87, 128.55, 128.49, 128.04, 76.56, 69.62, 69.57, 64.33, 64.26, 62.13, 45.62, 29.48, 23.17.ppm^{31}P NMR (101.25 MHz, BB, $CDCl_3$): δ - 0.87 ppm.

N-(4-hydroxybutyl)-phosphoglycolohydroxamic acid (2) (monosodium salt)

2-e was debenzylated by the method used for preparation of 1, to give 2 as the monosodium salt. 0.89 g, 100%.

^{1}H NMR (250 MHz, D_2O): δ 4.49 (d, *J* = 6.25 Hz, 2H) 3.52 (t, *J* = 6.5 Hz, 2H) 3.48 (t, *J* = 6.5 Hz, 2H) 1.52 (p, *J* = 6.5 Hz, 2H) 1.42 (t, *J* = 6.5 Hz, 2H). ^{13}C NMR (62.5 MHz, BB, D_2O): δ 171, 61.63, 61.18, 47.90, 28.29, 22.18. ^{31}P NMR (101.25 MHz, BB, D_2O): δ 2.47.

HR-MS (ESI negative): *m/z* 242.0429 (calcd for $C_7H_{13}NO_7P$: 242.0430).

4.2.8.3.3 Preparation of compound 3

3-a

To 2-e (1.2 mmol, 0.6 g) dissolved in DCM in presence of triethylamine (1.4 mmol, 0.142 g) at 0°C was added dropwise hexanoyl chloride (1.4 mmol, 0.19 g) dissolved in anhydrous DCM. After 3 h at RT, water was added and the mixture was vigorously stirred for 15min. The organic phase was separated, washed three times with water, dried and evaporated. The product was purified by flash-chromatography (pentane / AcOEt 6:4). 0.48 g, 66%.

^{1}H NMR (250 MHz, $CDCl_3$): δ 7.47 – 7.23 (m, 15H) 5.14 (d, *J* = 7.8 Hz, 4H) 4.78 (s, 2H) 4.7 (d, *J* = 11.1 Hz, 2H) 4.07 (t, *J* = 6.25Hz, 2H) 3.68 (t, *J* = 6.5 Hz, 2H) 2.3 (t, *J* = 7.5 Hz, 2H) 1.77 – 1.5 (m, 6H) 1.38 – 1.24 (m, 4H) 0.9 (t, *J* = 6.75 Hz, 3H). ^{13}C NMR (62.5 MHz, BB, $CDCl_3$): δ 179.7, 129.19, 128.88, 128.53, 128.47, 128.02, 69.53, 63.56,

45.6, 34.28, 31.33, 25.94, 24.66, 23.32, 22.32, 13.93 ppm. ^{31}P NMR (101.25 MHz, BB, $CDCl_3$): δ - 0.87 ppm.

N-(4-hydroxybutyl)-phosphoglycolohydroxamic acid hexanoate (3) (monosodium salt)

3-a was debenzylated by the method used for preparation of 1, to give 3 as the monosodium salt. 0.34 g, 100%.

^{1}H NMR (250 MHz, D_2O): δ 4.5 (d, *J* = 5.7 Hz, 2H) 4.05 (t, *J* = 5.85 Hz, 2H) 3.55 (t, *J* = 5.8 Hz, 2H) 2.29 (t, *J* = 7.5 Hz, 2H) 1.66 – 1.4 (m, 6H) 1.30 – 1.10 (m, 4H) 0.77 (t, *J* = 6.9 Hz, 3H). ^{13}C NMR (62.5 MHz, BB, D_2O): δ 177.56, 64.82, 61.51, 47.81, 34.02, 30.54, 25.02, 24.13, 22.46, 21.64, 13.21. ^{31}P NMR (101.25 MHz, BB, D_2O): δ 3.72.

HR-MS (ESI negative): *m/z* 340.1163 (cacld for $C_{12}H_{23}NO_8P$: 340.1161).

4.2.8.3.4 Preparation of compound 4

4-a

2-e 1.33 mmol, 0.68g) was treated by lauroyl chloride in the conditions described for synthesis of 3-a (DCM was replaced by ether to avoid formation of an emulsion during extraction). 0.568 g, 62%.

^{1}H NMR (250 MHz, $CDCl_3$): δ 7.46 – 7.3 (m, 15H) 5.15 (d, *J* = 7.8 Hz, 4H) 4.78 (s, 2H) 4.71 (d, *J* = 11.2 Hz, 2H) 4.08 (t, *J* = 6.2 Hz, 2H) 3.7 (t, *J* = 6.5 Hz, 2H) 2.3 (t, *J* = 7.4 Hz, 2H) 1.78 – 1.49 (m, 4H) 1.36 – 1.2 (m, 18H) 0.91 (t, *J* = 6.15 Hz, 3H). ^{13}C NMR (62.5 MHz, BB, $CDCl_3$): δ 173.9, 135.95, 133.83, 129.3, 129.21, 128.89, 128.55, 128.04, 69.63, 69.54, 64.23, 64.23, 63.58, 45.55, 34.34, 31.94, 29.64, 29.51, 29.37, 29.31, 29.21, 25.95, 25, 23.3, 22.73, 14.18 ppm. ^{31}P NMR (101.25 MHz, BB, $CDCl_3$): δ - 0.83 ppm.

N-(4-hydroxybutyl)-phosphoglycolohydroxamic acid laurate (4) (monosodium salt)

4-a was debenzylated by the method used for preparation of 3, to give 4 as the monosodium salt. 0.37 g, 95%.

^{1}H NMR (250 MHz, D_2O): δ 4.51 (d, *J* = 4.0 Hz, 2H) 4.07 – 3.93 (m, 2H) 3.58-3.45 (m, 2H) 2.2 (t, *J* = 6Hz, 2H) 1.66 - 1.42 (m, 6H) 1.29 - 1.05 (m, 16H), 0.75 (t, *J* = 6 Hz, 3H). ^{13}C NMR (62.5 MHz, BB, D_2O): δ 174.6, 64.37, 61.63, 34.11, 32.0, 29.85, 29.3, 25.36, 24.86, 22.66, 22.53, 13.85. ^{31}P NMR (101.25 MHz, BB, D_2O): δ 3.78.

HR-MS (ESI negative): *m/z* 424.2113 (calcd for $C_{18}H_{35}NO_8P$: 424.2100).

4.2.8.4 Biochemical results - IC_{50} determinations

The purified proteins were stored at 4° C in 85% saturating ammonium sulfate solution (25mM Tris/HCl pH 8. Fructose bisphosphate and inhibitor, made up at the appropriate concentration in a glycyl-glycine buffer (0.1 M pH 7.4, 0.2 M in AcOK), NADH (0.12 mM), GPDH (11 U), TIM (3 U) and aldolase (4 mU) were placed in a cuvette to make a final volume of 1.2 mL. The decrease in absorbance of NADH at 340 nm was monitored on a spectrophotometer over 1–2 min.[ii] IC_{50} were determined using a concentration of FBP equal to the determined Km for each enzyme. Representative examples are given below.

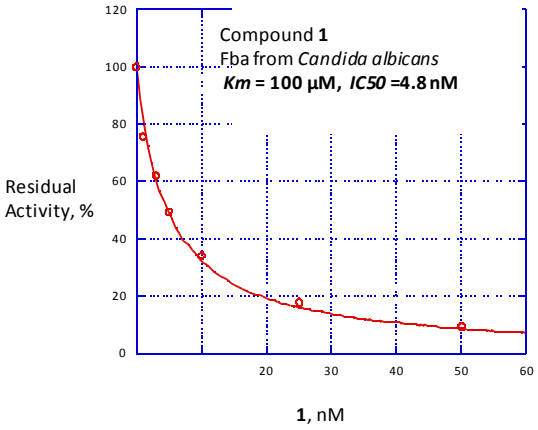
Compound 1
Fba from Candida albicans
Km = 100 µM, IC50 =4.8 nM
Residual Activity, %
1, nM

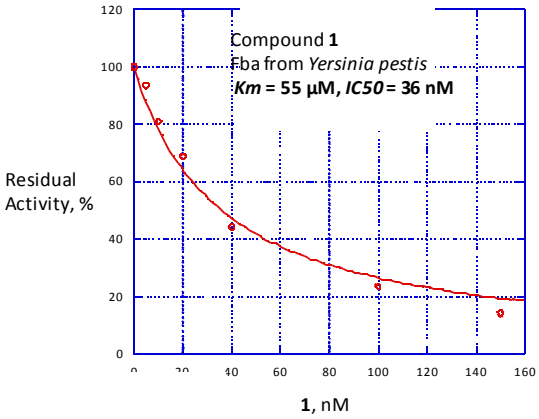
Compound 1
Fba from Yersinia pestis
Km = 55 µM, IC50 = 36 nM
Residual Activity, %
1, nM

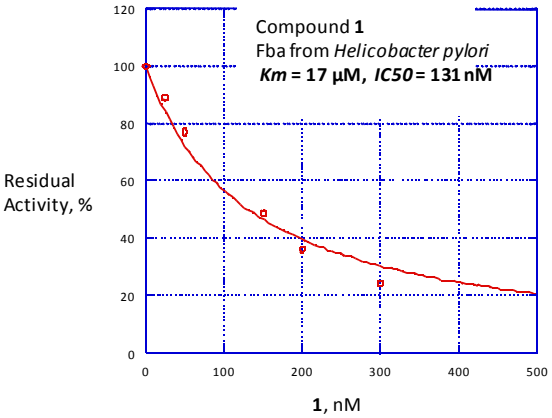
Compound 1
Fba from Helicobacter pylori
Km = 17 µM, IC50 = 131 nM
Residual Activity, %
1, nM

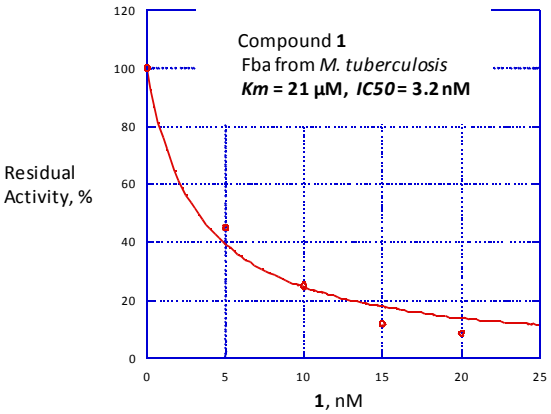
Compound 1
Fba from M. tuberculosis
Km = 21 µM, IC50 = 3.2 nM
Residual Activity, %
1, nM

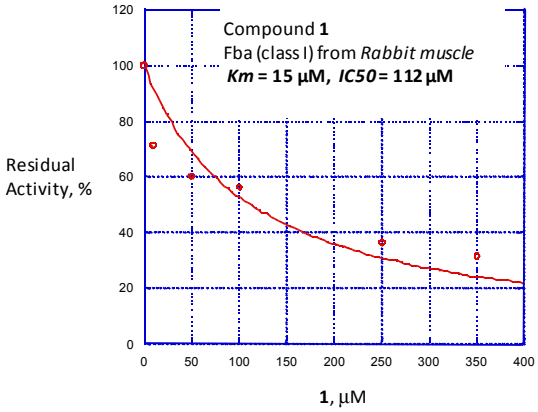
Compound 1
Fba (class I) from Rabbit muscle
Km = 15 µM, IC50 = 112 µM
Residual Activity, %
1, µM

4.2.8.5 Biochemical results - Ki determinations

Determinations of K_i for compounds 1 – 4 on Fba from *C. albicans* are given below as representative examples.

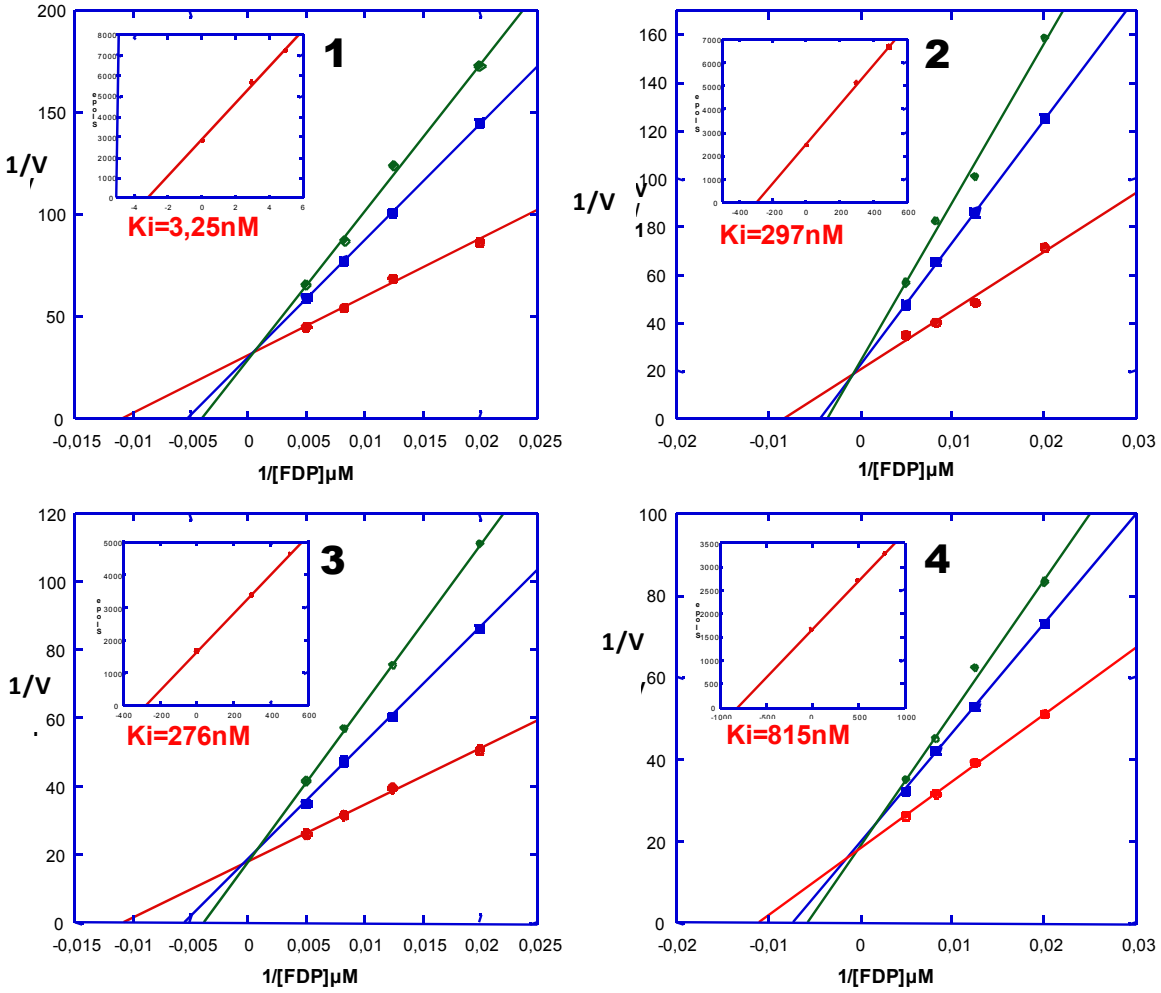

4.2.8.6 Structure solution of *H. pylori* Fba complexes with compounds 1 and 2

Crystallization of H. pylori. *H. pylori* aldolase crystals were grown by vapour diffusion from a mixture (1:1) of sample solution (10 mg mL^{-1} in 25 mM Tris·HCl pH 8.0, 10 mM inhibitor) and precipitant buffer [PEG 1000 (12 %), PEG 8000 (12 %), calcium

acetate (0.2 M) and Tris/HOAc (pH 8, 50 mM)]; 4µl drops were equilibrated at 23 °C against 1 mL reservoirs of precipitant solution. Crystals grew in 2 weeks.

Data collection and processing. H. pylori aldolase crystals were soaked in compound 1 and 2 buffer (mother liquor plus 10 mM compound 1 and 2) for 10 minutes. Prior to data collection, crystals were cryoprotected by transfer through a cryobuffer solution (compounds 1 and 2 plus 10% glycerol) and immediately flash frozen in a stream of gaseous N_2 cooled to 100° K. Diffraction data were collected from single crystals at beamline X29 of the National Synchrotron Light Source (Brookhaven National Laboratory, Upton, USA) with an ADSC Quantum 315r detector. All data sets were processed with XDS ([iii]) and SCALA from the CCP4 suite ([iv]) and the results are summarized in Table 5.

Structure solution and refinement: H. pylori Fba structures in complex with 1 and 2 were solved by molecular replacement with the molecular replacement program AutoMR (Phenix suite) ([v]) using native *H. pylori* Fba in complex with TF (PDB ID 3C56) as search model. The structure in complex with compounds 1 and 2 belong respectively to space group $P2_12_12_1$ (one homodimer in the asymmetric unit) and $P1$ (8 aldolase protomers in the asymmetric unit). The best solution was used as starting point for refinement for each liganded structure. The liganded structures were solved by iterative rounds of refinement (simulated annealing and minimization) with Phenix and model building using Coot ([vi]). Molprobity server ([vii]) and the Coot validating tools were used to optimize the structures during the refinement. Water molecules were automatically added by Phenix in initial rounds and manually near the end of refinement. Loop regions (residues 139-153) in each subunit were associated with regions of weak electron density.

Ligand modeling was based on interpretation of electron density shapes of $2F_o$-F_c and F_o-F_c annealed omit maps and using phenix.elbow command for topology and parameters generation. Binding by compound 1 and 2 were readily discernable and were associated with clearly defined electron densities in the active site. Difference electron density (F_o-F_c) annealed omit maps calculated in the final round of refinement confirmed identical binding of ligands in protomers. Final model statistics, calculated with Phenix,

Molprobity and SFCHECK ([viii]), are shown in Table 5. The coordinates and structure factors of *H. pylori* aldolase in complex with 1 and 2 have been deposited with the Protein Data Bank (PDB entry codes 3N9S and 3N9R respectively) ([ix]). The final structure models of compound 1 and 2 enzymatic complexes have R_{cryst} (R_{free}) values of 0.169 (0.214) and 0.161 (0.204) respectively. The corresponding Luzzati atomic coordinate errors were estimated at 0.20 and 0.19 Å, respectively. Ramachandran analysis with PROCHECK ([x]) placed at least 98.8 % of non-glycine and non-proline residues of the two structures in the most favorable region and with the remainder found in allowed regions, attesting to good model geometry in the structures.

Comparisons: Superpositions were performed with the super command in PyMOL with use of C_α atom coordinates of identical regions of amino acid sequences or by LSQ fit in Coot. Root mean square deviations (RMSD) based on superposition of equivalent C_α atoms are reported.

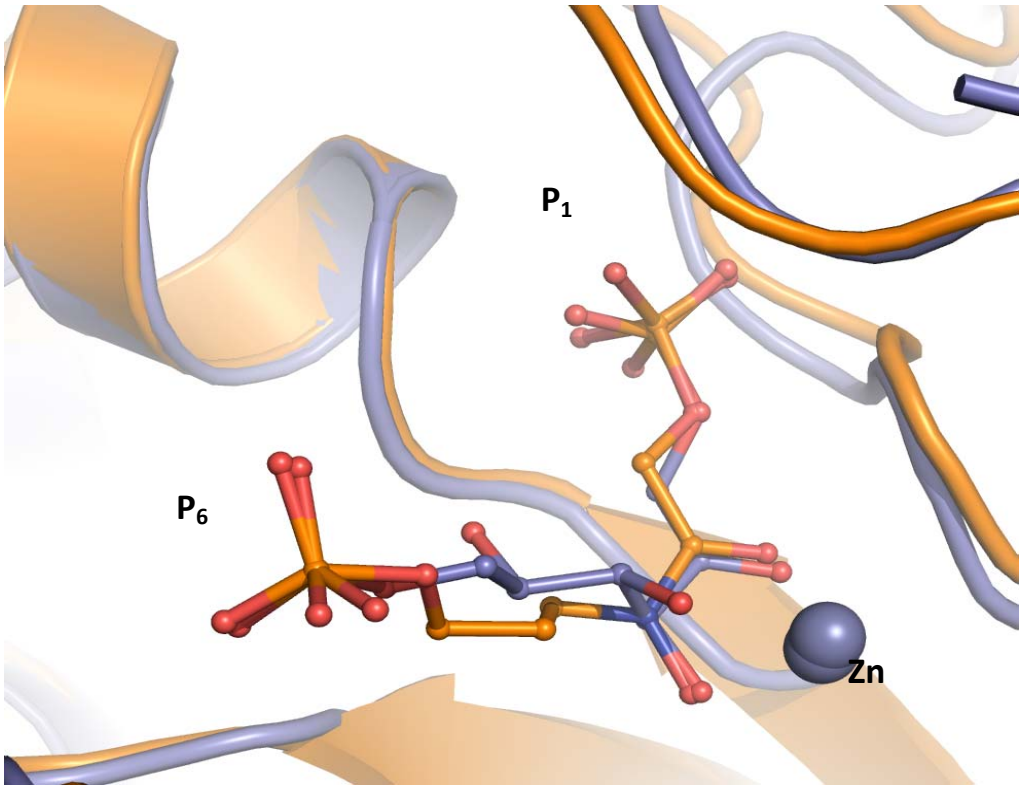

Figure 4-18. Superimposition of the structure of *H. pylori* Fba complexed with compound **TF** (orange, PDB 3C56) onto the structure *M. tuberculosis* Fba in complex with **FBP (**blue, PDB 3ELF).

The superimposition yielded an RMSD = 1.58 Å using all equivalent substrate atoms and 0.21 Å using Pi positions only.

Table 4-5. Data Collection and refinement statistics

Table 1. Data collection and refinement statistics

	H. pylori Ure in complex with compound 1	*H. pylori* Ure in complex with compound 2
Data Collection		
[illegible]	[illegible]	[illegible]
[illegible]	[illegible]	[illegible]
[illegible]	[illegible]	[illegible]
[illegible]	[illegible]	[illegible]
[illegible]	[illegible]	[illegible]
[illegible]	[illegible]	[illegible]
[illegible]	[illegible]	[illegible]
Refinement		
[illegible]	[illegible]	[illegible]
[illegible]		
[illegible]	[illegible]	[illegible]
[illegible]	[illegible]	[illegible]
[illegible]	[illegible]	[illegible]
[illegible]	[illegible]	[illegible]
[illegible]	[illegible]	[illegible]
[illegible]		
[illegible]	[illegible]	[illegible]
[illegible]	[illegible]	[illegible]
[illegible]		
[illegible]	[illegible]	[illegible]
[illegible]	[illegible]	[illegible]
[illegible]	[illegible]	[illegible]
[illegible]	[illegible]	[illegible]
[illegible]		
[illegible]	[illegible]	[illegible]
[illegible]	[illegible]	[illegible]
[illegible]	[illegible]	[illegible]

[illegible]

```
Giardia          MPLC-----------------------------------TL---RQMLGEARKHKYGV 20
Helicobacter     MLVK----------------------------------G---NEILLKAHKEGYGV 19
Thermus          MLVT----------------------------------G---LEILKKAREEGYGV 19
Candida          MAPPAVL-------------------------SKSGVIYGKDVKDLFDYAQEKGFAI 32
Magnaporthe      MGVFSEL-------------------------GLKPGVLYGEEVYKLFEHAKKNVYAI 33
Escherichia      MTGVSERRRSTCNLKYDEYKARRYRTRDMSKIFDFVKPGVITGDDVQKVFQVAKENNFAL 60
Yersinia         MSKIF---------------------------DFVKPGVITGDDVQKVFAVAKENNFAL 32
Mycobacterium    MPIA-----------------------------------TPEVYAEMLGQAKQNSYAF 23
                 *                                              .::  *::. :..

Giardia          GAFNVNNMEQIQGIMKAVVQLKSPVILQCSRGALKYSDMIY----------------LKK 64
Helicobacter     GAFNFVNFEMLNAIFEAGNEENSPLFIQASEGAIKYMGIDM----------------AVG 63
Thermus          GAFNVNNMEFLQAVLEAAEEQRSPVILALSEGAMKYGGR-A----------------LTL 62
Candida          PAINVTSSSTVVAALEAARDNKAPIILQTSQGGAAYFAGKGVDN-KDQAASIAGSIAAAH 91
Magnaporthe      PAINVTSSSTIIASLEAARDSKSPIILQMSQGGAAYFAGKGVSN-TNQEASIAGAVAAAH 92
Escherichia      PAVNCVGTDSINAVLETAAKVKAPVIVQFSNGGASFIAGKGVKSDVPQGAAILGAISGAH 120
Yersinia         PAVNCVGTDSINAVLETAAKVRAPVIVQFSNGGAAFIAGKGVKTDAPQGAAILGAISGAH 92
Mycobacterium    PAINCTSSETVNAAIKGFADAGSDGIIQFSTGGAEFGSGLGVKD-M-----VTGAVALAE 77
                  *.*  . . : . ::   .  :  ::  * *.  :

Giardia          LCEAALEKHP-DIPICIHLDHGDTL--------------ESVKMAIDLGFSSVMIDASHH 109
Helicobacter     MVK-IMCERYPHIPVALHLDHGTTF--------------ESCEKAVKAGFTSVMIDASHH 108
Thermus          MAV-ELAKEA-RVPVAVHLDHGSSY--------------ESVLRALRAGFTSVMIDKSHE 106
Candida          YIR-AIAPTY-GIPVVLHTDHCAKK-LLPWFDGMLKADEEFFAKTGTPLFSSHMLDLSEE 148
Magnaporthe      FIR-SIAPIY-GVPVVLHTDHCAKK-LLPWLDGMLDADEAFHKENGTPLFSSHMIDLSEE 149
Escherichia      HVH-QMAEHY-GVPVILHTDHCAKK-LLPWIDGLLDAGEKHFAATGKPLFSSHMIDLSEE 177
Yersinia         HVH-QMAEHY-GVPVILHTDHCAKK-LLPWLDGLLDAGEKHFAATGKPLFSSHMIDLSEE 149
Mycobacterium    FTH-VIAAKY-PVNVALHTDHCPKDKLDSYVRPLLAISAQRVSKGGNPLFQSHMWDGSAV 135
                      :      : : :* **  .                        * * * * *

Giardia          PFDENVRITKEVVAYAHARGVSVEAELGTLGGIEEDVQNT-----VQLTEPQDAKKFVEL 164
Helicobacter     AFEENLELTSKVVKMAHNAGVSVEAELGRLMGIEDNISVDEK--DAVLVNPKEAERFVKE 166
Thermus          DFETNVRETRRVVEAAHAVGVTVEAELGRLAGIEEHVAVDEK--DALLTNPEEARIFMER 164
Candida          TDDENIATCAKYFERMAKMGQWLEMEIGITGGEEDGVNNEHVEKDALYTSPETVFAVYES 208
Magnaporthe      PRDWNIETTAKYLKRAAPMKQWLEMEIGLTGGEEDGVNNEDVDNNSLYTQPEDIFAIHQA 209
Escherichia      SLQENIEICSKYLERMSKIGMTLEIELGCTGGEEDGVDNSHMDASALYTQPEDVDYAYTE 237
Yersinia         SLEENIEICSKYLTRMSKIGMTLEIELGCTGGEEDGVDNSHMDASSLYTQPQDVDYAYEK 209
Mycobacterium    PIDENLAIAQELLKAAAAAKIILEIEIGVVGGEEDGVANEIN--EKLYTSPEDFEKTIEA 193
                   : *:    . .          :* *:*   * *: :            ..*:

Giardia          -----TGVDALAVAIGTSHGAYKFKSESDIRLAIDRVKT----IS-------DLTGIPLV 208
Helicobacter     -----SQVDYLAPAIGTSHGAFKFKGEPK--LDFERLQE----VK-------RLTNIPLV 208
Thermus          -----TGADYLAVAIGTSHGAYKGKGRPF--IDHARLER----IA-------RLVPAPLV 206
Candida          LHK-ISPNFSIAAAFGNVHGVYKPG-NVQ--LRPEILGDHQVYAKKQIGTDA-KHPLYLV 263
Magnaporthe      LSP-ISKYFSIAAGFGNVHGVYKPG-NVR--LHPELLDKHQKYVIEKLGCEE-KKPIFFV 264
Escherichia      LSK-ISPRFTIAASFGNVHGVYKPG-NVV--LTPTILRDSQEYVSKKHNLP--HNSLNFV 291
Yersinia         LNA-ISPRFTIAASFGNVHGVYKPG-NVK--LTPTILRDSQDYVSKKHNLP--HNSLNFV 263
Mycobacterium    LGAGEHGKYLLAATFGNVHGVYKPG-NVK--LRPDILAQGQQVAAAKLGLPADAKPFDFV 250
                           :*  :*. **.:*   .    :    :                    :*

Giardia          MHGSSSVPKDVKDMINKYGGKMPDAVGVPIESIVHAIGEGVCKINVDSDSRMAMTGAIRK 268
Helicobacter     LHGASAIPDDVRKSYLDAGGDLKGSKGVPFEFLQESIKGGINKVNTDTDLRIAFIAEVRK 268
Thermus          LHGASAVPPELVERFRASGGEIGEAAGIHPEDIKKAISLGIAKINTDTDLRLAFTALIRE 266
Candida          FHGGS----------------------GSTQEEFNTAIKNGVVKVNLDTDCQYAYLTGIRD 302
Magnaporthe      FHGGS----------------------GSGDSEFQEAISYGVIKVNLDTDLQWAYLSGIRD 303
Escherichia      FHGGS----------------------GSTAQEIKDSVSYGVVKMNIDTDTQWATWEGVLN 330
Yersinia         FHGGS----------------------GSTAEEIKEAVSYGVVKMNIDTDTQWATWEGILN 302
Mycobacterium    FHGGS----------------------GSLKSEIEEALRYGVVKMNVDTDTQYAFTRPIAG 289
```

```
                :**.*                      *   . :  ::  *: *:* *:* : *    :
Giardia         VFVE------------------------------------------------------- 272
Helicobacter    VANE------------------------------------------------------- 272
Thermus         ALNKNPKEFDPRKYLGPAREAVKEVVKSRME-LFGSVGRAYAFTRPIAGHMFTNYDGVLK 325
Candida         YVTNK-----------------------IEYLKAPVGNPEGA----------------- 321
Magnaporthe     YVTSK-----------------------IEYLNSQVGNPDGA----------------- 322
Escherichia     YYKAN-----------------------EAYLQGQLGNPKGE----------------- 349
Yersinia        YYKKN-----------------------EGYLQGQLGNPEGA----------------- 321
Mycobacterium   HMFTNY----------------------DGVLK-----VDG------------------ 303

Giardia         ------HPEKFDPRDYLGPGRDAITEMLIPKIKAFGSAGHAGDYKVVSLEEAKAWYK 323
Helicobacter    ------DKSQFDLRKFFSPAQLALKNVVKERMKLLGSAN---------------KI 307
Thermus         VDGEVGVKKVYDPRSYLKKAEASMSQRVVQACNDLHCAGK-------------SLTH 369
Candida         ---DKPNKKYFDPRVWVREGEKTMSKRIAEALDIFHTKG----------------QL 359
Magnaporthe     ---DKPNKKYYDPRVWVREGEKTMKARIQQALKVFNAEN----------------TI 360
Escherichia     ---DQPNKKYYDPRVWLRAGQTSMIARLEKAFQELNAID----------------VL 387
Yersinia        ---DKPNKKYYDPRVWLRAAQVTMITRLELAFKELNAID----------------VL 359
Mycobacterium   ---EVGVKKVYDPRSYLKKAEASMSQRVVQACNDLHCAGK-------------SLTH 344
                       . :* * :. .. ::  :  . :  .
```

Figure 4-19. EXPRESSO (3DCoffee[xi]) multiple alignment of class II FBP aldolases.

The alignment used both sequence and structural information. Structures of class II aldolases used as input were bound structures in complex with **FBP**, bisphosphorylated inhibitors or sulfate molecules and corresponded to class II aldolases from species *Giardia*, *Helicobacter*, *Thermus*, *Escherichia* and *Mycobacterium* (PDB IDs: 3GAK, 3C56, 1RV8, 1DOS and 3ELF respectively). The active site residues binding P1- and P6-phosphates of **FBP** aligned onto those of *M. tuberculosis* are highlighted in blue while histidine residues chelating the zinc metal cofactor are highlighted in magenta. Residues aligned with Gly-56 and Gln-280 in *M. tuberculosis* are highlighted in black; Gly-56 is implicated in P7-phosphate binding of compound **1** while Gln-280 is implicated via a water molecule in P6 and P7-phosphate binding of compounds **TF** and **1**. The same water molecule also interacts with O7 of compound **2** and contacts O6 of compound ***2'*** as well as O7 of compound **2** in the secondary configuration.

4.2.8.7 References

i. Blom, N.S.; Tétreault, S.; Coulombe, R.; Sygusch, J. Novel active site in Escherichia coli fructose 1,6-bisphosphate aldolase. *Nature Struct. Biol*. **1996**, *3*, 856-62.

ii. Racker, E. Spectrophotometric measurement of hexokinase and phosphohexokinase activity. *J. Biol. Chem.* **1947**, *167*, 843-854.

iii. Kabsch, W. Automatic processing of rotation diffraction data from crystals of initially unknown symmetry and cell constants. *J. Appl. Cryst*. **1993**, *26*, 795-800.

iv. Collaborative computational Project, number 4. The CCP4 suite: programs for protein crystallography. *Acta Cryst.* **1994**, *D50*, 760-763

v. Adams, P.D.; Grosse-Kunstleve, R.W.; Hung, L.-W.; Ioerger, T.R.; McCoy, A.J.; Moriarty, N.W.; Read, R.J.; Sacchettini, J.C.; Sauter, N.K.; Terwilliger, T.C. PHENIX: building new software for automated crystallographic structure determination. *Acta Cryst.* **2002**, *D58*, 1948-1954.

vi. Jones, T. A.; Zou, J. Y.; Cowan, S. W.; Kjeldgaard, M. Structure validation by Cα geometry: φ, ψ and Cβ deviation. *Acta Crystallogr. A* **1991**, *47 (Pt 2)*, 110-119.

vii. Lovell, S.C.; Davis, I.W.; Arendall, W.B.III; de Bakker, P.I.W.; Word, J.M.; Prisant, M.G.; Richardson, J.S.; Richardson, D.C. Structure validation by C-alpha geometry: phi, psi, and C-beta deviation. *Proteins: Structure, Function, and Genetics.* **2003**, *50*, 437-450.

viii. Vaguine, A. A., Richell, J., Wodak, S. J. SFCHECK: a unified set of procedures for evaluating the quality of macromolecular structure-function data and their agreement with the atomic model. *Acta Crystallogr. D* **1999**, *55 (Pt 1)*, 191-205.

ix. Protein Data Bank, Research Collaboratory for Structural Bioinformatics, Rutgers University, New Brunswick, NJ. http://www.rcsb.org/

x. Laskowski, R. A.; MacArthur, M. W.; Moss, D. S.; Thornton, J. M. PROCHECK: a program to check the stereochemical quality of protein structures. *J. Appl. Cryst.* **1993**, *26*, 283-291.

xi. Notredame, C.; Higgins, D.G.; Heringa, J. T-coffee: a novel method for fast and accurate multiple sequence alignement. *J. Mol. Biol.* **2000**, *302*, 205-217.

CHAPITRE V

Conclusion

"Tout ce que je sais,
c'est que je ne sais rien."
Socrate

5 Conclusion

5.1 Bilan

Notre but initial était de détailler le mécanisme catalytique des FBPA de classe II en nous basant sur la résolution de structures cristallines. Bien que le caractère dynamique de ces enzymes soit tout d'abord apparu comme un problème, il s'est révélé au contraire responsable de l'originalité de cette catalyse et donc de notre étude.

5.1.1 Rôle d'Asp82, nouveau mécanisme d'abstraction du proton en O4 du FBP et reconnaissance des substrats.

Au chapitre 2, les nombreuses structures cristallographiques obtenues nous ont permis de décrire les premières étapes de la réaction de clivage et en particulier les modalités de l'échange de proton sur l'O4 du FBP. Peu d'études cristallographiques reposent sur la résolution et l'étude d'un aussi grand nombre de structures. Cette diversité nous a permis de les comparer, ce qui renforce nos interprétations.

L'observation d'une géométrie défavorable à l'abstraction de ce proton par le résidu préalablement identifié dans la littérature, Asp109 chez *E. coli* ou Asp82 chez *H. pylori*, nous a conduits à cristalliser et à étudier le mutant D82N. Les trempages de FBP ont permis d'obtenir des structures où le clivage avait eu lieu et ont donc invalidé le rôle préalablement attribué à ce résidu. Le méthyglyoxal qui est un produit très réactif pouvant à la fois réagir avec certains acides aminés (Takahashi, 1977) ou modifier des nucléotides (Krymkiewicz, 1973), a été identifié dans l'une des structures du mutant. La production de cette molécule par le mutant ayant été validée biochimiquement. D82 protège le substrat vis-à-vis de cette décomposition par la formation d'un lien hydrogène avec le proton situé sur l'oxygène O3. De plus, ce résidu est aussi important pour orienter la liaison des substrats et joue ainsi un rôle dans leur reconnaissance.

Après avoir écarté ce résidu comme initiateur du clivage, nous devions proposer un autre candidat. En identifiant dans nos structures quels résidus pouvaient à la fois être assez proches et posséder des caractéristiques leur permettant de remplir ce rôle, comme un pKa approprié, nous avons identifié l'His180 comme étant responsable de ce transfert. C'est ici que le caractère dynamique de notre catalyse est apparu primordial. La relocalisation du zinc catalytique et la réorientation des résidus le coordonnant est cruciale à la réalisation de 1) l'activation de l'hydroxyle O4 par l'His83, 2) la libération de l'His180 qui peut alors abstraire le proton et déclencher le clivage, et enfin 3) la stabilisation de l'énediolate par l'exposition complète du métal qui le coordonne. Malheureusement, les mutations de ces histidines ne nous ont pas permis d'obtenir des protéines stables et de valider notre identification biochimiquement ou par l'obtention d'autres structures.

Les réarrangements structuraux nécessaires à l'enzyme pour réaliser cette première partie de la catalyse ont donc pu être décrits par notre approche cristallographique. Cependant, aucune des structures obtenues ne nous offre de vue sur l'étape d'échange de proton sur le carbone C3 du DHAP. La boucle α5-β7 n'est visible que dans une de nos structures mais n'est pas localisée au site actif. Cela montre donc la nécessité des autres approches que nous avons explorées.

5.1.2 Mise au point et validation d'un protocole de simulation par dynamique moléculaire.

Les deux publications inclues dans le chapitre 3, ne portent pas sur l'étude de FBPA de classe II mais sur des classes I. Néanmoins, elles ont permis de tester l'utilisation d'une approche *in silico* portant sur des enzymes qui ont un repliement similaire à notre protéine d'intérêt et ce en présence d'inhibiteurs qui n'étaient pas décrit dans les champs de forces. La mise au point des paramètres de ces molécules puis leur test lors des simulations a demandé une grande rigueur, un esprit critique affuté et la réalisation de nombreuses simulations de tests et de validations. Ces simulations ont permis d'obtenir une vue dynamique des interactions entre les inhibiteurs et les enzymes. Ces analyses corroborent

parfaitement les données biochimiques et cinétiques et renforcent notre confiance dans cette méthode.

Les simulations obtenues chez les classes II ont été sources de découverte et nous encouragent à consolider et valider cette approche. Chez ecFBPA, nous avons reproduit la dynamique attendue de la boucle α7-β5. De plus, le fait d'isoler des géométries propices à l'abstraction du proton par Glu182 dans une échelle de temps plus courte qu'attendue montre que ce mouvement est favorisé par la structure et que notre protocole semble correct. Les résultats chez *H. pylori* nous ont initialement surpris mais l'analyse cinétique préliminaire des mutants E142A et E149A nous encouragent à approfondir cette étude.

Ainsi nos simulations de dynamique moléculaire se sont révélées être efficaces pour illustrer des phénomènes dynamiques mais semblent également pouvoir servir d'outils d'investigation.

5.1.3 Développement et optimisation d'inhibiteurs des FBPA de classes II

C'est dans le but d'obtenir des analogues capables de recruter et de piéger la boucle catalytique au site actif que nous avons initié ce projet collaboratif. Même si ce but n'a pas été atteint, cette approche s'est tout de même révélée très fructueuse.

Cette étude est surtout basée sur l'obtention d'analogues du FBP à partir de la modification du PGH, analogue du DHAP.

Dans un premier temps nous avons décrit les interactions entre un premier composé, le N-(3-Hydroxypropyl)-glycolohydroxamique acide bisphosphate, et notre enzyme (Fonvielle et al., 2008). C'est l'observation de la géométrie « tendue » de la coordination du zinc par ce composé qui a conduit à la synthèse du composé analogue du sedoheptulose bisphosphate, le N-(4-hydroxybutyl)-phospho-glycolohydroxamique acide bisphosphate, en y rajoutant un carbone. Ce composé qui est à la fois fortement inhibiteur et très sélectif est néanmoins polaire. Ce défaut le rend peu lipophilique, ce qui peut expliquer son absence d'effet sur la croissance des cultures bactériennes. Ceci nécessiterait d'apporter des

modifications au composé pour qu'il puisse traverser les membranes biologiques avant d'envisager une utilisation pharmacologique.

Les divers composés étudiés nous ont tout de même permis de mieux analyser nos propres structures, par exemple en identifiant la position du zinc la plus externe.

De plus, ces études ont mis en évidence une différence de réponse entre les deux sous-classes IIA et IIB. Cette caractéristique éveille un intérêt particulier car nous avons aussi obtenu des résultats différents d'une sous-classe à l'autre lors de nos simulations.

5.2 Perspectives

5.2.1 Poursuite des projets

5.2.1.1 Validation des dynamiques

Nos simulations demandent avant tout à être reproduites car une expérience *in silico* nécessite aussi la réalisation de duplicatas.

Comme nous l'avons exposé au chapitre 3.3, notre priorité est donnée à l'analyse des mutants chez *H. pylori*. Chez *E. coli*, la recherche d'effet isotopique du solvant sera aussi conduite.

La dynamique de la reptation de la boucle sera étudiée en détail et pourra permettre de déterminer les interactions qui guident ce mouvement.

Enfin, une des limitations de la dynamique de type newtonienne est l'impossibilité de simuler le clivage ou la formation de liens chimiques. Pour ce faire, des simulations hybrides dites QM/MM (mécanique quantique/mécanique moléculaire) sont envisageables (Wu et al., 2009). Ces dynamiques demandent une connaissance approfondie de la mécanique quantique mais pourraient permettre de suivre à la fois les variations de coordination du zinc et les changements au niveau des liens covalents de nos substrats (échange des protons et clivage/condensation du lien C3-C4).

5.2.1.2 Études d'autres résidus par mutagénèse

Un effort particulier doit être porté à la mutagénèse de His180/His226 (hpFBPA/ecFBPA) afin de valider plus solidement notre mécanisme. Mais la mutation des histidines coordonnant le zinc est délicate. Il semble primordial de conserver leur capacité à lier le zinc. Le choix d'une mutation en glutamate ou glutamine est alors plus judicieux. Ces résidus ont approximativement la même longueur qu'une histidine et peuvent toujours lier le zinc. Ces mutants sont en cours de production au laboratoire.

Une autre approche intéressante serait de muter deux résidus en cystéine pour favoriser la formation d'un pont disulfure et ainsi bloquer nos boucles. Nous essaierons alors de positionner un des deux résidus soit sur la boucle α7-β5, soit sur la boucle α8-β6 (celle portant l'histidine catalytique). Nous pourrons ainsi obtenir deux protéines doublement mutées pouvant conduire au piégeage d'un substrat intact, soit le DHAP (dans le cas de α7-β5), soit le FBP (dans le cas de α8-β6). His180 pourrait aussi être immobilisée en modifiant un résidu qui lui est proche afin qu'il lie son azote libre (Nδ1). Enfin, l'étude de la dynamique de la reptation de la boucle pourra aussi aider à choisir certains résidus à muter.

Les nouveaux appareils à notre disposition au département (spectrophotomètre 96 puits et robot de cristallisation) offrent aussi de nouvelles opportunités. La génération de librairies de mutants des résidus du site actif ou de la boucle catalytique, leurs tests cinétiques et leur cristallisation à moyenne échelle est envisageable. Une telle étude systématique pourrait se révéler très puissante mais demande un travail d'équipe concerté et efficace.

Les mutants les plus prometteurs pourront également être modélisés et simulés.

5.2.1.3 Optimisation des inhibiteurs

La modification des composés obtenus durant mon doctorat est en cours, particulièrement la synthèse de composés hydroxylés et la modification des groupements phosphates.

Nous finalisons une publication dans laquelle nos collaborateurs apportent la preuve du caractère essentielle de la FBPA de classe II chez *Mycobacterium tuberculosis*. Nous y présentons des structures de la FBPA de cette bactérie. Ces structures, en particulier celle en complexe avec le N-(4-hydroxybutyl)-phospho-glycolohydroxamique acide bis-phosphate, nous a permis de valider une approche *in silico* par arrimage moléculaire (« docking »). Nous pourrons ainsi cribler des banques de données de petites molécules à la recherche de nouveaux composés.

Cette approche par « docking » utilisera le site actif de l'enzyme comme récepteur mais également des conformations isolées de nos dynamiques dans l'optique de trouver des molécules bloquant le mouvement des boucles.

5.2.2 D'autres voies à explorer

5.2.2.1 Différences entre classe I et classe II

Les études de dynamique moléculaire et les cinétiques d'inhibition de nos composés soulignent l'existence de différences entre les deux sous-classes de FBPA métallodépendantes. Peu de résidus différent d'un site actif à l'autre et il semble difficile d'évaluer les répercutions de leur différences.

Des expériences de Titrage Calorimétrique en condition Isotherme (ITC) où l'inhibiteur N-(4-hydroxybutyl)-phospho-glycolohydroxamique acide bisphosphate était dilué dans une solution contenant soit la FBPA de *M. tuberculosis* soit celle de *H. pylori* ont permis d'identifier un comportement thermodynamique différent entre les deux enzymes. La liaison du ligand est exothermique dans le premier cas et endothermique dans le suivant. Des expériences avec les substrats naturels sont envisagées afin de reproduire ce phénomène.

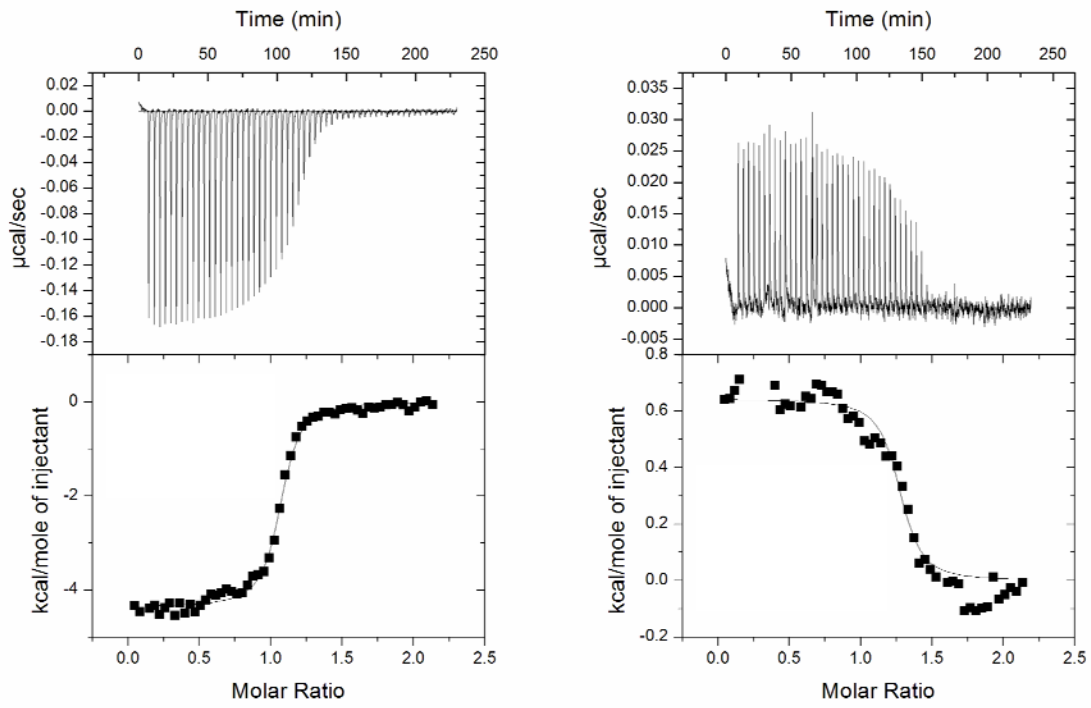

Figure 5-1. Thermogrammes des experiences ITC de liaison du N-(4-hydroxybutyl)-phospho-glycolohydroxamique acide bisphosphate sur mtFBPA (droite) et hpFBPA (gauche).

Comprendre les raisons de telles différences n'est pas chose facile. Une hypothèse plausible serait que les organismes n'utilisant pas ou peu la glycolyse mais principalement la néoglucogenèse, comme c'est le cas de *H. pylori* (Chalk, Roberts, and Blows, 1994), aient favorisé la sélection de certains résidus. Il est probable qu'une explication ne puisse être obtenue qu'à la lumière d'une analyse phylogénétique et fonctionnelle détaillée.

5.2.2.2 Cyclisation du FBP

Le FBP acyclique est très minoritaire (2%) en solution où l'on retrouve principalement la forme cyclique (Gray, 1971). Il semble donc probable que la FBPA catalyse l'ouverture du cycle, ce qui a déjà été suggéré chez les classes I (Choi and Tolan, 2004). La synthèse d'analogues non clivable du FBP cyclique et l'obtention de leur complexe avec une FBPA de classe II pourrait permettre de valider cette hypothèse et d'identifier les résidus requis pour l'ouverture.

5.2.2.3 Interactions des FBPA avec des protéines de l'hôte chez les bactéries pathogènes

Il a été démontré chez *Streptomyces pneumoniae* que la FBPA de classe II est exposée à la surface de la bactérie où elle joue le rôle d'une adhésine en interagissant avec des protéines de type FCR (Flamingo Cadherin Receptor) situées à la surface des cellules épithéliales de l'hôte (Blau et al., 2007). Il serait intéressant de caractériser l'interface d'interaction qui constituera un nouveau site à cibler pour le développement de composés antimicrobiens. Dans ce cas, ni la polarité, ni la taille de ces molécules ne seront des facteurs limitants puisqu'elles n'auront pas à franchir de membranes.

De telles interactions pourront être recherchées chez d'autres FBPA de classe II. Il est probable que les interfaces offrent plus de spécificité d'un organisme à l'autre que dans le cas d'un site actif optimisé pour lier une petite molécule. D'autre part, le développement d'inhibiteurs d'interaction protéine-protéine est difficile car ces interfaces sont généralement moins bien définies que la cavité d'un site actif. Néanmoins, ces difficultés ne sont pas insurmontables et le défi peut se révéler passionnant (Berg, 2008; Fry, 2008).

Bibliographie

Banerjee, P. C., Darzins, A., and Maitra, P. K. (1987). Gluconeogenic mutations in Pseudomonas aeruginosa: genetic linkage between fructose-bisphosphate aldolase and phosphoglycerate kinase. *J Gen Microbiol* **133**(4)**,** 1099-107.

Banerjee, P. C., Vanags, R. I., Chakrabarty, A. M., and Maitra, P. K. (1985). Fructose 1,6-bisphosphate aldolase activity is essential for synthesis of alginate from glucose by Pseudomonas aeruginosa. *J Bacteriol* **161**(1)**,** 458-60.

Banner, D. W., Bloomer, A., Petsko, G. A., Phillips, D. C., and Wilson, I. A. (1976). Atomic coordinates for triose phosphate isomerase from chicken muscle. *Biochem Biophys Res Commun* **72**(1)**,** 146-55.

Banner, D. W., Bloomer, A. C., Petsko, G. A., Phillips, D. C., Pogson, C. I., Wilson, I. A., Corran, P. H., Furth, A. J., Milman, J. D., Offord, R. E., Priddle, J. D., and Waley, S. G. (1975). Structure of chicken muscle triose phosphate isomerase determined crystallographically at 2.5 angstrom resolution using amino acid sequence data. *Nature* **255**(5510)**,** 609-14.

Baron, C. B., Greeley, P., and Coburn, R. F. (1998). Smooth muscle aldolase C-bound inositol 1,4,5-trisphosphate studied in vitro under physiological conditions. *Biochim Biophys Acta* **1401**(1)**,** 81-92.

Baron, C. B., Ozaki, S., Watanabe, Y., Hirata, M., LaBelle, E. F., and Coburn, R. F. (1995). Inositol 1,4,5-

trisphosphate binding to porcine tracheal smooth muscle aldolase. *J Biol Chem* **270**(35)**,** 20459-65.

Baron, C. B., Tolan, D. R., Choi, K. H., and Coburn, R. F. (1999). Aldolase A Ins(1,4,5)P3-binding domains as determined by site-directed mutagenesis. *Biochem J* **341 (Pt 3),** 805-12.

Belasco, J. G., and Knowles, J. R. (1983). Polarization of substrate carbonyl groups by yeast aldolase: investigation by Fourier transform infrared spectroscopy. *Biochemistry* **22**(1)**,** 122-9.

Berg, T. (2008). Small-molecule inhibitors of protein-protein interactions. *Curr Opin Drug Discov Devel* **11**(5)**,** 666-74.

Berry, A., and Marshall, K. E. (1993). Identification of zinc-binding ligands in the Class II fructose- 1,6-bisphosphate aldolase of Escherichia coli. *FEBS Letters* **318**(1)**,** 11-16.

Bianchini, G., Bocedi, A., Ascenzi, P., Gavuzzo, E., Mazza, F., and Aschi, M. (2006). Molecular dynamics simulation of Leishmania major surface metalloprotease GP63 (leishmanolysin). *Proteins* **64**(2)**,** 385-90.

Blau, K., Portnoi, M., Shagan, M., Kaganovich, A., Rom, S., Kafka, D., Chalifa Caspi, V., Porgador, A., Givon-Lavi, N., Gershoni, J. M., Dagan, R., and Mizrachi Nebenzahl, Y. (2007). Flamingo cadherin: a putative host receptor for Streptococcus pneumoniae. *J Infect Dis* **195**(12)**,** 1828-37.

Blom, N. S., Tétreault, S., Coulombe, R., and Sygusch, J. (1996). Novel active site in Escherichia coli fructose

1,6-bisphosphate aldolase. *Nat Struct Biol* **3**(10)**,** 856-862.

Bock, A., and Neidhardt, F. C. (1966a). Isolation of a Mutant of Escherichia coli with a Temperature-sensitive Fructose-1,6-Diphosphate Aldolase Activity. *J Bacteriol* **92**(2)**,** 464-9.

Bock, A., and Neidhardt, F. C. (1966b). Properties of a Mutant of Escherichia coli with a Temperature-sensitive Fructose-1,6-Diphosphate Aldolase. *J Bacteriol* **92**(2)**,** 470-6.

Boles, E., and Zimmermann, F. K. (1993). Saccharomyces cerevisiae phosphoglucose isomerase and fructose bisphosphate aldolase can be replaced functionally by the corresponding enzymes of Escherichia coli and Drosophila melanogaster. *Curr Genet* **23**(3)**,** 187-91.

Brown, L. M. (2000). Helicobacter pylori: epidemiology and routes of transmission. *Epidemiol Rev* **22**(2)**,** 283-97.

Buscaglia, C. A., Hol, W. G., Nussenzweig, V., and Cardozo, T. (2007). Modeling the interaction between aldolase and the thrombospondin-related anonymous protein, a key connection of the malaria parasite invasion machinery. *Proteins* **66**(3)**,** 528-37.

Buscaglia, C. A., Penesetti, D., Tao, M., and Nussenzweig, V. (2006). Characterization of an aldolase-binding site in the Wiskott-Aldrich syndrome protein. *J Biol Chem* **281**(3)**,** 1324-31.

Chalk, P. A., Roberts, A. D., and Blows, W. M. (1994). Metabolism of pyruvate and glucose by intact cells of

Helicobacter pylori studied by 13C NMR spectroscopy. *Microbiology* **140 (Pt 8),** 2085-92.

Choi, K. H., and Tolan, D. R. (2004). Presteady-state kinetic evidence for a ring-opening activity in fructose-1,6-(bis)phosphate aldolase. *J Am Chem Soc* **126**(11)**,** 3402-3.

Coincon, M., Daher, R., Fonvielle, M., Petra, G., Guerin, M., Jackson, M., Sygusch, J., and Therisod, M. (*In press*). Rational design, synthesis and evaluation of new selective inhibitors of microbial class II (zinc dependent) fructose bis-phosphate aldolases. *J Med Chem*.

Coincon, M., Heitz, A., Chiche, L., and Derreumaux, P. (2005). The betaalphabetaalphabeta elementary supersecondary structure of the Rossmann fold from porcine lactate dehydrogenase exhibits characteristics of a molten globule. *Proteins* **60**(4)**,** 740-5.

Coincon, M., Wang, W., Sygusch, J., and Seah, S. Y. K. (In preparation). Crystal structure of reaction intermediates in pyruvate Class II aldolase: Substrate cleavage and carbanion activation.

Cole, S. T., and Alzari, P. M. (2007). Towards new tuberculosis drugs. *Biochem Soc Trans* **35**(Pt 5)**,** 1321-4.

Collins, K. D. (1974). An activated intermediate analogue. The use of phosphoglycolohydroxamate as a stable analogue of a transiently occurring dihydroxyacetone phosphate-derived enolate in enzymatic catalysis. *J Biol Chem* **249**(1)**,** 136-42.

Commichau, F. M., Rothe, F. M., Herzberg, C., Wagner, E., Hellwig, D., Lehnik-Habrink, M., Hammer, E., Volker, U., and Stulke, J. (2009). Novel activities of glycolytic enzymes in Bacillus subtilis: interactions with essential proteins involved in mRNA processing. *Mol Cell Proteomics* **8**(6)**,** 1350-60.

Cooper, S. J., Leonard, G. A., McSweeney, S. M., Thompson, A. W., Naismith, J. H., Qamar, S., Plater, A., Berry, A., and Hunter, W. N. (1996). The crystal structure of a class II fructose-1,6-bisphosphate aldolase shows a novel binuclear metal-binding active site embedded in a familiar fold. *Structure* **4**(11)**,** 1303-1315.

da Fonseca, C. A., Jesuino, R. S., Felipe, M. S., Cunha, D. A., Brito, W. A., and Soares, C. M. (2001). Two-dimensional electrophoresis and characterization of antigens from Paracoccidioides brasiliensis. *Microbes Infect* **3**(7)**,** 535-42.

Dax, C., Coincon, M., Sygusch, J., and Blonski, C. (2005). Hydroxynaphthaldehyde phosphate derivatives as potent covalent Schiff base inhibitors of fructose-1,6-bisphosphate aldolase. *Biochemistry* **44**(14)**,** 5430-43.

Dax, C., Duffieux, F., Chabot, N., Coincon, M., Sygusch, J., Michels, P. A., and Blonski, C. (2006). Selective irreversible inhibition of fructose 1,6-bisphosphate aldolase from Trypanosoma brucei. *J Med Chem* **49**(5)**,** 1499-502.

Delfosse, V. (2008). Étude structurales de la protéine Pab87 de *Pyrococuus abyssi*. Mise en évidense d'une nouvelle famille de protéases auto-compartimentées? *Thèse*.

Dye, C. (2006). Global epidemiology of tuberculosis. *Lancet* **367**(9514)**,** 938-40.

Ellis, R. J. (2001). Macromolecular crowding: an important but neglected aspect of the intracellular environment. *Curr Opin Struct Biol* **11**(1)**,** 114-9.

Eswar, N., Webb, B., Marti-Renom, M. A., Madhusudhan, M. S., Eramian, D., Shen, M. Y., Pieper, U., and Sali, A. (2007). Comparative protein structure modeling using MODELLER. *Curr Protoc Protein Sci* **Chapter 2,** Unit 2 9.

Fernandez-Arenas, E., Molero, G., Nombela, C., Diez-Orejas, R., and Gil, C. (2004a). Contribution of the antibodies response induced by a low virulent Candida albicans strain in protection against systemic candidiasis. *Proteomics* **4**(4)**,** 1204-15.

Fernandez-Arenas, E., Molero, G., Nombela, C., Diez-Orejas, R., and Gil, C. (2004b). Low virulent strains of Candida albicans: unravelling the antigens for a future vaccine. *Proteomics* **4**(10)**,** 3007-20.

Fessner, W.-D., Schneider, A., Held, H., Sinerius, G., Walter, C., Hixon, M., and Schloss, J. V. (1996). The Mechanism of Class II, Metal-Dependent Aldolases. *Angewandte Chemie International Edition in English* **35**(19)**,** 2219-2221.

Fluegge, K., Schweier, O., Schiltz, E., Batsford, S., and Berner, R. (2004). Identification and immunoreactivity

of proteins released from Streptococcus agalactiae. *Eur J Clin Microbiol Infect Dis* **23**(11)**,** 818-24.

Fonvielle, M. (2006). Synthèse et évaluation de nouveaux inhibiteurs sélectifs de la fructose-1,6-bisphosphate aldolase de classe II. Vers de nouveaux antibiotiques de synthèse. *Thèse*.

Fonvielle, M., Coincon, M., Daher, R., Desbenoit, N., Kosieradzka, K., Barilone, N., Gicquel, B., Sygusch, J., Jackson, M., and Therisod, M. (2008). Synthesis and biochemical evaluation of selective inhibitors of class II fructose bisphosphate aldolases: towards new synthetic antibiotics. *Chemistry* **14**(28)**,** 8521-9.

Fonvielle, M., Weber, P., Dabkowska, K., and Therisod, M. (2004). New highly selective inhibitors of class II fructose-1,6-bisphosphate aldolases. *Bioorganic & Medicinal Chemistry Letters* **14**(11)**,** 2923-2926.

Frey, T., Newlin, L. L., and Atherly, A. G. (1975). Strain of Escherichia coli with a temperature-sensitive mutation affecting ribosomal ribonucleic acid accumulation. *J Bacteriol* **121**(3)**,** 923-32.

Fry, D. C. (2008). Drug-like inhibitors of protein-protein interactions: a structural examination of effective protein mimicry. *Curr Protein Pept Sci* **9**(3)**,** 240-7.

Fuccio, L., Eusebi, L. H., Zagari, R. M., and Bazzoli, F. (2009a). Helicobacter pylori eradication treatment reduces but does not abolish the risk of gastric cancer. *Am J Gastroenterol* **104**(12)**,** 3100; author reply 3101-2.

Fuccio, L., Zagari, R. M., Eusebi, L. H., Laterza, L., Cennamo, V., Ceroni, L., Grilli, D., and Bazzoli, F.

(2009b). Meta-analysis: can Helicobacter pylori eradication treatment reduce the risk for gastric cancer? *Ann Intern Med* **151**(2)**,** 121-8.

Galkin, A., Kulakova, L., Melamud, E., Li, L., Wu, C., Mariano, P., Dunaway-Mariano, D., Nash, T. E., and Herzberg, O. (2007). Characterization, kinetics, and crystal structures of fructose-1,6-bisphosphate aldolase from the human parasite, Giardia lamblia. *J Biol Chem* **282**(7)**,** 4859-67.

Galkin, A., Li, Z., Li, L., Kulakova, L., Pal, L. R., Dunaway-Mariano, D., and Herzberg, O. (2009). Structural insights into the substrate binding and stereoselectivity of giardia fructose-1,6-bisphosphate aldolase. *Biochemistry* **48**(14)**,** 3186-96.

Gandhi, N. R., Moll, A., Sturm, A. W., Pawinski, R., Govender, T., Lalloo, U., Zeller, K., Andrews, J., and Friedland, G. (2006). Extensively drug-resistant tuberculosis as a cause of death in patients co-infected with tuberculosis and HIV in a rural area of South Africa. *Lancet* **368**(9547)**,** 1575-80.

Gavalda, S., Braga, R., Dax, C., Vigroux, A., and Blonski, C. (2005). N-Sulfonyl hydroxamate derivatives as inhibitors of class II fructose-1,6-diphosphate aldolase. *Bioorg Med Chem Lett* **15**(24)**,** 5375-7.

Gerdes, S. Y., Scholle, M. D., Campbell, J. W., Balazsi, G., Ravasz, E., Daugherty, M. D., Somera, A. L., Kyrpides, N. C., Anderson, I., Gelfand, M. S., Bhattacharya, A., Kapatral, V., D'Souza, M., Baev, M. V., Grechkin, Y., Mseeh, F., Fonstein, M. Y., Overbeek, R., Barabasi, A.

L., Oltvai, Z. N., and Osterman, A. L. (2003). Experimental determination and system level analysis of essential genes in Escherichia coli MG1655. *J Bacteriol* **185**(19)**,** 5673-84.

Ghalambor, M. A., and Heath, E. C. (1962). The metabolism of L-fucose. II. The enzymatic cleavage of L-fuculose 1-phosphate. *J Biol Chem* **237,** 2427-33.

Ghalambor, M. A., and Heath, E. C. (1966). The biosynthesis of cell wall lipopolysaccharide in Escherichia coli. IV. Purification and properties of cytidine monophosphate 3-deoxy-d-manno-octulosonate synthetase. *J Biol Chem* **241**(13)**,** 3216-21.

Gijsen, H. J., Qiao, L., Fitz, W., and Wong, C. H. (1996). Recent Advances in the Chemoenzymatic Synthesis of Carbohydrates and Carbohydrate Mimetics. *Chem Rev* **96**(1)**,** 443-474.

Gotz, F., Fischer, S., and Schleifer, K. H. (1980). Purification and characterisation of an unusually heat-stable and acid/base-stable class I fructose-1,6-bisphosphate aldolase from Staphylococcus aureus. *Eur J Biochem* **108**(1)**,** 295-301.

Gray, G. R. (1971). An examination of D-fructose 1,6-diphosphate and related sugar phosphates by fourier transform 31 P nuclear magnetic resonance spectroscopy. *Biochemistry* **10**(25)**,** 4705-11.

Hall, D. R., Leonard, G. A., Reed, C. D., Watt, C. I., Berry, A., and Hunter, W. N. (1999). The crystal structure of Escherichia coli class II fructose-1,6-bisphosphate aldolase in complex with phosphoglycolohydroxamate

reveals details of mechanism and specificity. *Journal of Molecular Biology* **287**(2)**,** 383-394.

Heiss, K., Nie, H., Kumar, S., Daly, T. M., Bergman, L. W., and Matuschewski, K. (2008). Functional characterization of a redundant Plasmodium TRAP family invasin, TRAP-like protein, by aldolase binding and a genetic complementation test. *Eukaryot Cell* **7**(6)**,** 1062-70.

Henderson, I., Garcia-Junceda, E., Liu, K. K. C., Chen, Y. L., Shen, G. J., and Wong, C. H. (1994). Cloning, overexpression and isolation of the type II FDP aldolase from E. coli for specificity study and synthetic application. *Bioorganic & Medicinal Chemistry* **2**(8)**,** 837-843.

Hiratake, J. (2005). Enzyme inhibitors as chemical tools to study enzyme catalysis: rational design, synthesis, and applications. *Chem Rec* **5**(4)**,** 209-28.

Horecker, B. L., Rowley, P. T., Grazi, E., Cheng, T., and Tchola, O. (1963). The Mechanism of Action of Aldolases. Iv. Lysine as the Substrate-Binding Site. *Biochem Z* **338,** 36-51.

Ishihama, Y., Schmidt, T., Rappsilber, J., Mann, M., Hartl, F. U., Kerner, M. J., and Frishman, D. (2008). Protein abundance profiling of the Escherichia coli cytosol. *BMC Genomics* **9,** 102.

Izard, T., and Sygusch, J. (2004). Induced fit movements and metal cofactor selectivity of class II aldolases: structure of Thermus aquaticus fructose-1,6-bisphosphate aldolase. *J Biol Chem* **279**(12)**,** 11825-33.

Joerger, A. C., Mueller-Dieckmann, C., and Schulz, G. E. (2000). Structures of l-fuculose-1-phosphate aldolase mutants outlining motions during catalysis. *J Mol Biol* **303**(4)**,** 531-43.

Kamerlin, S. C., and Warshel, A. (2010). At the dawn of the 21st century: Is dynamics the missing link for understanding enzyme catalysis? *Proteins* **78**(6)**,** 1339-75.

Kao, A. W., Noda, Y., Johnson, J. H., Pessin, J. E., and Saltiel, A. R. (1999). Aldolase mediates the association of F-actin with the insulin-responsive glucose transporter GLUT4. *J Biol Chem* **274**(25)**,** 17742-7.

Karkhoff-Schweizer, R., and Knull, H. R. (1987). Demonstration of tubulin-glycolytic enzyme interactions using a novel electrophoretic approach. *Biochem Biophys Res Commun* **146**(2)**,** 827-31.

Kobes, R. D., Simpson, R. T., Vallee, R. L., and Rutter, W. J. (1969). A functional role of metal ions in a class II aldolase. *Biochemistry* **8**(2)**,** 585-8.

Koshland, D. E. (1958). Application of a Theory of Enzyme Specificity to Protein Synthesis. *Proc Natl Acad Sci U S A* **44**(2)**,** 98-104.

Koshland, D. E., Jr., Ray, W. J., Jr., and Erwin, M. J. (1958). Protein structure and enzyme action. *Fed Proc* **17**(4)**,** 1145-50.

Kroemer, M., Merkel, I., and Schulz, G. E. (2003). Structure and catalytic mechanism of L-rhamnulose-1-phosphate aldolase. *Biochemistry* **42**(36)**,** 10560-8.

Krymkiewicz, N. (1973). Reactions of methylglyoxal with nucleic acids. *FEBS Lett* **29**(1)**,** 51-54.

Kulkarni, R. R., Parreira, V. R., Sharif, S., and Prescott, J. F. (2007). Immunization of broiler chickens against Clostridium perfringens-induced necrotic enteritis. *Clin Vaccine Immunol* **14**(9)**,** 1070-7.

Lee, J. H., Bae, J., Kim, D., Choi, Y., Im, Y. J., Koh, S., Kim, J. S., Kim, M.-K., Kang, G. B., Hong, S.-I., Lee, D.-S., and Eom, S. H. (2006). Stereoselectivity of fructose-1,6-bisphosphate aldolase in Thermus caldophilus. *Biochemical and Biophysical Research Communications* **347**(3)**,** 616-625.

Lewis, D. J., and Lowe, G. (1977). Inhibition of fructose-1,6-bisphosphate aldolase from rabbit muscle and Bacillus stearothermophilus. *Eur J Biochem* **80**(1)**,** 119-33.

Ling, E., Feldman, G., Portnoi, M., Dagan, R., Overweg, K., Mulholland, F., Chalifa-Caspi, V., Wells, J., and Mizrachi-Nebenzahl, Y. (2004). Glycolytic enzymes associated with the cell surface of Streptococcus pneumoniae are antigenic in humans and elicit protective immune responses in the mouse. *Clin Exp Immunol* **138**(2)**,** 290-8.

Linz, B., Balloux, F., Moodley, Y., Manica, A., Liu, H., Roumagnac, P., Falush, D., Stamer, C., Prugnolle, F., van der Merwe, S. W., Yamaoka, Y., Graham, D. Y., Perez-Trallero, E., Wadstrom, T., Suerbaum, S., and Achtman, M. (2007). An African origin for the intimate

association between humans and Helicobacter pylori. *Nature* **445**(7130)**,** 915-8.

Lobo, Z. (1984). Saccharomyces cerevisiae aldolase mutants. *J Bacteriol* **160**(1)**,** 222-6.

Lolis, E., and Petsko, G. A. (1990). Transition-state analogues in protein crystallography: probes of the structural source of enzyme catalysis. *Annu Rev Biochem* **59,** 597-630.

Luby-Phelps, K. (2000). Cytoarchitecture and physical properties of cytoplasm: volume, viscosity, diffusion, intracellular surface area. *Int Rev Cytol* **192,** 189-221.

Lundmark, R., and Carlsson, S. R. (2004). Regulated membrane recruitment of dynamin-2 mediated by sorting nexin 9. *J Biol Chem* **279**(41)**,** 42694-702.

Maughan, D. W., Henkin, J. A., and Vigoreaux, J. O. (2005). Concentrations of glycolytic enzymes and other cytosolic proteins in the diffusible fraction of a vertebrate muscle proteome. *Mol Cell Proteomics* **4**(10)**,** 1541-9.

McCammon, J. A., Gelin, B. R., and Karplus, M. (1977). Dynamics of folded proteins. *Nature* **267**(5612)**,** 585-90.

Meloche, H. P., and Glusker, J. P. (1973). Aldolase catalysis: single base-mediated proton activation. *Science* **181**(97)**,** 350-2.

Mitchell, C., Morris, P. W., Lum, L., Spiegelman, G., and Vary, J. C. (1992). The amino acid sequence of a Bacillus subtilis phosphoprotein that matches an orfY-tsr coding sequence. *Mol Microbiol* **6**(10)**,** 1345-9.

Murzin, A. G., Brenner, S. E., Hubbard, T., and Chothia, C. (1995). SCOP: a structural classification of proteins database for the investigation of sequences and structures. *J Mol Biol* **247**(4)**,** 536-40.

Nagano, N., Orengo, C. A., and Thornton, J. M. (2002). One fold with many functions: the evolutionary relationships between TIM barrel families based on their sequences, structures and functions. *J Mol Biol* **321**(5)**,** 741-65.

Naismith, J. H., Ferrara, J. D., Bailey, S., Marshall, K., Dauter, Z., Wilson, K. S., Habash, J., Harrop, S. J., Berry, A. J., and Hunter, W. N. (1992). Initiating a crystallographic study of a class II fructose-1,6-bisphosphate aldolase. *J Mol Biol* **225**(4)**,** 1137-41.

O'Brien, R. J., and Nunn, P. P. (2001). The need for new drugs against tuberculosis. Obstacles, opportunities, and next steps. *Am J Respir Crit Care Med* **163**(5)**,** 1055-8.

O'Reilly, G., and Clarke, F. (1993). Identification of an actin binding region in aldolase. *FEBS Lett* **321**(1)**,** 69-72.

Palm, J. E., Weiland, M. E., Griffiths, W. J., Ljungstrom, I., and Svard, S. G. (2003). Identification of immunoreactive proteins during acute human giardiasis. *J Infect Dis* **187**(12)**,** 1849-59.

Pegan, S. D., Rukseree, K., Franzblau, S. G., and Mesecar, A. D. (2009). Structural Basis for Catalysis of a Tetrameric Class IIa Fructose 1,6-Bisphosphate Aldolase from Mycobacterium tuberculosis. *Journal of Molecular Biology* **386**(4)**,** 1038-1053.

Plater, A. R., Zgiby, S. M., Thomson, G. J., Qamar, S., Wharton, C. W., and Berry, A. (1999). Conserved

residues in the mechanism of the E. coli class II FBP-aldolase. *Journal of Molecular Biology* **285**(2)**,** 843-855.

Ponder, J. W., and Case, D. A. (2003). Force fields for protein simulations. *Adv Protein Chem* **66,** 27-85.

Pouyssegur, J., and Stoeber, F. (1974). Genetic control of the 2-keto-3-deoxy-d-gluconate metabolism in Escherichia coli K-12: kdg regulon. *J Bacteriol* **117**(2)**,** 641-51.

Pricer, W. E., Jr., and Horecker, B. L. (1960). Deoxyribose aldolase from Lactobacillus plantarum. *J Biol Chem* **235,** 1292-8.

Qamar, S., Marsh, K., and Berry, A. (1996). Identification of arginine 331 as an important active site residue in the class II fructose-1,6-bisphosphate aldolase of Escherichia coli. *Protein Sci* **5**(1)**,** 154-61.

Ray, P. H., and Benedict, C. D. (1980). Purification and characterization of specific 3-deoxy-D-manno-octulosonate 8-phosphate phosphatase from Escherichia coli B. *J Bacteriol* **142**(1)**,** 60-8.

Richards, O. C., and Rutter, W. J. (1961). Preparation and properties of yeast aldolase. *J Biol Chem* **236,** 3177-84.

Rodaki, A., Young, T., and Brown, A. J. (2006). Effects of depleting the essential central metabolic enzyme fructose-1,6-bisphosphate aldolase on the growth and viability of Candida albicans: implications for antifungal drug target discovery. *Eukaryot Cell* **5**(8)**,** 1371-7.

Romano, A. H., and Conway, T. (1996). Evolution of carbohydrate metabolic pathways. *Res Microbiol* **147**(6-7)**,** 448-55.

Ronai, Z. (1993). Glycolytic enzymes as DNA binding proteins. *Int J Biochem* **25**(7)**,** 1073-6.

Rose, I. A., O'Connell, E. L., and Mehler, A. H. (1965). Mechanism of the Aldolase Reaction. *J Biol Chem* **240,** 1758-65.

Rupp, B. (2009). "Biomolecular Crystallography: Principles, Practice, and Application to Structural Biology." 1st ed. Garland Science, New York.

Rutter, W. J. (1964). Evolution of Aldolase. *Fed Proc* **23,** 1248-57.

Rutter, W. J., and Ling, K. H. (1958). The mechanism of action of fructose diphosphate aldolase. *Biochim Biophys Acta* **30**(1)**,** 71-9.

Salama, N. R., Shepherd, B., and Falkow, S. (2004). Global transposon mutagenesis and essential gene analysis of Helicobacter pylori. *J Bacteriol* **186**(23)**,** 7926-35.

Sassetti, C. M., and Rubin, E. J. (2003). Genetic requirements for mycobacterial survival during infection. *Proc Natl Acad Sci U S A* **100**(22)**,** 12989-94.

Scamuffa, M. D., and Caprioli, R. M. (1980). Comparison of the mechanisms of two distinct aldolases from Escherichia coli grown on gluconeogenic substrates. *Biochim Biophys Acta* **614**(2)**,** 583-90.

Schaeffer, R. D., Fersht, A., and Daggett, V. (2008). Combining experiment and simulation in protein

folding: closing the gap for small model systems. *Curr Opin Struct Biol* **18**(1)**,** 4-9.

Schumperli, M., Pellaux, R., and Panke, S. (2007). Chemical and enzymatic routes to dihydroxyacetone phosphate. *Appl Microbiol Biotechnol* **75**(1)**,** 33-45.

Schwelberger, H. G., Kohlwein, S. D., and Paltauf, F. (1989). Molecular cloning, primary structure and disruption of the structural gene of aldolase from Saccharomyces cerevisiae. *Eur J Biochem* **180**(2)**,** 301-8.

Sibley, L. D. (2003). Toxoplasma gondii: perfecting an intracellular life style. *Traffic* **4**(9)**,** 581-6.

Siebers, B., Brinkmann, H., Dorr, C., Tjaden, B., Lilie, H., van der Oost, J., and Verhees, C. H. (2001). Archaeal fructose-1,6-bisphosphate aldolases constitute a new family of archaeal type class I aldolase. *J Biol Chem* **276**(31)**,** 28710-8.

Sinha, N., and Smith-Gill, S. J. (2005). Molecular dynamics simulation of a high-affinity antibody-protein complex: the binding site is a mosaic of locally flexible and preorganized rigid regions. *Cell Biochem Biophys* **43**(2)**,** 253-73.

Smith, G. M., and Mildvan, A. S. (1981). Nuclear magnetic resonance and chemical modification studies of the role of the metal in yeast aldolase. *Biochemistry* **20**(15)**,** 4340-6.

Smith, G. M., Mildvan, A. S., and Harper, E. T. (1980). Nuclear relaxation studies of the interaction of

substrates with a metalloaldolase from yeast. *Biochemistry* **19**(6)**,** 1248-55.

St-Jean, M. (2007). Multifonctionnalité de l'aldolase glycolytique : mécanisme catalytique et interaction avec un peptide de la protéine du syndrome Wiskott-Aldrich *Thèse*.

St-Jean, M., Blonski, C., and Sygusch, J. (2009). Charge stabilization and entropy reduction of central lysine residues in fructose-bisphosphate aldolase. *Biochemistry* **48**(21)**,** 4528-37.

St-Jean, M., Izard, T., and Sygusch, J. (2007). A hydrophobic pocket in the active site of glycolytic aldolase mediates interactions with Wiskott-Aldrich syndrome protein. *J Biol Chem* **282**(19)**,** 14309-15.

St-Jean, M., Lafrance-Vanasse, J., Liotard, B., and Sygusch, J. (2005). High resolution reaction intermediates of rabbit muscle fructose-1,6-bisphosphate aldolase: substrate cleavage and induced fit. *J Biol Chem* **280**(29)**,** 27262-70.

St-Jean, M., and Sygusch, J. (2007). Stereospecific proton transfer by a mobile catalyst in mammalian fructose-1,6-bisphosphate aldolase. *J Biol Chem* **282**(42)**,** 31028-37.

Starnes, G. L., Coincon, M., Sygusch, J., and Sibley, L. D. (2009). Aldolase is essential for energy production and bridging adhesin-actin cytoskeletal interactions during parasite invasion of host cells. *Cell Host Microbe* **5**(4)**,** 353-64.

Su, C. H., Merlie, J. P., and Goldfine, H. (1975). Rapid cessation of phospholipid synthesis in fructose-1,6-diphosphate aldolase mutants of Escherichia coli. *J Bacteriol* **122**(2)**,** 565-9.

Takahashi, K. (1977). The reactions of phenylglyoxal and related reagents with amino acids. *J Biochem* **81**(2)**,** 395-402.

Takayama, S., McGarvey, G. J., and Wong, C. H. (1997). Microbial aldolases and transketolases: new biocatalytic approaches to simple and complex sugars. *Annu Rev Microbiol* **51,** 285-310.

Talbot, N. J. (2003). On the trail of a cereal killer: Exploring the biology of Magnaporthe grisea. *Annu Rev Microbiol* **57,** 177-202.

Thomson, G. J., Howlett, G. J., Ashcroft, A. E., and Berry, A. (1998). The dhnA gene of Escherichia coli encodes a class I fructose bisphosphate aldolase. *Biochem J* **331 (Pt 2),** 437-45.

Tunio, S. A., Oldfield, N. J., Berry, A., Ala'Aldeen, D. A., Wooldridge, K. G., and Turner, D. P. (2010). The moonlighting protein fructose-1, 6-bisphosphate aldolase of Neisseria meningitidis: surface localization and role in host cell adhesion. *Mol Microbiol* **76**(3)**,** 605-15.

Vogiatzi, P., Cassone, M., Luzzi, I., Lucchetti, C., Otvos, L., Jr., and Giordano, A. (2007). Helicobacter pylori as a class I carcinogen: physiopathology and management strategies. *J Cell Biochem* **102**(2)**,** 264-73.

Volker, K. W., and Knull, H. (1997). A glycolytic enzyme binding domain on tubulin. *Arch Biochem Biophys* **338**(2)**,** 237-43.

Volker, K. W., and Knull, H. R. (1993). Glycolytic enzyme-tubulin interactions: role of tubulin carboxy terminals. *J Mol Recognit* **6**(4)**,** 167-77.

Volker, K. W., Reinitz, C. A., and Knull, H. R. (1995). Glycolytic enzymes and assembly of microtubule networks. *Comp Biochem Physiol B Biochem Mol Biol* **112**(3)**,** 503-14.

Walsh, J. L., Keith, T. J., and Knull, H. R. (1989). Glycolytic enzyme interactions with tubulin and microtubules. *Biochim Biophys Acta* **999**(1)**,** 64-70.

Wang, J., Morris, A. J., Tolan, D. R., and Pagliaro, L. (1996). The molecular nature of the F-actin binding activity of aldolase revealed with site-directed mutants. *J Biol Chem* **271**(12)**,** 6861-5.

Warburg, O., Christian,W. (1943). Isolation und Kristallisation des Garungsferments Zymohexase. *Biochemische Zeitschrift* **314,** 149-176.

Weissbach, A., and Hurwitz, J. (1959). The formation of 2-keto-3-deoxyheptonic acid in extracts of Escherichia coli B. I. Identification. *J Biol Chem* **234**(4)**,** 705-9.

Whitesides, G. M., and Wong, C.-H. (1985). Enzymes as Catalysts in Synthetic Organic Chemistry [New Synthetic Methods (53)]. *Angewandte Chemie International Edition in English* **24**(8)**,** 617-638.

Witke, C., and Gotz, F. (1993). Cloning, sequencing, and characterization of the gene encoding the class I

fructose-1,6-bisphosphate aldolase of Staphylococcus carnosus. *J Bacteriol* **175**(22)**,** 7495-9.

Wong, C. H. (1996). Chemoenzymatic synthesis: application to the study of carbohydrate recognition. *Acta Chem Scand* **50**(3)**,** 211-8.

Wu, R., Hu, P., Wang, S., Cao, Z., and Zhang, Y. (2009). Flexibility of Catalytic Zinc Coordination in Thermolysin and HDAC8: A Born−Oppenheimer ab Initio QM/MM Molecular Dynamics Study. *Journal of Chemical Theory and Computation* **6**(1)**,** 337-343.

Yin, Z., Stead, D., Selway, L., Walker, J., Riba-Garcia, I., McLnerney, T., Gaskell, S., Oliver, S. G., Cash, P., and Brown, A. J. (2004). Proteomic response to amino acid starvation in Candida albicans and Saccharomyces cerevisiae. *Proteomics* **4**(8)**,** 2425-36.

Zgiby, S., Plater, A. R., Bates, M. A., Thomson, G. J., and Berry, A. (2002). A functional role for a flexible loop containing Glu182 in the class II fructose-1,6-bisphosphate aldolase from Escherichia coli. *Journal of Molecular Biology* **315**(2)**,** 131-140.

Zgiby, S. M., Thomson, G. J., Qamar, S., and Berry, A. (2000). Exploring substrate binding and discrimination in fructose1, 6-bisphosphate and tagatose 1,6-bisphosphate aldolases. *Eur J Biochem* **267**(6)**,** 1858-68.

Zimmer, D. B., Wright Sadosky, P., and Weber, D. J. (2003). Molecular mechanisms of S100-target protein interactions. *Microsc Res Tech* **60**(6)**,** 552-9.